BRNO UNIVERSITY OF TECHNOLOGY
VYSOKÉ UČENÍ TECHNICKÉ V BRNĚ

FACULTY OF ELECTRICAL ENGINEERING AND COMMUNICATION
FAKULTA ELEKTROTECHNIKY
A KOMUNIKAČNÍCH TECHNOLOGIÍ

DEPARTMENT OF CONTROL AND INSTRUMENTATION
ÚSTAV AUTOMATIZACE A MĚŘICÍ TECHNIKY

AERIAL ENVIRONMENTAL MAPPING IN RECONNAISSANCE ROBOTICS
BEZPILOTNÍ PRŮZKUM PROSTŘEDÍ V MOBILNÍ ROBOTICE

DOCTORAL THESIS
DIZERTAČNÍ PRÁCE

AUTHOR — **Ing. Petr Gábrlík**
AUTOR PRÁCE

SUPERVISOR — **prof. Ing. Luděk Žalud, Ph.D.**
ŠKOLITEL

BRNO 2020

ABSTRACT

In the last decade, aerial photogrammetry performed with small unmanned aircraft systems has been developed into a progressive technology applicable across multiple fields and branches. The regular approach employing control points for georeferencing is characterized by high accuracy and reliability; however, it can also be considered generally unusable in some special scenarios. This thesis has been conceived to design and discuss a sensor system that allows direct georeferencing in unmanned photogrammetry; in this context, the author also proposes relevant calibration methods and verifies the performance of the entire setup. A significant portion of the presented research involves identifying new opportunities for the novel mapping method. Two of the potential applications are characterized thoroughly: Environmental mapping, namely, the determination of snow cover parameters, and robotic radiation search. These activities embody tasks where the system enables us to eliminate the human health risks associated with a concrete environment. The actual benefits and overall usability are assessed within real-world experiments.

KEYWORDS

Aerial photogrammetry, unmanned aircraft systems, mobile robotics, environmental mapping, CBRNE.

ABSTRAKT

Letecká fotogrammetrie v oblasti bezpilotních systémů představuje rychle rozvíjející se obor nalézající uplatnění napříč nejen průmyslovými odvětvími. Široce rozšířená metoda nepřímého georeferencování založená na vlícovacích bodech sice dosahuje vysoké přesnosti a spolehlivosti, v některých speciálních aplikacích nicméně není použitelná. Tato disertační práce se zabývá vývojem senzorického systému pro přímé georeferencování aplikovatelného na malých bezpilotních prostředcích a dále také návrhem vhodných kalibračních metod a testováním přesnosti. Významná část práce je věnována novým oblastem, kde může navržený systém pomoci eliminovat bezpečnostní rizika spojená s daným prostředím. V tomto kontextu byl systém testován v reálných podmínkách při mapování sněhu v horských oblastech a při robotickém mapování radiace.

KLÍČOVÁ SLOVA

Letecká fotogrammetrie, bezpilotní letadla, mobilní robotika, environmentální mapování, CBRNE.

GÁBRLÍK, Petr. *Aerial Environmental Mapping in Reconnaissance Robotics*. Brno, 2020, 217 p. Doctoral thesis. Brno University of Technology, Faculty of Electrical Engineering and Communication, Department of Control and Instrumentation. Advised by prof. Ing. Luděk Žalud, Ph.D.

DECLARATION

I declare that I have written the Doctoral Thesis titled "Aerial Environmental Mapping in Reconnaissance Robotics" independently, under the guidance of the advisor and using exclusively the technical references and other sources of information cited in the thesis and listed in the comprehensive bibliography at the end of the thesis.

As the author I furthermore declare that, with respect to the creation of this Doctoral Thesis, I have not infringed any copyright or violated anyone's personal and/or ownership rights. In this context, I am fully aware of the consequences of breaking Regulation § 11 of the Copyright Act No. 121/2000 Coll. of the Czech Republic, as amended, and of any breach of rights related to intellectual property or introduced within amendments to relevant Acts such as the Intellectual Property Act or the Criminal Code, Act No. 40/2009 Coll., Section 2, Head VI, Part 4.

Brno ....

author's signature

ACKNOWLEDGEMENT

I would like to thank my supervisor, Ludek Zalud, for his invaluable guidance and help through each stage of my Ph.D. study, and my colleagues from the Robotics and AI group, where Tomas Jilek and Tomas Lazna in particular have deserved special mention for their assistance during the field experiments. I am also very grateful to Premysl Janata of Mendel University in Brno for the instrumentation-related support, without which the research would have been immensely difficult to perform; to Petra Kalvodova, for patiently reading and commenting on my work; and to Petr Sladek, who contributed his knowledge to secure the experiments involving ionizing radiation. I thank Anders la Cour-Harbo, my supervisor at Aalborg University, where I gathered intensive professional experience and gained an insight into the workings of a different research facility. Thanks should also go to Premysl Dohnal, for proofreading selected portions of the text, and to Pavol Harar, for inspiring me in how to compose a cumulative dissertation. Last but not least, it is a pleasant duty to mention my family and fiancée Romana, who supported me tirelessly all along.

The results presented would not have been attainable without the instrumentation of CEITEC, a research center of Brno University of Technology, and the R&D projects I participated in; of these, the most significant ones were *Robotics 4 Industry 4.0* (CZ.02.1.01/0.0/0.0/15_003/0000470) funded by European Regional Development Fund, and *Centre for Applied Cybernetics 3* (TE01020197), a project of the Technology Agency of the Czech Republic. My publications were also supported by the Internal science fund of Brno University of Technology (FEKT-S-14-2429, FEKT-S-17-4234).

Contents

I. Preamble **9**

1. Introduction **10**

1.1. Motivation 13

1.2. Aims and Objectives 15

1.3. Outline 16

2. State of the Art **17**

2.1. Photogrammetry 17

2.2. Georeferencing 20

3. Research Summary **26**

4. Concluding Discussion **31**

Bibliography **40**

II. Publications **41**

A. Precise Multi-Sensor Georeferencing System for Micro UAVs **42**

B. Calibration and Accuracy Assessment in a Direct Georeferencing ... **57**

C. Cooperation Between an Unmanned Aerial Vehicle and ... **93**

D. Towards Automatic UAS-Based Snow-Field Monitoring for ... **124**

E. Using an Automated Heterogeneous Robotic System for Radiation ... **157**

III. Appendices **214**

A. List of Author's Publications **215**

Part I.

Preamble

1. Introduction

At present, unmanned aircraft embody a very progressive and fast-growing technology. Although pilotless flying vehicles have existed since the second half of the 20$^{\text{th}}$ century, they have been almost exclusively utilized by the military for reconnaissance and weapon carrying purposes. At the turn of the millennium, the technological advancement and descending cost of key components produced an increased interest on the part of civil corporations and institutions, such as universities, science centers, and commercial subjects. In this context, multi-rotor machines have become especially popular, representing a concept very different from that of the military vehicles employed in the previous century. This category gained in importance mainly thanks to the aircraft's ability to hover and handle relatively weighty payload with respect to its size.

A massive expansion of unmanned aircraft systems (UAS) occurred in the last decade. In the U.S., the number of registered unmanned vehicles reached 1.5 million at the beginning of 2020 (considering both commercial and leisure operators) [1], and up to 2.8 million items are expected in 2024 [2]: In other words, the market may double within four years. However, the actual numbers can be much higher, as not all of the vehicles are subjected to registration, with a certain amount operated illegally. In the Czech Republic, where commercially used UASs are registered, the count has grown from 27 in 2012 to 3,155 in early 2020 [3]. Major interest is observable also within the scientific community: *Web of Science*, a leading citation database, contains more than 5,000 UAS-relevant records published in 2019, while fewer than 800 items had been released in the year of 2010[1] (Figure 1.1).

Today, it seems almost impossible to believe that the currently most famous commercial UAS manufacturer, Shenzhen DJI Sciences and Technologies Ltd., better known as DJI, released their first consumer-grade UAS *Phantom* not long ago, in 2013. Presently, DJI has a global market share of approximately 70% [4]. Most of the aircraft sold range within the consumer category; however, a visible trend to

[1]The search was limited by the following terms contained in the title, abstract, and keywords of indexed articles and proceedings: UAS, UAV, drone, unmanned aircraft system, unmanned aerial vehicle, unmanned aircraft, RPAS, remotely piloted aircraft system. The data are valid for 2 July 2020, and they do not reflect the research outcomes unpublished or unindexed to that date.

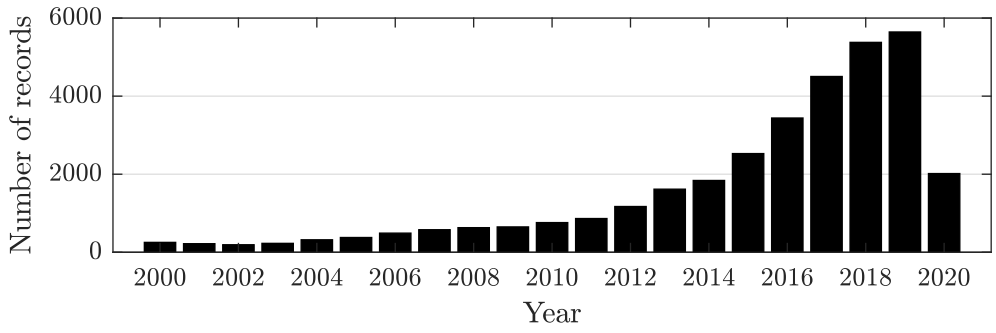

Figure 1.1.: The number of UAS-related articles and proceedings indexed by the *Web of Science* database according to the publishing year (non-cumulative graph).

cover the professional and industrial segments has appeared in the recent years.

The term *UAS* is typically used to denote systems including aircraft without a human pilot aboard, i.e., unmanned aerial vehicles (UAVs) and associated elements such as a ground station, communication system, and support equipment. The diversity of the systems is enormous: The dimensions and weights vary from, for example, 20 meters and 18,000 kg (wingspan and gross weight) in the well-known *General Atomics MQ-9A Reaper* unmanned combat aerial vehicle [5] to 0.3 m and 0.9 kg in the *DJI Mavic 2*, a popular consumer-grade vehicle [6]. This thesis focuses on commonly available commercial UASs and aircraft utilized in the civil sector, assuming size and weight values that enable single-person manipulation and operation. The discussed vehicles are very promising in many segments, predominantly thanks to the following benefits: low cost, wide availability, and easy and safe operation. Unmanned aircraft can be classified according to other parameters too, such criteria comprising endurance, maximum speed, and reachable altitude; the most important factor, however, rests in the maximum take-off mass (MTOM), which plays a substantial role even in the new European Commission regulation 2019/945 [7]. According to this categorization, the above-defined aircraft fall within the C2 and C3 classes, where the corresponding MTOM limits are 4 and 25 kg, respectively; in the literature, the UAS categories are often called light, mini, or small. The discussed aircraft typically allow flying with an extra payload of up to several kilograms, a value sufficient for the objectives of this thesis.

Alongside the rapid expansion of civil unmanned systems, many new options have opened up across diverse fields, yielding applications previously deemed unfeasible via piloted vehicles, due to, above all, economic reasons, safety concerns, or a lack of suitable technologies. Consequently, the current usage includes, among others, automatic package delivery, security and monitoring, close-range inspection and remote sensing, pesticide spraying, entertainment purposes (such as movie shooting),

search and rescue operations, and leisure tasks. From the professional perspective, remote sensing in particular has gained immense popularity across multiple industries. Generally, this technique involves acquiring information about objects or the Earth in a contactless manner and may be performed via passive (e.g., visible and infrared imaging) or active sensors, including, for example, a radar or a LiDAR. The former of these two approaches is by far the more widely utilized one, especially as regards image sensor-based passive sensing in the visible spectrum: The sensors are usually cheap and light-weight, thus being appropriate for every UAS class. Moreover, thanks to the present computer vision (CV) algorithms and computing power, the image data are suitable for not only producing the actual aerial imagery and orthophotos but also generating high-resolution spatial data, such as point clouds and digital elevation models (DEM). This technology is basically known as photogrammetry.

Unmanned aircraft, along with photogrammetry, became a true game changer in many industries. The technique proved to be useful in estimating snow depth in the Arctic [8], performing tree inventories [9], inspecting transmission lines [10], monitoring crop height [11], visualizing archaeological sites [12], detecting topographic changes [13], computing stockpile volumes [14], monitoring radiation waste storage facilities [15], inspecting bridges [16], and many other activities. The papers, in general, emphasize similar benefits compared to conventional methods, namely, the low operation cost, easy and fast deployment, and superior resolution.

As the photogrammetric results are commonly processed via geographic information systems (GIS) to supplement other map layers or loaded in other software tools to extract dimensions and object sizes, compute volumes, or analyze trends, accurate georeferencing constitutes a vital procedure. A widespread technique rests in indirect georeferencing, a method utilizing ground control points (GCP) visible across the aerial imagery to deliver reliable, highly accurate outcomes even with inexpensive onboard sensors. Conversely, direct georeferencing, which relies on precise onboard sensors, is somewhat less popular: The approach is characterized by considerable complexity of the system, the necessity to perform inter-sensor calibration and synchronization, lower accuracy and reliability, and an overall higher cost. However, against these drawbacks there also stand several indisputable benefits, including but not limited to independence from the ground targets, an aspect that endows the method with wide applicability in many industries, those that involve environments featuring major accessibility difficulties or safety risks in particular.

The topics relating to GCP-independent remote sensing have constituted the main research interest of the author of the thesis since 2014. At that time, this subdomain was rather marginal within small unmanned aircraft; however, the expansion of UASs and associated applications in the present decade has contributed to the

broader focus on the discussed topic. The outcomes of the thesis are then to be viewed in this context, as at least some of the author's original results from several years ago may have become relatively common knowledge. Nevertheless, the progress currently observable across the research teams and the commercial sector confirms that the study direction was chosen appropriately; despite this, however, various aspects have not been addressed sufficiently, especially as regards possible new applications.

Last but not least, further dissemination of UAS applications is limited by the legislation, which is only gradually modified to cover the rapid technological advancement, often restricts faster progress, and may embody a bureaucratic burden; such concerns nevertheless appear to be rather irrelevant in affiliated fields, including terrestrial robotics. The challenges and possibilities of the discussed UAS class are also addressed within the forecast of the Federal Aviation Administration (FAA[2]) [17]:

> *While introduction of UAS in the NAS* (national airspace system, author's note) *has opened up numerous possibilities, it has brought operational challenges including safe integration into the NAS. Despite these challenges, the UAS sector holds enormous promise; potential uses include modelers experimenting with small UAS (sUAS) performing numerous functions such as aerial photography; recreational flying for personal uses; sUAS experimenting with package delivery on a commercial basis; delivery of medical supplies; and provision of support for search and rescue missions following natural calamities.*

1.1. Motivation

The widely employed UAS photogrammetry relies on control points, thus being essentially inapplicable in situations where the ground targets cannot be utilized for some reason; in this context, one can mention potentially hazardous environments, such as those involving chemical, biological, radiological, nuclear, and explosive (CBRNE) risks. For example, the 2011 Fukushima Daiichi nuclear accident showed the potential of unmanned vehicles in inspecting highly contaminated areas (Figure 1.2a); from the author's perspective, the capabilities of the technology were further illustrated by the 2014 Vrbetice (the Czech Republic) incident, where an exploding ammunition depot caused significant damage to immovable property

[2]Federal Aviation Administration embodies the civil aviation authority under the United States' Department of Transportation.

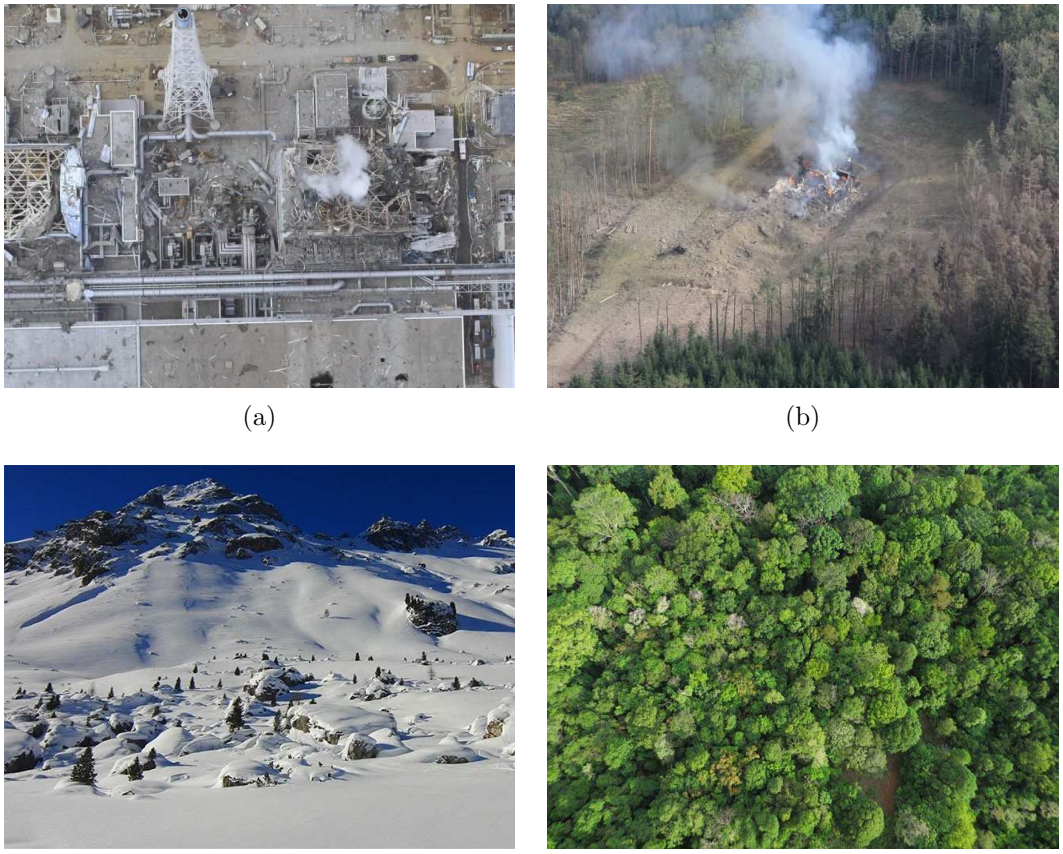

(a) (b)

(c) (d)

Figure 1.2.: Examples of real-world scenarios where the indirect georeferencing technique is generally inapplicable: the collapsed reactor buildings of the Fukushima Daiichi nuclear power plant after the disaster [19] (a); the ruined ammunition depot in Vrbetice [20] (b); estimation of the snow cover parameters in Alpine terrain [18] (c); dense forest mapping [21] (d).

and greatly reduced the land usability options (Figure 1.2b). In similar scenarios, up-to-date, accurately georeferenced orthophotos and DEMs may support the ground operations, including the navigation of terrestrial robots or analyses centered on structural and topographical changes. Human safety risks, however, are omnipresent in natural environments, too. The mapping of snow covers in mountainous regions, a task performable with UASs [18], comprises a serious danger of avalanches, making the deployment of GCPs very difficult 1.2c.

The use of indirect georeferencing is limited also by problems other than human health-related risks: The technique requires good visibility of the GCPs from the air, and sufficient GNSS satellite observation must be ensured to localize the targets; such conditions are hardly achievable in, for instance, dense forests 1.2d.

Forest mapping and tree inventorization are commonly carried out via unmanned aircraft, and if the ground work involving GCP deployment were eliminated, the method would offer not only markedly improved applicability but also reduced time of the supporting field activities; such a time-saving scenario may then lead towards effective cost cutting.

The areas where GCP-free UAS photogrammetry embodies a potentially beneficial approach can be summarized as follows:

- Inaccessible areas (e.g., post-disaster locations, mountainous regions).
- Dangerous environments (e.g., environments with CBRNE threats).
- Poor sky visibility areas (such as forests).
- Time-limited operations: The deployment of GCPs is time-intensive.
- Automated missions: Direct georeferencing improves the automation rate of the data acquisition and processing.

1.2. Aims and Objectives

The aim of the research presented herein is to develop a sensor system for ground control point-free aerial photogrammetry performed via small unmanned aircraft. Such a system would expand the usability limits of UASs, especially in human-hostile environments as discussed above. Currently, direct georeferencing is employed rather marginally within the relevant UAS class, as the key component to achieve high object accuracies, namely, the GNSS receiver capable of carrier-phase tracking, was not available until recently. State-of-the-art technologies in navigation systems and digital cameras allow us to construct lightweight photogrammetric tools; despite this advantage, however, various issues and aspects have to be addressed, involving in particular those that relate to system calibration, performance determination, and overall applicability in real-world applications and scenarios.

The central aims of the thesis can be defined as follows:

Aim 1: Developing a multi-sensor system to facilitate direct georeferencing in aerial photogrammetry performed via small UASs; the adopted approach integrates state-of-the-art technologies in the given segment.

Aim 2: Designing a calibration procedure for the system and determining its performance.

Aim 3: Verifying the system's usability and usefulness in real-world conditions and scenarios related to mobile robotics and environmental mapping, above all, missions where the common GCP-based UAS photogrammetry is inapplicable.

1.3. Outline

This thesis discusses the author's main research results via compiling some of his major publications. The actual text is organized into two sections: *Preamble* and *Publications*. The first, or introductory, part proposes the aims and objectives, and presents the *state of the art* in the above-characterized research domains, photogrammetry and georeferencing in particular. Additionally, the *Research Summary* chapter provides an overview of the author's most significant research activities and publications, and the section *Concluding Discussion* summarizes the outcomes with respect to the original goals.

The second portion, *Publications*, is dedicated to selected results produced by the author, containing five full-text papers that cover the entire span of the research activities; four of the articles, namely, one proceedings item and three journal papers, were already peer-reviewed, while the remaining manuscript is currently under review (August 2020). Each publication is introduced by fundamental information on its actual character, version, funding, and the author's contribution.

A complete list of the author's articles, including both those which strongly relate to the discussed field and those concerning different UAS topics, is presented in appendix within the *List of Author's Publications* section.

2. State of the Art

This section summarizes the state-of-the-art in the necessary components to perform the control point-free UAS photogrammetry; namely, the attention is directed to a photogrammetry pipeline integrated within the actual software tools, and georeferencing possibilities and results given by available sensors for the discussed UAS classes. Current trends in UAS photogrammetry deployment within environmental mapping and CBRNE robotics is discussed later in the Publications section with respect to the individual topics discussed therein.

2.1. Photogrammetry

Aerial photogrammetry, a technique that allows obtaining spatial information about objects visible at aerial images, and reconstructing positions, sizes and shapes, is older than digital cameras, GNSSs, computers, and unmanned aircraft, namely, components closely related with the photogrammetry of these days. A fundamental textbook *Photogrammetry* by Prof. Karl Kraus[1] from 1982 [22], and the subsequent editions of this book covered the photogrammetry area thoroughly for the first time. Nevertheless, although the technology changed profoundly, the basic principles describing a camera's central projection in three-dimensional space, collinearity equations, stereoprocessing approaches, aerial triangulation etc. remain unchanged. Thanks to the wide availability of computing power and CV algorithms, the well known principles are presently completed with new methods enabling, for example, high-density geometry reconstruction and fully automatic processing.

Typical photogrammetric products utilized in remote sensing are the orthophoto and items representing the spatial model of the real world, namely, the point cloud, mesh, or DEM. Generating such outcomes from aerial imagery is not feasible by a simple method; the processing is comprehensive and involves numerous different techniques to attain sub-results necessary for the subsequent phases (Figure 2.1). Such complete pipelines are currently integrated within multiple professional software tools, such as Pix4D Pix4Dmapper [23], or Agisoft Metashape[2] (formerly

[1] Institute of Photogrammetry and Remote Sensing, Vienna University of Technology

[2] Agisoft Metashape was exclusively utilized for the photogrammetric processing in all of the author's publications presented in this thesis.

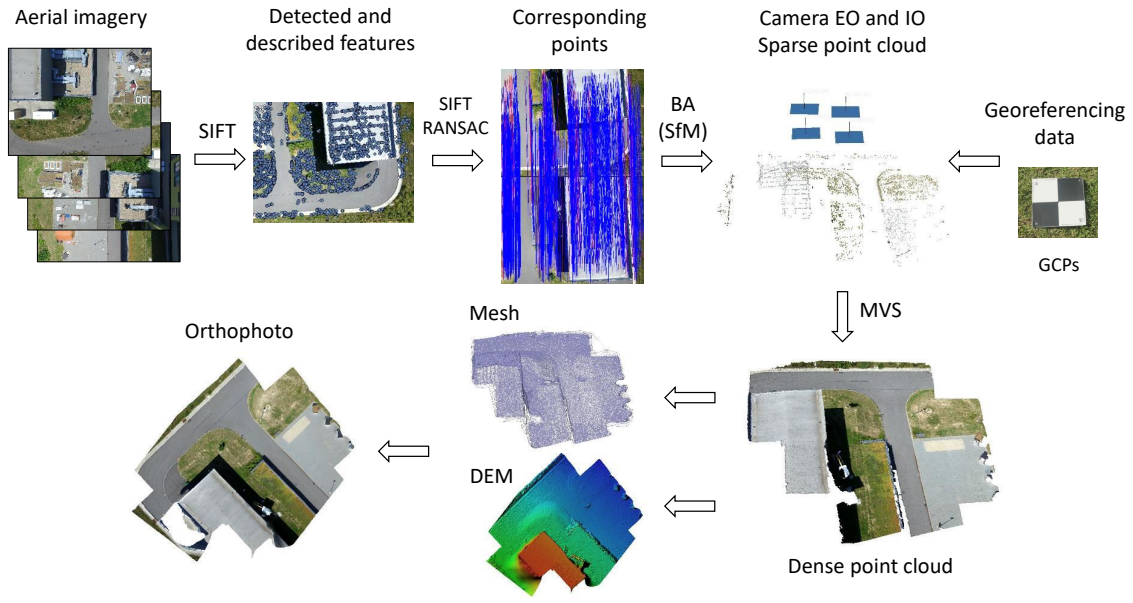

Figure 2.1.: One of the possible processing workflow integrated in current photogrammetric softwares.

known as Agisoft Photoscan) [24], a widely used photogrammetry pipeline tool within a research community.

An essential task for the geometry reconstruction is to determine corresponding points across the overlapped images; in other words, this activity can be characterized as searching for significant (feature) points in images that have different pixel coordinates but belong to the same object point in the real world [25]. Numerous algorithms for local feature detection and description have been designed thus far; one of the widely employed ones is Scale Invariant Feature Transform (SIFT) [26] and its derivatives. The SIFT algorithm integrates both feature detection, i.e., searching for locations which are locally significant and may be found in other images (corners, typically), and feature description, a procedure involving gradient-based numerical description of the keypoint surrounding. The technique's robustness may be increased by applying an outlayer detection algorithm to filter wrong cross-image matches, for example, RANdom SAmple Consensus (RANSAC) [25]. An evident prerequisite for the feature matching rests in the necessity of a rich and non-repetitive texture, which, together with sufficient lighting conditions, forms a major constraint for the photogrammetry in general.

The detection of the corresponding points typically embodies the first pipeline step, and is a precondition for camera pose estimation and sparse point cloud generation. In the past, this task was facilitated via manually selected tie points visible within overlapped images; however, the aforementioned CV-based technique enables automatic selection of even thousands points securing high robustness of the sub-

sequent processing phases. Although various approaches are available to determine camera orientations (both the exterior and the interior ones[3]), and object point coordinates, the most widely employed one with respect to optimality and applicability to multiple images is bundle adjustment (BA) [25, 27, 28]. This method encompasses one comprehensive least-square approach to estimate the camera poses and 3D point locations simultaneously, and thanks to the high redundancy facilitated by the significant amount of image corresponding points, the method is further usable in estimating extra unknown parameters – camera intrinsic orientation, for example (BA with self calibration/additional parameters) [22]. The self- calibration ability is one of the central reasons why non-metric consumer-grade cameras find broad application in current photogrammetry.

The point cloud generated by using this method may give us an insight into the scene structure (BA embodies a Structure from Motion (SfM) method); still, such a point cloud is usually very sparse with respect to the considered applications. A dense structure reconstruction is achievable by employing a stereo matching method applied to image pairs or multiple images at once, i.e., Multi-View Stereo (MVS). The algorithms accomplish the given task from the overlapped images and known camera exterior and interior orientations obtainable from, for example, BA [29, 25]. Even though numerous MVS implementations exist, dense pixelwise correspondence search remains the central challenge in this field, especially considering uncontrolled environment with scene and lighting variabilities [30, 29, 31, 32]. State-of-the-art MVS algorithms nevertheless enable us to attain high-density, homogeneous structure reconstruction; however, the results may still not be satisfactory at poorly textured and illuminated areas.

While point-based scene description can be utilized directly in some applications, it is typically converted into a continuous representation, such as a triangle mesh or DEM. The former of these products is commonly used in computer graphics or, in the context of aerial photogrammetry, to generate a textured 3D model of a certain area. The task is achievable via numerous methods; one of the most widely favored ones rests in 3D Delaunay triangulation and its derivatives [33, 34]. The latter option, the DEM, describes the surface model by employing a regular grid of height values. The evident drawback of this format lies in the fact that only one height value is assignable to each cell; still, this representation is well suited for many tasks. The raster models are commonly utilized for spatial analysis in GISs, which enables us to derive slopes, aspect, or detect topographic changes exploiting simple calculations over overlapped, georeferenced layers; another target

[3]Exterior (EO) and interior orientations (IO) stand for camera extrinsic and intrinsic parameters, respectively; namely, the camera position and attitude, and numerous linear and non-linear IO parameters, such as the focal length, principal point coordinates, and distortion parameters.

field is mobile robotics, where the technique resolves navigation problems by means of various path search algorithms. The DEM generation task mainly deals with transforming irregular spatial data into a regular grid, namely, a procedure involving the derivation of height values which have not been observed; a task achievable by an interpolation [28, 35].

The products of the aforementioned processing steps enable us to generate the orthophoto, a typical outcome of photogrammetry that embodies an image of the object in orthogonal parallel projection. Since this type of projection is hardly achievable by employing real cameras, orthophotos are usually composed synthetically, via a known surface model. The process, or indirect transformation, involves four steps: initializing an empty orthophoto image matrix; finding the height coordinate from the surface model at the same horizontal location (this procedure necessarily embodies an interpolation); determining corresponding image coordinates by utilizing the known EO and IO; assigning the image pixel value to the corresponding orthophoto location (this step requires the interpolation of the pixel values) [22]. In aerial photogrammetry, the orthophoto regularly consists of multiple aerial images captured at different time moments and coordinates to cover a larger area; thus, the orthophoto pixel values are determined from multiple images. The achieved parallel projection ensures that the performed distance measurements at the orthophoto equal the distances in the actual reference frame.

Even though the photogrammetric techniques are still being investigated by various researchers and offer many opportunities for improvement, the aims of this thesis do not consist in modifying the processing pipeline, enhancing current methods, or developing new ones; rather than that, the goal is to employ state-of-the-art software tools to support GCP-free remote sensing in complex or novel robotic and environmental mapping tasks.

2.2. Georeferencing

If no georeferencing data are involved in the above-described pipeline, the photogrammetry products may be computed relatively to, for example, the first camera exterior orientation; the usability of such outcomes is, however, somewhat limited. Two major georeferencing approaches are applied in general: indirect and direct georeferencing (IG and DG, respectively). While the former option uses ground control points with known object coordinates, the latter one relies on direct measurements of a camera's exterior orientation parameters. In both cases, the referencing to an object frame can be achieved via multiple manners or within different stages of the processing pipeline. Once a relative photogrammetric model and camera poses have been determined, the referencing may be accomplished by means of 7-parameter

similarity transformation involving three translations, three rotations, and one scaling parameter [36, 22, 37]. Even though the least-square method is utilized to find the best fit of the model and the referencing data (GCPs or/and absolute camera EOs), non-linear model deformations cannot be compensated this way. A more suitable approach introduces the referencing data into the BA procedure along with detected corresponding points which leads to the optimal solution with respect to not only matching points and camera parameters, but also the reference points with known object coordinates (GCPs) [28, 36, 22].

Whereas in the case of IG the estimation of a camera's extrinsic parameters forms a vital step, this procedure is not required within the DG, since the positions and orientations of the cameras are estimated directly, exploiting an onboard sensor. Still, the direct use of the estimated EO is not usual (especially in UAS photogrammetry); instead, the values are refined during an optimization process to find the overall best fit. This technique, computer vision-assisted DG, may possibly reduce some errors and increase the accuracy of photogrammetric products in general. Last but not least, the georeferencing approaches could be advantageously combined: Utilizing direct EO measurements together with GCPs may lead to accurate and reliable results even with a small number of control points; moreover, these points could help us to suppress some systematic errors or inaccuracies in the camera calibration.

Obtaining the geographical coordinates of the real-world object points forms an essential task, regardless of the georeferencing approach applied. In the case of the indirect technique, the task comprises determining the coordinates of the GCPs (black and white patterned targets or natural significant points). This step is feasible in multiple ways; most frequently, land surveying equipment, such as total stations and GNSSs, is utilized. The former instrument was designed for accurate angle and distance measurements enabling relative coordinate determination via triangulation techniques and determining absolute locations by comprising points from the geodetic point field. Even though modern robotic total stations allow automatic tracking of moving objects, their main advantage rest in the high reliability and precision during the localization of static object points.

The latter technology is applicable within both georeferencing methods in UAS photogrammetry. GNSS finds wide use across many branches; aerial photogrammetry, however, places higher demands on the accuracy than the prevailing applications. The centimeter accuracy level, namely, the desired precision range in this field [22], is attainable thanks to the carrier-phase tracking technique. Within this approach, the phase of the carrier wave is measured in addition to the standard code-based measurements, enabling us to determine a location with sub-wavelength precision (the wavelengths are approximately 2 decimeter long, depending on the used frequencies). The central problem within this task rests in determining the

number of carrier cycles between the satellite and the receiver (rover), i.e., an integer ambiguity search [38]. For this reason, another static GNSS receiver is required to provide observations at exactly known coordinates, facilitating the solution of the ambiguity problem at the rover site. Such a task may be accomplished in the real time or within post-processing, referred to as real-time kinematics (RTK) and post-processed kinematic (PPK), respectively.

The carrier-phase GNSS embodies a suitable technology for the direct camera position estimation; nevertheless, with respect to the UAS dynamics, limited GNSS positioning rate, and the necessity to determine the camera orientation, the sensor system for DG has to be completed with an inertial navigation system (INS). Such devices typically integrate both an inertial measurement unit (IMU) involving accelerometers and gyroscopes for 3D linear acceleration and angular rate measurement, respectively, and a navigation processor to estimate velocities, position, attitude, and other quantities (a task commonly accomplished by using the extended Kalman filter (EKF) [39]) [38]. Due to the cumulative errors present therein, the auxiliary data from an absolute sensor, such as the GNSS or a magnetometer, have to be included in the estimation process. The GNSS/INS integration enables us to not only increase the position estimation rate but also bridge over possible brief GNSS outages. However, the position and attitude determined via this approach never correspond to the camera's EO, due to the physical displacement and misalignment of the GNSS antenna, IMU, and image sensor. This problem is tackled through inter-sensor calibration, a topic addressed within many research projects and also the author's publication included in this thesis (paper *Calibration and Accuracy Assessment in a Direct ...*).

The indirect technique is profitable mainly within those applications where high accuracy and reliability are required; researchers mostly report centimeter-level object accuracy even with uncalibrated (consumer-grade) cameras and fast-flying UASs. For example, *Barry and Coakley* presented the RMS object error rates of 2.3 and 3.5 cm in the XY plane and Z coordinate, respectively; the aerial data were acquired using a fixed-wing UAS flying at 90 m AGL (10 mm GSD) [40]. Similar results, 5.3 and 6.8 cm RMSE, respectively, were achieved by *Fazeli et al.* with a four-rotor UAS flying at 120 m AGL (24 mm GSD) [41] and by *Casella et al.*, who reported even sub-GSD accuracy, namely, 18 mm when flying at 70 m AGL [42]. Some of the present research outcomes render achievable accuracy approaching GSD level; however, the georeferencing quality depends on not only the accuracy of the GCPs but also the number and spatial distribution of these points. This topic previously embodied a topical issue in the context of manned photogrammetry [22] and still remains a problem of interest [43, 44].

Direct EO determination began to be discussed and examined at the turn of

the millennium, given the increasing availability of GPS. The promising technology trend could be illustrated through the 1999 article *Direct Geocoding – is Aerial Triangulation Obsolete?* by M. Cramer [45], which assessed this method in the context of manned photogrammetry; however, other authors analyzed the topic too (e.g., J. Skaloud, M. Rehak) [46, 37, 47]. Nevertheless, meter or slightly sub-meter attainable accuracy could not compete with the traditional GCP-based approach in many applications.

Multi-sensor integration for UAS remote sensing has embodied an openly discussed problem since the beginning of the 2010s, thanks to the wider availability of differential and PPK/RTK GNSSs and INSs with a reasonable size and pricing. This field involves many aspects; attention is paid to the system design and inter-sensor calibration, together with estimating the time delays, assessing the accuracy, and finding proper use cases. The calibration of the displacement and misalignment of individual sensors, namely, estimating the lever arms and boresight angles, is attainable in multiple ways, such as using laser scanning of the sensor system [48] or employing a close-range or in-situ calibration field to produce reference, aerial triangulation-based EO data [48, 49]. The latter technique is, in general, more suitable, but its reliability may be affected by a synchronization delay between the camera and the GNSS/INS. The delay is laboratory-determinable via a special tool allowing us to capture the exact time moment of the image acquisition with respect to the synchronization signal [50, 49]; alternatively, the task can be subjected to a comprehensive in-flight estimation procedure comprising multiple calibration parameters. In practice, any inaccurate synchronization translates the time error into an exterior orientation error [50].

At the time the author of this thesis started outlining his concept of a multi-sensor system, UASs integrating such technology were not commonly available, and relevant topics were discussed almost exclusively within research groups. Early multi-sensor integration for UASs had been proposed by *M. Nagai et al.* in 2009 [51]; in the project, a 300 kg helicopter was fitted with GPS/IMU and a stereo camera system to achieve decimeter-level georeferencing accuracy exploiting hybrid INS supported by bundle block adjustment. Accurate georeferencing utilizing a compact, eight-rotor flying platform was characterized in a 2012 paper published by *M. Blaha et al.* [52]. The post-processed, differential GPS increased the positioning accuracy by an order of magnitude; still, the decimeter-level accuracy did not meet the original expectations. Nevertheless, the presented technique for obtaining reference positioning data via a robotic total station may be considered an innovative solution. In the same year, another article demonstrated sub-meter image georeferencing accuracy in a UAS weighting less than 1 kg [53].

Integrating an RTK GNSS onto a micro UAS, a step necessary for increasing

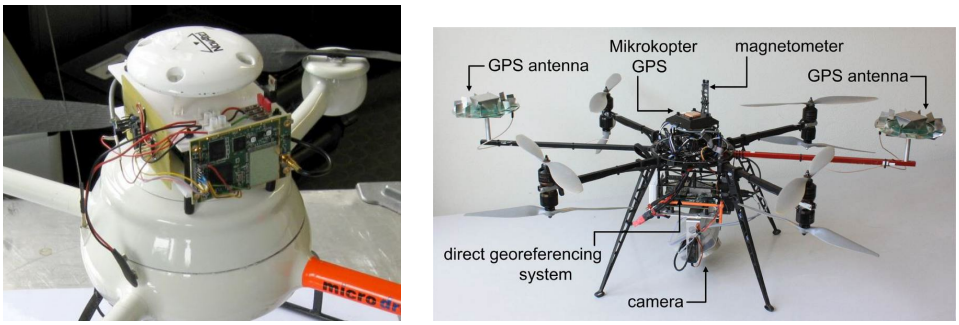

(a) (b)

Figure 2.2.: An example of early experimental setups comprising multi-sensor systems for direct EO determination in UAS photogrammetry from 2012 (a) [54] and 2015 (b) [49].

the georeferencing accuracy, was described within the 2012 paper by *M. Rieke et al.* [54] (Figure 2.2a). Even though the setup did not fulfill the original accuracy expectations, it addressed the fundamental problems associated with the approach, such as correction transmission or data synchronization. A comprehensive study was introduced by *M. Rehak* in 2013 [50]; the custom-built multi-rotor UAS equipped with an RTK GPS receiver and in-house INS was subjected to various calibration procedures, including those determining the camera's IO parameters, shutter lag, and lever arms. The preliminary results obtained by using a close-range calibration field indicated the possibility of attaining a centimeter-level image georeferencing accuracy; yet, real-world photogrammetry missions still need to be performed to determine the object point georeferencing quality. Very promising results were presented by *C. Eling et al.* in their 2015 study [49]; the multi-sensor system integrated a dual-antenna RTK GNSS receiver to provide not only the accurate position but also true-heading information to support attitude estimation (Figure 2.2b). Even though the presented georeferencing accuracy ranging within the centimeter level was achieved under close-to-ideal flight conditions (20 m AGL altitude, 2 m/s speed), the outcomes definitely suggest that the DG may possibly compete with the GCP-based approach. At that time, related topics were addressed by other researchers as well (e.g., [55, 56, 57, 58, 41]).

The aforementioned studies, all published relatively recently, indicate that the direct georeferencing technique in UAS photogrammetry is gaining in popularity among researchers and will likely become an alternative to the control point-based technique. Still, with respect to the high demands on the sensor system, its calibration, and inter-sensor synchronization, an overall improvement of the method's reliability poses a challenge to be addressed in the future. Moreover, most of the hitherto published results were obtained in almost ideal conditions; thus, the perfor-

mance in real-word scenarios remains a factor to be analyzed in depth. Despite the fact that UAS photogrammetry has many aspects in common with its alternative branch practised via manned aircraft, certain characteristics, such as the ability to operate automatically or acquire products with superior resolution via low-altitude flying, open new possibilities for the future.

3. Research Summary

At the very beginning, the author's main research interest was within the development of a multi-rotor UAS intended to complete ATEROS (formerly known as CASSANDRA) [59, 60], a heterogeneous mobile robotic system developed by the Robotics and AI group headed by Prof. Zalud at Brno University of Technology. The central purpose of the multi-robot system rests in performing various reconnaissance and CBRNE missions via diverse terrestrial platforms. Robots from the Orpheus family, an underlying project designed to develop a four-wheel portable platform, have been utilized within various missions and experiments, such as those involving radiation mapping or water contamination measurement [61, 62]. Integrating the individual platforms into the ATEROS system allows the operator to control the robots remotely, by utilizing a uniform user interface, and to switch between them with regard to the actual needs of the mission; alternatively, some platforms are capable of performing certain mission tasks automatically, eliminating user interventions. To improve the system's overall usability, an aerial platform, a four-rotor UAS Uranus, was developed and integrated into ATEROS. These tasks constituted the author's main research aims until 2014; with respect to the expansion of unmanned systems, as discussed in the introduction, and also due to the increasing availability of suitable platforms on the market, the more recent aims and objectives shifted towards the application of UASs in environmental mapping and CBRNE robotics. More concretely in this context, increased emphasis was put on topics subsumed within ground control point-free aerial photogrammetry and, simultaneously, the utilization of the method in the discussed domains of robotics.

As the thesis stresses the author's selected publications, this section is intended to describe the context of the individual research outcomes and associated activities, together with those released through other papers not included herein. The results are also graphically summarized within Table 3.1.

The initial assignments in the discussed field mainly concerned the testing of the hardware components that allow us to directly determine the EO parameters; the components consisted in a carrier-phase measurement-enabled GNSS and an INS enabling the inclusion of external aiding data into the estimation process. The eventual sensor setup comprised a dual-antenna GNSS receiver that facilitated determining via the RTK technology not only the accurate position but also the true heading;

2014/2015 • **Prior work**

Hardware components testing, designing sensor system, and performing initial non-flight and flight tests. Publishing the preliminary findings at local conferences.

2015/2016 • **Internship at Aalborg University (AAU)**

Obtaining new experiences in UAS and photogrammetry field, and conducting experiments with a fixed-wing UAS.

2016 • **Precise Multi-Sensor Georeferencing System for ...**

Conference paper

Describing the multi-sensor system design and the results of the first test flight with the fully operable system.

2018 • **Calibration and Accuracy Assessment in a Direct ...**

Journal article

Introducing a calibration procedure for the sensor system, and performing a comprehensive accuracy assessment.

2018 • **Cooperation Between an Unmanned Aerial Vehicle ...**

Journal article

Designing a multi-robot procedure for a radiation source localization, and conducting tests utilizing previously obtained data.

2019 • **Towards Automatic UAS-Based Snow-Field ...**

Journal article

Real condition system testing during the mapping of a snow cover depth in the Krkonose Mountains.

2020 • **Using an Automated Heterogeneous Robotic System ...**

Submitted manuscript

Introducing a state-of-the-art multi-robot method for radiation surveys integrating both photogrammetry and radiation measurements, and performing a comprehensive experiment.

Table 3.1.: The timeline of the selected publications and related activities.

Figure 3.1.: The initial test flight with an early sensor system version showed the necessity of certain construction modification, but also verified the compatibility with UAS's hardware components (2015).

such an approach was unusual within UASs at that time. By using several non-flight experiments, we validated the functionality of the concept and released the preliminary results at local conferences [63]. Still, these early publication outcomes pointed to the author's rather limited orientation in the photogrammetry field. The first UAS flight with a trial version of the sensor system was completed in 2015 (Figure 3.1), thanks to the supporting instrumentation from Mendel University in Brno. For the author, the lack of an unmanned platform embodied a considerable obstacle preventing faster development and testing cycles.

A worthwhile opportunity to foster the author's professional development consisted in the internship guaranteed by the department of *Automation and Control* at *Aalborg University*, where Assoc. Prof. A. la Cour-Harbo provided much of his valuable experience in drone research. The field testing with a fixed-wing UAS enabled the author to markedly expand his knowledge of photogrammetry and unmanned mission planning.

The fully operable multi-sensor system was initially published within a paper entitled *Precise Multi-Sensor Georeferencing System for Micro UAVs* [64], presented at *14th IFAC Conference on Programmable Devices and Embedded Systems* in 2016. The article comprises information about the sensor setup, test flight results, and ideas concerning the system calibration and time synchronization.

The calibration, namely, a procedure estimating the synchronization delay and the displacement and misalignment of the individual sensors, is of vital importance for achieving a high georeferencing accuracy. An in-flight calibration method employing aerial triangulation-based reference data to support the least-square estimation of the aforementioned calibration parameters was designed and then released in the

International Journal of Remote Sensing[1] in 2018 through the article *Calibration and Accuracy Assessment in a Direct Georeferencing System for UAS Photogrammetry* [65]. This key publication addresses not only the calibration technique but also the overall verification of the system's performance via a comprehensive experiment confirming the reachability of a centimeter-level object accuracy during a common UAS photogrammetry mission.

As the presented PhD research was motivated predominantly by the effort to find new opportunities for control point-free remote sensing in environmental mapping and tasks involving CBRNE threads, the next step rested in subjecting the technology to tests based on real-world scenarios. The subsequent paper entitled *Cooperation Between an Unmanned Aerial Vehicle and an Unmanned Ground Vehicle in Highly Accurate Localization of Gamma Radiation Hotspots* [66], published in the *International Journal of Advanced Robotic Systems*[2] in 2018, assessed the potential of cooperation between UASs and UGVs during radiation search missions. This application perfectly fits the *Robotics and AI* group scope, and the data collected within previous experiments were employed to design a procedure for highly automated radiation source localization.

The usability of the multi-sensor system was further verified within another real-word application: An experiment conducted in cooperation with the Krkonose Mountains National Park Administration demonstrated the benefits of the approach during an estimation of the snow field depth in a remote mountainous area. The elimination of ground controls reduces the field work required and the potential risks associated with avalanches. The task is thoroughly described in the article *Towards Automatic UAS-Based Snow-Field Monitoring for Microclimate Research* [67] published in *Sensors*[3] in 2019; this paper also addresses the workflow from the aerial imagery acquisition to the estimation of the snow field parameters.

Utilizing the findings presented within the above-mentioned paper on radiation search, we proposed a state-of-the-art procedure to facilitate highly automated multi-platform radiation surveys. The activities in the given field culminated with a comprehensive experiment to demonstrate the benefits of combining diverse robotic platforms to accomplish such a CBRNE task. Further, the design and use of a three-phase technique that involves aerial photogrammetry to enable aerial and terrestrial radiation mapping are the central topics of the manuscript *Using an Automated Heterogeneous Robotic System for Radiation Surveys* [68], which is currently being

[1] IF 2.49, Q2 in the *remote sensing* category, special issue titled *Unmanned Aerial Systems (UAS) for Environmental Applications*

[2] IF 1.22, Q4 in the *robotics* category, special issue titled *Mobile Robots*

[3] IF 3.28, Q1 in the *instruments and instrumentation* category, special issue titled *UAV or Drones for Remote Sensing Applications in GPS/GNSS Enabled and GPS/GNSS Denied Environments*

considered for publication (August 2020). Beyond the scope of this assignment, the author published two other conference papers analyzing UAS-based radiation mapping simulation [69, 70].

4. Concluding Discussion

The results achieved within this Ph.D. research are classifiable into three areas corresponding to the original aims defined within the Aims and Objectives section. In this context, the initial efforts consisted in the development of the photogrammetric system for UASs, and due to certain circumstances, the outcome can be considered unique with respect to similar research pursued elsewhere at the time. As a suitable unmanned platform was unavailable to the author during the initial phases of the project, the adopted concept had to integrate all necessary components on a single rigid frame, making the system completely independent of the UAS. This approach generally enables the user to employ the system in different vehicles, without the need of recalibration; however, the actual usability is limited to multi-rotor UASs with a payload capacity of not less than 2.5 kg. The system's portability was verified via testing by various UAS operators, namely, Mendel University in Brno, the Krkonose Mountains National Park Administration, and the Military Technical Institute of the Czech Republic (Figure 4.1). The components integrated into the system represent the state of the art in the given segment, allowing us to attain a georeferencing accuracy at the same level as that known from GCP-based photogrammetry; moreover, the dual-antenna design to secure reliable attitude estimation constituted a pioneering solution within the UAS market.

Considering the different system calibration techniques published by other researchers, a custom-made procedure was designed to fulfill the specific requirements of the research. The proposed in-flight method estimates not only the geometric parameters, such as the displacement of the sensors, but also the synchronization delay. This embodies a step of vital importance, especially in systems involving consumer-grade sensors (for instance, digital cameras). While the calibration is supported by some photogrammetric softwares, its functionalities are limited to the lever arm estimation, omitting possible delay; this drawback then may cause poor accuracy in the results. Using the custom-made calibrating procedure to improve the georeferencing performance was assessed thoroughly by means of a test flight emulating a real-world photogrammetry mission. Although the outcomes indicate that the indirect method clearly outperforms the direct one, the object accuracy achieved (approx. 4 cm spatial RMS error at a GSD of 2 cm) fully satisfies the requirements of the above-defined applications in field robotics.

(a) (b)

Figure 4.1.: The designed multi-sensor system was employed on different unmanned platforms: a DJI S800, in snow mapping (a), and a BRUS UAS, within a multi-robot radiation mapping experiment (b).

With respect to the extensive progress in UASs that was materialized during the last decade, the situation in the discussed field changed considerably, too. In view of the decreasing costs of crucial components, the carrier phase-enabled GNSS in particular, major UAS manufacturers introduced platforms allowing accurate geo-referencing of aerial imagery (e.g., the SenseFly eBee plus, 2016; DJI Phantom 4 RTK, 2018; Yuneec H520 RTK, 2019; and DJI Matrice 300 RTK, 2020). Moreover, some of the products comprise a dual antenna RTK system to support attitude determination, an approach tested since 2014 by the author of this thesis. Even though the author's research appears to have been directed in an appropriate manner, as presently indicated by the trends in the commercial sphere, the room for further improvement is rather limited (due to precisely the multiple options available on the market); the interests and efforts to ensure further enhancement of the concept should thus be shifted towards tackling new tasks associated with the actual use of this technology.

Assessing the applicability of the sensor system in both real-world scenarios involving CBRNE robotics and environmental mapping embodied a vital part of the project. In this context, two distinct processes were addressed, namely, snow cover mapping in mountainous regions and radiation search. Considering the former of these two tasks, the usefulness of the system was verified via cooperation with the Krkonose Mountains National Park Administration, a joint activity to estimate the snow depth at a prominent snow field (Mapa republiky). The technology met the expectations as regards eliminating the safety risks related to the usage of GCPs, and the attained accuracy satisfied the requirements for the given assignment. Still, assuming the actual conditions, utilizing several check points is recommendable to increase the overall reliability of the mapping products.

The latter area examined, robotic radiation mapping and source localization, was analyzed thoroughly within several conference and journal articles, and the results obtained during the simulations and experiments may be regarded as reaching beyond the state of the art in this field. The control point free photogrammetry proved to be a key method to provide updated and accurate maps of regions comprising CBRNE risks; the products enabled us, above all, to solve the path planning problems connected with the diverse robotic platforms employed to fulfill the radiation mapping tasks.

Although the comprehensive technique for multi-robot mapping described in the last of the papers within the thesis was designed to eliminate human operators as much as possible, the current trends in robotics are towards real-time data processing, allowing us to reach an even higher level of autonomy. In applications where the absolute accuracy of mapping products does not stand at the forefront of the efforts, simultaneous localization and mapping (SLAM), together with data-driven mission planning, may change the mapping process markedly, paving the way for fully autonomous systems. Such approaches embody a suitable options for employing robots in GNSS-denied environments, or speeding-up threat's localization during CBRNE missions. Still, UAS photogrammetry as interpreted in this thesis will certainly become a standard tool within diverse fields in the future, especially in those applications, where GIS embodies a standard processing tool.

Bibliography

[1] Federal Aviation Administration. UAS by the Numbers, 2020. [cit. 2020-06-24]. URL: https://www.faa.gov/uas/resources/by_the_numbers/.

[2] Federal Aviation Administration. Fact Sheet - The Federal Aviation Administration (FAA) Aerospace Forecast Fiscal Years (FY) 2020-2040, 2020. [cit. 2020-06-24]. URL: https://www.faa.gov/news/fact_sheets/news_story.cfm?newsId=24756.

[3] Urad pro civilni letectvi. Vyrocni zprava UCL 2019, 2020. [cit. 2020-08-25]. URL: https://www.caa.cz/wp-content/uploads/2020/07/VZ_UCL2019_FIN.pdf.

[4] Allison Lampert. Amid privacy backlash, China's DJI unveils drone-to-phone tracking. *Reuters*, November 2019. [cit. 2020-6-24]. URL: https://www.reuters.com/article/us-aviation-drones-idUSKBN1XN2JR.

[5] Alexander Stillwell. *Special Forces in Action: Elite forces operations, 1991-2011.* Amber Books Ltd, London, December 2012. ISBN: 978-1-909160-42-2.

[6] DJI. Mavic 2 - See the Bigger Picture, 2020. [cit. 2020-7-2]. URL: https://www.dji.com/cz/mavic-2.

[7] European Commission. Commission Delegated Regulation (EU) 2019/945 of 12 March 2019 on unmanned aircraft systems and on third-country operators of unmanned aircraft systems, June 2019. [cit. 2019-6-11]. URL: http://data.europa.eu/eli/reg_del/2019/945/oj/eng.

[8] Emiliano Cimoli, Marco Marcer, Baptiste Vandecrux, Carl E. Bggild, Guy Williams, and Sebastian B. Simonsen. Application of Low-Cost UASs and Digital Photogrammetry for High-Resolution Snow Depth Mapping in the Arctic. *Remote Sensing*, 9(11):1144, November 2017. URL: http://www.mdpi.com/2072-4292/9/11/1144, doi:10.3390/rs9111144.

[9] Tom Mikita, Pemysl Janata, and Peter Surov. Forest Stand Inventory Based on Combined Aerial and Terrestrial Close-Range Photogrammetry. *Forests*, 7(8):165, July 2016. URL: http://www.mdpi.com/1999-4907/7/8/165, doi:10.3390/f7080165.

[10] San Jiang, Wanshou Jiang, Wei Huang, and Liang Yang. UAV-Based Oblique Photogrammetry for Outdoor Data Acquisition and Offsite Visual Inspection of Transmission Line. *Remote Sensing*, 9(3):278, March 2017. URL: https://www.mdpi.com/2072-4292/9/3/278, doi:10.3390/rs9030278.

[11] D. Belton, P. Helmholz, J. Long, and A. Zerihun. Crop Height Monitoring Using a Consumer-Grade Camera and UAV Technology. *PFG Journal of Photogrammetry, Remote Sensing and Geoinformation Science*, 87(5):249–262, December 2019. URL: https://doi.org/10.1007/s41064-019-00087-8, doi:10.1007/s41064-019-00087-8.

[12] Jitte Waagen. New technology and archaeological practice. Improving the primary archaeological recording process in excavation by means of UAS photogrammetry. *Journal of Archaeological Science*, 101:11–20, 2019. URL: http://www.sciencedirect.com/science/article/pii/S0305440318306423, doi:https://doi.org/10.1016/j.jas.2018.10.011.

[13] Mike R. James, Stuart Robson, and Mark W. Smith. 3-D uncertainty-based topographic change detection with structure-from-motion photogrammetry: precision maps for ground control and directly georeferenced surveys. *Earth Surface Processes and Landforms*, 42(12):1769–1788, 2017. URL: http://onlinelibrary.wiley.com/doi/10.1002/esp.4125/abstract, doi:10.1002/esp.4125.

[14] Grazia Tucci, Antonio Gebbia, Alessandro Conti, Lidia Fiorini, and Claudio Lubello. Monitoring and Computation of the Volumes of Stockpiles of Bulk Material by Means of UAV Photogrammetric Surveying. *Remote Sensing*, 11(12):1471, January 2019. Number: 12 Publisher: Multidisciplinary Digital Publishing Institute. URL: https://www.mdpi.com/2072-4292/11/12/1471, doi:10.3390/rs11121471.

[15] Dean Connor, Peter Martin, Chris Hutson, Huw Pullin, Nick Smith, and Tom Scott. The Use of Unmanned Aerial Vehicles for Rapid and Repeatable 3D Radiological Site Characterization-18352. In *Waste Management Symposia 2018*, Phoenix, 2018. URL: https://research-information.bristol.ac.uk/en/publications/the-use-of-unmanned-aerial-vehicles-for-rapid-and-repeatable-3d-radiological-site-characterization18352(29a7ebf7-f38a-4d87-b60d-b51a7afb1227).html.

[16] Ali Khaloo, David Lattanzi, Keith Cunningham, Rodney DellAndrea, and Mark Riley. Unmanned aerial vehicle inspection of the Placer River Trail Bridge through image-based 3D modelling. *Structure and Infrastructure Engineering*, 14(1):124–136, January 2018. URL: https://doi.org/10.1080/15732479.2017.1330891, doi:10.1080/15732479.2017.1330891.

[17] Federal Aviation Administration. FAA Aerospace Forecast: Fiscal Years 2020-2040, 2020. [cit. 2020-7-9]. URL: https://www.faa.gov/data_research/aviation/aerospace_forecasts/media/FY2020-40_FAA_Aerospace_Forecast.pdf.

[18] Marc S. Adams, Yves Bhler, and Reinhard Fromm. Multitemporal Accuracy and Precision Assessment of Unmanned Aerial System Photogrammetry for Slope-Scale Snow Depth Maps in Alpine Terrain. *Pure and Applied Geophysics*, 175(9):3303–3324, September 2018. URL: https://doi.org/10.1007/s00024-017-1748-y, doi:10.1007/s00024-017-1748-y.

[19] Daily Mail Reporter. First clear pictures show the true devastation at the Fukushima nuclear plant as Japan flies unmanned drone over stricken reactor, April 2011. [cit. 2018-5-30]. URL: http://www.dailymail.co.uk/news/article-1372589/First-clear-pictures-true-devastation-Fukushima-nuclear-plant-Japan-flies-unmanned-drone-stricken-reactor.html.

[20] Monika Kozumplikova. 03-Vybuch munice ve skladu ve Vrbeticich, 3. den rano - Policie Ceske republiky, 2014. [cit. 2020-7-15]. URL: https://www.policie.cz/clanek/archiv-zpravodajstvi-uo-zlin-2015-03-vybuch-munice-ve-skladu-ve-vrbeticich-3-den-rano.aspx.

[21] Lian Pin Koh and Serge Wich. TED Global 2013 speaker Lian Pin Koh on Conservation Drones, 2013. [cit. 2018-5-29]. URL: http://robohub.org/ted-global-2013-speaker-lian-pin-koh-on-conservation-drones/.

[22] Karl Kraus. *Photogrammetry: Geometry from Images and Laser Scans*, volume 2nd ed. Walter de Gruyter, Berlin, 2007. ISBN: 978-3-11-019007-6.

[23] Pix4D. Pix4Dmapper, 2020. [cit. 2020-7-24]. URL: https://www.pix4d.com/product/pix4dmapper-photogrammetry-software.

[24] Agisoft LLC. Metashape, 2020. [cit. 2020-7-24]. URL: https://www.agisoft.com/.

[25] Richard Szeliski. *Computer Vision: Algorithms and Applications*. Texts in Computer Science. Springer, London, 2011. ISBN: 978-1-84882-934-3. URL: https://www.springer.com/gp/book/9781848829343.

[26] David G. Lowe. Distinctive Image Features from Scale-Invariant Keypoints. *International Journal of Computer Vision*, 60(2):91–110, November 2004. URL: https://doi.org/10.1023/B:VISI.0000029664.99615.94, doi:10.1023/B:VISI.0000029664.99615.94.

[27] Richard Hartley and Andrew Zisserman. *Multiple View Geometry in Computer Vision*, volume 2nd ed. Cambridge University Press, Cambridge, 2003. ISBN: 978-0-521-54051-3. URL: https://www.cambridge.org/core/books/multiple-view-geometry-in-computer-vision/0B6F289C78B2B23F596CAA76D3D43F7A.

[28] Wolfgang Frstner and Bernhard P. Wrobel. *Photogrammetric Computer Vision: Statistics, Geometry, Orientation and Reconstruction*. Geometry and Computing. Springer International Publishing, 2016. ISBN: 978-3-319-11549-8. URL: https://www.springer.com/us/book/9783319115498.

[29] Steven M. Seitz, Brian Curless, James Diebel, Daniel Scharstein, and Richard Szeliski. A Comparison and Evaluation of Multi-View Stereo Reconstruction Algorithms. In *Proceedings of the 2006 IEEE Computer Society Conference on Computer Vision and Pattern Recognition - Volume 1*, CVPR '06, pages 519–528, USA, June 2006. IEEE Computer Society. URL: https://doi.org/10.1109/CVPR.2006.19, doi:10.1109/CVPR.2006.19.

[30] Johannes L. Schnberger, Enliang Zheng, Jan-Michael Frahm, and Marc Pollefeys. Pixelwise View Selection for Unstructured Multi-View Stereo. In Bastian Leibe, Jiri Matas, Nicu Sebe, and Max Welling, editors, *Computer Vision ECCV 2016*, Lecture Notes in Computer Science, pages 501–518, Cham, 2016. Springer International Publishing. ISBN: 978-3-319-46487-9. URL: https://link.springer.com/chapter/10.1007/978-3-319-46487-9_31, doi:10.1007/978-3-319-46487-9_31.

[31] Yasutaka Furukawa, Brian Curless, Steven M. Seitz, and Richard Szeliski. Towards Internet-scale multi-view stereo. In *2010 IEEE Computer Society Conference on Computer Vision and Pattern Recognition*, pages 1434–1441, June 2010. ISSN: 1063-6919. URL: https://ieeexplore.ieee.org/document/5539802, doi:10.1109/CVPR.2010.5539802.

[32] Christian Bailer, Manuel Finckh, and Hendrik P. A. Lensch. Scale Robust Multi View Stereo. In Andrew Fitzgibbon, Svetlana Lazebnik, Pietro Perona, Yoichi Sato, and Cordelia Schmid, editors, *Computer Vision ECCV 2012*, Lecture Notes in Computer Science, pages 398–411, Berlin, Heidelberg, 2012. Springer. URL: https://link.springer.com/chapter/10.1007/978-3-642-33712-3_29, doi:10.1007/978-3-642-33712-3_29.

[33] Matthew Berger, Andrea Tagliasacchi, Lee M. Seversky, Pierre Alliez, Joshua A. Levine, Andrei Sharf, and Claudio T. Silva. State of the Art in Surface Reconstruction from Point Clouds. In *Eurographics 2014 - State of the Art Reports*. The Eurographics Association, 2014. ISSN: 1017-4656. URL: https://diglib.eg.org:443/xmlui/handle/10.2312/egst.20141040.161-185, doi:10.2312/egst.20141040.

[34] Christian Mostegel, Rudolf Prettenthaler, Friedrich Fraundorfer, and Horst Bischof. Scalable Surface Reconstruction from Point Clouds with Extreme Scale and Density Diversity. In *2017 IEEE Conference on Computer Vision and Pattern Recognition (CVPR)*, pages 2501–2510, July 2017. ISSN: 1063-6919. URL: https://ieeexplore.ieee.org/document/8099751, doi:10.1109/CVPR.2017.268.

[35] Hong Wei and Marc Bartels. 3D Digital Elevation Model Generation. In Nick Pears, Yonghuai Liu, and Peter Bunting, editors, *3D Imaging, Analysis and Applications*, pages 367–415. Springer, London, 2012. URL: https://link.springer.com/chapter/10.1007%2F978-1-4471-4063-4_9, doi:10.1007/978-1-4471-4063-4_9.

[36] Agisoft LLC. Agisoft Metashape User Manual: Professional Edition, Version 1.6, 2020. [cit. 2020-7-29]. URL: https://www.agisoft.com/pdf/metashape-pro_1_6_en.pdf.

[37] Michael Cramer. Performance of GPS/Inertial Solutions in Photogrammetry. In *Photogrammetric Week 01*, pages 49–62. Wichmann Verlag, Heidelberg, 2001. ISBN: 3-87907-359-7.

[38] Paul D. Groves. *Principles of GNSS, inertial, and multisensor integrated navigation systems*. GNSS technology and applications series (Artech House). Artech House, Boston, 2nd ed. edition, 2013. ISBN: 978-1-60807-005-3.

[39] Robert Grover Brown and Patrick Y. C. Hwang. *Introduction to Random Signals and Applied Kalman Filtering with Matlab Exercises*. John Wiley & Sons, 2012. ISBN: 978-0-470-60969-9.

[40] P. Barry and R. Coakley. Field Accuracy Test of RPAS Photogrammetry. In *ISPRS - International Archives of the Photogrammetry, Remote Sensing and Spatial Information Sciences*, volume XL-1-W2, pages 27–31. Copernicus GmbH, August 2013. ISSN: 1682-1750. URL: https://www.int-arch-photogramm-remote-sens-spatial-inf-sci.net/XL-1-W2/27/2013/, doi:https://doi.org/10.5194/isprsarchives-XL-1-W2-27-2013.

[41] H. Fazeli, F. Samadzadegan, and F. Dadrasjavan. Evaluating the Potential of RTK-UAV for Automatic Point Cloud Generation in 3D Rapid Mapping. In *ISPRS - International Archives of the Photogrammetry, Remote Sensing and Spatial Information Sciences*, volume XLI-B6, pages 221–226. Copernicus GmbH, June 2016. URL: http://www.int-arch-photogramm-remote-sens-spatial-inf-sci.net/XLI-B6/221/2016/, doi:10.5194/isprs-archives-XLI-B6-221-2016.

[42] Vittorio Casella, Filiberto Chiabrando, Marica Franzini, and Ambrogio Manzino. Accuracy Assessment of a Photogrammetric UAV Block by using Different Software and Adopting Diverse Processing Strategies. In *Proceedings of the 5th International Conference on Geographical Information Systems Theory, Applications and Management - Volume 1: GISTAM*, pages 77–87, August 2020. URL: https://www.scitepress.org/PublicationsDetail.aspx?ID=TjW+9sV77Xo=&t=1, doi:10.5220/0007710800770087.

[43] Jos Manuel Galvn Rangel, Gil Rito Gonalves, and Juan Antonio Prez. The impact of number and spatial distribution of GCPs on the positional accuracy of geospatial products derived from low-cost UASs. *International Journal of Remote Sensing*, 39(21):7154–7171, November 2018. URL: https://doi.org/10.1080/01431161.2018.1515508, doi:10.1080/01431161.2018.1515508.

[44] Valeria-Ersilia Oniga, Ana-Ioana Breaban, Norbert Pfeifer, and Constantin Chirila. Determining the Suitable Number of Ground Control Points for UAS Images Georeferencing by Varying Number and Spatial Distribution. *Remote Sensing*, 12(5):876, January 2020. URL: https://www.mdpi.com/2072-4292/12/5/876, doi:10.3390/rs12050876.

[45] Michael Cramer. Direct Geocoding - is Aerial Triangulation Obsolete? In D. Fritsch and R. Spiller, editors, *Proceedings of the Photogrammetric Week'99*, pages 59–70, Heidelberg, 1999. Wichmann Verlag. URL: https://phowo.ifp.uni-stuttgart.de/publications/phowo99/cramer.pdf.

[46] J. Skaloud, M. Cramer, and K. P. Schwarz. Exterior Orientation By Direct Measurement Of Camera Position And Attitude. In *International Archives of Photogrammetry and Remote Sensing*, volume 31(B3), pages 125–130, 1996. URL: https://www.isprs.org/proceedings/XXXI/congress/part3/125_XXXI-part3.pdf.

[47] Jan Skaloud. Direct Georeferencing in Aerial Photogrammetric Mapping. *Photogrammetric Engineering & Remote Sensing*, 68(3):207, 209–210, March 2002. URL: https://infoscience.epfl.ch/record/29200/.

[48] Eling Christian, Lasse Klingbeil, Markus Wieland, and Heiner Kuhlmann. Direct Georeferencing of Micro Aerial Vehicles System Design, System Calibration and First Evaluation Tests. *Photogrammetrie - Fernerkundung - Geoinformation*, 2014(4):227–237, 2014. doi:10.1127/1432-8364/2014/0200.

[49] C. Eling, M. Wieland, C. Hess, L. Klingbeil, and H. Kuhlmann. Development and Evaluation of a UAV Based Mapping System for Remote Sensing and Surveying Applications. In *ISPRS - International Archives of the Photogrammetry, Remote Sensing and Spatial Information Sciences*, volume XL-1/W4, pages 233–239, August 2015. URL: http://www.int-arch-photogramm-remote-sens-spatial-inf-sci.net/XL-1-W4/233/2015/, doi:10.5194/isprsarchives-XL-1-W4-233-2015.

[50] M. Rehak, R. Mabillard, and J. Skaloud. A micro-UAV with the capability of direct georeferencing. volume 40, pages 317–323. ISPRS, 2013. URL: https://www.int-arch-photogramm-remote-sens-spatial-inf-sci.net/XL-1-W2/317/2013/, doi:10.5194/isprsarchives-XL-1-W2-317-2013.

[51] M. Nagai, Tianen Chen, R. Shibasaki, H. Kumagai, and A. Ahmed. UAV-Borne 3-D Mapping System by Multisensor Integration. *IEEE Transactions on Geoscience and Remote Sensing*, 47(3):701–708, March 2009. doi:10.1109/TGRS.2008.2010314.

[52] M. Blaha, H. Eisenbeiss, D. Grimm, and P. Limpach. Direct Georeferencing of UAVs. *ISPRS - International Archives of the Photogrammetry, Remote Sensing and Spatial Information Sciences*, XXXVIII-1/C22:131–136, September 2012. URL: http://www.int-arch-photogramm-remote-sens-spatial-inf-sci.net/XXXVIII-1-C22/131/2011/isprsarchives-XXXVIII-1-C22-131-2011.html, doi:10.5194/isprsarchives-XXXVIII-1-C22-131-2011.

[53] N. Pfeifer, P. Glira, and C. Briese. Direct Georeferencing with on Board Navigation Components of Light Weight Uav Platforms. *ISPRS - International Archives of the Photogrammetry, Remote Sensing and Spatial Information Sciences*, 39B7:487–492, August 2012. URL: http://adsabs.harvard.edu/abs/2012ISPAr39B7..487P, doi:10.5194/isprsarchives-XXXIX-B7-487-2012.

[54] M. Rieke, T. Foerster, J. Geipel, and T. Prinz. High-precision Positioning and Real-time Data Processing of UAV-Systems. *ISPRS - International Archives of the Photogrammetry, Remote Sensing and Spatial Information Sciences*, XXXVIII-1/C22:119–124, September 2012. URL: http://www.int-arch-photogramm-remote-sens-spatial-inf-sci.net/XXXVIII-1-C22/119/2011/, doi:10.5194/isprsarchives-XXXVIII-1-C22-119-2011.

[55] D. Turner, A. Lucieer, and L. Wallace. Direct Georeferencing of Ultrahigh-Resolution UAV Imagery. *IEEE Transactions on Geoscience and Remote Sensing*, 52(5):2738–2745, May 2014. URL: https://ieeexplore.ieee.org/document/6553130, doi:10.1109/TGRS.2013.2265295.

[56] C. F. Lo, M. L. Tsai, K. W. Chiang, C. H. Chu, G. J. Tsai, C. K. Cheng, N. El-Sheimy, and H. Ayman. The Direct Georeferencing Application and Performance Analysis of Uav Helicopter in Gcp-Free Area. In *The International Archives of Photogrammetry, Remote Sensing and Spatial Information Sciences; Gottingen*, volume XL, pages 151–157, Gottingen, Germany, 2015. Copernicus GmbH. URL: https://search.proquest.com/docview/1756968633/abstract/B238140DB5964263PQ/1, doi:http://dx.doi.org/10.5194/isprsarchives-XL-1-W4-151-2015.

[57] Apostol Panayotov. Photogrammetric Accuracy of Real Time Kinematic Enabled Unmanned Aerial Vehicle Systems, October 2015. [cit. 2016-7-26]. URL: http://uas.usgs.gov/pdf/Reports/USGS_FINAL_REPORT_10212015.pdf.

[58] Mozhdeh Shahbazi, Gunho Sohn, Jerome Theau, and Patrick Menard. Development and Evaluation of a UAV-Photogrammetry System for Precise 3D Environmental Modeling. *Sensors*, 15(11):27493–27524, November 2015. URL: https://www.mdpi.com/1424-8220/15/11/27493, doi:10.3390/s151127493.

[59] L. Zalud, L. Kopecny, F. Burian, and T. Florian. Cassandra - heterogeneous reconnaissance robotic system for dangerous environments. In *2011 IEEE/SICE International Symposium on System Integration (SII)*, pages 1275–1280, December 2011. doi:10.1109/SII.2011.6147632.

[60] F. Burian, L. Zalud, P. Kocmanova, T. Jilek, and L. Kopecny. Multi-robot system for disaster area exploration. In *WIT Transactions on Ecology and the Environment*, volume 184, pages 263–274, Southampton, June 2014. WIT Press. URL: http://library.witpress.com/viewpaper.asp?pcode=FRIAR14-022-1, doi:10.2495/FRIAR140221.

[61] Tomas Jilek. Radiation intensity mapping in outdoor environments using a mobile robot with RTK GNSS. In *International Conference on Military Technologies (ICMT) 2015*, pages 1–7, Brno, Czech Republic, 2015. IEEE. doi:10.1109/MILTECHS.2015.7153755.

[62] Lukas Nejdl, Jiri Kudr, Branislav Ruttkay-Nedecky, Zbynek Heger, Lukas Zima, Ludek Zalud, Sona Krizkova, Vojtech Adam, Marketa Vaculovicova, and Rene Kizek. Remote-Controlled Robotic Platform for Electrochemical Determination of Water Contaminated by Heavy Metal Ions. *International Journal of Electrochemical Science*, 10(4):3635–3643, 2015. URL: http://www.electrochemsci.org/papers/vol10/100403635.pdf.

[63] Petr Gabrlik. The Use of Direct Georeferencing in Aerial Photogrammetry with Micro UAV. In *IFAC-PapersOnLine*, volume 48, pages 380–385, Amsterdam, 2015. Elsevier. URL: https://www.sciencedirect.com/science/article/pii/S2405896315008393, doi:10.1016/j.ifacol.2015.07.064.

[64] Petr Gabrlik, Ales Jelinek, and Premysl Janata. Precise Multi-Sensor Georeferencing System for Micro UAVs. In *IFAC-PapersOnLine*, volume 49, pages 170–175, Amsterdam, 2016. Elsevier. URL: http://www.sciencedirect.com/science/article/pii/S2405896316326659, doi:10.1016/j.ifacol.2016.12.029.

[65] Petr Gabrlik, Anders la Cour-Harbo, Petra Kalvodova, Ludek Zalud, and Premysl Janata. Calibration and accuracy assessment in a direct georeferencing system for UAS photogrammetry. *International Journal of Remote Sensing*, 39(15-16):4931–4959, August 2018. URL: https://doi.org/10.1080/01431161.2018.1434331, doi:10.1080/01431161.2018.1434331.

[66] Tomas Lazna, Petr Gabrlik, Tomas Jilek, and Ludek Zalud. Cooperation between an unmanned aerial vehicle and an unmanned ground vehicle in highly accurate localization of gamma radiation hotspots. *International Journal of Advanced Robotic Systems*, 15(1):1–16, January 2018. URL: https://doi.org/10.1177/1729881417750787, doi:10.1177/1729881417750787.

[67] Petr Gabrlik, Premysl Janata, Ludek Zalud, and Josef Harcarik. Towards Automatic UAS-Based Snow-Field Monitoring for Microclimate Research. *Sensors*, 19(8):1945, January 2019. URL: https://www.mdpi.com/1424-8220/19/8/1945, doi:10.3390/s19081945.

[68] Petr Gabrlik, Tomas Lazna, Tomas Jilek, Petr Sladek, and Ludek Zalud. Using an Automated Heterogeneous Robotic System for Radiation Surveys. *arXiv*, June 2020. Submitted manuscript. URL: http://arxiv.org/abs/2006.16066.

[69] Petr Gabrlik and Tomas Lazna. Simulation of a Gamma Radiation Mapping Using Unmanned Aerial System. In *IFAC-PapersOnLine*, volume 51, pages 256–262, Amsterdam, 2018. Elsevier. URL: http://www.sciencedirect.com/science/article/pii/S2405896318309091, doi:10.1016/j.ifacol.2018.07.163.

[70] Tomas Lazna, Petr Gabrlik, Tomas Jilek, and Frantisek Burian. Simulating UAS-Based Radiation Mapping on a Building Surface. In *Modelling and Simulation for Autonomous Systems*, volume 11995 of *Lecture Notes in Computer Science*, pages 130–147, Cham, 2020. Springer. URL: https://link.springer.com/chapter/10.1007%2F978-3-030-43890-6_11, doi:10.1007/978-3-030-43890-6_11.

Part II.

Publications

A. Precise Multi-Sensor Georeferencing System for Micro UAVs

Outline

A.1. Introduction 44
A.2. Methods 46
A.3. Results 50
A.4. Discussion 53
A.5. Conclusion 55
Bibliography 56

Bibliographic Information

GABRLIK, Petr, Ales JELINEK and Premysl JANATA. Precise Multi-Sensor Georeferencing System for Micro UAVs. In: *IFAC-PapersOnLine* [online]. Cham: Elsevier, 2016, pp. 170–175 [cit. 2020-08-25]. DOI: 10.1016/j.ifacol.2016.12.029. ISSN 2405-8963. Available from: `https://linkinghub.elsevier.com/retrieve/pii/S2405896316326659`

Abstract

In aerial photogrammetry, the direct georeferencing technique using micro Unmanned Aerial Vehicles (UAVs) is generally used less frequently than the indirect approach, especially due to the intensive calibration and equipment-related requirements. Conversely, this technique offers several advantages which can be beneficial in some applications. This paper discusses the development and testing of a precise multi-sensor system for the direct georeferencing of aerial imagery. The system comprises a dual-antenna Real Time Kinematic (RTK) Global Navigation Satellite

System (GNSS) receiver with a centimeter level accuracy and an Inertial Navigation System (INS), which fuses inertial and position information to provide accurate navigation and orientation data in real time. Special attention is paid to the time synchronization of various sensor data and lever arm correction. The 3D print technology was applied to ensure low weight and high modularity of the system, which can be easily modified and mounted to different types of UAVs. The paper also describes a test flight mission and the processing workflow, from the data acquisition to the import of the georeferenced orthophoto to a Geographic Information System (GIS).

Author's Contribution

The author designed and constructed a significant part of the presented system, analyzed related research, participated in the experiments, and processed the results. He also wrote the manuscript independently and contributed to its finalization.

Author contribution: 85 %

Acknowledgement

The completion of this paper was made possible by the grant No. FEKT-S-14-2429 – *The research of new control methods, measurement procedures, and intelligent instruments in automation*, funded by the Internal science fund of Brno University of Technology.

Copyright and Version Notice

A.1. Introduction

Unmanned Aerial Vehicles (UAVs) as a platform for aerial remote sensing and photogrammetry are steadily gaining in popularity. The main reasons for such progress are the availability and cost of the sensing equipment, including not only GNSS receivers, INS units, and digital cameras but also actual UAV platforms. Importantly, the vehicles find use in applications where manned aircraft are unsuitable due to their cost or technical limitations. In this context, one of the prospective domains is agriculture, in which UAVs can be utilized for crop growth monitoring, as discussed by [1] or [2]. Another example of use consists in close range mapping of archaeological sites. [3] present the workflow and results of Pompeii Theaters mapping and [4] summarize the benefits of this innovative approach. All of these applications exploit UAV remote sensing to benefit from its low cost as well as fast and safe operation. Our paper also outlines the development of a multi-robot reconnaissance system, previously described in [5] and [6].

UAVs can be categorized by many different parameters; in most cases, however, the optimal criterion rests in takeoff weight. This parameter typically relates directly to the amount of equipment carried onboard. [7] subdivide takeoff weight into five categories, of which the most significant ones in the civilian sector are *Micro* (less than 5 kg) and *Light* (5 to 50 kg); these groups also form the basis of our research.

Aerial photogrammetry usually yields an orthophoto, a point cloud, or a Digital Terrain Model (DTM). These products can be imported to a GIS or a classification software tool for the subsequent processing; as a rule, however, georeferenced data are required. There are two main approaches to image data georeferencing. The first of these, the indirect georeferencing technique, uses a UAV as the image data acquisition platform, while the onboard Position and Orientation System (POS) is employed only for the stabilization and navigation of the UAV. The image data are georeferenced indirectly by using Ground Control Points (GCP), which are visible on the images and whose positions are known (measured during the land survey). A significant advantage of this approach lies in that a UAV does not have to be equipped with an accurate POS, which is expensive and adds extra payload. The other benefit is that the indirect approach estimates the position and orientation of the image/principal point directly (generally referred to as exterior orientation), thus, no correction of the camera position offset and orientation misalignment is needed. The relationship between the image point and the object point can be described via the 7-parameter similarity (Helmert) transformation based on the central projection, as shown in (A.1). In this equation, the exterior orientation is represented by the position vector $[X_0(t), Y_0(t), Z_0(t)]_L^T$ and three attitude coordinates, $\omega(t)$, $\phi(t)$, and $\kappa(t)$ (photogrammetry angles) as the parameters of the rotation ma-

trix. The last remaining parameter of the transformation is scale, $\lambda(t)$, which is different for every point. Using this formula, a point with coordinates $\xi(t)$ and $\eta(t)$ in the image system can be transformed to a local system, where it is described by the vector $[X(t), Y(t), Z(t)]_L^T$. The only time invariant parameter consists in the focal length c, which embodies one of the camera interior parameters. The projection is described in more detail within [8] and [9].

$$\begin{bmatrix} X(t) \\ Y(t) \\ Z(t) \end{bmatrix}_L = \begin{bmatrix} X_0(t) \\ Y_0(t) \\ Z_0(t) \end{bmatrix}_L + \lambda(t)\mathbf{R}_\mathbf{I}^\mathbf{L}(\omega(t), \phi(t), \kappa(t)) \begin{bmatrix} \xi(t) \\ \eta(t) \\ -c \end{bmatrix}_I \tag{A.1}$$

Indirect georeferencing yields accurate positioning results, which mainly depend on the accuracy of the GCP position measurement. The need to perform land survey may be a disadvantage in some applications.

The alternative approach is called direct georeferencing and utilizes onboard sensors for image georeferencing. Exterior orientation is typically measured by using a GNSS receiver and an INS unit mounted on the aircraft. This method requires a higher payload capability, accurate sensor time synchronization, and misalignment calibration. The transform (A.1) has to be complemented with six time-invariant parameters: the position vector $[X_I, Y_I, Z_I]_B^T$, referred to as the lever arm, which describes the offset between the GNSS antenna and the image sensor (principal point); and three angles, $\Delta\omega$, $\Delta\phi$, and $\Delta\kappa$, which characterize the angular misalignment between the INS unit and the image sensor (boresight angles). The transform takes the form (A.2) (discussed in more detail by [8]).

$$\begin{aligned} \begin{bmatrix} X(t) \\ Y(t) \\ Z(t) \end{bmatrix}_L &= \begin{bmatrix} X_0(t) \\ Y_0(t) \\ Z_0(t) \end{bmatrix}_L + \mathbf{R}_\mathbf{B}^\mathbf{L}(\omega(t), \phi(t), \kappa(t)) \\ &\left(\begin{bmatrix} X_I \\ Y_I \\ Z_I \end{bmatrix}_B + \lambda(t)\mathbf{R}_\mathbf{I}^\mathbf{B}(\Delta\omega, \Delta\phi, \Delta\kappa) \begin{bmatrix} \xi(t) \\ \eta(t) \\ -c \end{bmatrix}_I \right) \end{aligned} \tag{A.2}$$

The accuracy of image georeferencing performed via the direct approach depends on the accuracy of the onboard POS; however, as the direct technique relies on a multisensor system, time synchronization and the calibration of the lever arm and the boresight angles play a major role, too. [1] present a micro UAV multisensor system equipped with a Differential Global Positioning System (DGPS) receiver, in which the achieved mosaics spatial accuracy equals ∼0.11 m. A significant advantage of this approach compared to the indirect technique consists in that no terrestrial measurement is needed.

This paper discusses the development of a multisensor system for *micro/light* UAVs. The system is designed for the direct georeferencing of not only aerial imagery but also laser scans. In the initial sections of the study, the used sensors and equipment are described. Additionally, these parts focus on time synchronization and the data logging system. The following chapters then present the testing of the system, including the test flight, and outlines the first results. The paper also briefly characterizes the workflow from the flight data acquisition to the data processing in a dedicated photogrammetry software and shows the import of the georeferenced orthophoto to a the GIS.

A.2. Methods

A.2.1. Sensor System

To measure the UAV position, we used an RTK GNSS receiver Trimble BD982, namely, a single board embedded receiver which supports L1/L2/L5 GPS and L1/L2 GLONASS signals and provides a dual-antenna input for true heading measurement. When data correction is employed, the receiver delivers the position with an accuracy in the order of centimeters, and the heading accuracy is estimated at a tenth of a degree (with a baseline of 2 meters). The maximum data output frequency corresponds to 50 Hz and can be provided through using several serial channels or ethernet. The RTK corrections are transmitted by a base station located within the radio range of the UAV, via a 2.4 GHz transmitter in real time.

Another component of the onboard POS is an SBG Systems lightweight INS Ellipse-E; this unit includes an Inertial Measurement Unit (IMU) based on the MicroElectroMechanical Systems (MEMS) technology and runs an Extended Kalman Filter (EKF). The filter fuses inertial and aiding data, namely, the GNSS position and heading information in this case, to provide accurate orientation and navigation data with a maximum output frequency of 200 Hz. The INS is shown in Figure A.1.

The system comprises a Canon PowerShot G16 small-format digital camera (Figure A.1) with a sensor resolution of 4,000 × 3,000 pixels (12 MP) and a 6.1–30.5 mm (28–140 mm full frame equivalent) f/1.8–2.8 lens. Although this non-calibrated camera was designed for hobby purposes, it can be effectively used in low-altitude UAV photogrammetric applications. The device meets the basic requirements, including manual setting of the shutter speed, aperture value, and focus distance; moreover, it is equipped with a remote terminal for external triggering and an external flash connector to enable synchronization. Further advantages rest in the low weight and small size. The interior parameters, such as the focal length, principal point offset, and lens geometric distortion, are estimable during the image data process-

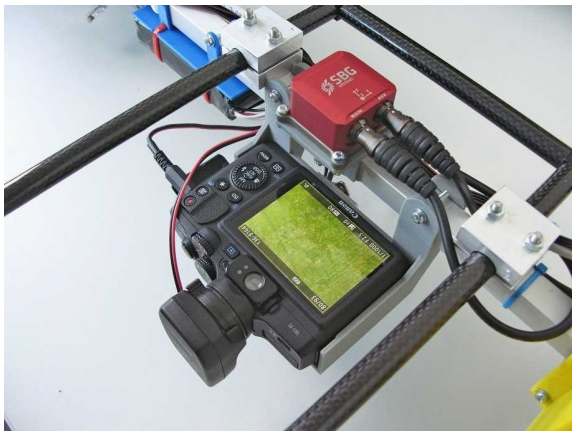

Figure A.1.: Camera and INS (the red box) mounted in the middle of aluminum rail.

ing via photogrammetric software (self-calibration based on the bundle adjustment method), a technique employed by, for example, [10]; alternatively, the parameters can be obtained by means of laboratory pre-calibration, as shown by [11].

A.2.2. Synchronization and Logging System

In multisensor systems, where the measured data depend on the position of vehicle, time synchronization embodies a very important task. UAVs typically cannot measure when static (due to construction limitations or energy efficiency reasons); thus, the time synchronization error causes a position error in the resulting photogrammetry products.

The described system ensures accurate time measurement by exploiting a GNSS receiver, which encloses time information to every output message. This receiver communicates the position, heading, and UTC-related data to the INS unit via an RS-232 interface with a frequency of 50 Hz. The accurate time synchronization between these two devices is achieved via a Pulse Per Second (PPS) signal generated by BD982. Once the time has been synchronized, the INS provides fused navigation and orientation data with an accurate time stamp.

The applied camera is not equipped with a synchronization interface, and every captured image contains only the camera system time information in the EXIF data. Such time information is not accurate enough to allow synchronization with the INS output data, and therefore an event- triggered output is used. The camera is triggered via a remote terminal (a wired shutter), from a single board computer Banana Pi R1 at pre- specified time intervals; after the image has been captured, a flash synchronization impulse from the camera's hotshoe adapter is employed as the

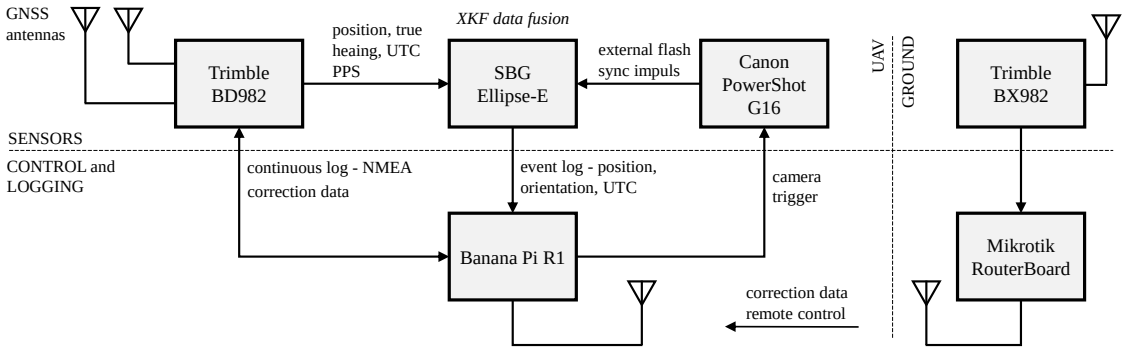

Figure A.2.: Block diagram of sensor integration and control.

event for the INS data output. This feedback approach ensures that these two types of data will become synchronized and that the number of images on the camera's SD card will be the same as the number of INS output logs on the SSD of the Banaba Pi, which functions as the data logger. Such a method was successfully utilized in the UAV multisensor system described by [1].

The Banana Pi R1 performs also the GNSS data logging and the correction data transmission. The GNSS log contains additional information about the receiver status, and the data are saved continuously, at the frequency of 50 Hz. If the UAV's Flight Management Unit (FMU) enables the camera to trigger according to the flight plan, the synchronization and logging system will work properly. The block diagram of the sensors' integration and synchronization is illustrated in Figure A.2.

A.2.3. Frame and UAV Platform

The frame of the multisensor system is compact and easily modifiable. All the equipment is mounted on a aluminum rail, with a GNSS antenna placed at each end; the remaining components are situated close to the center. Every part of the system is mounted via special, 3D printer-made holders, whose positions can be easily altered to adjust the center of gravity. The frame is compatible with any UAV having the payload capability of 2.5 kg. The system is completely independent from the UAV platform, as it has its own battery source and a communication interface.

In the project described herein, the multisensor system is mounted on the popular DJI S800 Spreading Wings platform, as shown in Figure A.3. The S800 is a six-rotor UAV with a payload of around 3 kg and 10 minutes' flight time; the vehicle relies on the DJI Wookong M flight controller, which allows both manual and autonomous flight according to the planned trajectory.

Figure A.3.: UAV DJI S800 equipped with the multisensor mapping equipment.

A.2.4. Data Processing

The image data processing is performed by using PhotoScan Professional, a software tool designed to facilitate photogrammetric processing of digital images and to generate 3D spatial data. The tool finds application in not only aerial imagery processing but also object surface reconstruction. The actual procedure starts with the alignment stage, where the relative exterior orientations of the cameras are estimated via feature points and a sparse point cloud is generated. During the subsequent optimizing phase, the interior parameters of the physically present camera are determined. Once both the exterior and the interior orientations are established, the dense point cloud of the surface geometry can be computed. This process exploits multiview stereo reconstruction, and the resulting point cloud allows us to generate the mesh, DTM, and orthophoto. Photoscan supports direct and indirect georeferencing. If the camera positions are known (typically measured with onboard sensors), the imagery and the point cloud will be georeferenced directly by utilizing the data; if, however, the positions remain unknown, the imagery can be georeferenced via visible GCPs after the alignment stage. The whole process is described in more detail within [1] and [4].

The data from the BD982 GNSS receiver and the Ellipse-E INS are delivered in the NMEA 0183 standard and do not require special processing. After being parsed, the camera-triggered INS data, which contain the positions and attitudes of the cameras, are imported to Photoscan for georeferencing, as described above.

A.3. Results

A.3.1. Test Flight

This chapter summarizes the results of one of the first test flights. The low altitude flight was performed at Botanical Garden of Mendel University in Brno, the Czech Republic (N 49.2141908, E 16.6148036 - WGS84), in June 2016. This location is suitable for the given purpose thanks to its overall area of 11 ha and inaccessibility to the general public. The aim consisted in verifying the functionality of the sensors, data logging, and synchronization; measuring the signal level of the GNSS receiver and the communication link; and also confirming the UAV's flight characteristics. The test lasted approximately 5 minutes, yielding 42 images taken inside an area of 0.5 ha and at altitudes of up to 45 meters above ground level (AGL). During the flight, no GCPs or Test Points (TP) were used, with no RTK corrections transmitted to the GNSS receiver. Although photogrammetric missions are typically conducted within the autonomous flight mode (waypoint-based navigation), the UAV was remotely controlled to enable flight stability verification.

The weight of the multisensor system did not have a negative impact on the flight, as the DJI S800 is capable of flying with more than 3 kg payload. Since the mass of the sensing equipment is not concentrated close to the UAV's center of gravity but rather along the 1.5 meter long aluminum rail, a markedly more significant aspect is the moment of inertia, which can affect the flight stability. In this context, we can point out that although the stability of the *roll* axis worsened somewhat, it did not have a distinctly adverse impact on the controllability and safety.

A.3.2. Position and Orientation Measurement

The accuracy of position measurement performed with a GNSS receiver depends on many factors, the most important of these being the number of satellites tracked and the solution mode. In our case, the BD982 receiver used 6 satellites during the flight, and, as mentioned in the previous section, RTK corrections from the base station were not applied; instead, the receiver was configured to utilize a Satellite-Based Augmentation System (SBAS), and thus it worked in the differential mode.

The position data are fused with the inertial data in the SBG Ellipse-E INS unit; the latter cannot improve the accuracy of the position measurement with the GNSS receiver but are capable of covering possible satellite signal outages and interpolating the satellite measurement. Table. A.1 presents the estimated accuracy of the position measurement delivered by each of the devices; the GNSS receiver's estimation is assumed to be more relevant. The 1σ standard deviation for all three axes is less than one meter.

Table A.1.: The position measurement accuracy estimated by the GNSS receiver and the INS unit.

Device	Latitude 1σ [m]	Longitude 1σ [m]	Altitude 1σ [m]
BD982	0.905	0.510	0.938
Ellipse-E	0.26	0.26	0.72

The orientation (attitude) is measured primarily by the INS unit, which is equipped with inertial sensors; the GNSS receiver is employed as aiding equipment. The receiver provides the accurate true heading and tilt information, measured via moving baseline (the other GNSS antenna). During the flight, the moving baseline operated in RTK Fix (the differential carrier phase solution), and 9 satellites were utilized. The estimated accuracy of the attitude measurement was not logged.

A.3.3. Lever Arm Compensation

As the position obtained from the GNSS receiver does not correspond to the camera's principal point position (Section A.1), the displacement has to be compensated. These offsets were determined in a laboratory before the flight, with a millimeter-level accuracy. The displacement of both the position antenna with respect to the INS and the camera against the INS was saved into the INS flash memory, and thus the INS position output corresponded to the camera's principal point position. The Ellipse-E INS is also able to refine the GNSS lever arm during operation. The level arm compensation should not affect the accuracy of the GNSS position measurement, because the theoretical accuracy in the RTK mode is at the centimeter level.

A.3.4. Camera Synchronization and Calibration

The technique of the INS and image data time synchronization was described in Section A.2.2. The synchronization error is expected to consists of two parts. The first component is formed by the time interval between the synchronizing impulse for the external flash and the image capture. This interval was acquired by using a microphone and an oscilloscope, enabling us to compare the electronic synchronization impulse with the acoustic signal of shutter's sound; it was found that the rising edge of the synchronizing signal is delayed by 2.4 milliseconds against the shutter. The second component of the synchronization error follows from the sampling frequency of the INS. The maximal data output frequency of the INS corresponds to 200 Hz, and the same frequency is applied to read the external events. As the cam-

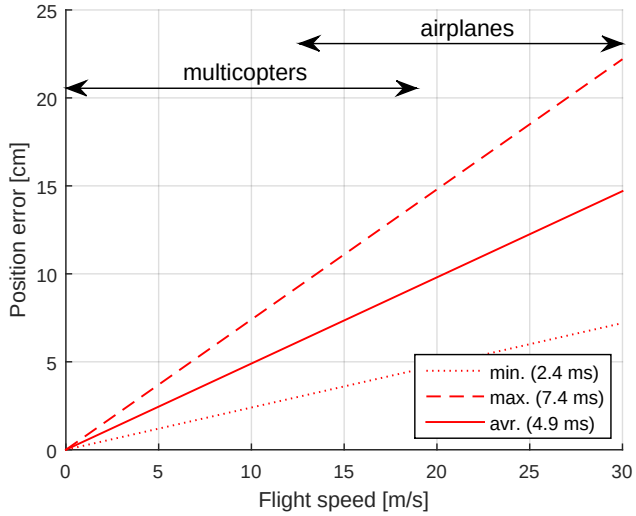

Figure A.4.: The position error related to the flight speed and the synchronization error (minimal, average, and maximal).

era triggering is not synchronized with the INS sampling, this synchronization error ranges within the interval of 0–5 milliseconds. Both errors combined will yield the final error of 2.4–7.4 milliseconds. Figure A.4 relates the positioning error caused by the time synchronization error to the UAV flight speed and the synchronization error size. The average positioning error for a UAV flying at the speed of 10 m/s is about 5 centimeters, namely, the approximate RTK positioning error level.

The camera's interior parameters were estimated by using Photoscan (see Section A.3.5). The software supports inflight calibration, which comprises estimation of the focal length f; principal point coordinates c_x and c_y; radial distortion coefficients k_1, k_2, k_3, and k_4; and tangential distortion coefficients p_1, p_2, p_3, and p_4. These parameters are then applied in the subsequent alignment and point cloud generation. The only initial parameter was the focal length of 6.1 mm, optimized to 6.086 mm.

A.3.5. Photogrammetry Results

For the photogrammetric processing, 14 aerial photographs were chosen. Since the cameras' exterior orientation values were obtained via onboard sensors, the data were imported to Photoscan before the alignment (although we measured both the position and the orientation, only the position data were imported in this test). Photoscan utilizes the data as the initial values for the alignment process and also for the point cloud georeferencing. Table A.2 presents the errors between the estimated and the measured positions of the cameras.

Table A.2.: The error between the estimated and the measured positions.

Error type	X-axis [cm]	Y-axis [cm]	Z-axis [cm]
Mean	0.0	0.0	0.0
Std. dev. (1σ)	9.9	9.2	17.1
Max. abs.	16.6	14.5	32.1

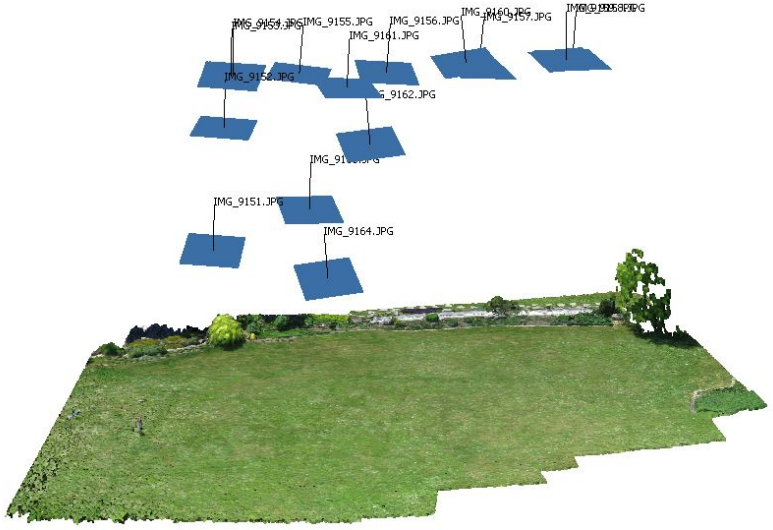

Figure A.5.: The textured digital surface model of the test area; the blue rectangles represent the image planes.

Photoscan can estimate only the relative position and orientation of the cameras, and therefore the mean position error is zero for all the three axes. The standard deviation (1σ) is at the centimeter level for all the axes, meaning that the estimation sufficiently corresponds to the measurement. After we aligned and georeferenced the cameras, the dense point cloud containing more than 2 million points was generated. This point cloud then yielded the desired textured mesh (shown in Figure A.5) and facilitated the orhophoto generation.

The orthophoto, together with the world file generated by Photoscan, was imported to the QGIS geographic information system. Figure A.6 illustrates the orthophoto as a layer over the CUZK WMS orthophoto layer.

A.4. Discussion

The multisensor system mostly operated as expected; the described flight test and data processing nevertheless pointed to several issues that could be eliminated or

Figure A.6.: The georeferenced orthophoto over the CUZK WMS layer in QGIS.

improved in the future. The mechanical structure of the system slightly affects the flight stability due to the high moment of inertia, which may affect the overall safety during autonomous flights and in windy weather conditions. This problem is solvable via reducing the length of the aluminum rail and shifting the sensing system closer to the UAV's center of gravity; the reduced length can partially lessen the vibrations, which otherwise cause image blurring.

The GNSS worked properly during the whole test flight, with no outage of the satellites or disturbance by the UAV's electronics. The positioning accuracy was improved by using SBAS corrections, and the 1σ error did not exceed one meter in any of three axes. The accuracy will improve significantly if RTK correction is utilized. The moving baseline operated in RTK fix, and therefore true heading measurement was employed as the aiding input for the INS unit.

The cameras' positioning accuracy can be enhanced by reducing the time synchronization error between the image and the INS data. Although the measured error is in milliseconds, the position error can exceed the RTK positioning accuracy, depending on the flight speed. Another solution then consists in lowering the flight speed. Multicopters are able to capture images in the static position, potentially eliminating the impact of the time synchronization error; such a mode, however, is generally less time and energy effective.

The Photoscan Professional software appears to be a convenient tool for the photogrammetry processing and direct georeferencing because it allows inflight camera calibration and import of the measured cameras' exterior orientation values. This approach may eliminate the need of GCPs, thereby expanding the automation options. Nevertheless, using some test points is still recommended to facilitate the accuracy verification.

A.5. Conclusion

Within the research, an accurate multisensor system to enable aerial imagery georeferencing in *micro/light* UAVs was designed. Our implementation demonstrates that direct georeferencing eliminates to a great extent human interaction during the data acquisition and processing stages. Using suitable CV-based photogrammetric software, a directly georeferenced point cloud and other products can be generated. The resulting accuracy markedly depends on the position accuracy of the applied GNSS receiver, time synchronization, lever arm compensation, and camera calibration. All these aspects were taken into account during the designing of the multisensor system, and the first test flight outcomes indicate that the approach can potentially compete with the indirect method. Future research will exploit RTK correction to reach the centimeter-level positioning accuracy, and the performance of direct georeferencing will be verified by utilizing ground test points.

Bibliography

[1] D. Turner, A. Lucieer, and L. Wallace. Direct Georeferencing of Ultrahigh-Resolution UAV Imagery. *IEEE Transactions on Geoscience and Remote Sensing*, 52(5):2738–2745, May 2014. doi:10.1109/TGRS.2013.2265295.

[2] R.B. Haarbrink and H. Eisenbeiss. Accurate DSM Production from Unmanned Helicopter Systems. In *International Archives of the Photogrammetry, Remote Sensing and Spatial Information Sciences*, volume XXXVII(B1), pages 1259–1264, 2008. doi:10.3929/ethz-b-000011976.

[3] R. Saleri, V. Cappellini, N. Nony, L. De Luca, M. Pierrot-Deseilligny, E. Bardiere, and M. Campi. UAV photogrammetry for archaeological survey: The Theaters area of Pompeii. In *Digital Heritage International Congress (DigitalHeritage), 2013*, volume 2, pages 497–502, October 2013. doi:10.1109/DigitalHeritage.2013.6744818.

[4] G. Verhoeven, M. Doneus, Ch. Briese, and F. Vermeulen. Mapping by matching: a computer vision-based approach to fast and accurate georeferencing of archaeological aerial photographs. *Journal of Archaeological Science*, 39(7):2060–2070, July 2012. URL: http://www.sciencedirect.com/science/article/pii/S0305440312000866, doi:10.1016/j.jas.2012.02.022.

[5] L. Zalud, L. Kopecny, F. Burian, and T. Florian. Cassandra - heterogeneous reconnaissance robotic system for dangerous environments. In *2011 IEEE/SICE International Symposium on System Integration (SII)*, pages 1275–1280, December 2011. doi:10.1109/SII.2011.6147632.

[6] F. Burian, L. Zalud, P. Kocmanova, T. Jilek, and L. Kopecny. Multi-robot system for disaster area exploration. In *WIT Transactions on Ecology and the Environment*, pages 263–274, June 2014. URL: http://library.witpress.com/viewpaper.asp?pcode=FRIAR14-022-1, doi:10.2495/FRIAR140221.

[7] Maziar Arjomandi, Shane Agostino, Matthew Mammone, Matthieu Nelson, and Tong Zhou. Classification of Unmanned Aerial Vehicles, 2006. [cit. 2014-4-17]. URL: `http://afrsweb.usda.gov/SP2UserFiles/Place/62351500/Unmanned.pdf`.

[8] Michael Cramer. *Performance of GPS/Inertial Solutions in Photogrammetry.* Wichmann Verlag, Heidelberg, 2001. ISBN: 3-87907-359-7.

[9] Karl Kraus. *Photogrammetry: Geometry from Images and Laser Scans*, volume 2nd ed. Walter de Gruyter, Berlin, 2007. ISBN: 978-3-11-019007-6.

[10] D. Gonzlez-Aguilera, J. Fernndez-Hernndez, J. Mancera-Taboada, P. Rodrguez-Gonzlvez, D. Hernndez-Lpez, B. Felipe-Garca, I. Gozalo-Sanz, and B. Arias-Perez. 3d Modelling and Accuracy Assessment of Granite Quarry Using Unmmanned Aerial Vehicle. *ISPRS Annals of Photogrammetry, Remote Sensing and Spatial Information Sciences*, I-3:37–42, July 2012. URL: `http://www.readcube.com/articles/10.5194/isprsannals-I-3-37-2012?locale=en`, `doi:10.5194/isprsannals-I-3-37-2012`.

[11] A. Ahmad and A.M. Samad. Aerial mapping using high resolution digital camera and unmanned aerial vehicle for Geographical Information System. In *2010 6th International Colloquium on Signal Processing and its Applications*, pages 1–6, May 2010. URL: `https://ieeexplore.ieee.org/document/5545303`, `doi:10.1109/CSPA.2010.5545303`.

B. Calibration and Accuracy Assessment in a Direct Georeferencing System for UAS Photogrammetry

Outline

B.1. Introduction 59
B.2. Methods 61
B.3. Results 74
B.4. Discussion 83
B.5. Conclusion 88
Bibliography 92

Bibliographic Information

GABRLIK, Petr, Anders la COUR-HARBO, Petra KALVODOVA, Ludek ZALUD and Premysl JANATA. Calibration and accuracy assessment in a direct georeferencing system for UAS photogrammetry. *International Journal of Remote Sensing* [online]. 2018, **39**(15–16), 4931–4959 [cit. 2020-08-25]. DOI: 10.1080/01431161.2018.1434331. ISSN 0143-1161. Available from: `https://www.tandfonline.com/doi/full/10.1080/01431161.2018.1434331`

Abstract

Unmanned aerial systems (UAS) have already proven useful in fields and disciplines such as agriculture, forestry, or environmental mapping, and they have also found application during natural and nuclear disasters. In many cases, the environment is inaccessible or dangerous for a human being, meaning that the widely used technique

of aerial imagery georeferencing via ground control points cannot be employed. The present paper introduces a custom-built multi-sensor system for direct georeferencing, a concept that enables georeferencing to be performed without an access to the mapping area and ensures centimetre-level object accuracy. The proposed system comprises leading navigation system technologies in the weight category of micro and light UASs. A highly accurate global navigation satellite system receiver integrating the real time kinematic technology supports an inertial navigation system where data from various sensors are fused. Special attention is paid to the time synchronisation of all sensors, and a method for the field calibration of the system is designed. The multi-sensor system is completely independent of the used UAS.

The authors also discuss the verification of the proposed system's performance on a real mission. To make the results credible, a high number of test points are used, with both the direct and the indirect georeferencing techniques subjected to comparison, together with different calibration methods. The achieved spatial object accuracy (about 4 cm RMSE) is sufficient for most applications.

Author's Contribution

The author surveyed and reviewed related research, designed the calibration method, participated in the testing of the system, and processed the results. He was also exclusively responsible for writing the manuscript and contributed to its finalization.

Author contribution: 80 %

Acknowledgement

This work was supported by European Regional Development Fund under the project Robotics for Industry 4.0 (reg. no. CZ.02.1.01/0.0/0.0/15_003/0000470) and by the Technology Agency of the Czech Republic under the project TE01020197 "Centre for Applied Cybernetics 3".

Copyright and Version Notice

B.1. Introduction

Unmanned aerial systems (UAS) have become an important part of aerial photogrammetry. Compared to manned aircraft, they bring substantial advantages, especially in terms of the operating costs. The devices allow fast and safe aerial data acquisition, which significantly reduces the long product cycle known from traditional photogrammetry utilizing manned aircraft. Conversely, their payload capability and endurance is limited, therefore UASs are suitable for mapping local areas only. The payload limitation leads to the use of consumer-grade sensors, which are usually smaller and lighter than survey-grade sensors and metric cameras but provide lower accuracy and parameter stability. This drawback is partly compensated for by the low flight altitude, which allows us to reach superior ground resolution.

Most photogrammetry missions performed by micro and light UASs (below 5 kg and 5–50 kg respectively according [1]) rely on ground control points (GCP). The method using ground points to facilitate aerial imagery georeferencing is called indirect georeferencing (IG). Combining an onboard consumer-grade camera and survey-grade positioning equipment for ground measurement allows us to reach the centimetre-level spatial accuracy of an orthophoto or digital elevation model (DEM). [2] present the RMSE accuracy of 2.3 cm and 3.5 cm for the XY plane and Z axis, respectively, while using fixed-wing aircraft flying at 90 m above ground level (AGL). Similar results are presented in [3], where the indirect georeferencing was supported by real time kinematics (RTK) enabled global positioning system (GPS) onboard UASs. The results are not very reliable due to the small number of test points (TP). A credible outcome of indirect georeferencing is presented by [4], whose multi-rotor UAS flying at 120 m AGL reached the spatial accuracy of 1.7 cm and 2.9 cm RMSE for the XY plane and Z axis, respectively. The main disadvantage of IG approach consists in the need of ground measurement, a time-consuming and sometimes even infeasible technique.

In recent years, lightweight survey-grade global navigation satellite systems (GNSS) receivers and inertial navigation systems (INS) have become available on the market. Their use onboard UASs allows the direct georeferencing (DG) of aerial imagery, eliminating the need of GCPs. The technique is commonly supported by feature-based computer vision (CV) algorithms to ensure position and attitude refinement; however, the approach also places high demands on the calibration of the onboard sensor system, especially on the lever arm compensation and time synchronisation. The accurate direct georeferencing systems used in micro and light UASs are discussed within several recent papers. Thus, for example, [4] present the RMSE accuracy of 16.4 cm and 23.5 cm for the XY plane and Z axis, respectively; the

values were achieved using a multi-rotor UAS equipped with a single-frequency RTK module flying at 120 m AGL, and the accuracy was determined using 32 TPs. The implementation of the differential GPS (DGPS) onboard a multi-rotor UAS is outlined by [5]. In this case, the orthophoto accuracy of 11 cm (mean) was reached. The differential GNSS receiver was further employed by [6]; the approach enables carrier phase measurement, but the reached object accuracy is in the order of meters when flying at 100 m AGL. Contrariwise, the superior ground accuracy values of 0.9, 0.6, and 0.9 cm RMS for the X, Y, and Z axes, respectively, are presented in a relevant study by [7]. These results were obtained thanks to a dual-frequency dual-antenna RTK GPS receiver, precise camera synchronisation, and lever arm compensation. However, only a small number of test points (9) was used for the accuracy determination, and the flight altitude was lower than normal in UAS missions (20 m AGL).

Different aspects of DG in the context of lightweight UASs are discussed in multiple other papers. For example, relevant studies by [8] and [9] describe multi-sensor system design and performance testing; [10] focus on determining the exterior orientation accuracy; [11] address various challenges related to data collection and processing, as well as quality control; and [12] introduce an error analysis of DG systems. These and similar recent contributions suggest that GCP-free photogrammetry performed by lightweight UASs has a great potential in the future.

B.1.1. Contribution of the Research

The problems common to the current implementations of DG systems in micro/light UASs encompass the use of low accuracy GNSS receivers; the lack of INS/IMU, important for lever arm compensation; the insufficient accuracy of time synchronisation; and unreliable ground accuracy determination. The research discussed herein aims to employ the state-of-the-art technology in navigation and camera systems in the weight category suitable for micro/light UASs, utilizing available commercial software to facilitate photogrammetric processing with a high degree of automation; such an approach allows us to achieve a superior object accuracy without using GCPs. Thus, a custom multi-sensor system for UASs, comprising all necessary hardware, was developed and tested previously ([13]). In this context, the present paper introduces a custom calibration process for the given system, including the field estimation of major parameters. To render the procedures and their results credible, special attention was paid to accuracy determination in order to verify and confirm the proposed solution. The designed system exploits todays technologies (digital imaging and processing, integrated sensors, and UAS systems in particular) to enable fully automated aerial photogrammetry.

The system was developed at CEITEC laboratories and embodies a part of the ATEROS (Autonomous Telepresence Robotic System) robotic system ([14], [15]) structured by the team of Prof. Ludek Zalud. ATEROS comprises mainly terrestrial mobile robots with autonomous functions used for exploration and environmental mapping ([16]), but its applicability is significantly expanded through employing a UAS capable of accurate aerial mapping.

The paper is subdivided into three main portions. Section B.2 describes the basic theory of georeferencing in photogrammetry and discusses the designed multi-sensor system, including the calibration, data acquisition and processing. Section B.3 presents the accuracy of the direct georeferencing of aerial imagery, focusing especially on object accuracy. The results are then outlined in Section B.4, where a comparison with existing realisations is proposed.

B.2. Methods

This section introduces the methods and equipment used in the research. Following an insight into the theory of georeferencing and calibration, the UAS and the custom-built multi-sensor system are presented. Attention is also paid to the data processing and aerial data acquisition.

B.2.1. Georeferencing in UAS Photogrammetry

B.1 Comparing the indirect and direct georeferencing techniques in UAS photogrammetry will not yield an unambiguous result, because each of the options exhibits certain advantages and disadvantages. The indirect approach, however, finds more frequent use, due in particular to less intensive requirements on the equipment carried by a UAS; further, the ground measurement of GCPs can be replaced by an existing georeferenced orthophoto when a high absolute accuracy is not needed. The DG technique places high demands on the system calibration, namely, the calibration of lever arms, angular misalignment of onboard sensors, and time synchronisation. Equation (B.1) describes the relationship between an image point $(\xi(t), \eta(t), -c)^{\mathrm{T}}_{\mathrm{C}}$ in camera system C, and an object point $(X(t), Y(t), Z(t))^{\mathrm{T}}_{\mathrm{L}}$ in local system L applied for DG. T letter in superscript is reserved for vector and matrix transposition; capital letters in vector subscript denote to a reference system; and in the case of rotation matrices, capital letters in subscript and superscript describe reference

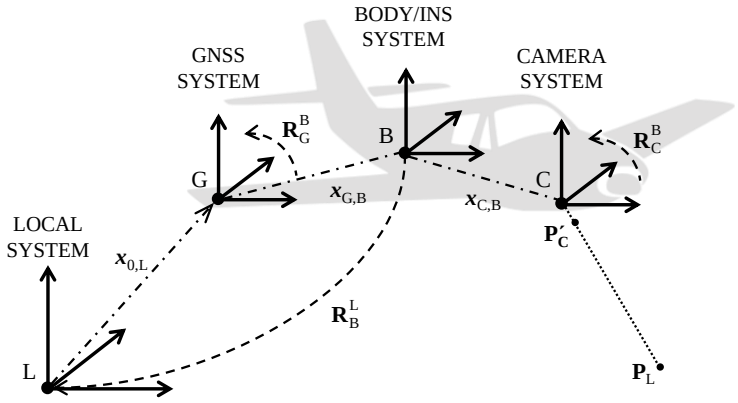

Figure B.1.: The relationship between the reference systems.

systems as follows: $\mathbf{R}_{\text{from}}^{\text{to}}$. Variable t always represents time.

$$\begin{bmatrix} X(t) \\ Y(t) \\ Z(t) \end{bmatrix}_{\mathrm{L}} = \begin{bmatrix} X_0(t) \\ Y_0(t) \\ Z_0(t) \end{bmatrix}_{\mathrm{L}} + \mathbf{R}_{\mathrm{B}}^{\mathrm{L}}(\omega(t), \phi(t), \kappa(t)) \left(\begin{bmatrix} X_{\mathrm{L}} \\ Y_{\mathrm{L}} \\ Z_{\mathrm{L}} \end{bmatrix}_{\mathrm{B}} + \lambda(\xi, \eta) \mathbf{R}_{\mathrm{C}}^{\mathrm{B}}(\Delta\omega, \Delta\phi, \Delta\kappa) \begin{bmatrix} \xi(t) \\ \eta(t) \\ -c \end{bmatrix}_{\mathrm{C}} \right) \tag{B.1}$$

The formula comprises a spatial similarity transformation ([17], [18]) and a vector $(X_{\mathrm{L}}, Y_{\mathrm{L}}, Z_{\mathrm{L}})_{\mathrm{B}}^{\mathrm{T}}$ describing the distance (or lever arm) between the GNSS antenna and the camera perspective center in the body system B; another component of the formula consists in a rotation matrix, $\mathbf{R}_{\mathrm{C}}^{\mathrm{B}}$, characterizing the angular misalignment (or boresight angles) between the body and the camera system. These elements, together with the camera focal length c, are ideally constant. Vector $(X_0(t), Y_0(t), Z_0(t))_{\mathrm{L}}^{\mathrm{T}}$ expresses the position measured by the GNSS receiver in the local system, and rotation matrix $\mathbf{R}_{\mathrm{B}}^{\mathrm{L}}$ is obtained via INS measurement. By extension, the scale $\lambda(\xi, \eta)$ is not a constant either: it is individual for every image point.

In practice, an INS unit and a GNSS antenna are physically located at different places; thus, we introduce two different reference systems, namely, body B and GNSS G. Their mutual relationship is illustrated in Figure B.1.

Once the 6 parameters defining the position and attitude of a camera – often referred to as camera exterior orientation or extrinsic parameters – are known, the position of an object point can be reconstructed if the object point is visible in at least two overlapped images. Subsequently, we get a pair of equations (B.2) for each of the images, and these formulae are solvable as they form a system of four equations with three unknowns $(X, Y, Z)_{\mathrm{L}}^{\mathrm{T}}$, namely, the object position. The

Table B.1.: The table of parameters calibrated in this paper.

Parameter	Number of param.	Note
Lever arm (translation vector)	3	Pre-calibrated, custom field calibration
Boresight angles	3	Pre-calibrated, *not used*
Synchronisation delay	1	Custom field calibration
Camera interior parameters	Up to 13	Pre-calibrated, field calibrated

elements r_{ij} in (B.2) represent the components of the rotation matrix transforming point from the camera system into the local system, where i represents row index and j column index. If, however, the object point is visible on a single image only, the Z coordinate cannot be reconstructed, because there are infinitely many solutions. The equations (B.2), often called collinearity equations, are typically solved using least square estimation. If aerial photographs exhibit large forward and side overlaps (Section B.2.7), a highly over-determined system of equations can be used to estimate other unknowns, including camera interior parameters.

$$\begin{aligned} X &= X_0 + (Z - Z_0)\frac{r_{11}\xi + r_{12}\eta + r_{13}c}{r_{31}\xi + r_{32}\eta + r_{33}c} \\ Y &= Y_0 + (Z - Z_0)\frac{r_{21}\xi + r_{22}\eta + r_{23}c}{r_{31}\xi + r_{32}\eta + r_{33}c} \end{aligned} \tag{B.2}$$

B.2.2. System Calibration

As mentioned in the previous section, direct georeferencing requires calibration. In our research, several calibration techniques (Table B.1) are used to facilitate accurate object point determination. This subsection then introduces a custom system calibration procedure designed to estimate the constant parameters directly related to the DG accuracy, namely, the lever arm offset, base station offset, and synchronisation delay. The estimation of the parameters is not implemented in common photogrammetric software tools, because complex data are needed for the processing. The difference between a position measured by a GNSS receiver (transformed into a camera perspective centre using initial lever arm calibration) and the true position of an image comprises the aforementioned elements:

- Offset in the body B system (lever arm – 3D vector).
- Offset in the local L system (base station position error – 3D vector).
- Offset caused by a delay between the moment of capturing the image and that of storing the data (synchronisation delay – scalar).

The lever arm $\boldsymbol{x}_{\mathrm{lv,B}} = (X_{\mathrm{L}}, Y_{\mathrm{L}}, Z_{\mathrm{L}})^{\mathrm{T}}_{\mathrm{B}}$ outlined in equation (B.1) can be split into two main parts (B.3): the distance $\boldsymbol{x}_{\mathrm{g,B}} = (X_{\mathrm{G}}, Y_{\mathrm{G}}, Z_{\mathrm{G}})^{\mathrm{T}}_{\mathrm{B}}$ between the GNSS antenna and the INS unit, and the distance $\boldsymbol{x}_{\mathrm{c,B}} = (X_{\mathrm{C}}, Y_{\mathrm{C}}, Z_{\mathrm{C}})^{\mathrm{T}}_{\mathrm{B}}$ between the INS unit and the camera perspective centre (Figure B.1). These two vectors are pre-calibrated (laboratory-estimated) before a flight and saved into the INS unit; the measured GNSS position is thus transformed to the camera perspective centre in real time. The total lever arm is then refined by the vector $\boldsymbol{\Delta}_{\mathrm{lv,B}} = (\Delta_{\mathrm{lvx}}, \Delta_{\mathrm{lvy}}, \Delta_{\mathrm{lvz}})^{\mathrm{T}}_{\mathrm{B}}$ obtained through the custom calibration.

$$\boldsymbol{x}_{\mathrm{lv,B}} = \boldsymbol{x}_{\mathrm{g,B}} + \boldsymbol{x}_{\mathrm{c,B}} + \boldsymbol{\Delta}_{\mathrm{lv,B}} \tag{B.3}$$

The boresight angles, similarly to the lever arm, can be pre-calibrated before a flight and then re-calibrated during the field calibration. Our research involved using the Agisoft Photoscan Professional photogrammetric software, which implements CV-based algorithms; further, the attitude of the aerial images (photogrammetric angles) is also estimable during the alignment stage, and the boresight angles thus need not be calibrated for the actual processing.

The base station offset $\boldsymbol{\Delta}_{0,\mathrm{L}} = (\Delta_{0\mathrm{x}}, \Delta_{0\mathrm{y}}, \Delta_{0\mathrm{z}})^{\mathrm{T}}_{\mathrm{L}}$ is the position error of the terrestrial GNSS receiver providing correction data for the onboard GNSS receiver. This inaccuracy then causes error in the multi-sensor system position measurement within the local reference system L. Since the offset remains constant during a mission, it can be estimated using the proposed calibration; however, the offset is specific for each base station, and thus it is not a calibration parameter of our system (contrary to the lever arm, which does not change).

The last estimated parameter lies in the synchronisation delay Δ_{t} between the camera shutter and GNSS/INS data logging. The error vector caused by this delay depends on not only the delay size but also the flight speed and direction (course). Since both the speed and the course are measured by the INS, the delay is estimable, as are the lever arm and base station offset. Based on the technical realisation, the delay can be positive or negative.

The problem consists in that the true (reference) position of the images is normally unavailable. For this purpose, indirect imagery georeferencing is applicable; the process is also known as aerial triangulation (AT). It can be argued that the procedure does not yield reference data, because the result is obtained through least-square estimation. However, with a large number of images taken in a suitable arrangement, and assuming multiple tie points and accurately measured ground control points, the estimated exterior orientation can be considered credible. Figure B.2 illustrates the difference between the true image position (obtained via AT) and the measured image position (GNSS/INS-derived); the discrepancy arises predominantly from the

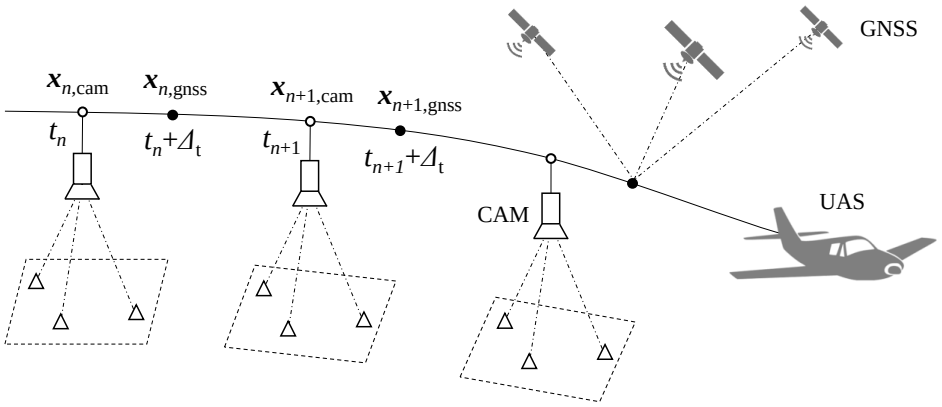

Figure B.2.: The difference between the AT-estimated image position $\boldsymbol{x}_{n,cam}$ and the GNSS/INS derived image position $\boldsymbol{x}_{n,gnss}$ is caused mainly by the lever arm and synchronisation delay Δ_t.

aforementioned parameters. The GNSS and AT data are compared in Section B.3.2.

$$\boldsymbol{x}_{\mathrm{e,L}} - \boldsymbol{x}_{\mathrm{m,L}} = \boldsymbol{\Delta}_{0,\mathrm{L}} + \mathbf{R}_\mathrm{B}^\mathrm{L}\boldsymbol{\Delta}_{\mathrm{lv,B}} + \mathbf{R}_\mathrm{v}\boldsymbol{v}_\mathrm{B}\Delta_\mathrm{t} \tag{B.4}$$

Equation (B.4) represents the observation equation for the custom calibration to be assembled for every image. The difference between the estimated $\boldsymbol{x}_{\mathrm{e,L}} = (x_\mathrm{e}, y_\mathrm{e}, z_\mathrm{e})^\mathrm{T}_\mathrm{L}$ and measured $\boldsymbol{x}_{\mathrm{m,L}} = (x_\mathrm{m}, y_\mathrm{m}, z_\mathrm{m})^\mathrm{T}_\mathrm{L}$ image positions on the left-hand side is minimised by the unknowns $\boldsymbol{\Delta}_{0,\mathrm{L}}$ (base station offset), $\boldsymbol{\Delta}_{\mathrm{lv,B}}$ (lever arm offset), and Δ_t (synchronisation delay). The rotation matrix $\mathbf{R}_\mathrm{B}^\mathrm{L}$ transforms the lever arm vector from the body B to the local system L, and $\mathbf{R}_\mathrm{v}$ rotates the speed vector $\boldsymbol{v}_\mathrm{B} = (v_\mathrm{x}, v_\mathrm{y}, v_\mathrm{z})^\mathrm{T}_\mathrm{B}$ to the local system L. If the issue is solved in 3D, we obtain three equations (B.5) based on (B.4) for every image; this may mean hundreds of equations per calibration flight (N denotes the number of images). By contrast, there are 7 unknown parameters only (overlined). The elements p_{ij} and q_{ij} represent the components of the rotation matrices $\mathbf{R}_\mathrm{B}^\mathrm{L}$ and $\mathbf{R}_\mathrm{v}$ respectively, where i symbolises row index and j column index.

$$\begin{aligned}
x_{\mathrm{e}i} - x_{\mathrm{m}i} &= \overline{\Delta}_{0\mathrm{x}} + p_{11i}\overline{\Delta}_{\mathrm{lvx}} + p_{12i}\overline{\Delta}_{\mathrm{lvy}} + p_{13i}\overline{\Delta}_{\mathrm{lvz}} + (q_{11i}v_{\mathrm{x}i} + q_{12i}v_{\mathrm{y}i} + q_{13i}v_{\mathrm{z}i})\overline{\Delta}_\mathrm{t} \\
y_{\mathrm{e}i} - y_{\mathrm{m}i} &= \overline{\Delta}_{0\mathrm{y}} + p_{21i}\overline{\Delta}_{\mathrm{lvx}} + p_{22i}\overline{\Delta}_{\mathrm{lvy}} + p_{23i}\overline{\Delta}_{\mathrm{lvz}} + (q_{21i}v_{\mathrm{x}i} + q_{22i}v_{\mathrm{y}i} + q_{23i}v_{\mathrm{z}i})\overline{\Delta}_\mathrm{t} \\
z_{\mathrm{e}i} - z_{\mathrm{m}i} &= \overline{\Delta}_{0\mathrm{z}} + p_{31i}\overline{\Delta}_{\mathrm{lvx}} + p_{32i}\overline{\Delta}_{\mathrm{lvy}} + p_{33i}\overline{\Delta}_{\mathrm{lvz}} + (q_{31i}v_{\mathrm{x}i} + q_{32i}v_{\mathrm{y}i} + q_{33i}v_{\mathrm{z}i})\overline{\Delta}_\mathrm{t} \\
& \qquad\qquad i = 1, 2, 3...N
\end{aligned} \tag{B.5}$$

The over-determined system of equations is then solved using the Gauss-Newton iterative method ([19]). The vector of residuals $\boldsymbol{r}$ comprises the set of equations (B.5) $\boldsymbol{r} = \boldsymbol{f}(\Delta_{0\mathrm{x}}, \Delta_{0\mathrm{y}}, \Delta_{0\mathrm{z}}, \Delta_{\mathrm{lvx}}, \Delta_{\mathrm{lvy}}, \Delta_{\mathrm{lvz}}, \Delta_\mathrm{t})$, and $\boldsymbol{\theta}$ represents the vector of the 7 calibration parameters, which is initialised by an initial approximation $\boldsymbol{\theta}_0$. This vector

is updated in each iteration step k of the Gauss-Newton algorithm (B.6). $\mathbf{J}_\mathrm{r}$ stands for the Jacobian matrix, namely, the matrix of the first-order partial derivatives of $\boldsymbol{r}$.

$$\boldsymbol{\theta}_{k+1} = \boldsymbol{\theta}_k - (\mathbf{J}_\mathrm{r}^\intercal \mathbf{J}_\mathrm{r})^{-1} \mathbf{J}_\mathrm{r}^\intercal \boldsymbol{r}(\boldsymbol{\theta}_k), \tag{B.6}$$

The iteration ends once the given convergence conditions have been satisfied, typically when the difference $\boldsymbol{\theta}_{k+1} - \boldsymbol{\theta}_k$ is smaller than the value given for each unknown variable. The above-described calibration was implemented in Matlab and can be employed to estimate the unknown parameters in any calibration flight. However, two datasets are required: the reference image positions (AT-estimated in Photoscan within this research) and the GNSS/INS-derived data for every image, including the position, attitude, course, and speed.

The calibration parameters of the multi-sensor system, namely, the lever arm vector and the synchronisation delay, are applied to refine the measured position of every image, utilising another Matlab script (section B.2.8); the data can be then used for the direct georeferencing. The outcomes of the custom calibration are presented in the Section B.3.

B.2.3. Camera Calibration

Camera interior orientation (also intrinsic parameters) embodies a set of parameters characterizing the mechanical arrangement of the elements of a camera and a lens. A camera model based on central projection (equations (B.1), (B.2)) typically comprises the following linear parameters: focal length (c); principal point offset (ξ_0, η_0); and affinity and non-orthogonality coefficients (b_1, b_2) ([20]). Based on Brown's model ([21], [22]), the distortion of a lens is described by radial (k_1–k_4) and tangential (p_1–p_4) non-linear parameters. The camera model applied in this paper is outlined in [23].

Although there are many camera calibration techniques, this paper aims to employ only two of the approaches most common in UAS photogrammetry. The former is pre-calibration using a checker board; we performed this step with Agisoft Lens. The software estimates the parameters via a pattern on the computer screen, whereas the photographs are captured from a close distance with different poses and positions. A disadvantage is that the focus setting varies from a real photogrammetry mission, and thus the intrinsic parameters can differ slightly.

The latter method rests in field (also on-site, on-the-job) calibration, where the camera interior orientation is estimated using actual project images, or real aerial data processed via Agisoft Photoscan in the described case. Advantageously, the desired actual camera parameters are estimated; however, we must also satisfy several

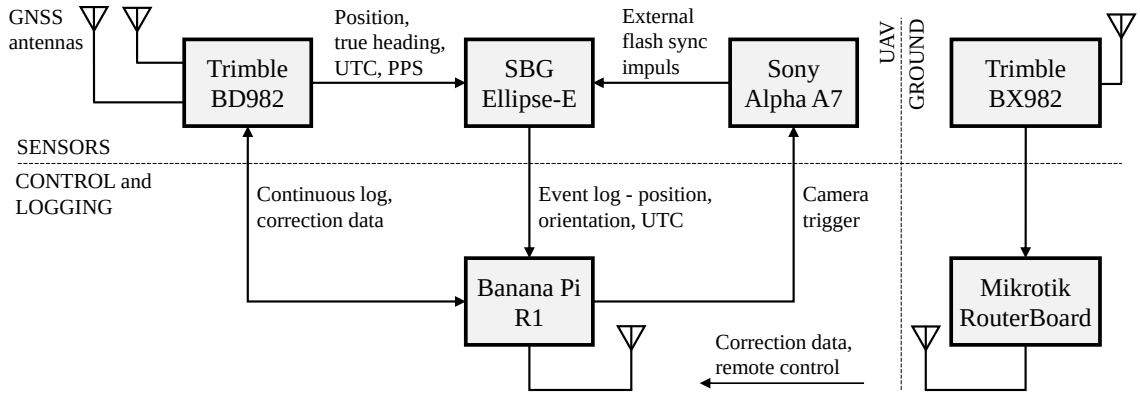

(a)

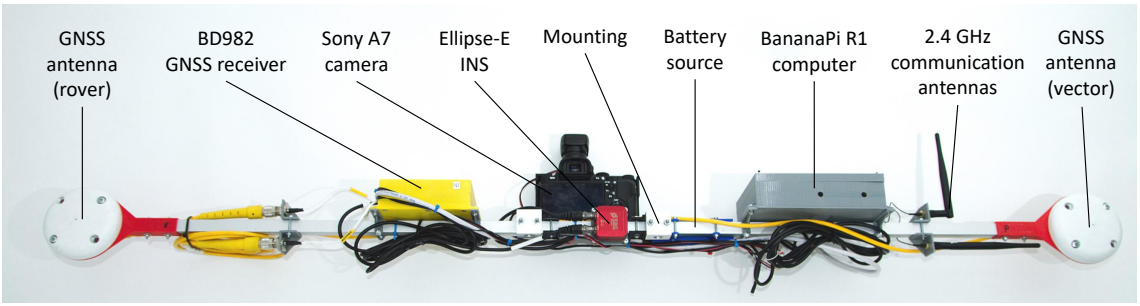

(b)

Figure B.3.: The custom-built multi-sensor system for the direct georeferencing.

conditions to obtain accurate results. Thus, for example, large overlaps should be present to locate points on many images, and the camera should cover a wide range of angles. If such conditions are met, the field calibration is more accurate than the pre-calibration; conversely, multiple photogrammetry projects comprise nadir photographs arranged in strips and blocks, which produce improper estimation conditions. These aspects are outlined by [24] and [25].

Both of the aforementioned approaches, namely, checker board pre-calibration and field calibration, are tested, and the performance is assessed using the object accuracy within Section B.3.4.

B.2.4. Multi-Sensor System

Besides the digital camera, the direct georeferencing technique in photogrammetry requires several other sensors and equipment onboard a UAS. Being the subject of a previous research, the development of the multi-sensor and logging system was published within [13].

To facilitate accurate position measurement, a Trimble BD982 GNSS receiver was used. This receiver supports the RTK technique to enhance the accuracy to centimetre-level, and a dual antenna input allows true heading measurement; the

applied antennas are located 1.2 meters apart. The correction data for the receiver are obtained from a custom base station in real time. The base station comprises a 2.4 GHz wireless unit and another Trimble BD982 GNSS receiver configured to generate the correction data. The station has to be placed on a point with a known position to ensure absolute measurement accuracy (Section B.2.6).

The attitude is measured using an SBG Ellipse-E INS unit, which integrates inertial sensors and fuses their data with external aiding data in an extended Kalman filter. The aiding data from the Trimble receiver provide an absolute position and heading reference with the frequency of 50 Hz; the fused navigation data are computed at 200 Hz. The INS also integrates the lever arm compensation between the GNSS antenna and the INS and between the INS and the camera sensor.

The multi-sensor system presented in the above-mentioned paper contained a Canon PowerShot G16 digital camera, later replaced with a Sony Alpha A7 camera having a Voigtlander lens to ensure better stability of the lens parameters and a higher image quality. The new camera is equipped with a full-frame sensor providing the resolution of 6,000 × 4,000 px and a 15 mm / F 4.5 fixed lens suitable for the pre-calibration. More parameters are presented in Table B.2.

An essential part of a direct georeferencing system for UASs is embodied in the accurate time synchronisation of all sensors. The GNSS receiver and the INS are synchronised using a pulse per second (PPS) signal and NMEA messages containing UTC time. Unfortunately, most common consumer-grade cameras are not equipped with a synchronisation interface, and therefore a hot shoe adapter was used for the given purpose. Once an image has been taken, the signal for the external flash is used as the event signal for the INS, which then saves the current position, attitude, and other data. This approach has already been successfully employed in other similar projects, for example, that completed by [5]. Despite the fact, a delay still exists between the actual image capturing and data storage; thus, the calibration and refinement of the measured data are needed (Section B.2.2).

The data from the GNSS receiver and the INS are stored on the SSD storage of an onboard Linux computer BananaPi R1, which also finds application in triggering the camera at specific time intervals. The image data are stored on the SD card of the camera. The described multi-sensor system is shown in Figures B.3a and B.3b.

B.2.5. UAS Platform

To test the multi-sensor system, we used a DJI S800 UAS (Figure B.4), an 80 cm span hexacopter capable of flying for approximately 10 minutes with the payload of 2-3 kg. The UAS is fitted with a Wookong M flight controller to support automatic flight based on selected waypoints; for this reason, the device contains a

Figure B.4.: The DJI S800 UAS equipped with the custom-built multi-sensor system.

Table B.2.: The parameters of the custom-built multi-sensor system.

Parameter	Value
Position accuracy (BD982)[a]	Horizontal: 8 mm, vertical: 15 mm
Attitude accuracy (Ellipse-E)[b]	Roll/pitch: 0.1°, heading: 0.4°
Camera resolution	6,000 × 4,000 px
Camera lens	15 mm / F 4.5
Operational time	120 mins
Distance from base	1,000 m
Dimensions	1.5 × 0.2 × 0.2 m
Weight	2.6 kg

[a] 1σ error in the RTK mode, according to the manufacturer's specification.

[b] The RTK mode in the airborne applications, according to the manufacturer's specification.

low-accurate GPS receiver. The whole multi-sensor system can be easily mounted on the UAS without modifying its structure. The UAS and the multi-sensor system are completely independent of each other, mainly thanks to having autonomous power sources and communication interfaces.

The hoverability and high payload capacity are the central reasons why multi-rotor UASs are often employed in photogrammetry missions similar to that outlined herein ([26], [7], [5]).

B.2.6. Test Area and Ground Measurement

The test mission took place at the campus of Brno University of Technology, Brno, Czech Republic (49°13'41.61"N, 16°34'19.002"E — WGS84, Figure B.5). The relevant area occupies almost 20,000 m^2 of grassy terrain with large height differences, multiple paths, and artificial objects. The locality meets the requirements for the

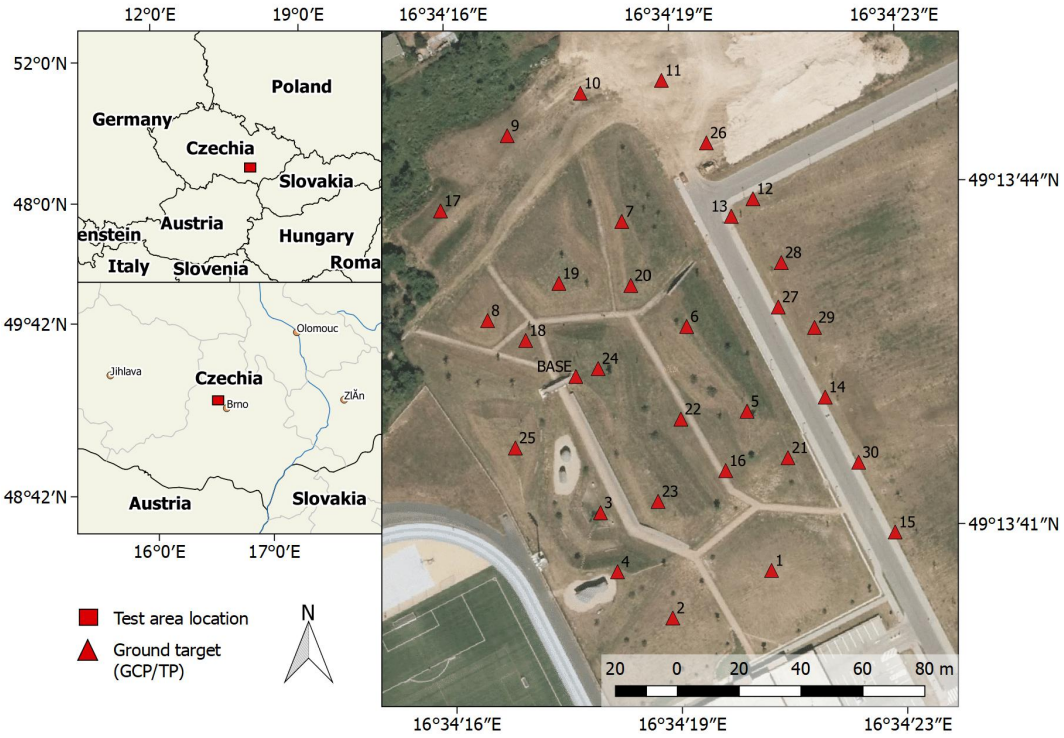

Figure B.5.: The test area and the distribution of the ground targets, which can be employed as GCPs or TPs (orthophoto adopted from [27]).

operation of UASs, including the horizontal distance from buildings and urbanised zones.

The test area comprised 30 systematically distributed ground targets usable as ground control points (GCP) for imagery georeferencing or as test points (TP) to enable accuracy assessment. We used 20 cm squared, black and white patterned paper targets having clearly defined centres (Figure B.6a). Every target was glued onto a solid support and fixed to the ground using iron nails.

The position of every single target was obtained using a survey-grade Topcon HiPer Pro RTK GNSS receiver; this step was performed twice – before and after the flight. The device receives the correction data from CZEPOS (the provider of correction data from the Czech network of reference stations) via GSM; during the measurement, the receiver was stabilised with a tripod (Figure B.6b). The position of the base station reference point (Section B.2.4) was measured independently, using a Topcon GPT 3003N total station and a Topcon AT-G4 levelling instrument in the S-JTSK coordinate system (coordinates X, Y) and the Baltic Vertical Datum height system. After this measurement phase, adjustment was performed (coordinate h). The coordinates were transformed into the ETRS89 system via a local transformation key; the RMS error in the coordinates X, Y is 0.06 m. Figure B.5 shows an ortophoto from the CUZK (The Administration of Land Surveying and

(a) (b)

Figure B.6.: A detail of a ground target captured from the ground (a) and the process of the position measurement using survey-grade GNSS receiver (b). Location: 49°13'44.48"N, 16°34'16.14"E — WGS84.

Cadastre of Czech Republic) containing the coordinates of the ground targets and the base station.

B.2.7. Aerial Data Acquisition

The aerial data were acquired on 23 February 2017, together with the measurement of the ground targets. The weather allowed us to carry out the UAS flight and the photogrammetry measurement: it was overcast, 12 °C, with the wind of about 1–3 m s^{-1}. Since the UAS supports automatic flight according to GPS coordinates, the parameters of the flight trajectory and image acquisition were set before the flight.

Several parameters are constant; thus, we have the sensor resolution of 6,000 × 4,000 px, focal length of 15 mm (Section B.2.4), and the lowest possible safe AGL altitude of approximately 50 m. Under these conditions, the ground sample distance (GSD) corresponds to about 2 cm (or slightly more in lower-positioned locations).

The minimum forward and side overlaps for the object reconstruction are 50 % and 0 %, respectively; in practice, however, using a 60 % forward and a 30 % side overlap is recommended due to flight navigation inaccuracies ([17]). Larger overlaps, such as those between 60 % and 90 %, are typically applied when precise surface reconstruction is needed ([5] and [28]); however, the processing time increases dramatically ([29]). In our case, the camera was triggered every 2 seconds, and the flight speed equalled 5 m s^{-1}; such values should ensure the minimum forward overlap of 80 % for the whole test area. The flight trajectory contained 7 strips having the length of 200 meters and spacing of 20 meters. This configuration then led to 80 % side overlap. Table B.3 summarises the flight trajectory parameters.

The flight lasted 8 minutes, enabling us to capture 194 images. The data from the

Table B.3.: The parameters of the flight trajectory and image acquisition.

Parameter	Symbol[a]	Value
Distance between strips	A	20 m
Length of a strip	L	200 m
Number of a strips	-	7
Base (distance between consecutive images)	B	10 m
Flying altitude AGL	h	50 m
Flying speed	v	5 m s^{-1}
Time between images	t	2 s
Principal distance	c	15 mm
Photo scale	m_b	3333
Forward overlap	l	88 %
Side overlap	q	80 %
Footprint of image on the ground	-	120 × 80 m
Ground resolution	-	2 cm px^{-1}
Shutter speed	-	2000^{-1} s
Aperture	f	4.5
ISO	-	Auto (2,000–2,500)

[a]The symbols are based on [17].

INS were saved every time an image was taken, and the raw data from the GNSS receiver were saved continuously with the frequency of 50 Hz.

B.2.8. Data Processing

The present subsection describes the data processing workflow applied once the system calibration (Section B.2.2), and possibly also camera pre-calibration (Section B.2.3), has been performed. The calibrations provide the data enabling us to increase the accuracy of the exterior orientation measurement and photogrammetry processing.

Basically, there are two data types obtained during a photogrammetry mission, namely, GNSS/INS and image data. As the GNSS module receives the RTK correction data from the custom base station, the position is computed in real time. The INS fuses inertial and aiding data in real time too, and therefore no postprocessing is needed. The data parsing and conversion to an appropriate format, and also the position data refinement based on the proposed custom calibration (Section B.2.2), are performed in Matlab. As regards the image data, we only apply some luminance transformations and subsequently convert the data from the RAW image format

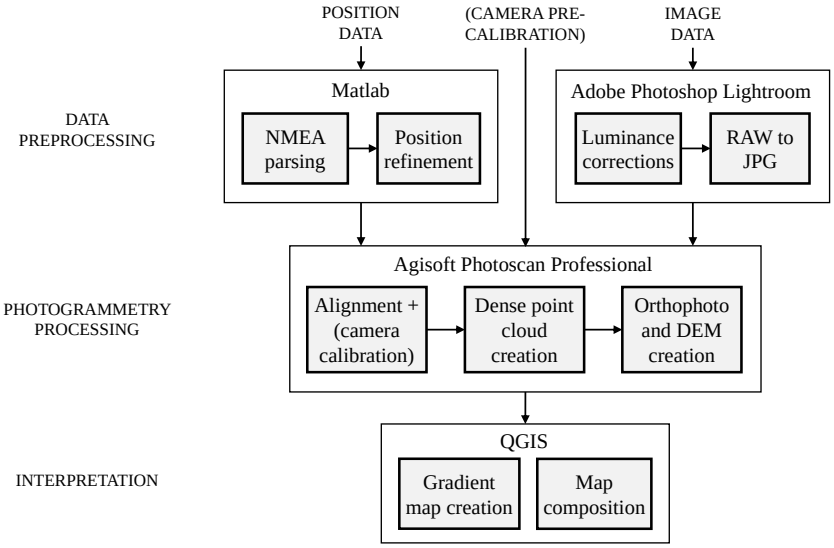

Figure B.7.: The sequence of the data processing operations.

into the JPG format with minimal compression. The processing is illustrated in Figure B.7.

For the photogrammetric processing, Agisoft Photoscan Professional v1.3.1 is used. This software was designed to facilitate surface reconstruction using digital image data, to generate georeferenced orthophotos and spatial models, and to support both direct and indirect georeferencing. The processing starts with the detection of feature points, which are matched across the whole image set. After filtering, the selected and matched tie points are used for the sparse point cloud creation, a process called structure-from-motion (SfM) ([30]). During this alignment stage, the interior and relative exterior orientations are also estimated. Within the following step, georeferencing can be performed via importing either the image position data measured by the onboard sensors or the positions of the GCPs obtained during ground measurement. This procedure exploits the similarity transformation already mentioned in Section B.2.1. We should note in this context that the GNSS/INS data can be imported also before the align stage to speed up the processing.

Once the interior and exterior orientations of every image are known, the dense point cloud can be generated, utilizing multiview stereo reconstruction. As the operation is realised on pixel-level, we obtain a point cloud containing milions of points. Such a dense cloud then constitutes the basis for a true orthophoto, mesh, or DEM.

Photoscan allows us to use ground targets in two specific ways, namely, as GCPs for indirect georeferencing or as test/check points (TP/ChP) for an accuracy assessment. In both cases, the image position of the targets must be determined manually. If the imagery is georeferenced indirectly, some targets should be reserved as TPs.

The influence exerted by the number and distribution of GCPs on ground accuracy is discussed in, for example, [31]. Conversely, direct georeferencing facilitates using all available targets as TPs.

Photoscan is widely employed in scientific papers discussing aerial photogrammetry performed via manned and unmanned aircraft ([3], [5], [32] etc.) because it implements state-of-the-art CV algorithms, ensures a clear workflow, offers multiple import and export options, and is reasonably priced.

B.3. Results

This section presents the achieved results; the accuracy of the ground and aerial data; the outcomes of the system calibration; and, finally, the object accuracy. In most cases, the results are expressed using root-mean-square error (RMSE), defined by (B.7), where x_i is the observed value, $\hat{x}_i$ the reference value, and N the number of observations.

$$\mathrm{RMSE} = \sqrt{\frac{1}{N}\sum_{i=1}^{N}(x_i - \hat{x}_i)^2} \tag{B.7}$$

A multi-dimensional RMS error RMSE_D is then computed according to (B.8), where D denotes the number of dimensions. This equation finds use in expressing the accuracy of the XY and XYZ positions.

$$\mathrm{RMSE}_D = \sqrt{\sum_{j=1}^{D}(\mathrm{RMSE})_j^2} \tag{B.8}$$

B.3.1. Ground Measurement

As already mentioned in Section B.2.6, the positions of the ground targets were measured before and after the flight, observing the delay of about 2 hours to ensure a different constellation of satellites. Such an approach is commonly practised to verify whether the data are consistent and whether an error did not affect one of the measurements.

As no reference measurement is performed, we can only compare the data with each other: $\boldsymbol{\Delta} = \boldsymbol{x}_{1,\mathrm{L}} - \boldsymbol{x}_{2,\mathrm{L}}$. The results indicate (Table B.4) that the ground measurement is consistent and does not contain major deviations – the RMS error is approximately 1 cm in all axes. In the given respect, the Z axis exhibits the maximum error, one of about 4 cm; however, this is an isolated case, as clearly shown in Figure B.8. Within the subsequent processing (GCPs and TPs), the averaged value of the measurements is used for every target.

Table B.4.: A comparison of the first and second measurements of ground targets.

Error type	$\boldsymbol{X}$ (mm)	$\boldsymbol{Y}$ (mm)	$\boldsymbol{Z}$ (mm)	$\boldsymbol{XY}$ (mm)	$\boldsymbol{XYZ}$ (mm)
RMS	5.2	10.4	12.8	11.7	17.3
Min (absolute)	0.7	0.3	1.0	1.4	4.1
Max (absolute)	10.4	22.6	39.0	23.1	39.8

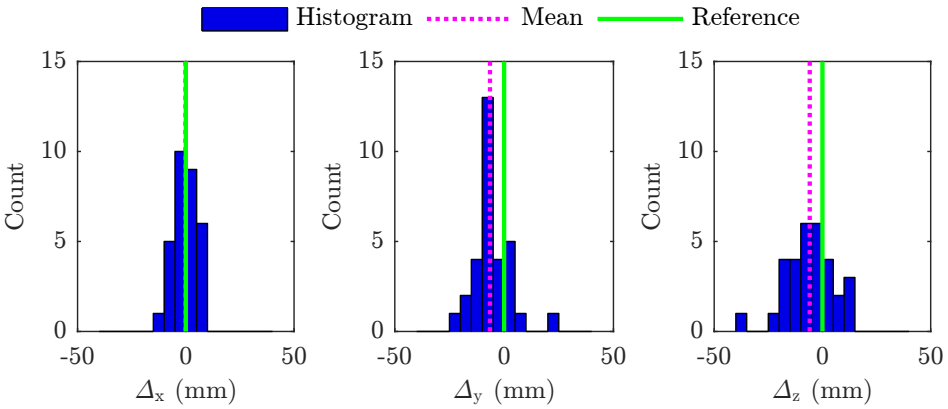

Figure B.8.: The histograms of errors between the first and second measurements.

B.3.2. Flight and Aerial Data

From the 194 images, only 137 were selected for processing. The images taken during the take-off and landing were manually selected and removed. Otherwise, this step can be carried out automatically since the coordinates of the start and end of the trajectory are known. The captured images, despite being perfectly sharp, are affected by a pair of significant issues due to the equipment used. Firstly, the wide angle lens mounted on the full frame camera caused the landing gear to be visible in all the images (Figure B.9a); however, this is not a serious problem, because relevant portions of an image can be excluded from the processing by a constant mask. Secondly, we had to eliminate lens vignetting via compensation in Adobe Photoshop Lightroom. The RAW image files were then converted into JPG at minimum compression.

Although each photograph contains several targets, their image quality depends on the position in the given image. In the corners, above all, the geometric and brightness distortion deforms the targets, rendering them unsuitable for processing. Contrary to that, the targets found in the central portion of an image exhibit clearly recognizable centres; the size of the targets corresponds to 10 – 15 pixels, as expected (Figure B.9b).

The flight parameters described in Section B.2.7 are theoretical and may vary slightly due to navigation inaccuracies and the low-accuracy GPS receiver incorpo-

(a) (b)

Figure B.9.: The sample of one of the images from UAS after brightness transformation (a) and the detail of a target from the same image (b). Location: 49°13'41.61"N, 16°34'19.002"E — WGS84.

rated in the flight control unit. This fact nevertheless should not affect the outcome of the experiment, because large overlaps are applied. The average flight speed measured by the GNSS/INS, excluding the take-off and landing phases, is 4.5 m s^{-1}. The average flight altitude above the starting point equals 46.3 m according to the GNSS/INS. As the starting point was situated at one of the highest locations within the area, the altitude AGL is more prominent in most of the zone.

The accuracy of the camera position measurement can be determined using aerial triangulation. To facilitate this step, Photoscan was employed for the indirect aerial imagery georeferencing, and all the 30 targets assumed the role of GCPs. During the processing, the interior orientation of the camera was also estimated, and the set of parameters was exported as the reference camera calibration. The upper half of Table B.5 presents the errors of the onboard position measurement compared to AT (Photoscan). The RMS errors of 162 mm for the horizontal position and 21 mm for the Z axis are rather unusual for a GNSS measurement: as a rule, horizontal accuracy is better than vertical. The non-standard condition probably arises from the synchronisation error between the INS measurement and the image capture moment, and this assumption is actually proven in Figure B.10a, where the horizontal error of all the camera positions is clearly in the direction of the flight.

B.3.3. Calibration

The custom calibration described in Section B.2.2 uses the position data measured by the onboard sensors and obtained via AT to estimate the lever arm correction vector, synchronisation delay, and base station offset. Due to the nature of the flight trajectory, only the horizontal components of the vectors are estimated. A solution is found using the Gauss-Newton method, which estimates the unknowns

Table B.5.: The accuracy of the camera position measured by the onboard sensors before and after the custom calibration. The reference position is obtained from AT.

Calibration	Error type	$\boldsymbol{X}$ (mm)	$\boldsymbol{Y}$ (mm)	$\boldsymbol{Z}$ (mm)	$\boldsymbol{XY}$ (mm)	$\boldsymbol{XYZ}$ (mm)
No	Mean	-2.5	-38.2	8.7	157.4	158.9
	RMS	72.6	145.1	21.4	162.3	163.7
	Min (absolute)	7.1	1.4	0.3	79.1	94.3
	Max (absolute)	152.9	286.5	75.2	301.2	302.8
Yes	Mean	3.1	-19.4	8.7	37.0	43.0
	RMS	21.3	44.9	21.4	49.7	54.1
	Min (absolute)	0.1	0.1	0.3	2.5	3.8
	Max (absolute)	75.7	152.3	75.2	157.7	160.7

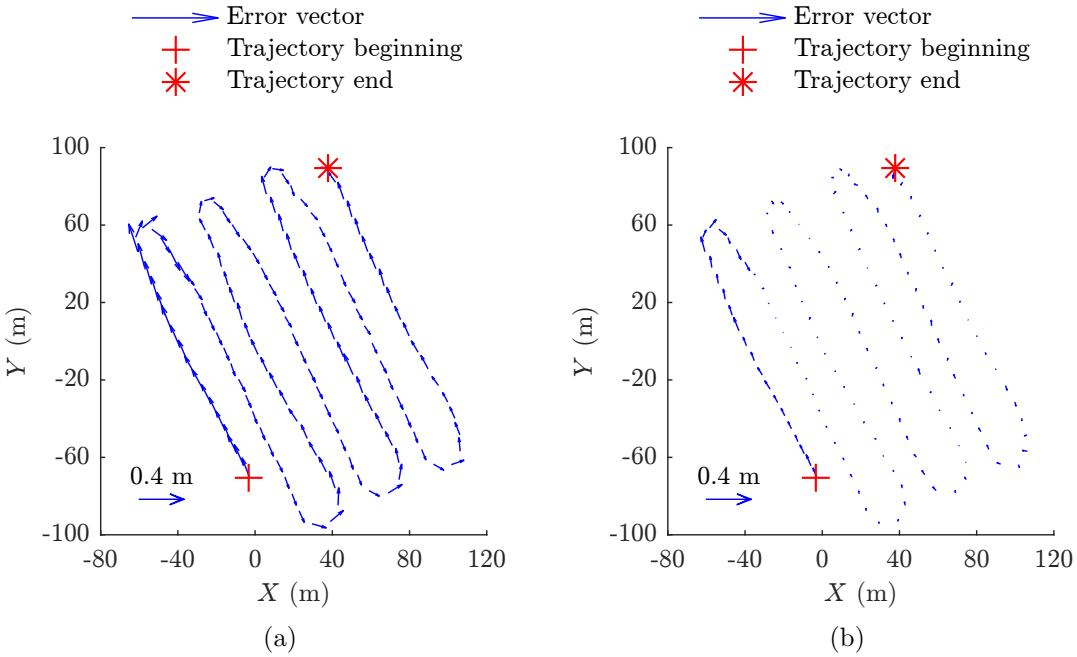

Figure B.10.: The camera position measurement error before (a) and after (b) the custom calibration. The arrows head from the AT (reference) position to the measured one, and they are 50x enlarged.

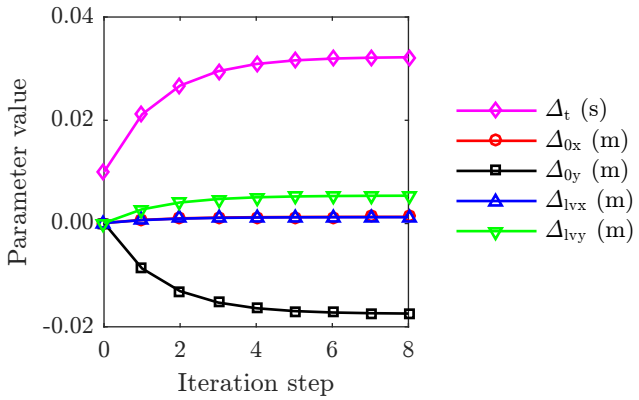

Figure B.11.: The value of the unknown parameters during the estimation process.

iteratively to minimise the observation error (B.4). The vertical components of the lever arm and base station offset are correlated and cannot be separated during the estimation. The initial values for the lever arm correction and base station offset were chosen close to zero as the lever arm had been pre-calibrated and the base station offset is expected to be minimal. The initial value for the synchronisation delay was set to 0.01 second, according to the documentation of the INS unit and the camera parameters.

The five unknowns were obtained during 8 iteration steps, as illustrated in Figure B.11. We found the following values of the unknowns: synchronisation delay Δ_t = 32.2 ms; lever arm offset ($\Delta_{lvx}, \Delta_{lvy}$)=(1.2, 5.4) mm; and base station offset (Δ_{0x}, Δ_{0y})=(1.3, -17.4) mm. These estimated parameters, excepting the base station offset, are ideally constant and can be used as the set of calibration parameters in future measurements. The parameters were employed to correct the measured position, which was again compared with the position obtained from AT. Table B.5 shows that, after the calibration, the spatial RMS error decreased from 164 mm to 54 mm, producing an improvement of 67 %. With the sole exception of the trajectory origin (mainly the first strip), the error vectors are compensated, as demonstrated in Figure B.10b.

B.3.4. Object Accuracy

This section discusses the object point determination accuracy, namely, the accuracy of an orthophoto, point cloud, or another aerial photogrammetry product. The photogrammetric processing was invariably performed with Photoscan; in the georeferencing and calibration, however, different techniques were tested and compared. The accuracy was determined using ground targets, or test points, whose positions were measured by means of survey-grade equipment (Section B.2.6). The results

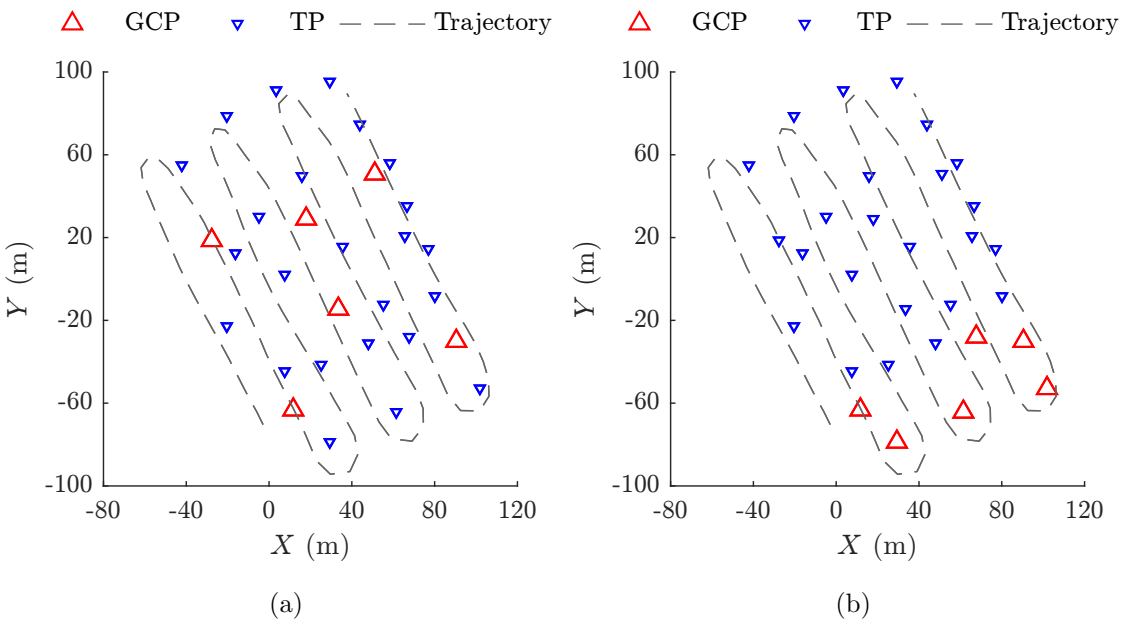

Figure B.12.: The distribution of the GCPs and TPs for the indirect georeferencing in versions #1a (a) and #1b (b).

are summarised in Table B.6, inspired by [18], who studied a similar topic in the context of manned aircraft, and further illustrated in Figure B.13.

First of all, we tested the accuracy of indirect georeferencing, the most common georeferencing technique in UAS photogrammetry. Version #1a in Table B.6 presents the object accuracy of IG, where 6 well-distributed GPCs were used (Figure B.12a), with the interior orientation parameters estimated during the photo alignment stage (field calibration). The RMS error did not exceed 1 cm for the X and Y and 2 cm for the Z coordinates (see Figures B.14a and B.14b for a graphical interpretation). The procedure was then repeated using another 6 GCPs, which, however were not distributed properly: all the GCPs lay in one part of the area, close to each other (Figure B.12b). Such an arrangement corresponds to a situation where a portion of an area is inaccessible for some reason. The results indicate (version #1b) that the accuracy deteriorated, especially in the Z coordinate; at this axis, the RMS error increased almost five times, to 9 cm. The error is mostly systematic: the mean error corresponds about 7 cm. The interior orientation parameters can be pre-calibrated in a laboratory or during a calibration flight. Version #1c is nearly the same as #1a, the only difference consisting in that the interior orientation was not field-calibrated; instead, pre-calibrated parameters were used (Section B.2.3). In terms of accuracy, this configuration performs significantly worse: the spatial RMS error increases by almost an order of magnitude, and the mean error dominates in the Z coordinate.

Table B.6.: The object point determination accuracy acquired using different techniques and calibrations.

#	Configuration	GCP/ TP	Mean (mm)					RMSE (mm)				
			X	***Y***	***Z***	***XY***	***XYZ***	***X***	***Y***	***Z***	***XY***	***XYZ***
1a	IG well distr. *fc*	6/24	-3	-4	-6	5	8	9	9	20	12	24
1b	IG bad distr. *fc*	6/24	1	12	-72	12	73	7	19	92	20	94
1c	IG well distr. *pc*	6/24	-3	-3	-52	4	52	29	45	129	53	139
2a	DG-AT *fc*	0/30	2	33	-39	33	51	20	38	43	43	61
2b	DG-AT *pc*	0/30	-69	-89	429	113	444	159	197	439	253	507
2c	DG-AT *sc fc*	0/30	6	23	17	24	29	19	27	25	33	41
2d	DG-AT *sc pc*	0/30	-75	-115	458	137	478	178	229	471	290	553
3a	DG-AT + 1 GCP *sc fc*	1/29	7	10	14	12	18	18	17	22	25	33

Abbrev: *fc* – field-calibrated camera; *pc* – pre-calibrated camera; *sc* – system (custom) calibration.

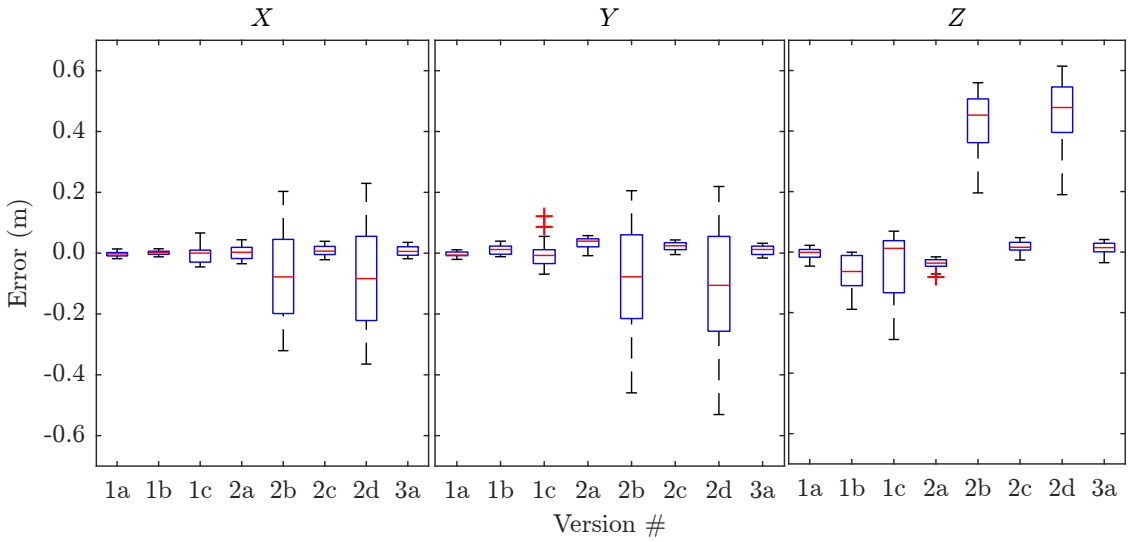

Figure B.13.: The object accuracy in all of the eight configurations.

The second part of Table B.6 introduces the results of the direct georeferencing process, whose application embodies the central aim of the present paper. In the given context, DG denotes georeferencing without the use of GCPs and cannot be interpreted as *traditional* DG, because it is assisted by computer vision-based AT. The said traditional approach, which computes the object position directly through the use of the six exterior orientation elements measured by the onboard sensors, is not tested in this paper.

DG requires an accurate placement of sensors and time synchronisation. Version #2a results in a configuration where the lever arms between the GNSS antenna, INS unit, and camera were measured before the flight and saved into the

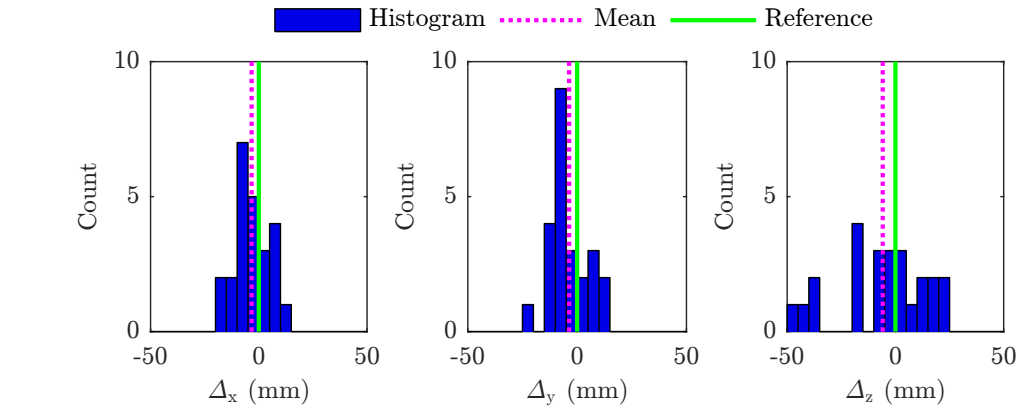

(a)

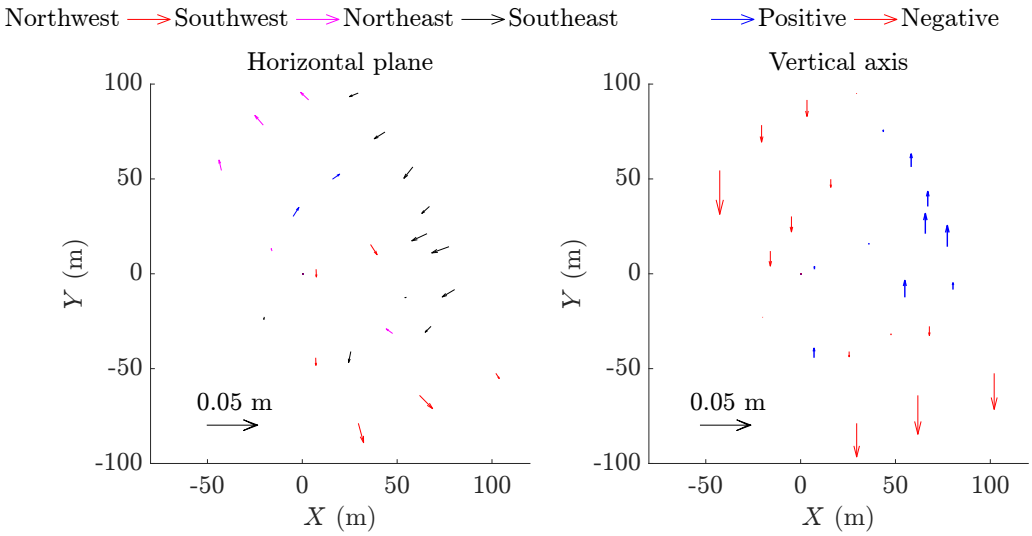

(b)

Figure B.14.: The object accuracy obtained via IG in version #1a. The histogram (a) shows the error distribution, and the plot (b) demonstrates the relationship between the error vectors and the test point positions (the vectors are enlarged 500 times).

INS unit; the time synchronisation is ensured by the hardware, as described in Section B.2.4. During the photo alignment stage, the obtained position was refined, and the photogrammetric angles and interior orientation were estimated. The RMS error reached 2 cm for the X axis and about 4 cm for the Y and Z axes. The accuracy is 2 to 3 times worse compared to the IG in version #1a, and the mean error dominates. Once the pre-calibrated interior orientation parameters have been applied (version #2b), the accuracy decreased significantly. Both the mean and the RMS spatial errors increased by an order of magnitude.

In the previous chapters, we discussed a custom calibration procedure to estimate

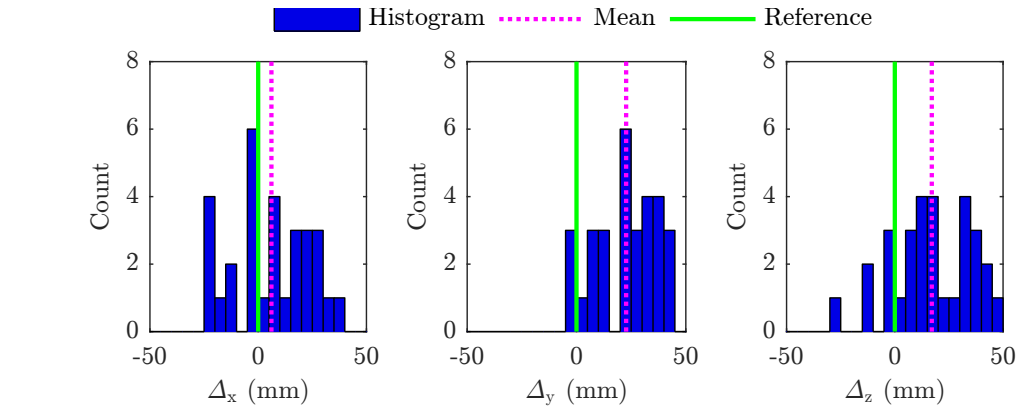

(a)

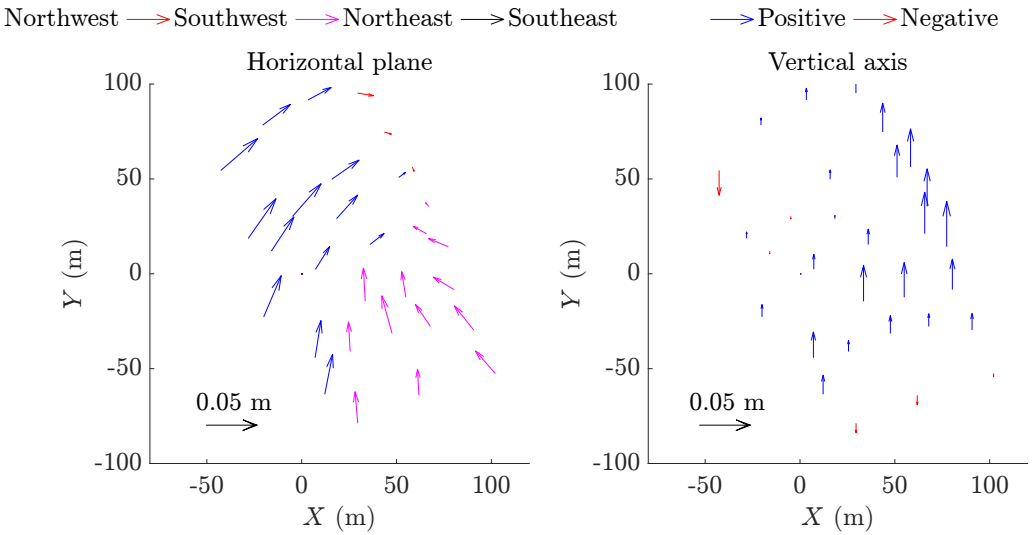

(b)

Figure B.15.: The object accuracy obtained via DG in version #2c. The histogram (a) shows the error distribution, and the plot (b) demonstrates the relationship between the error vectors and the test point positions (the vectors are enlarged 500 times).

the synchronisation delay and lever arm offset. These parameters are constant and can be used for refining the measured data. Version #2c yields accuracy results acquired using custom calibration; contrary to #2a, #2c produced an improvement in all the axes, Y and Z in particular. After the custom calibration, the RMS error does not exceed 3 cm in all the axes (see Figures B.15a and B.15b for a graphical interpretation). The synchronisation delay compensation plays a major role here because it causes a position error depending on the speed and direction of the flight. When we supported the custom calibration with camera pre-calibration (version #2d), an accuracy decrease was observed, similarly to the previous cases.

Figure B.16.: A part of the georeferenced point cloud containing 29 million points. Location: 49°13'41.61"N, 16°34'19.002"E — WGS84.

The above-outlined results show that the field calibration of some constant parameters can increase the accuracy of DG; however, there are also certain systematic errors ineliminable without GCPs. This problem was already discussed by [18], and it mainly consists in the offset of the position measurement performed by an onboard GNSS receiver and the inaccurate field calibration of camera interior parameters. These systematic errors can be potentially compensated by a GCP. In version #3a, one GCP from the peripheral zone of the measured area (GCP #1, Figure B.5) was used during the processing, together with the onboard GNSS/INS data. Each of the axes exhibits a slight improvement compared to version #2c, but the Y axis is prominent in this respect as the RMS error decreased by almost 1 cm. Since the mean error decreased too, the GNSS measurement shift was most probably compensated.

After the alignment stage, once the exterior orientation of all the images has been estimated, Photoscan can generate a georeferenced dense point cloud. Figure B.16 displays a point cloud containing almost 29 million of points, which corresponds to a density of about 800 points m^{-2}. Based on this, an orthophoto, mesh, or DEM can be created.

B.4. Discussion

In this section, the results of the previous chapter are analyzed and compared with other current research papers. We also briefly discuss the perspectives of DG systems in micro- and light UASs.

B.4.1. Positioning

In order to assess the positioning accuracy of the designed multi-sensor system, we would need to possess reference data; however, as this category of UASs has very limited payload capabilities, it is not possible to carry another set of sensors providing better accuracy. The drawback can be eliminated via several suitable methods, and these are defined as follows: i) using a larger UAS or manned aircraft carrying a calibrated positioning system; ii) tracking the position of a UAS from the ground (presented in [33]); iii) utilizing AT to estimate the camera exterior orientation. We applied the last approach since 30 targets had already been distributed in the area. A comparison of the position data from AT and the GNSS/INS system showed a very clearly visible systematic error depending on the flight direction (Figure B.10a). The proposed custom calibration then enabled us to establish that the error arises mainly from the synchronisation delay between the GNSS/INS and the camera shutter. The delay of 32 ms notably exceeds the expected value, and a closer look at the error vectors after the calibration (Figure B.10b) will reveal a persisting systematic error in the flight direction at the beginning of the trajectory. This issue may arise from the fact that the delay was not constant throughout the flight; a step change in the delay could cause such behaviour. Another problem possibly rests in the estimation of the INS internal parameters: Ellipse-E INS utilises an extended Kalman filter to estimate the lever arms and angular misalignments between the GNSS and INS reference frames during an operation. Even though the parameters were initialised based on laboratory estimation, insufficient dynamics at the origin of the flight trajectory could cause their inaccurate estimation. The incorrect lever arm in the longitudinal axis might also produce the error visible in Figure B.10b. These assumptions are nevertheless still to be verified within future experiments. Regardless of this problem, the spatial positioning RMS error decreased by 67 % (to 54 mm) after the proposed system calibration.

The above-described practice shows that AT embodies a beneficial tool to evaluate the performance of DG systems and to calibrate them whenever no other reference data are available. As AT can estimate the full set of parameters related to the exterior orientation, a similar calibration technique can be used for evaluating and calibrating the angular elements (photogrammetric angles). However, the accuracy achievable with AT depends on the quality and distribution of the GCPs, as examined by, e.g., [31]. The proposed calibration can nevertheless succeed only if certain flight parameters are met:

- The heading (azimuth) must not be constant throughout the flight; otherwise, the lever arm correction and the base station offset correlate and cannot be separated.

- The same condition applies to the lever arm correction and the synchronisation delay. These two parameters correlate perfectly and cannot be separated if the flight speed is constant, with the heading and course remaining mutually dependent throughout the flight.

- The synchronisation delay estimation presumes a linear flight trajectory and is thus applicable in small delays only.

B.4.2. Georeferencing Performance

The previous section discussed positioning accuracy, an essential aspect of DG; object accuracy, however, depends also on the interior orientation and the performance of the CV methods implemented in the photogrammetric software used. Further, object accuracy can be evaluated directly, by being compared with ground measurement.

If we compare the object accuracies of the IG and DG used within the presented mission, then the IG clearly outperforms the other technique. The IG in version #1a reached the spatial RMS error of 2.4 cm, which is almost twice the accuracy of the DG in version #2c, namely, 4.1 cm. In both these cases, the interior orientation was field calibrated. Custom flight calibration proved to be very beneficial for the applied DG, yielding the improvement of 32 %; yet, at the same time, it should be noted that a major role is assumed here by the compensation of the synchronisation delay, which exceeded the originally expected value. The above two versions are also comparable using the graphical representation of errors in Figures B.14 and B.15. The character of the DG errors in Figure B.15b is more systematic than that of the IG errors in Figure B.14b, meaning that some space still remains available for improving the proposed system.

Contrary to the custom system calibration, the interior orientation pre-calibration resulted in significant degradation of the object accuracy. In all of the pre-calibrated versions, the accuracy decreased by an order of magnitude. This observation shows that the lens interior parameters are not stable, mainly due to excessive clearances in the individual parts and mount of the camera. In our case, the camera field calibration allowed accurate interior orientation estimation according to the object accuracy assessment; the same outcomes are outlined in a relevant study by [24].

The IG object accuracy presented in this paper (1.2 cm RMS for XY and 2.0 cm RMS for Z) is similar to the accuracies identified by [2]; [3]; and [4] (see Section B.1 of the present article). If certain conditions are satisfied, the technique outlined herein ensures stable and predictable outcomes. From the perspective of georeferencing, the following items must be taken into account:

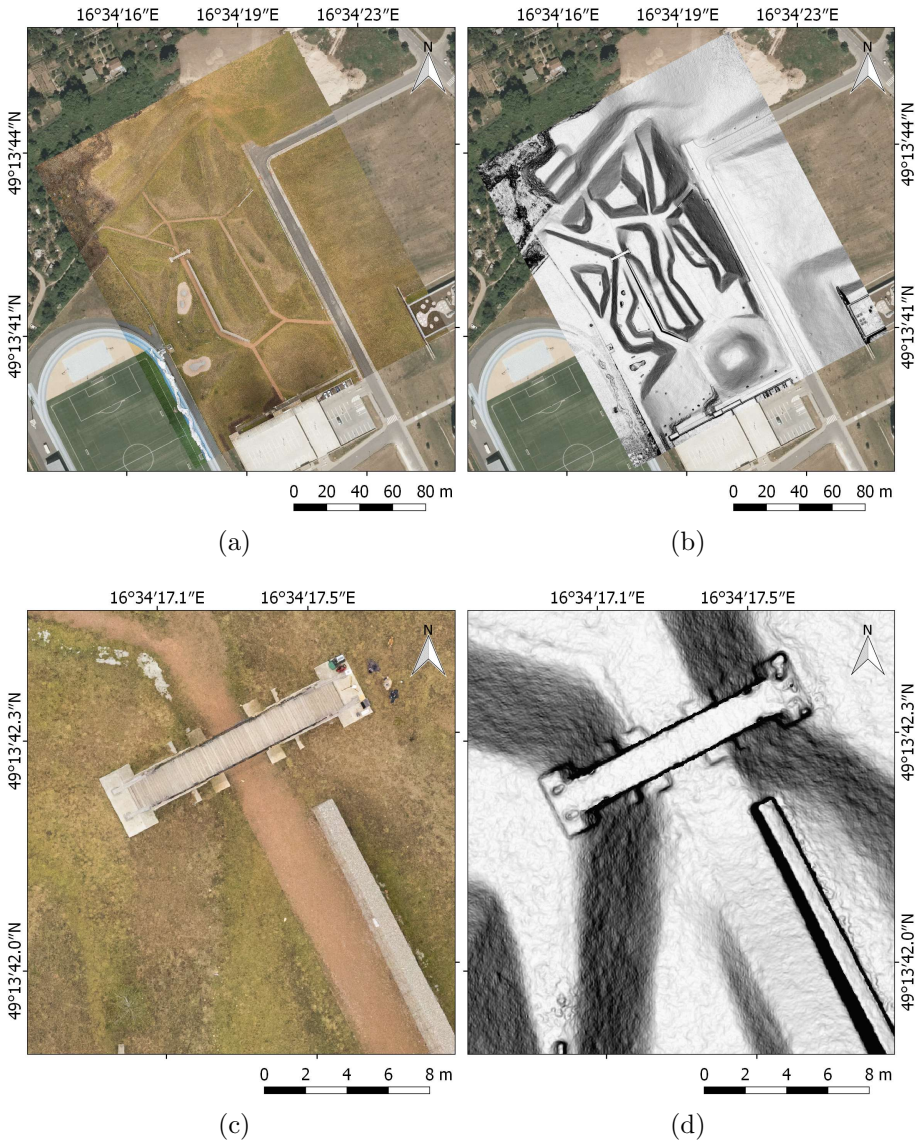

Figure B.17.: The ortophoto (a) and gradient map (b) created via the presented multi-sensor system as a layer over the orthophoto map adopted from [27]. Figures (c) and (d) show a detail of the bridge where the base station was located.

- The object accuracy directly depends on the accuracy of GCPs.
- Any inappropriate distribution of GCPs may negatively affect the object accuracy.

The established DG object accuracy (3.3 cm RMS for XY and 2.5 cm RMS for Z) appears to range among the top values achieved within the current research into the given problem. Such a result was obtained thanks to the state-of-the-art navigation and camera systems and the proposed custom calibration, which utilised

complex data from the onboard sensors and AT to estimate the unknown parameters. Synchronisation delay estimation in particular is not common in today's implementations. Moreover, the performance of our solution was determined thoroughly to produce credible outcomes. Comparable results are outlined by [7], who employ a dual-antenna RTK-GNSS system carried by a multi-rotor UAS. Special attention is also paid to the time synchronisation and lever arm calibration. The object accuracy was tested during two flights; the first measurement yielded the RMS of 3.8 cm for XY and 3.0 cm for Z, and the second one resulted in 1.1 cm for XY and 0.9 cm for Z. Even though such outcomes are, in fact, very good, it should also be noted that the flight altitude (20 m) and speed (2 m s^{-1}) were low, and the performance of the second flight was verified on 9 test points only. The spatial accuracy of about 11 cm is presented by [5]; their solution is nevertheless limited by a less accurate DGPS receiver. By comparison, [4] employed a low-cost RTK-GPS module, albeit only to also achieve the object accuracy at the decimetre level: 16.4 cm RMS for the XY and 23.5 cm for the Z axes. This is due to inaccurate time synchronisation and lever arm calibration.

In general, the accuracy of direct georeferencing is typically affected by the following factors:

- None or inaccurate lever arm calibration between the GNSS antenna and the camera perspective centre.
- Inaccurate time synchronisation between the onboard positioning system and the camera shutter.
- Inaccurate estimation of the interior orientation (camera parameters).

Traditional direct georeferencing, where the measured exterior orientation is directly used for the actual georeferencing, has become rather obsolete, especially in UAS photogrammetry. At present, specialised softwares estimate the photogrammetric angles and refine the measured positions, making attitude measurement redundant in the context of the application discussed herein. Figure B.17 shows several outputs of the described mission: a directly georeferenced true orthophoto map with the ground resolution of about 2 cm px^{-1}, and a gradient map to illustrate the shape of the terrain.

B.4.3. Outlook

Although DG systems for micro- and light UASs do not match the accuracy of IG ones and are generally more challenging in terms of the calibration and equipment, they show a major potential for future use within diverse fields and disciplines. The

advantage is obvious: the absence of GCPs saves a large amount of time and enables fully automated data processing. These systems have expanded primarily due to the decreasing cost and size of accurate INS and RTK-GNSS systems. In recent years, such UAS systems for DG have begun to appear on the market. For example, senseFly ([34]) offers a UAS equipped with an RTK-GNSS receiver designed for DG with the object accuracy of 3 cm at each axis (according to the specification). This fixed-wing UAS is capable of flying for almost 1 hour, thus covering several square kilometres; the independence from GCPs is then highly beneficial. Such UASs are typically not as sophisticated as the solution proposed within this paper, which exploits the leading navigation system technologies. A case study presented on [35] shows that a centimetre-level object accuracy can also be reached using much simpler equipment, namely, a fixed-wing UAS fitted with a single-antenna single-frequency GNSS receiver supporting post processed kinematic (PPK); the UAS does not comprise a dedicated INS unit. In all the cases, however, it is good practice to use some test points for the accuracy assessment and quality assurance.

B.5. Conclusion

This paper presents a custom-built system for the direct georeferencing of aerial imagery, designed specially for micro- and light UASs. The related multi-sensor system was implemented and successfully tested during several missions; one of the experiments is described in detail herein. To achieve high accuracy, we employed leading navigation system technologies, namely, an RTK-GNSS receiver and an INS unit to fuse the positioning and inertial data. The proposed field calibration method enables the system to attain centimetre-level object accuracy without the need of ground control points.

A significant portion of the research consisted in assessing the accuracy of the whole system; for that reason, 30 test points were deployed within the test area. The performance of the direct and the indirect georeferencing methods and different calibration techniques was examined. The applied direct georeferencing, supported by the proposed field calibration, yielded the spatial object accuracy of 4.1 cm RMS, which is an improvement of 32 % compared to the accuracy without the calibration. The object accuracy of 2.4 cm RMS was achieved via the indirect georeferencing method, using 6 test points as GCPs. The results indicate that IG can be very accurate even with a consumer-grade camera and no additional onboard sensors. However, the introduced DG object accuracy is sufficient for most applications, and the fact that ground measurement is not necessary constitutes a highly beneficial aspect.

The presented multi-sensor system for UASs finds use in fields where GCPs can-

not be utilised. Such a situation usually occurs in areas inaccessible or dangerous to humans, including zones of natural disasters, radiation hotspot localisation, or environmental mapping. The system was successfully employed in a gamma radiation mapping experiment which examined the potential of cooperation between UAS and UGV during the localisation of hotspots; the outcomes are presented in [36] and [37].

Bibliography

[1] Maziar Arjomandi, Shane Agostino, Matthew Mammone, Matthieu Nelson, and Tong Zhou. Classification of Unmanned Aerial Vehicles, 2006. URL: http://afrsweb.usda.gov/SP2UserFiles/Place/62351500/Unmanned.pdf.

[2] P. Barry and R. Coakley. Field Accuracy Test of RPAS Photogrammetry. *ISPRS - International Archives of the Photogrammetry, Remote Sensing and Spatial Information Sciences*, XL-1/W2:27–31, August 2013. URL: http://www.int-arch-photogramm-remote-sens-spatial-inf-sci.net/XL-1-W2/27/2013/, doi:10.5194/isprsarchives-XL-1-W2-27-2013.

[3] Apostol Panayotov. Photogrammetric Accuracy of Real Time Kinematic Enabled Unmanned Aerial Vehicle Systems, October 2015. URL: http://uas.usgs.gov/pdf/Reports/USGS_FINAL_REPORT_10212015.pdf.

[4] H. Fazeli, F. Samadzadegan, and F. Dadrasjavan. Evaluating the Potential of RTK-UAV for Automatic Point Cloud Generation in 3d Rapid Mapping. In *ISPRS - International Archives of the Photogrammetry, Remote Sensing and Spatial Information Sciences*, volume XLI-B6, pages 221–226. Copernicus GmbH, June 2016. URL: http://www.int-arch-photogramm-remote-sens-spatial-inf-sci.net/XLI-B6/221/2016/, doi:10.5194/isprs-archives-XLI-B6-221-2016.

[5] D. Turner, A. Lucieer, and L. Wallace. Direct Georeferencing of Ultrahigh-Resolution UAV Imagery. *IEEE Transactions on Geoscience and Remote Sensing*, 52(5):2738–2745, May 2014. doi:10.1109/TGRS.2013.2265295.

[6] C. F. Lo, M. L. Tsai, K. W. Chiang, C. H. Chu, G. J. Tsai, C. K. Cheng, N. El-Sheimy, and H. Ayman. The Direct Georeferencing Application and Performance Analysis of Uav Helicopter in Gcp-Free Area. In *The International Archives of Photogrammetry, Remote Sensing and Spatial Information Sciences; Gottingen*, volume XL, pages 151–157, Gottingen, Germany, 2015. Copernicus GmbH. URL: https://search.proquest.com/docview/1756968633/abstract/B238140DB5964263PQ/1, doi:http://dx.doi.org/10.5194/isprsarchives-XL-1-W4-151-2015.

[7] C. Eling, M. Wieland, C. Hess, L. Klingbeil, and H. Kuhlmann. Development and Evaluation of a UAV Based Mapping System for Remote Sensing and Surveying Applications. *ISPRS - International Archives of the Photogrammetry, Remote Sensing and Spatial Information Sciences*, XL-1/W4:233–239, August 2015. URL: http://www.int-arch-photogramm-remote-sens-spatial-inf-sci.net/XL-1-W4/233/2015/, doi:10.5194/isprsarchives-XL-1-W4-233-2015.

[8] M. Sakr, Z. Lari, and N. El-Sheimy. Design and Implementation of a Low-Cost Uav-Based Multi-Sensor Payload for Rapid-Response Mapping Applications. *ISPRS - International Archives of the Photogrammetry, Remote Sensing and Spatial Information Sciences*, 41B1:1017–1022, June 2016. URL: http://adsabs.harvard.edu/abs/2016ISPAr41B1.1017S, doi:10.5194/isprs-archives-XLI-B1-1017-2016.

[9] M. Rehak, R. Mabillard, and J. Skaloud. A micro-UAV with the capability of direct georeferencing. volume 40, pages 317–323. ISPRS, 2013. URL: https://www.int-arch-photogramm-remote-sens-spatial-inf-sci.net/XL-1-W2/317/2013/, doi:10.5194/isprsarchives-XL-1-W2-317-2013.

[10] N. Pfeifer, P. Glira, and C. Briese. Direct Georeferencing with on Board Navigation Components of Light Weight Uav Platforms. *ISPRS - International Archives of the Photogrammetry, Remote Sensing and Spatial Information Sciences*, 39B7:487–492, August 2012. URL: http://adsabs.harvard.edu/abs/2012ISPAr39B7..487P, doi:10.5194/isprsarchives-XXXIX-B7-487-2012.

[11] Z. Lari and N. El-Sheimy. System Considerations and Challendes in 3d Mapping and Modeling Using Low-Cost Uav Systems. *ISPRS - International Archives of the Photogrammetry, Remote Sensing and Spatial Information Sciences*, 3:343–348, August 2015. URL: http://adsabs.harvard.edu/abs/2015ISPAr.XL3..343L, doi:10.5194/isprsarchives-XL-3-W3-343-2015.

[12] Ahmed S. Elsharkawy and Ayman F. Habib. Error Analysis for the Airborne Direct Georeferincing Technique. *ISPRS - International Archives of the Photogrammetry, Remote Sensing and Spatial Information Sciences*, 41B1:1213–1219, October 2016. URL: http://adsabs.harvard.edu/abs/2016ISPAr41B1.1213E, doi:10.5194/isprs-archives-XLI-B1-1213-2016.

[13] Petr Gabrlik, Ales Jelinek, and Premysl Janata. Precise Multi-Sensor Georeferencing System for Micro UAVs. In *IFAC-PapersOnLine*, volume 49, pages 170–175, Amsterdam, 2016. Elsevier. URL: http://www.sciencedirect.com/science/article/pii/S2405896316326659, doi:10.1016/j.ifacol.2016.12.029.

[14] Ludek Zalud, Petra Kocmanova, Frantisek Burian, Tomas Jilek, Petr Kalvoda, and Lukas Kopecny. Calibration and Evaluation of Parameters in A 3d Proximity Rotating Scanner. *Elektronika Ir Elektrotechnika*, 21(1):3–12, 2015. doi:10.5755/j01.eee.21.1.7299.

[15] Petra Kocmanova and Ludek Zalud. Multispectral Stereoscopic Robotic Head Calibration and Evaluation. In *Modelling and Simulation for Autonomous Systems*, Lecture Notes in Computer Science, pages 173–184. Springer, Cham, April 2015. URL: https://link.springer.com/chapter/10.1007/978-3-319-22383-4_13, doi:10.1007/978-3-319-22383-4_13.

[16] T. Jilek. Radiation intensity mapping in outdoor environments using a mobile robot with RTK GNSS. In *International Conference on Military Technologies (ICMT) 2015*, pages 1–7, May 2015. doi:10.1109/MILTECHS.2015.7153755.

[17] Karl Kraus. *Photogrammetry: Geometry from Images and Laser Scans*, volume 2nd ed. Walter de Gruyter, Berlin, 2007. ISBN: 978-3-11-019007-6.

[18] Michael Cramer. Performance of GPS/Inertial Solutions in Photogrammetry. pages 49–62, 2001. ISBN: 3-87907-359-7.

[19] Peter Deuflhard. Least Squares Problems: Gauss-Newton Methods. In *Newton Methods for Nonlinear Problems*, Springer Series in Computational Mathematics, pages 173–231. Springer, Berlin, Heidelberg, 2011. DOI: 10.1007/978-3-642-23899-4_4. URL: https://link.springer.com/chapter/10.1007/978-3-642-23899-4_4.

[20] Richard Hartley and Andrew Zisserman. *Multiple View Geometry in Computer Vision*, volume 2nd ed. Cambridge University Press, Cambridge, 2003. URL: https://www.cambridge.org/core/books/multiple-view-geometry-in-computer-vision/0B6F289C78B2B23F596CAA76D3D43F7A, doi:10.1017/CBO9780511811685.

[21] Duane C. Brown. Decentering Distortion of Lenses. *Photogrammetric Engineering*, 32(3):444–462, 1966. URL: http://www.close-range.com/docs/Decentering_Distortion_of_Lenses_Brown_1966_may_444-462.pdf.

[22] Duane C. Brown. Close-range camera calibration. *Photogrammetric Engineering*, 37(8):855–866, 1971. URL: https://www.asprs.org/wp-content/uploads/pers/1971journal/aug/1971_aug_855-866.pdf.

[23] Agisoft. Agisoft PhotoScan User Manual: Professional Edition, Version 1.3, 2017. URL: http://www.agisoft.com/pdf/photoscan-pro_1_3_en.pdf.

[24] Steve Harwin, Arko Lucieer, and Jon Osborn. The Impact of the Calibration Method on the Accuracy of Point Clouds Derived Using Unmanned Aerial Vehicle Multi-View Stereopsis. *Remote Sensing*, 7(9):11933–11953, September 2015. URL: http://www.mdpi.com/2072-4292/7/9/11933, doi:10.3390/rs70911933.

[25] Soohee Han, Jinhwan Park, and Wonhee Lee. On-Site vs. Laboratorial Implementation of Camera Self-Calibration for UAV Photogrammetry. *Journal of the Korean Society of Surveying, Geodesy, Photogrammetry and Cartography*, 34(4):349–356, August 2016. DOI: 10.7848/ksgpc.2016.34.4.349. doi:10.7848/ksgpc.2016.34.4.349.

[26] M. Rieke, T. Foerster, J. Geipel, and T. Prinz. High-precision Positioning and Real-time Data Processing of UAV-Systems. *ISPRS - International Archives of the Photogrammetry, Remote Sensing and Spatial Information Sciences*, XXXVIII-1/C22:119–124, September 2012. URL: http://www.int-arch-photogramm-remote-sens-spatial-inf-sci.net/XXXVIII-1-C22/119/2011/, doi:10.5194/isprsarchives-XXXVIII-1-C22-119-2011.

[27] CUZK. CUZK - Geoportal, 2010. [cit: 2017-3-15]. URL: http://geoportal.cuzk.cz.

[28] Tomi Rosnell and Eija Honkavaara. Point Cloud Generation from Aerial Image Data Acquired by a Quadrocopter Type Micro Unmanned Aerial Vehicle and a Digital Still Camera. *Sensors*, 12(1):453–480, January 2012. URL: http://www.mdpi.com/1424-8220/12/1/453, doi:10.3390/s120100453.

[29] Jorge Torres-Sanchez, Francisca Lopez-Granados, Irene Borra-Serrano, and Jose Manuel Pena. Assessing UAV-collected image overlap influence on computation time and digital surface model accuracy in olive orchards. *Precision Agriculture*, 19:1–19, February 2017. URL: https://link.springer.com/article/10.1007/s11119-017-9502-0, doi:10.1007/s11119-017-9502-0.

[30] G. Verhoeven, M. Doneus, Ch. Briese, and F. Vermeulen. Mapping by matching: a computer vision-based approach to fast and accurate georeferencing of archaeological aerial photographs. *Journal of Archaeological Science*, 39(7):2060–2070, July 2012.

URL: http://www.sciencedirect.com/science/article/pii/S0305440312000866, doi:10.1016/j.jas.2012.02.022.

[31] Dami Vericat, James Brasington, Joe Wheaton, and Michaela Cowie. Accuracy assessment of aerial photographs acquired using lighter-than-air blimps: low-cost tools for mapping river corridors. *River Research and Applications*, 25(8):985–1000, October 2009. URL: http://onlinelibrary.wiley.com/doi/10.1002/rra.1198/abstract, doi:10.1002/rra.1198.

[32] Mohammad Reza Faraji, Xiaojun Qi, and Austin Jensen. Computer visionbased orthorectification and georeferencing of aerial image sets. *Journal of Applied Remote Sensing*, 10(3):036027–036027, 2016. URL: http://dx.doi.org/10.1117/1.JRS.10.036027, doi:10.1117/1.JRS.10.036027.

[33] M. Blaha, H. Eisenbeiss, D. Grimm, and P. Limpach. Direct Georeferencing of UAVs. *ISPRS - International Archives of the Photogrammetry, Remote Sensing and Spatial Information Sciences*, XXXVIII-1/C22:131–136, September 2012. URL: http://www.int-arch-photogramm-remote-sens-spatial-inf-sci.net/XXXVIII-1-C22/131/2011/isprsarchives-XXXVIII-1-C22-131-2011.html, doi:10.5194/isprsarchives-XXXVIII-1-C22-131-2011.

[34] senseFly. eBee Plus, 2017. [cit: 2018-2-7]. URL: https://www.sensefly.com/drones/ebee-plus.html.

[35] 3DroneMapping. 3dronemapping completes PPK trials, 2016. [cit: 2017-7-31]. URL: https://3dronemapping.com/3dronemapping-completes-ppk-trials/.

[36] Tomas Lazna, Petr Gabrlik, Tomas Jilek, and Ludek Zalud. Cooperation between an unmanned aerial vehicle and an unmanned ground vehicle in highly accurate localization of gamma radiation hotspots. *International Journal of Advanced Robotic Systems*, 15(1):1–16, January 2018. URL: https://doi.org/10.1177/1729881417750787, doi:10.1177/1729881417750787.

[37] Tomas Lazna, Tomas Jilek, Petr Gabrlik, and Ludek Zalud. Multi-robotic area exploration for environmental protection. In *Lecture Notes in Computer Science*, volume 10444, pages 240–254, Cham, January 2017. Springer. URL: https://link.springer.com/chapter/10.1007/978-3-319-64635-0_18, doi:10.1007/978-3-319-64635-0_18.

C. Cooperation Between an Unmanned Aerial Vehicle and an Unmanned Ground Vehicle in Highly Accurate Localization of Gamma Radiation Hotspots

Outline

C.1. Introduction 96
C.2. Methods 97
C.3. Results 109
C.4. Discussion 116
C.5. Conclusion 119
Bibliography 123

Bibliographic Information

LAZNA, Tomas, Petr GABRLIK, Tomas JILEK and Ludek ZALUD. Cooperation between an unmanned aerial vehicle and an unmanned ground vehicle in highly accurate localization of gamma radiation hotspots. *International Journal of Advanced Robotic Systems* [online]. 2018, **15**(1), 1–16 [cit. 2020-08-25]. DOI: 10.1177/1729881417750787. ISSN 1729-8814. Available from: `http://journals.sagepub.com/doi/10.1177/1729881417750787`

Abstract

The paper discusses the highly autonomous robotic search and localization of radiation sources in outdoor environments. The cooperation between a human operator,

an unmanned aerial vehicle (UAV), and an unmanned ground vehicle (UGV) is used to render the given mission highly effective, in accordance with the idea that the search for potential radiation sources should be fast, precise, and reliable. Each of the components assumes its own role in the mission; the UAV (in our case, a multirotor) is responsible for fast data acquisition to create an accurate orthophoto and terrain map of the zone of interest. Aerial imagery is georeferenced directly, using an onboard sensor system, and no ground markers are required. The UAV can also perform rough radiation measurement, if necessary. Since the map contains 3D information about the environment, algorithms to compute the spatial gradient, which represents the rideability, can be designed. Based on the primary aerial map, the human operator defines the area of interest to be examined by the applied UGV carrying highly sensitive gamma-radiation probe/probes. As the actual survey typically embodies the most time-consuming problem within the mission, major emphasis is put on optimizing the UGV trajectory planning; however, the dual-probe (differential) approach to facilitate directional sensitivity also finds use in the given context. The UGV path planning from the pre-mission position to the center of the area of interest is carried out in the automated mode, similarly to the previously mentioned steps.

Although the human operator remains indispensable, most of the tasks are performed autonomously, thus substantially reducing the load on the operator to enable them to focus on other actions during the search mission. Although gamma radiation is used as the demonstrator, most of the proposed algorithms and tasks are applicable on a markedly wider basis, including, for example, chemical, biological, radiological, and nuclear missions and environmental measurement tasks.

Author's Contribution

The author was responsible primarily for the tasks related to the aerial system, namely, the mission planning, aerial data acquisition, and relevant processing. Moreover, he was involved in designing the method and interpreting the results; thus, he wrote the sections UAV and Aerial Mapping and significantly contributed to the Introduction, Process Description, Discussion and Conclusion chapters. The author is also credited with finalizing the manuscript.

Author contribution: 30 %

Acknowledgement

This work was supported by the European Regional Development Fund under the project Robotics 4 Industry 4.0 (reg. no. CZ.02.1.01/0.0/0.0/15_003/0000470).

Copyright and Version Notice

C.1. Introduction

At present, new security challenges appear within multiple related fields and disciplines. In this connection, the advancement in modern warfare suggests that chemical, biological, radiological, and nuclear (CBRN) defense will assume increasing importance. The U. S. Department of Health and Human Services defines several types of terrorist attacks involving sources of ionizing radiation [1]; the perpetrators of such acts may rely on dirty bombs, devices having the potential to disperse radioactive material in urban zones. As radiological sources are commonly present in medical or scientific facilities, they appear rather vulnerable in terms of becoming a target or an instrument of criminal practices [2]. In any case of such misuse, it would be vital to localize and dispose of the dangerous sources without unnecessary delay.

Current scientific literature outlines various methods to perform the actual retrieval and elimination operations; for instance, one of the conventional techniques relies on airborne spectrometry, where the detectors are carried by a helicopter through the region of interest (ROI) along a regular trajectory. An example of this approach is found in paper [3]. The advantage of such a procedure consists in the possibility of quickly exploring a relatively large region, while the main drawback is the low accuracy of estimating the hotspot locations. However, a detector can also be attached to an unmanned aerial vehicle (UAV), as presented in research reports [4, 5]. The benefits and disadvantages are similar to those characterizing the use of a helicopter; in this connection, UAVs nevertheless exhibit smaller payloads and shorter flying ranges, although they also feature lower initial costs.

If a high localization accuracy is required, ground-based assets have to be employed. The actual localization should not be performed by humans due to health risks, and as an unmanned ground vehicle (UGV) is less prone to radiation damage, it finds application in such reconnaissance tasks. Using UGVs in the discussed domain is demonstrated in articles [6, 7, 8, 9, 10]. A custom solution offering a high accuracy of the localization of gamma radiation hotspots is introduced within the present paper.

The proposed solution consists of an aerial and a ground platform, both working in the semi-autonomous mode. A UAV is utilized to acquire a three-dimensional map of the ROI via photogrammetric techniques. The map assists a UGV to plan a trajectory along which the hotspots are searched. In addition, the UAV may carry a detector to provide general information related to the positions of the radiation hotspots. A central advantage of our approach lies in the fact that no prior environmental map is needed, and the goal rests in identifying a solution that overcomes the state-of-the-art methods in certain particular aspects.

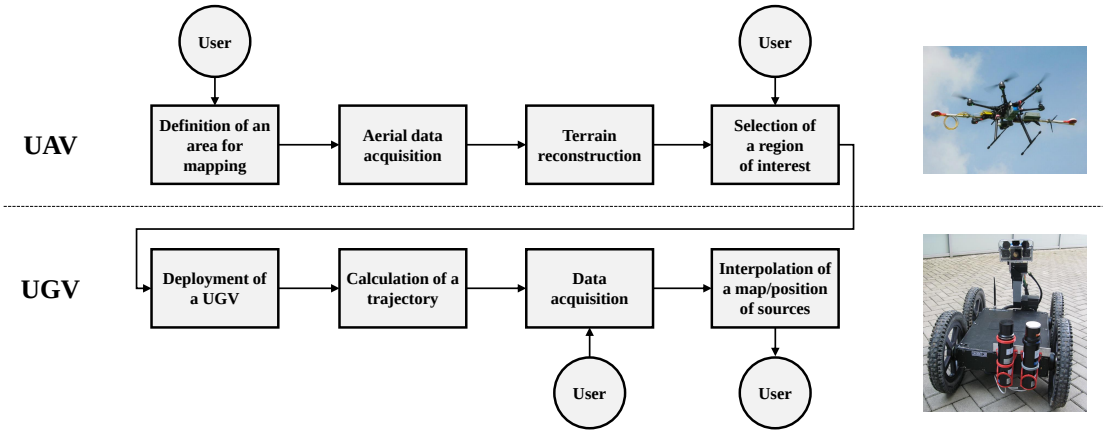

Figure C.1.: The sequence of the operations forming the entire process.

The article is organized as follows: Section 'Methods' discusses the methods and equipment employed, together with several localization algorithms; chapter 'Results' offers an overview of the results achieved, including the performance, time efficiency, and accuracy typical of the individual maps and methods; and section 'Discussion' compares the results with those outlined in the referenced literature, introducing the relevant advantages and disadvantages.

C.2. Methods

The following chapter presents the working scheme of the proposed system; both the UAV and the UGV are described in detail. The final part of this section introduces the algorithms used.

C.2.1. Process Description

The sequence of steps to ensure information related to the gamma radiation hotspots is illustrated in Figure C.1. The entire process is controlled by a human operator (user).

At the initial stage, the operator has to plan a flight trajectory for the UAV to cover the potentially affected area; then, the UAV acquires images along the defined trajectory, and these are used to reconstruct the 3D model of the area. The model assists the operator in selecting the proper region of interest rideable for the UGV, considering the presence of possible radiation hotspots. The ROI is a polygon defined by a sequence of vertices.

The UGV is deployed near the border of the mapped area. First, the trajectory from the deployment position to the edge of the ROI is calculated to avoid the obstacles and slopes found by the UAV; subsequently, the operator chooses the

Figure C.2.: The DJI S800 UAV equipped with the multi-sensor system for direct georeferencing.

UGV working mode. In general terms, two modes are available: mapping and localization. While the former procedure yields a map of the radiation distribution in the area, the latter one enables us to localize the radiation sources as quickly as possible; the corresponding data are then acquired in a suitable manner. Finally, the measurement is interpolated in order to provide either a map or a set of the sources' coordinates, and the results are communicated to the operator.

C.2.2. UAV

In aerial mapping, the benefit of unmanned aerial vehicles consists in their fast and safe operation at a very reasonable price, especially when compared to manned aircraft. For this reason, UAVs are convenient primarily for the mapping of local areas as their operational time is rather limited; conversely, however, the vehicles can produce a refreshed map on a daily basis, thus significantly reducing the product cycle known from traditional mapping. UAVs have already proven useful in fields and disciplines such as agriculture, civil engineering, archaelogy, or environmental and radiation mapping. Currently, projects are being executed which focus on direct radiation mapping via onboard sensors [4, 11] and combine radiation mapping with UAV photogrammetry to facilitate 3D surface reconstruction [12]; this paper nevertheless aims to explore the potential for cooperation between UAVs and UGVs.

To perform the aerial mapping, we used a six-rotor DJI S800 Spreading Wings UAV fitted with a DJI Wookong M flight controller supporting an autonomous flight according to a given trajectory. As regards the experimental aicraft, the most important utility parameter was the payload limit of about 3 kg, which allowed us to carry the required equipment (see Table C.1 for more parameters). The UAV comprises a custom-built multi-sensor system facilitating the direct georeferencing (DG)

Table C.1.: The parameters of the UAV DJI S800 and the UGV Orpheus-X3 [13, 14].

Parameter	UAV	UGV
Dimensions	1.0 × 1.2 × 0.5 m	1.0 × 0.6 × 0.4 m
Weight	8 kg	51 kg
Operational time	10 mins	120 mins
Drive type	multi-rotor	wheel-differential
Operating speed	5 $m \cdot s^{-1}$	0.6 $m \cdot s^{-1}$
Maximum speed	26 $m \cdot s^{-1}$	4.2 $m \cdot s^{-1}$

Table C.2.: The parameters of the custom-built multi-sensor system for UAVs to enable the direct georeferencing of aerial imagery.

Parameter	Value
Position accuracy (BD982)[a]	horizontal: 8 mm, vertical: 15 mm
Attitude accuracy (Ellipse-E)[b]	roll/pitch: 0.1°, heading: 0.4°
Camera resolution	6,000 × 4,000 px
Camera lens	15 mm
Operational time	120 mins
Distance from base	1,000 m
Dimensions	1.5 × 0.2 × 0.2 m
Weight	2.6 kg

[a] 1σ error in the RTK mode, according to the manufacturer's specification.

[b] The RTK mode in the airborne applications, according to the manufacturer's specification.

of aerial imagery (Figure C.2), an operation that enables us to create a georeferenced orthophoto, point cloud, or digital elevation model (DEM) without requiring ground control points (GCP).

The multi-sensor system comprises a digital camera Sony Alpha A7, a global navigation satellite system (GNSS) receiver Trimble BD982, an inertial navigation system (INS) SBG Ellipse-E, and a single board computer Banana Pi R1 (Figure C.3). The GNSS receiver measures the position with centimeter-level accuracy when real time kinematic (RTK) correction data are transmitted, and as it is equipped with two antennas for vector measurement, the device also measures the orientation around two axes. The position and orientation data are used as an auxiliary input for the INS, which provides data output at a frequency of up to 200 Hz. Since all the sensors are precisely synchronized, once an image has been captured, the position and orientation data are saved into the onboard SSD data storage (more parameters are contained in Table C.2). The multi-sensor system mounted on the

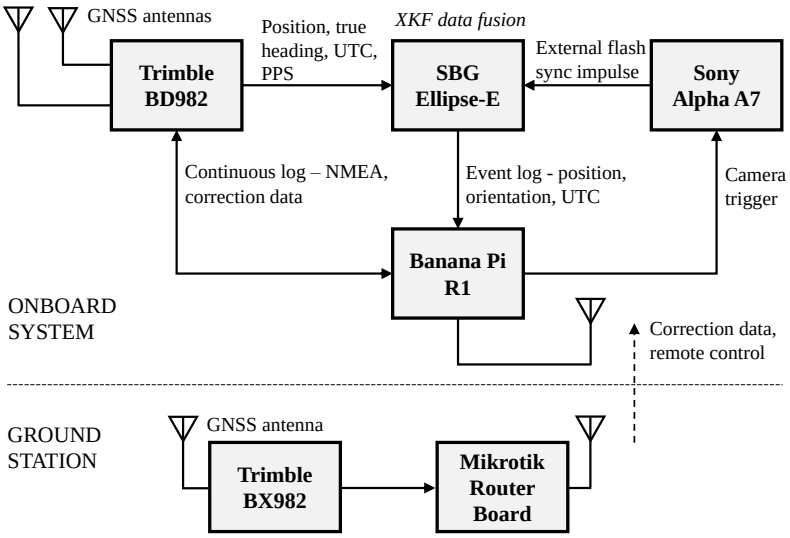

Figure C.3.: The multi-sensor system for the UAV and ground station.

UAV is shown in Figure C.2 and described in more detail within [15].

Both the position and the image data from the onboard sensors are processed using photogrammetric software Agisoft Photoscan Professional. This SW integrates computer vision-based algorithms performing structure from motion (SfM) to allow the surface reconstruction, and it offers two georeferencing options: indirect (IG), using GCPs, and direct, utilizing onboard data. We may benefit from DG as the only approach to produce accurately georeferenced maps of areas inaccessible for humans (which is the case with radiation mapping). To achieve centimeter-level object accuracy, a method for calibrating the designed system was developed [16]. The calibration process involves the field estimation of the lever arms and the synchronization delay between the camera shutter and the INS unit; these steps significantly increase the accuracy of the position measurement of the camera perspective center.

In our experiment, the UAV is used only for the aerial photogrammetry, enabling us to create a highly detailed, up-to-date orthophoto and DEM. These products are applicable for both the localization of the ROI and the UGV navigation. If the UAV were equipped also with radiation detectors, it would locate the ROI more reliably.

C.2.3. UGV

The UGV is an Orpheus-X3 civil reconnaissance robot, a four-wheeled mid-size vehicle equipped with a sensor head carrying cameras. The robot has the ability to carry all the equipment needed for this type of mission, namely, devices to facilitate self-localization, gamma detectors with counting electronics, and a control module with the designed algorithms. The whole system, namely, the robot carrying the equipment, is represented in Figure C.4. The basic parameters of the robot are shown

Figure C.4.: The Orpheus-X3 carrying the equipment.

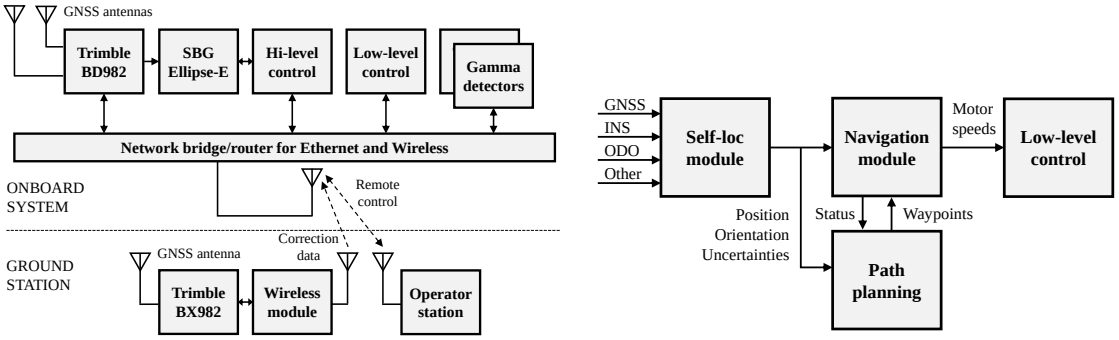

Figure C.5.: The interconnection of the components (a), and the control diagram of the simplified robot drive (b).

in Table C.1. The interconnection between the main components of Orpheus-X3 is shown in Figure C.5a. The robot is capable of autonomous driving. A simplified block scheme of all major modules for the robot motion control is drawn in Figure C.5b; all the blocks of this scheme will be described in detail within the following paragraphs.

In applications that require the autonomous motion control of a mobile robot, the self-localization task must be solved in real time. The self-localization module of the Orpheus-X3 mobile robot is designed exploiting the modular concept with real-time data output; such an approach allows the quick and easy integration of localization data from different sources. The data fusion is based on uncertainties of the input data. In standard missions, the self-localization module includes solutions from an RTK GNSS (Trimble BD982), a MEMS-based INS (SBG Ellipse-E), and wheel odometry (data from the motor drivers). One of the central advantages of an RTK GNSS is the high accuracy without any drift caused by the length of the measuring period or traveled distance. The applied RTK GNSS receiver can be connected

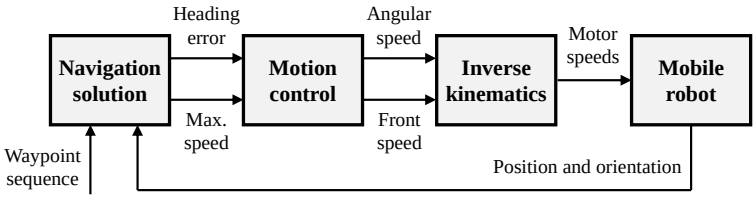

Figure C.6.: The block scheme of the module.

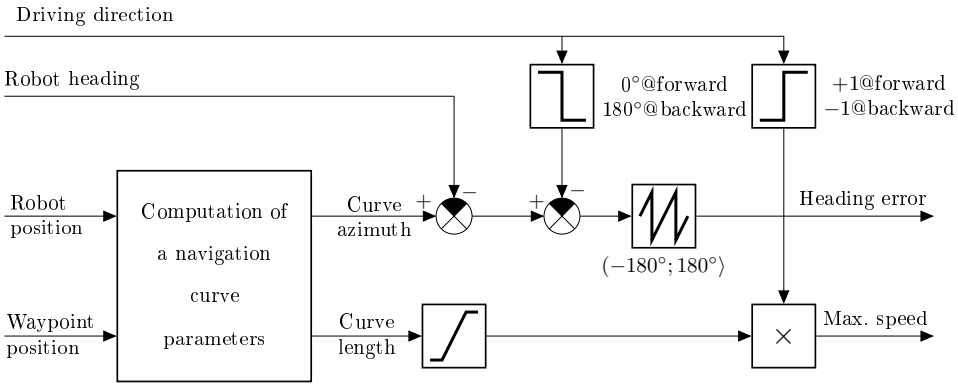

Figure C.7.: The scheme of the navigation solution solver.

to two antennas, allowing drift-less heading measurement from the position vector between the two antennas. The localization data from special methods (including, for example, SLAM) can be also integrated if the uncertainties of the values are known. In environments with a good open sky view, an RTK GNSS is usable as the only solution. To increase the robustness of the entire self-localization module, we may also employ some relative methods to bypass the time when the RTK solution is unavailable due to reasons such as reinitialization. The position estimation accuracy reaches the level of centimeters, and the orientation (azimuth) is better than 0.5 deg if the RTK solutions are fixed. As regards accuracy, more results are obtainable from the PhD thesis [17].

The Orpheus-X3 also integrates a navigation module (Figure C.6) to control the robot motion, utilizing an externally computed requested trajectory. The trajectory is defined as a sequence of waypoints in the WGS-84 coordinate system. The internal computational scheme of the navigation solution (block No. 1 in Figure C.6) is presented in Figure C.7. The robot motion parameters, such as the turning radius and maximum speeds, can be dynamically adjusted during a mission via an integrated application interface from the related hi-level control module. The sequence of waypoints is also dynamically modifiable from the path planner module during a mission. More information about the navigation algorithms is outlined within paper [14] and PhD thesis [17].

The gamma radiation detection system comprises scintillation detectors and mea-

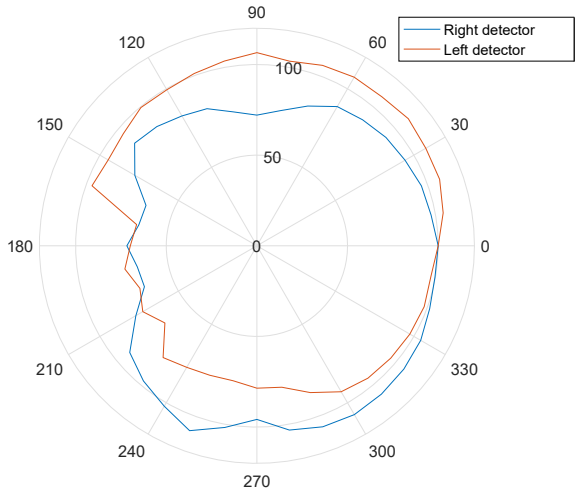

Figure C.8.: The directional characteristics of the detection system.

suring electronics. A pair of 2-inch sodium iodide doped with thallium (NaI(Tl)) detectors are used as scintillators. The detectors are integrated with photomultiplier tubes having a standard 14-pin base. Multichannel analyzers NuNA MCB3 manufactured by NUVIA are used as the electronics; the analyzers ensure a high voltage source, a preamplifier, and ADC sampling and processing. The detector tubes are equipped with lead shielding, and one half of each spherical detector is covered with a 2 mm layer of lead facing the other detector. The reason for such a configuration is to intensify the directional sensitivity of the resulting detection system. The directional characteristics of the detectors placed on the robot are introduced in Figure C.8; however, these remain valid only if the distance between the detector centers equals 106 mm.

C.2.4. Optimal Path to the Area of Interest

The terrain negotiability of a UGV is markedly affected by its actual slope pattern. In this context, it appears very helpful if the entire system can assist the operator in finding the shortest possible path to the target area from places accessible using the regular transport infrastructure. The main obstacles for a UGV are areas where the slope of the terrain exceeds the limit value of the given UGV. The slope map is computed from a DEM, which constitutes a product of UAV photogrammetry. The paths from the starting positions to the requested target are obtained using an A* algorithm [18] in a binarized and down-sampled slope map; the down-sampling of the map is needed due to a significant reduction of the computational demands. The size of a cell in a down-sampled obstacle map should be slightly higher than the width of the applied UGV. Lowering this size below this limit has no effect because of the impossibility to pass through a corridor with the width of one pixel, whereas

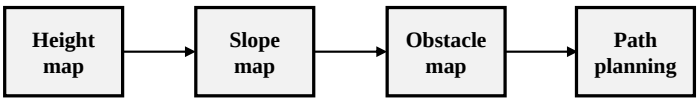

Figure C.9.: The procedure for planning the path to the ROI.

increasing it worsens the resolution and may cause the loss of the trajectory. The down-sampling algorithm must preserve the thin lines that represent high slopes in the terrain.

Another approach to reduce the computational demands consists in using lossless compression algorithms (e. g., quadtree [29]) on a primary hi-resolution binary map. These algorithms can also be employed in lossy compression applications, where the cell size of a leaf (the last level of the tree) is larger than in the original map. In the given case, however, the workflow must be changed, with the primary binary map packed using a quadtree algorithm at the start of the data processing. Further, the path planning algorithm must be modified to natively handle the compressed data without fully expanding to an equidistant grid. Compared to the basic down-sampling, this procedure significantly reduces the number of points needed to travel through a path planning algorithm while keeping the same resolution of the map. Such an optimization then markedly affects the computational demands. Due to the negligible duration (only several seconds) of the trajectory planning operation as opposed to the DEM calculation time (which amounts to several hours if a computing grid is not utilized), the benefits of more advanced obstacle map compression techniques are unimportant in the described application.

Yet another option for diminishing the computational demands of the path planning process is to employ an optimized method to find the shortest trajectory instead of the fundamental variant of the A* algorithm. A good candidate can be seen in the *J*ump Point Search [30] algorithm, which is capable of reducing the running time by an order of magnitude. Due to both the planned ranges of the areas where the trajectories are searched and the applied map resolutions, the trajectory planning time is not critical in the context of the DEM generation time. When large areas (exceeding $\sim$1 km^2) are considered, it is suitable to ensure the time optimization of the path planning process by means of a better performing algorithm or to compress the map, thus reducing the number of points into which the objects in the map are divided.

The starting position securing the shortest path to the target spot is preferred. The whole sequence of tasks is shown in Figure C.9.

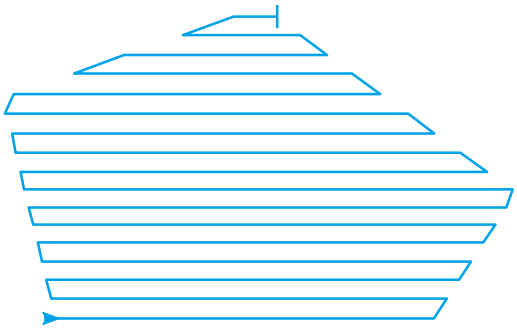

Figure C.10.: A schematic example of the mapping trajectory.

C.2.5. Methods for Path Planning and Field Mapping

An algorithm specified by the adjective *m*apping constitutes an elementary algorithm to measure environmental quantities such as the dose rate in the region of interest. The idea is to pass the entire area along the parallel equidistant lines and to measure the dose or count rate periodically. If the line spacing and the robot's speed are small enough, even subtle changes in the radiation field can be noticed; thus, even weak sources can be found. This is apparently a significant advantage of the mapping operation. The drawback then rests in that the time requirements increase rapidly with the size of the measured area. A schematic example of a mapping trajectory in a pentagonal ROI is shown in Figure C.10.

The waypoints for the navigation module are generated on parallel lines inside the polygon which defines the boundaries of the ROI. It is convenient to make the lines parallel to one of the polygon's longer edges in a manner where all the lines intersect the polygon at not more than two points. When such conditions have been satisfied, the resulting trajectory becomes more efficient for the robot because the number of the turns required is minimized.

The parallel lines are separated by pre-defined spacing, a critical parameter related to the algorithm's capability of finding low-activity point radiation sources in the area. The lower the spacing, the weaker the sources localizable and the longer the timespan needed to acquire the data. Given that we know the intensity of the weakest source to be found, the optimal value of the parameter is computable. In the worst case, the source is located exactly halfway between two trajectory lines. The dose rate generated by the source should be at least three times higher than the background one, $\dot{D}_B$. Since the background may rise above the normal level in the stricken area, it is necessary to measure its value once the robot has been deployed. The spacing parameter is then given by the following equation:

$$d = 2\sqrt{\frac{\dot{D}_1}{3 \cdot \dot{D}_B}} \tag{C.1}$$

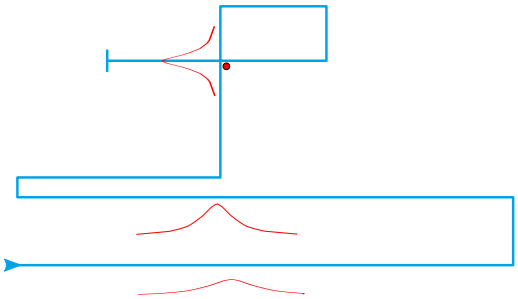

Figure C.11.: A schematic example of the strong source search trajectory.

where $\dot{D}_1$ stands for the dose rate generated by the weakest source to be searched for at the distance of 1 meter. If a particular radionuclide is to be found, this value may be computed from its activity.

The mapping yields a set of scattered data points. Each of such points comprises the coordinates and spectra acquired by both detectors during a measurement period. The data points are not very suitable for visualization and further map processing, namely, the conversion to a 3D point cloud. Thus, the calculation of the radiation intensity (either the total count or the dose rate) at points in a regular grid is needed. This step can be carried out through a Delaunay triangulation [19]. After the interpolation has been performed, the data become visualizable and interpretable by the operator. If any point source is present in the mapped ROI, its position may be computed automatically, as will be described later.

In any situation where finding only one strong source is required and timing is important, the mapping algorithm may be extended as outlined below. The extension exploits the dynamic change of the trajectory in accordance with the measured data.

First, the robot follows a basic mapping trajectory. Once the end of the line has been reached, the data are examined to yield a significant peak in the radiation intensity. If peaks are found in two neighboring lines and their positions correlate, the trajectory is altered, and the robot continues in a direction perpendicular to the mapping lines passing through the center of the peak projections to the current line. The new direction is maintained until another significant peak in the measured radiation intensity appears. Afterwards, the final part of the trajectory denoted as a *l*oop is planned, and its purpose consists in acquiring a sufficient amount of data points in the vicinity of the anticipated source position in order to determine that position more accurately. A schematic example of the measurement trajectory is shown in Figure C.11

A disadvantage of the above-described algorithm is the dependence of the result on the initial mutual position of the robot and the source. The algorithm presented below exploits the directional characteristics of the detectors, meaning that its per-

formance should not depend excessively on the initial conditions and, under some circumstances, multiple sources can be found.

As the difference between the detectors' directional characteristics is rather indistinctive, we have to find a more effective way to acquire data in order to gain relevant information about the direction in which a source is present. A measurement cycle along a closed loop seems promising because all possible angles between the detectors and the sources are assumed. For a certain azimuth of the robot, an extremal ratio of the detectors' responses should be measured if a source is present within the detectable range. This is a principle similar to that found in the peaks measured by the authors of paper [20]. Obviously, the robot can simply rotate in place, but it may be convenient to choose a circular trajectory instead because the range has increased and the extremum is anticipated also in the count rate values due to the inverse square law. Since the sum of the count rates is burdened by a statistical error lower than that of the rates' ratio, this should lead to better estimation of the direction.

Assuming the robot maintains a constant speed once it has reached the circle, a cyclic dataset with equidistant data points will result from the measurement. If there are multiple sources adequately separated by an angle, more than one dominant peak can be present, and it does not suffice to only find the maximum. Real data are very noisy, requiring a robust peak detector. A simple peak is defined as a point having a value greater than its two neighboring points; the peaks are then compared to the reference levels evaluated for each peak in the following manner:

1. The nearest point with a greater or equal value is found to the left of the examined peak.

2. The point exhibiting the lowest value is found in the interval bounded by the peak and the point from step 1.

3. Steps 1 and 2 are repeated to the right of the peak.

4. The higher of the two interval minima specifies the reference level.

If the peak amplitude is greater than or equal to the reference level multiplied by the desired relative prominence, the peak is accepted. Once the peaks have been identified, it is convenient to fit their neighborhood using an appropriate function. This procedure is performed for several reasons, including that, due to the dead time, the point in the correct direction may not exhibit the maximum count rate. In the given context, we can also assume that the actual maximum is somewhere between the samples. The interpolation then provides the subsample precision. A quadratic polynomial ensures sufficient results, and its parameters are computable via the least squares method.

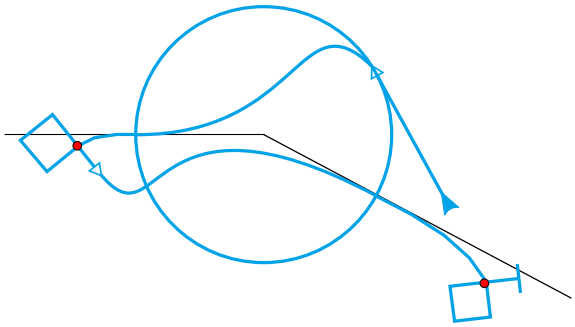

Figure C.12.: A schematic example of the circular algorithm trajectory.

One detector is pointed outwards and the other inwards. By comparing the count rates in the peak, we can then determine whether the source is located outside or inside the circle.

Due to multiple effects, such as an overlap of the radiation fields, the initial direction estimation may not be accurate; however, taking advantage of the directional sensitivity, the error can be compensated. The detection system is arranged in such a manner that the difference of the count rates measured by both detectors converges to zero if the source lies in the axis of the robot. Thus, the effort is to minimize the difference by changing the azimuth of the robot while the vehicle is approaching the source. The value by which the azimuth is altered should depend on both the present and the past measured differences. Given the current readings from the detectors on the right-hand and left-hand sides, $R(t)$ and $L(t)$, and considering the previous readings, $R(t-1)$ and $L(t-1)$, the desired azimuth change may be expressed as

$$\begin{aligned}\Delta\phi = K_1\frac{R(t)-L(t)}{R(t)+L(t)} + K_2\frac{R(t-1)-L(t-1)}{R(t-1)+L(t-1)} + \\ + K_3\frac{R(t)}{L(t)} - \frac{R(t-1)}{L(t-1)},\end{aligned} \tag{C.2}$$

where K_1, K_2, and K_3 are conveniently chosen constants. Note that whenever the robot heads left from the source, the count rate measured by the right-hand detector increases while the other one decreases; as a consequence, the change of the azimuth is positive – in other words, the robot starts to head more to the right.

When the total count rate drops during three or more sampling periods in a row, it can be assumed that the robot has already passed around the source. In that case, the final part of the trajectory, or the loop, as presented previously, can be planned. Once the source has been localized, the robot may proceed in another direction where a source is anticipated. The schematic example of such a measurement trajectory is shown in Figure C.12; the actual location of the source is marked by the red point, and the black lines represent the initial direction estimation.

An obvious disadvantage of the presented algorithm rests in the limited explo-

Table C.3.: The object accuracy (RMS error) achieved with the direct and indirect georeferencing methods in UAV photogrammetry.

Method	GCP/TP	X [mm]	Y [mm]	Z [mm]
DG	0/30	19	27	25
IG	6/24	9	9	20

ration range provided by one circle. However, it is possible to cover a larger area using a set of complementary circles, applying the algorithm to each one of them.

Each of the three above-presented strategies allows us to find point radiation sources. As proposed earlier, the process of determining the sources' coordinates can be automated: First, a data point denoted as *m*aximum, which is as close as possible to the source, has to be chosen; in the latter two algorithms, the data point should be one acquired along the final loop and having the largest total count rate. Regarding the mapping, the interpolated map has to be searched for two-dimensional prominent peaks, which should correspond to the centers of the individual hotspots. Afterwards, the data points measured within the defined radius around each maximum are selected for further processing; the radius should be proportional to the total count rate in a given maximum. The points are then fitted with a suitable function. If the selected radius corresponds well to the source intensity, the paraboloid of revolution secures sufficient interpolation, and its parameters are simply computable via the least squares method. Better interpolation can be achieved using a two-dimensional Gaussian function.

C.3. Results

This section summarizes the achieved results; the outcomes of the aerial mapping, path planning, and localization of radiation sources are presented graphically.

C.3.1. Aerial Mapping

A region of approximately 30,000 m^2 accommodating a potential radiation source was mapped by a UAV carrying a multi-sensor system for direct georeferencing. During an 8-minute automatic flight, 137 photographs were taken. The flight trajectory and image capture period had been set to meet the requirement of 80 % side and 80 % forward overlap. As the applied full-frame camera was fitted with a 15 mm lens and the flight altitude corresponded to 50 meters above the ground level (AGL), the ground resolution of the images is about 2 cm/px.

Once the onboard position data have been refined using custom calibration, we

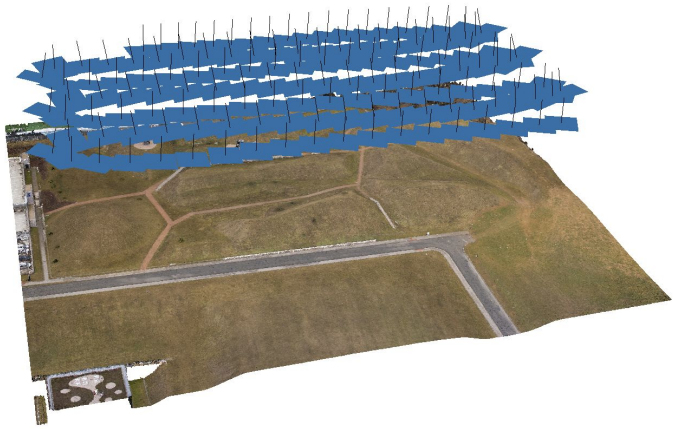

Figure C.13.: The textured point cloud containing 29 million points; the blue rectangles represent the image planes, whose positions were measured using the onboard system.

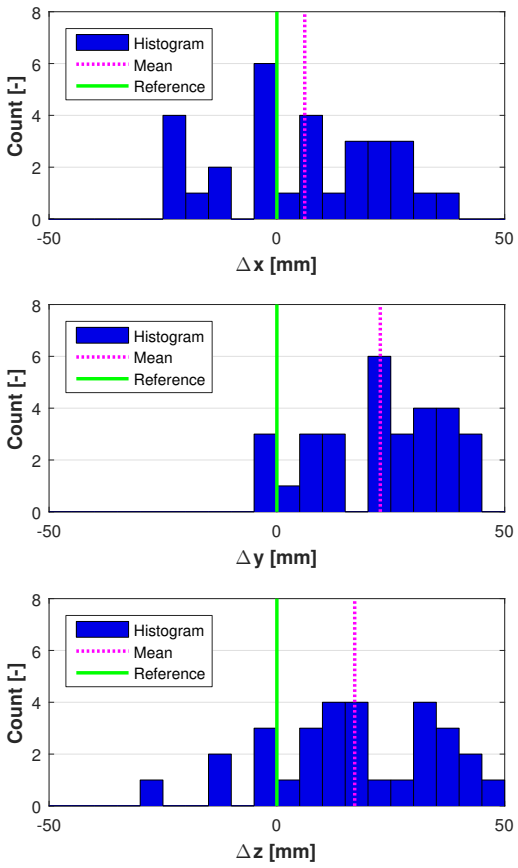

Figure C.14.: The position error distribution in the terrain model generated using the UAV, without the GCPs (determined on 30 TPs).

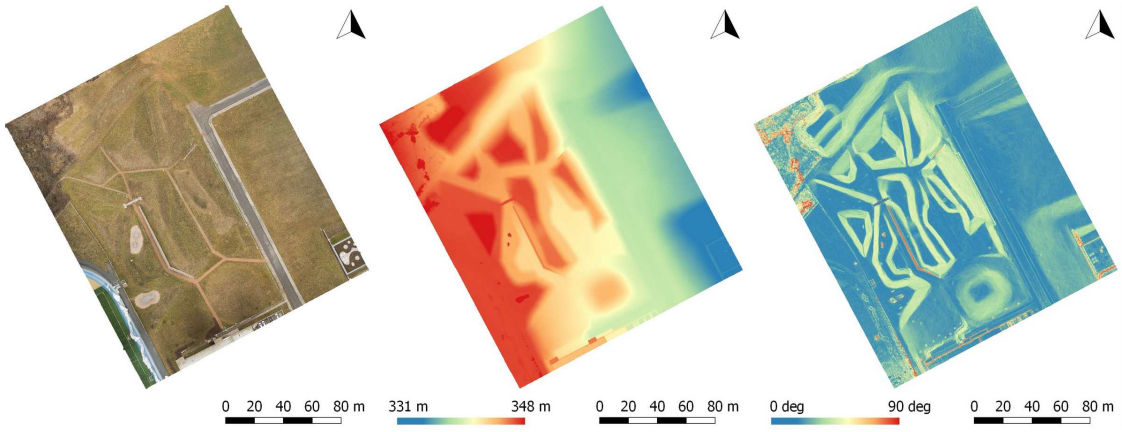

(a) (b) (c)

Figure C.15.: The georeferenced ortophoto (a), digital elevation model (b), and gradient map (c), all generated using UAV photogrammetry without the GCPs.

employed them for terrain reconstruction together with the image data. Photoscan was used to generate a dense point cloud with a density of about 800 points/m^2 (Figure C.13); although the point cloud was georeferenced directly, without any GCP, thirty markers were distributed across the area due to accuracy assessment. The positions of these markers were measured with a survey-grade GNSS receiver just before and after the flight. Table C.3 presents the RMS error of the object position determined in all the 30 markers, or test points (TP). The RMS error did not exceed 3 cm for each axis, and the spatial error equalled 4.1 cm RMS. The histograms in Figure C.14 present the error distribution within the measurement, assessed using the TPs.

The same set of image data was exploited in testing the performance of indirect georeferencing, which is a techique widely used in UAV photogrammetry. Six markers were used as the georeferencing GCPs, and the remaining 24 ones assumed the role of TPs. As presented in Table C.3, the RMS error did not exceed 1 cm in the X and Y axes and 2 cm in the Z axis. The spatial RMS error of 2.4 cm was about twice smaller compared to that found in DG. Despite this excellent result, IG requires GCPs to enable georeferencing, and the technique thus cannot be utilized in situations where the area of interest is inaccessible to humans, as is the case with radiation contamination.

The georeferenced point cloud is then employed for the creation of other products, namely, a true orthophoto and a digital elevation model (Figure C.15a and C.15b). These two map layers can significantly simplify the process of localizing a source of radiation (if a visible damage is observable) and, above all, help us to navigate

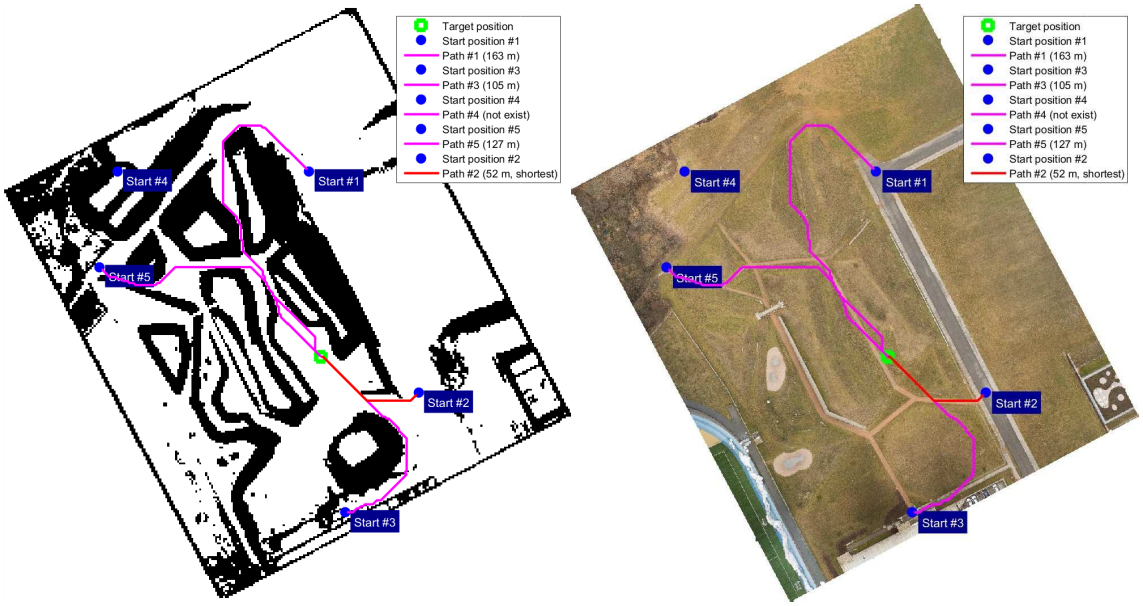

(a) (b)

Figure C.16.: The obstacle (a) and orthophoto (b) maps with possible trajectories to the target.

the UGV across the area. Because the applied UGV is not capable of operating on steep slopes, a gradient map layer (Figure C.15c) constitutes an instrument towards finding an appropriate trajectory to ROI.

C.3.2. Path to the Area of Interest

A binary obstacle map is obtained from the successfully formed DEM to retrieve the shortest path to the ROI. The slope threshold limit to mark a relevant cell in the map as an obstacle for the UGV is 15 degrees. The cell size in the down-sampled obstacle map was set to 150 % of the robot width, yielding a map with 300 x 285 pixels (0.9 m/pixel). Such a resolution allows us to find one path within seconds on a common PC unit. The possible mission starting positions were manually selected in the orthophoto map. The identified trajectories to the target spot are shown in Figures C.16a and C.16b. The point at which the robot was unloaded from the car was chosen from among the starting positions offering the shortest paths (with the most advantageous one being 83 m long). The final path was planned using also the A* algorithm, and it ran between the unloading point and the first waypoint of the polygon where the mapping had been performed.

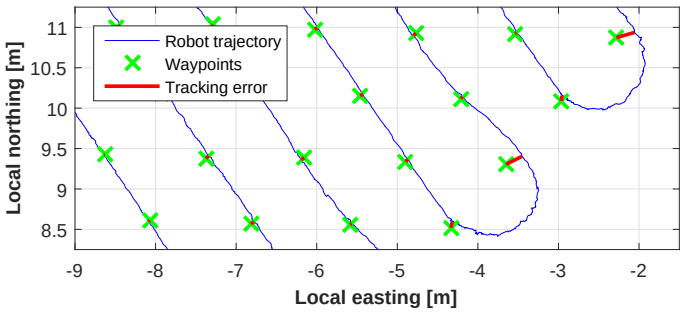

Figure C.17.: The errors in waypoint tracking on the trajectory.

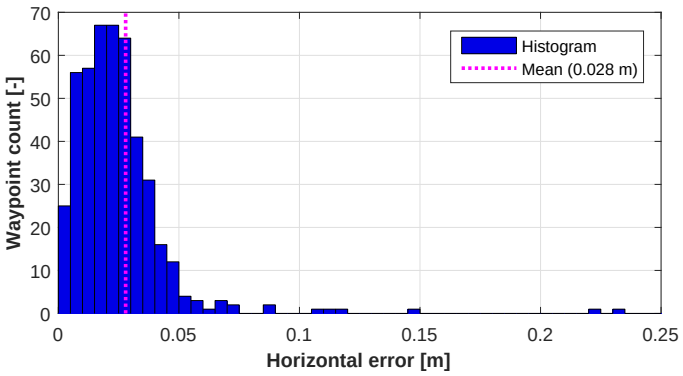

Figure C.18.: The errors in waypoint tracking on the trajectory.

C.3.3. Robot Navigation Accuracy

The robot navigation accuracy was determined as the waypoint tracking accuracy. The relevant value was estimated from the real trajectory of the mobile robot and the positions of the waypoints to be passed around. The error distance between the robot trajectory and a waypoint embodies the closest distance between a waypoint and the real robot trajectory, as demonstrated in Figure C.17. The histogram of the error distance related to the waypoint tracking along the entire trajectory applied within the standard mapping method is presented in Figure C.18. The error distances are evaluated on the horizontal plane (east-north). The average error equals 2.8 cm.

C.3.4. Radiation Sources Localization

The proposed methods to localize gamma radiation sources were first simulated and then tested with actual radionuclides. There are two main reasons to run the simulations: a) The behavior of the algorithms is influenced by several parameters to be set prior to any experiment, e. g., the peak prominence and azimuth change constants; and b) it is vital to set up the experiments in a manner that enables the algorithms to work as expected, meaning that when the experiments are prepared using simulation, the time needed on site can be reduced.

The radioactive decay of a source is a process describable with the Poisson distribution. The probability of the emission of x photons is expressed as [21]

$$p(x = X) = \mathcal{P}(x; \lambda) = \frac{e^{-\lambda}\lambda^x}{x!}, \tag{C.3}$$

where λ denotes the mean emission of photons and its value is proportional to the source's activity. On the short-term basis, this activity is approximately constant in the employed radionuclides. In the long-term run, it decays following the equation [21]

$$A = A_0 e^{-\frac{t}{T_{1/2}\ln(2)}}, \tag{C.4}$$

where $T_{1/2}$ is the half-time of the radionuclide, and A_0 represents its original activity (usually stated in the calibration protocol).

Since the λ values are typically in the order of thousands and the Poisson distribution is numerically stable within the order of tens at most, the sources were approximately modeled using the normal distribution. The radiation background was modeled with the uniform distribution. The detectors were assumed to exhibit 100% conversion efficiency, and only their directional characteristics were considered. The dependence of the registered counts on the distance from a source is given by the inverse square law. Given the parameters of the sources, it is possible to calculate the counts registered in a measurement period by the detectors at any point. The total count detected by the detector k can be obtained from the equation

$$C_k = c_B + \sum_{r=1}^{R} c_{k,r}, \tag{C.5}$$

where $c_B \leftarrow \mathcal{U}([c_{B,min}; c_{B,max}])$ is the contribution of the background, and $c_{k,r}$ denotes the count rate due to the source r. The relevant value is given as

$$c_{k,r} = \frac{K_k(\phi_{k,r})a_r}{||\boldsymbol{x}_k - \boldsymbol{x}_r||^2 + h_k^2}, \tag{C.6}$$

where $K_k(\phi)$ is the sensitivity in the direction ϕ; $\phi_{k,r}$ is the angular coordinate of the source r in the coordinate system of the detector k; $a_r \leftarrow \mathcal{P}(\lambda_r)$ stands for the number of emitted photons; $\boldsymbol{x}_k$ and $\boldsymbol{x}_r$ are the coordinates of the detector and the source, respectively; and h_k is the height of the detector k above the ground. The simulations were run for multiple values of each parameter within the relevant possible range, with the parameter values set according to a convenient optimality criterion.

The radionuclides used for the experimenting are summarized in Table C.4, together with their actual activities. All the experiments took place in the same polygon that had been defined using the map acquired by the UAV. The positions of the

Table C.4.: The parameters of the radionuclides.

Label	Radionuclide	Activity [MBq]
S_1	^{60}Co	8.0
S_2	^{60}Co	40.0
S_3	^{137}Cs	65.6
S_4	^{137}Cs	0.22
S_5	^{60}Co	0.35

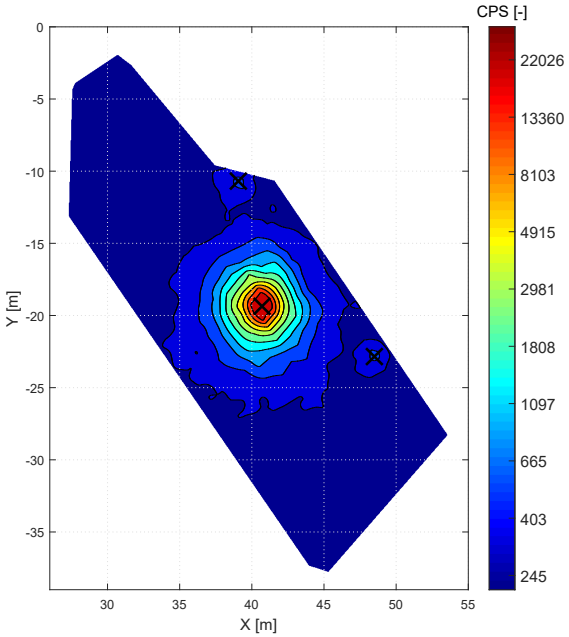

Figure C.19.: The result of the mapping algorithm.

sources were measured prior to the experiments in order to provide the reference data.

To test the mapping algorithm, sources S_1, S_4, and S_5 were placed in the ROI, with the spacing sufficient to facilitate their differentiation. The distance between the parallel lines was set to 1 meter. The data acquisition took 15 minutes and 3 seconds. The map resulting from the application of a Delaunay triangulation is shown in Figure C.19, where the black crosses mark the positions of the sources gained through the interpolation. The mean error of the computed positions corresponded to 0.06 meters.

The next algorithm, strong source search, was tested using source S_3. After the passage of the first two lines, we localized the direction in which the source had been estimated. The whole localization process lasted 2 minutes and 53 seconds, including the final loop around the source. The resulting trajectory consisting of data points is visualized in Figure C.20a. The achieved position error equals 0.04 meters (the

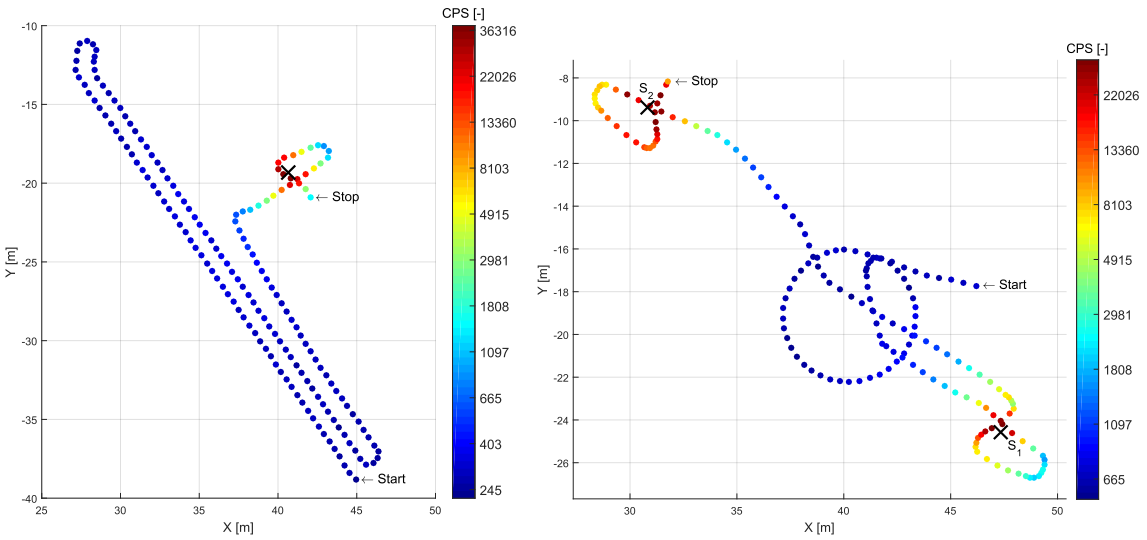

Figure C.20.: The result obtained with the strong source search algorithm.

same order as in the mapping). The experiment was repeated using source S_2, where the achieved error corresponded to 0.94 meters. Since the azimuth was not corrected while approaching the source, the result strongly depended on the accuracy of the initial estimation.

First of all, the circular algorithm was verified with one source (S_2); the source was located after 1 minute and 28 seconds, with the position error of 0.52 meters. After the actual completion, another experiment was set up, using two sources (S_1 and S_2) placed inside the area in such a manner that the circular trajectory lay between them. The resulting trajectory can be seen in Figure C.20b; apparently, the initial estimation of the direction in which source S_2 can be found is rather inaccurate. However, thanks to the proposed continuous correction of the azimuth, both the sources were eventually located, and the mean position error corresponded to 0.40 meters. The entire experiment took 2 minutes and 54 seconds.

C.4. Discussion

The UAV has proven to embody a very effective tool for fast and accurate aerial mapping. The presented custom-built multi-sensor system to facilitate direct georeferencing can be carried by any UAV that exhibits a sufficient payload capacity, thus enabling the actual photogrammetry to be performed without using GCPs. This is essential when mapping areas inaccessible or dangerous to humans, including, for example, those characteristic of natural disasters or radiation mapping. The elimination of GCPs also allows us to automate the entire mapping process, resulting in

no need of human interaction during the data acquisition processing.

The spatial ground accuracy of the multi-sensor system related to the above flight mission is 4.1 cm RMS, a sufficient accuracy rate for UGV navigation. This is a result surpassing those achieved within similar projects. Turner et al. [22] obtained the spatial accuracy of 11 cm using a multicopter carrying a DSLR camera synchronized with a positioning system based on a DGPS receiver. Fazeli et al. [23] then used a low-cost RTK GPS module to perform DG; however, they generated a spatial error of 29 cm RMS due to inaccurate time synchronization. A system similar to the one presented in this research report is characterized in a related paper by Eling et al. [24], who also used a multicopter UAV equipped with a dual antenna RTK GPS receiver, paying special attention to the calibration and time synchronization. The experiment yielded very accurate results, namely, 1.4 cm RMS for the XYZ axes, but these were achieved with a very low altitude and flight speed (20 m AGL, 2 m/s).

If we compare the accuracies of DG with those of IG, the former are typically slightly worse but remain comparable in selected cases. The object accuracy of a model georeferenced using IG mainly depends on the quality of the ground markers (GCPs), but it also reflects the flight altitude and ground resolution. The spatial error of the IG technique is normally within centimeters, as presented in, for example, the corresponding papers by Fazeli et al. [23], Barry et al. [25], and Panayotov [26]. But, as already mentioned, this approach is not suitable for our application due to the need of ground markers.

In the present article, the UAV was employed for optical mapping only; nevertheless, if a higher payload capacity were available, a detector of ionizing radiation could also be carried. In such a case, the orthophoto would be expanded to include the radiation intensity layer an outcome very beneficial for localizing the ROI. Yet this type of radiation maps cannot be as accurate and detailed as that produced by ground mapping (UGVs), because a typical flight altitude of a UAV is within tens of meters AGL. Ionizing radiation mapping via UAV is discussed in, for example, papers by Kaiser et al. [12], Torii et al. [27] or Martin et al. [28].

Since the UGV does not possess the ability to avoid obstacles autonomously, the digital elevation model is a valuable aid for the operator to define the region where the UGV can operate safely.

In this paper, three different strategies to survey the ROI are introduced and tested in real conditions. The basic surveying method consists in a mapping algorithm which provides reference of the time costs and localization accuracy for the other algorithms. Mapping the selected ROI with the area of 438 m^2 took approximately 15 minutes, with the line spacing corresponding to 1 meter. Since the trajectory was planned evenly inside the ROI, the dependence of the time intensity on the region's

area is rather linear. This fact embodies the major disadvantage of the mapping: the given operating time of the UGV equalled 120 minutes, and the maximum region that can be surveyed within a single action is limited to an area of roughly 3,500 m^2. Conversely, the advantages include the ability to negotiate radiation hotspots other than isotropic point sources – for example, area or directional sources (such as a radionuclide in an open lead container). Both the sensitivity and the accuracy of the method may be increased by setting smaller line spacing and lower forward speed of the robot; the survey, however, is then likely to be more time-consuming.

The methods based on a dynamic change of the trajectory in accordance with the information provided by the detectors reduce the time consumption while ensuring a similar accuracy. Together with the time saving feature, the strong source search algorithm provides two considerable benefits: First, if no source is found or present, the operator still gains the data allowing them to reconstruct the radiation map; second, the method is independent from the applied detection system and thus can be employed with other types of detectors, even the non-spectrometric ones. A disadvantage rests in the marked dependence of the result on the position of the source with respect to the initial position of the robot.

The circular algorithm, however, remains unaffected by this drawback and was discussed in the present paper as an alternative to the strong source search algorithm, which can beneficially exploit a direction-sensitive detection system. The relevant experiment proved that, under certain conditions, more than one source is localizable. The central importance of the algorithm nevertheless consists in its being a fundamental block for a more advanced localization algorithm to explore larger areas. Considering sources detectable at the distance of 4 meters (in the case of the detection system outlined in this paper, such sources consist in radionuclides ^{60}Co or ^{137}Cs, showing activity in the order of tens of megabecquerels), one circle covers the area of approximately 200 m^2. Within the experiments, such a circular trajectory was completed during 48 seconds. But assuming also the time consumption associated with the movement between the circles, a primary survey of the ROI chosen in this paper would last roughly 2 minutes – a major reduction of the time cost compared to the mapping.

The mapping algorithm provides localization accuracy in the order of centimeters. Johsi et al. [3] present a helicopter-borne radiation detection system and discuss the localization of a source having an intensity similar to that exhibited by the sources in our experiments. The obtained localization accuracy is within the order of meters, embodying a result expectable with respect the character of the method. More interesting, however, appears to be a comparison with the achievements of UGVs. Lin et al. [6] proposed a method for localizing a radiological source via a mobile robot; the technique exploits an artificial potential field and a particle filter

which, respectively, can negotiate the obstacles and simplify the localization. The method was verified by means of a simulation only with one source, with the achieved estimation error amounting to 0.02 meters. Ristic et al. [7] then presented an information-driven source search method. The concept was tested using Monte Carlo simulations in a square area (100 × 100 m) accommodating one source, with the results comprising an average search that took 90 seconds and yielded an accuracy in the order of tenths of meters. The relevant simulation cycles were verified using two datasets measured in real conditions. Although the method appears to be promising in terms of the time efficiency, it is still awaiting practical application. Other innovative surveying strategies were introduced by Cortez et al. [9], who nevertheless verified their research only in an area of 60 × 60 cm, insufficiently for the discussed scenarios. The localization accuracy of the method is limited to 4 cm. A rather different scheme is described by Duckworth et al. [10]; their source is localized inside a collapsed building, and the process strongly depends on the assistance from an operator. Eventually, it took a minute to localize the source inside a 6 × 6 m space.

The results within the present article are outlined using CPS values because the detectors were not properly calibrated prior to the experiments. Regarding the pursued goal, namely, the localization of radiation hotspots, the information value of the count rate is sufficient. The human operator may decide on the severity of the situation by comparing the values measured inside the ROI and the background value acquired after the deployment of the UGV. As the measured spectra are stored, they can be later approximately converted to dosimetric quantities if desirable – for example, as information for the operative team charged with the elimination of the given risk.

Although the radiation map is acquirable via the UGV alone, there are several reasons for choosing the proposed cooperation with the UAV. The main advantage consists in the possibility of using the DEM, which allows the UGV to navigate between terrain obstacles and can be beneficial for the operative team as well. Furthermore, if the radiation layer is measured during the aerial data acquisition, the area to be searched by the UGV can be reduced to save time and energy. In general, the cooperative approach combines the advantages of UAV and UGV-based solutions, minimizing the disadvantages related to the stand-alone operation of each of these systems.

C.5. Conclusion

This paper outlined the process of localizing ionization radiation sources via cooperation between a UAV and a UGV. All the presented methods were duly implemented,

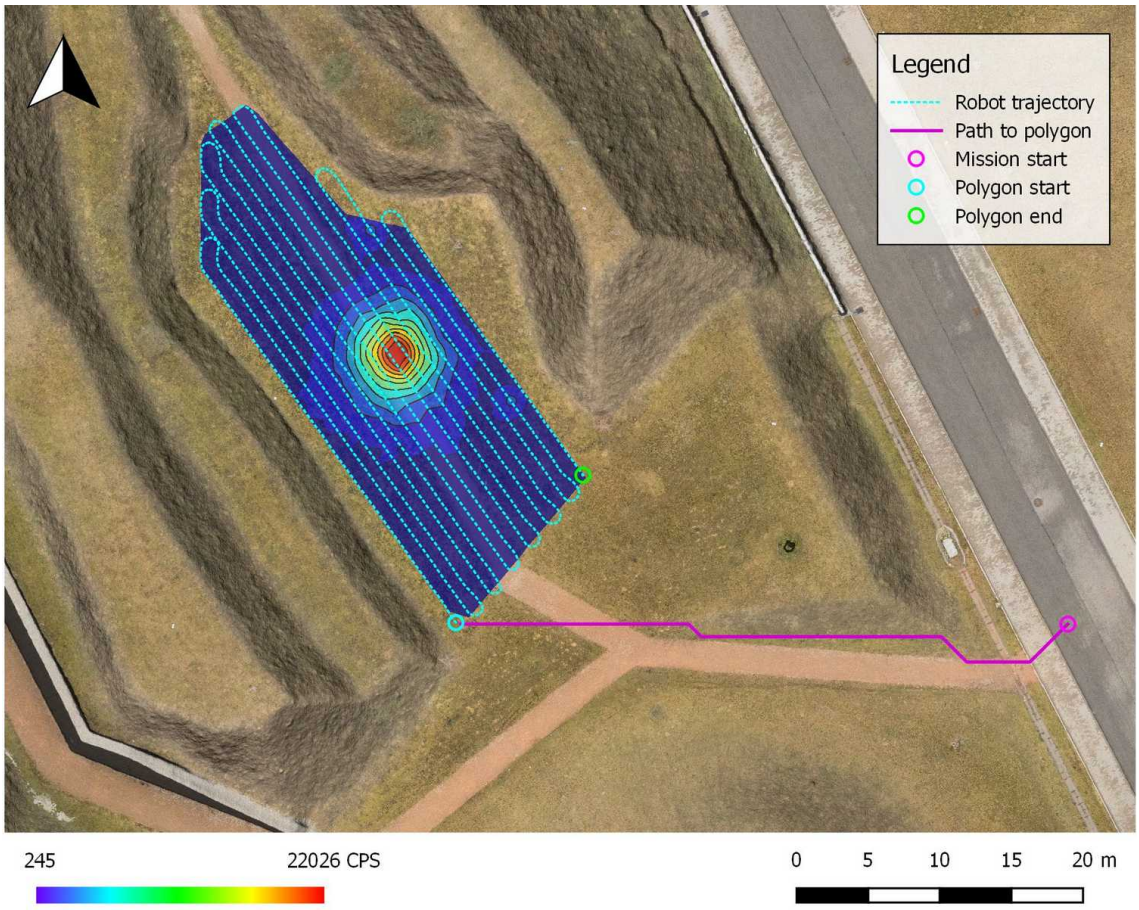

Figure C.21.: Georeferenced map containing orthophoto layer with hill shading created using UAV photogrammetry complemented by the gama radiation intensity layer created by UGV.

and special attention was paid to verifying the theoretical assumptions via a real mission as many similar projects rely on simulated data only. A UAV equipped with a custom-built multi-sensor system was employed to acquire the aerial data, and since this system had been designed for direct georeferencing, the technique does not require ground markers. The object accuracy obtained through photogrammetry corresponded to 4 cm RMS, and both an orthophoto and a DEM were used for the UGV trajectory planning.

An Orpheus-X3 UGV equipped with a purpose-designed gamma radiation detection system was used to test several strategies facilitating radiation source localization. Regarding the general mapping method, the localization accuracy of 6 cm was achieved in the strong and weak sources placed simultaneously inside the selected ROI. Subsequently, an information-driven method based on the data acquired by an omnidirectional detector was designed and tested, enabling us to localize a single source at a rate approximately five times faster than that achievable with the

mapping algorithm. Further, a pair of radiation detectors were utilized to assemble a detection system with considerable directional sensitivity. A modified algorithm exploiting such sensitivity, however, may ensure even better time efficiency; under certain conditions, the method allows us to localize a single source ten times faster compared to the basic method. When confronted with the common approaches in terms of the localization accuracy, the improved procedure performs worse by an order of magnitude; yet the resulting information suffices for neutralizing a source. Figure C.21 illustrates the composition of both the aerial and the ground mapping processes.

In the future, UAVs equipped with gamma detectors will likely be usable in rough radiation mapping, allowing the automatic detection of ROIs. This, along with implementing obstacle avoidance in UGVs, would lead to the more autonomous localization of radiation sources.

Bibliography

[1] Radiological Dispersal Device Playbook. *Public Health Emergancy*. Washington, DC: U. S. Department of Health and Human Services, 2015. [cit. 2017-3-12] URL: `https://www.phe.gov/preparedness/planning/playbooks/rdd/Pages/default.aspx`

[2] Ferguson C. D., Kazi T. and Perera J. *Commercial Radioactive Sources: Surveying the Security Risks*. Occasional paper No. 11. Monterey, California: Monterey Institute of International Studies, Center for Nonproliferation Studies, 2003. ISBN: 1-885350-06-6. URL: `https://www.nonproliferation.org/wp-content/uploads/2016/09/op11.pdf`

[3] Johsi T., Quiter B., Maltz J., et al. Measurement of the Energy-Dependent Angular Response of the ARES Detector System and Application to Aerial Imaging. *IEEE Transactions on Nuclear Science*, 64(7), 2015. DOI: 10.1109/TNS.2017.2693988. URL: `https://ieeexplore.ieee.org/document/7898808`

[4] Hartman J., Barzilov A. and Novikov I. Remote sensing of neutron and gamma radiation using aerial unmanned autonomous system. In *2015 IEEE Nuclear Science Symposium and Medical Imaging Conference (NSS/MIC)*, 2015. DOI: 10.1109/NSSMIC.2015.7581763. URL: `https://ieeexplore.ieee.org/document/7581763`

[5] Aleotti J., Micconi G., Caselli S., et al. Unmanned aerial vehicle equipped with spectroscopic CdZnTe detector for detection and identification of radiological and nuclear material. In *2015 IEEE Nuclear Science Symposium and Medical Imaging Conference (NSS/MIC)*, 2015. DOI: 10.1109/NSSMIC.2015.7582264. URL: `https://ieeexplore.ieee.org/document/7582264`

[6] Lin H. I., Tzeng H. J. Searching a radiological source by a mobile robot. In *2015 International Conference on Fuzzy Theory and Its Applications (iFUZZY)*, 2015. DOI: 10.1109/iFUZZY.2015.7391884. URL: `https://ieeexplore.ieee.org/abstract/document/7391884`

[7] Ristic B., Morelande M., Gunatilaka A. Information driven search for point sources of gamma radiation. *Signal Processing*, 2010, 90(4):122539. DOI: 10.1016/j.sigpro.2009.10.006. URL: `https://www.sciencedirect.com/science/article/pii/S0165168409004277`

[8] Wilde G. A., Murphy R. R., Shell D. A., Marianno C. M. A man-packable unmanned surface vehicle for radiation localization and forensics. In *2015 IEEE International Symposium on Safety, Security, and Rescue Robotics (SSRR)*, 2015. DOI: 10.1109/SSRR.2015.7442944. URL: https://ieeexplore.ieee.org/document/7442944

[9] Cortez R. A., Papageorgiou X., Tanner H. G., Klimenko A. V., Borozdin K. N., Lumia R., et al. Smart radiation sensor management. *IEEE Robotics Automation Magazine*, 2008, 15(3):8593. DOI: 10.1109/MRA.2008.928590. URL: https://ieeexplore.ieee.org/document/4624587

[10] Duckworth D., Shrewsbury B., Murphy R. Run the robot backward. In *2013 IEEE International Symposium on Safety, Security, and Rescue Robotics (SSRR)*, 2013. DOI: 10.1109/SSRR.2013.6719372. URL: https://ieeexplore.ieee.org/document/6719372

[11] Martin P. G., Payton O. D., Fardoulisi J. S., et al. The use of unmanned aerial systems for the mapping of legacy uranium mines. *Journal of Environmental Radioactivity*, 2015, vol. 143, 135-140. DOI: 10.1016/j.jenvrad.2015.02.004. URL: https://www.sciencedirect.com/science/article/pii/S0265931X15000314

[12] Kaiser R., Darby I., Matos M., et al. UAV-based Mobile Gamma Spectrometry. In *CTBT Science and Technology 2017 Conference*, 2017. [cit. 2020-8-25] URL: http://www.physics.adelaide.edu.au/cssm/workshops/inpc2016/talks/Kaiser_Thu_R1_1605.pdf

[13] Zalud L. and Kocmanova P. Multispectral Stereoscopic Robotic Head Calibration and Evaluation. In *International Workshop on Modelling and Simulation for Autonomous Systems*, 2015, 173-184, DOI: 10.1007/978-3-319-22383-4_13. URL: https://link.springer.com/chapter/10.1007/978-3-319-22383-4_13

[14] Jilek T., Radiation intensity mapping in outdoor environments using a mobile robot with RTK GNSS. In *International Conference on Military Technologies (ICMT) 2015*, 2015. DOI: 10.1109/MILTECHS.2015.7153755. URL: https://ieeexplore.ieee.org/abstract/document/7153755

[15] Gabrlik P., Jelinek A., Janata P. Precise Multi-Sensor Georeferencing System for Micro UAVs. In *14th IFAC Conference on Programmable Devices and Embedded Systems (PDES)*, 2016, 49(25): 170-175. DOI: 10.1016/j.ifacol.2016.12.029. URL: https://www.sciencedirect.com/science/article/pii/S2405896316326659

[16] Gabrlik P., la Cour-Harbo A., Kalvodova P., Zalud L., and Janata P. Calibration and Accuracy Assessment in a Direct Georeferencing System for UAS Photogrammetry. *International Journal of Remote Sensing*. 2018, 39(15-16), 4931-4959. DOI: 10.1080/01431161.2018.1434331. URL: https://www.tandfonline.com/doi/full/10.1080/01431161.2018.1434331

[17] Jilek T., Advanced navigation in heterogeneous multi-robot systems in outdoor environment. *PhD thesis*, Brno, 2015. URL: https://dspace.vutbr.cz/handle/11012/51783

[18] Hart P. E., Nilsson N. J., Raphael B. A Formal Basis for the Heuristic Determination of Minimum Cost Paths. *IEEE Transactions on Systems Science and Cybernetics*, 4(2): 100-107. DOI: 10.1109/TSSC.1968.300136. URL: https://ieeexplore.ieee.org/document/4082128

[19] Amidror I. Scattered data interpolation methods for electronic imaging systems: a survey. *Journal of Electronic Imaging*, 2002, 11(2), 157-176. URL: http://molly.magic.rit.edu/~mac/test/paper_pdf.pdf

[20] Miller A., Machrafi R., Mohany A. Development of a semi-autonomous directional and spectroscopic radiation detection mobile platform. *Radiation Measurements*, 2015, vol. 72, 53-59. DOI: 10.1016/j.radmeas.2014.11.009. URL: https://www.sciencedirect.com/science/article/pii/S1350448714003229

[21] Ahmed S. N. Physics and Engineering of Radiation Detection. Elsevier Science Limited, 2007. ISBN: 978-0-12-045581-2.

[22] Turner D., Lucieer A. and Wallace L. Direct Georeferencing of Ultrahigh-Resolution UAV Imagery. *IEEE Transactions on Geoscience and Remote Sensing*, 2014, 52(5): 2738-2745. DOI: 10.1109/TGRS.2013.2265295. URL: https://ieeexplore.ieee.org/document/6553130

[23] Fazeli H., Samadzadegan F and Dadrasjavan F. Evaluation the Potential of RTK-UAV for Automatic Point Cloud Generation in 3D Rapid Mapping. In *ISPRS - International Archives of the Photogrammetry, Remote Sensing and Spatial Information Sciences*, 2016, XLI(B6): 221-226. DOI: 10.5194/isprs-archives-XLI-B6-221-2016. URL: https://www.int-arch-photogramm-remote-sens-spatial-inf-sci.net/XLI-B6/221/2016/

[24] Eling C., Wieland M., Hess C. et al. Development and Evaluation of a UAV Based Mapping System for Remote Sensing and Surveying Applications. In *ISPRS - International Archives of the Photogrammetry, Remote Sensing and Spatial Information Sciences*, 2015, XL-1(W4): 233-239. DOI: 10.5194/isprsarchives-XL-1-W4-233-2015. URL: https://www.int-arch-photogramm-remote-sens-spatial-inf-sci.net/XL-1-W4/233/2015/

[25] Barry P. and Coakley R. Field Accuracy Test of RPAS Photogrammetry. In *ISPRS - International Archives of the Photogrammetry, Remote Sensing and Spatial Information Sciences* , 2013, XL-1(W2): 27-31. DOI: 10.5194/isprsarchives-XL-1-W2-27-2013. URL: https://www.int-arch-photogramm-remote-sens-spatial-inf-sci.net/XL-1-W2/27/2013/

[26] Panayotov A. Photogrammetric Accuracy of Real Time Kinematic Enabled Unmanned Aerial Vehicle Systems. *Study conducted by the University of Colorado, Denver and Juniper Unmanned Aerial Systems for the United States Geological Survey*, 2015. [cit. 2016-7-26]. URL: http://uas.usgs.gov/pdf/Reports/USGS_FINAL_REPORT_10212015.pdf

[27] Torii T. and Sanada Y. Radiation measurement by unmanned aircraft after Fukushima Daiichi nuclear power plant accident. In *Remotely Piloted Aircraft Systems Symposium ICAO Headquarters*, Montreal, 2015. [cit. 2016-8-23]. URL: https://www.icao.int/Meetings/RPAS/RPASSymposiumPresentation/Day%201%20Session%202%20Massaki%20Nakadate.pdf

[28] Martin P. G., Payton O. D., Fardoulis J. S.. The use of unmanned aerial systems for the mapping of legacy uranium mines. *Journal of Environmental Radioactivity*, 2015, vol. 143, 135-140. DOI: 10.1016/j.jenvrad.2015.02.004. URL: https://www.sciencedirect.com/science/article/pii/S0265931X15000314

[29] Finkel R. A., Bentley J. L. Quad trees a data structure for retrieval on composite keys. *Acta Informatica*, 1974, vol. 4, 1-9 DOI: 10.1007/BF00288933. URL: https://link.springer.com/article/10.1007/BF00288933

[30] Harabor D., Grastien A. The JPS Pathfinding System. In *Proceedings of the Fifth Annual Symposium on Combinatorial Search*, 2012. ISBN: 9781577355847. URL: https://research.monash.edu/en/publications/the-jps-pathfinding-system

D. Towards Automatic UAS-Based Snow-Field Monitoring for Microclimate Research

Outline

D.1. Introduction 126
D.2. Materials and Methods 128
D.3. Results 141
D.4. Discussion 147
D.5. Conclusions 150
Bibliography 156

Bibliographic Information

GABRLIK, Petr, Premysl JANATA, Ludek ZALUD and Josef HARCARIK. Towards Automatic UAS-Based Snow-Field Monitoring for Microclimate Research. *Sensors* [online]. 2019, **19**(8), 1–23 [cit. 2020-08-25]. DOI: 10.3390/s19081945. ISSN 1424-8220. Available from: `https://www.mdpi.com/1424-8220/19/8/1945`

Abstract

This article presents unmanned aerial system (UAS)-based photogrammetry as an efficient method for the estimation of snow-field parameters, including snow depth, volume, and snow-covered area. Unlike similar studies employing UASs, this method benefits from the rapid development of compact, high-accuracy global navigation satellite system (GNSS) receivers. Our custom-built, multi-sensor system for UAS photogrammetry facilitates attaining centimeter- to decimeter-level object accuracy without deploying ground control points; this technique is generally known as direct georeferencing. The method was demonstrated at Mapa Republiky, a snow field

located in the Krkonose, a mountain range in the Czech Republic. The location has attracted the interest of scientists due to its specific characteristics; multiple approaches to snow-field parameter estimation have thus been employed in that area to date. According to the results achieved within this study, the proposed method can be considered the optimum solution since it not only attains superior density and spatial object accuracy (approximately one decimeter) but also significantly reduces the data collection time and, above all, eliminates field work to markedly reduce the health risks associated with avalanches.

Author's Contribution

The author contributed extensively to all parts of the article. He surveyed and analyzed related research and was the principal participant in designing the method, preparing the experiment, ensuring the field activities, processing the data, and interpreting the results. Moreover, the author was exclusively responsible for the writing the manuscript and is credited with finalizing the text.

Author contribution: 90 %

Acknowledgement

This work was supported by the European Regional Development Fund under the project Robotics for Industry 4.0 (reg. no. CZ.02.1.01/0.0/0.0/15_003/0000470).

Copyright and Version Notice

D.1. Introduction

Environmental mapping embodies a relevant target field for unmanned aerial system (UAS)-based photogrammetry. The low cost, safety, and flexibility of operation allow us to employ aerial mapping in domains where manned aircraft cannot be utilized profitably. One of the possible applications consists in snow cover mapping, which is beneficial within, for example, avalanche and flood forecasting, local and regional climate research, and hydropower energy situation analysis. Dependable information about snow conditions is especially important for northern countries, where the snow cover is present for a significant part of the year.

There are various methods to estimate certain snow cover parameters, and each of these techniques is beneficial at a different scale and in diverse applications. The basic parameter rests in determining the presence of snow, namely, the snow covered area (SCA). Such information is of interest mainly for the investigation of trends in large areas (or, more concretely, at the level of regions and countries) and finds use in climate and hydrological research. In general terms, two determining approaches are typically employed: optical and microwave-based survey. Snow coverage is recognizable from aerial imagery (collected from manned aircraft or satellites) only with a clear, cloudless view [1, 2]. Conversely, radar-based observation is independent of the weather conditions, although the resolution and accuracy are typically lower [2, 3, 4]. In any case, the information value of the SCA is limited because it does not describe the amount of snow or the relevant content of water.

The snow depth (SD) indicator provides us with a better insight into the amount of the accumulated snow. The SD in a certain area can be estimated via either interpolating data from a network of observation stations [5] or as a result of a fusion of point measurements and satellite-based observations [6]. In certain conditions, snow depth is also estimable from radar-based measurements or by using the light detection and ranging (LiDAR) technology; terrestrial and airborne laser scanning (TLS, ALS) have been recently utilized for this purpose [7, 8, 9]. The most meaningful indicator in this context is the snow water equivalent (SWE), describing the amount of water contained in the snow cover. This type of information is crucial for hydrologists, especially as regards flood prediction during snow melting periods. Similarly to SD estimation, the SWE is frequently obtained from in-situ measurements. The spatial resolution is increased either via fusing space-born radiometric measurements [10] and ground observations [11] or by utilizing snow models [4].

Manned aircraft and satellite-based estimation of the snow cover parameters are not suitable for small areas and applications that require high accuracy, the reasons being the low resolution, low estimation accuracy, and substantial cost. Considering other relevant approaches, the resolution of the point measurements is not sufficient

due to the sparse network of observation stations. In such cases, unmanned aircraft can be employed effectively. Micro and light UASs (below 5 kg and 50 kg [12], respectively), the categories addressed within this study, are profitably employed in many fields of aerial mapping, such as agriculture [13], forestry [14], geodesy [15], archaeology [16], or environmental mapping [17]. However, due to their limited endurance, sensitivity to weather conditions, and relevant legal restrictions, the vehicles are not suitable for global area mapping, including flights at the regional level. Conversely, the concept ensures fast, safe, low-cost, and flexible operation, and it enables us to reach superior accuracy and resolution.

Most of the recent UAS-based snow mapping projects utilize aerial photogrammetry for snow depth estimation. Studies [7, 8, 18], for example, compare photogrammetry and indirect georeferencing-based snow depth estimation with terrestrial laser scanning in mountainous regions. The results indicate that both methods are suitable for the given purpose and achieve comparable accuracies. Indirect georeferencing (IG), a technique relying on ground targets, can be successfully replaced with visual landmark-based co-registration; however, as pointed out within sources [19, 20, 21], common visible points must exist in both snow-covered and snow-free scenes. According to [7, 18], photogrammetric accuracy in snow mapping can be enhanced utilizing near-infrared (NIR) cameras instead of visible-spectrum ones since the former perform well even in weak lighting conditions. In terms of the UAS type, all of the referenced projects (except for [7]) use multi-copters to carry out the discussed photogrammetric task, mainly because of their greater wind resistance and higher payload capacity. The articles further indicate that UAS-based snow mapping is appropriate for areas up to tens of thousands of square meters. The idea of the photogrammetry-based depth estimation lies in that the actual surface model of the snow cover is compared with a reference snow-free model. Relevant reference data can be obtained in multiple ways. The common approach is to create the snow-free surface model via the same technique, namely, UAS photogrammetry, in a period when there is no snow cover [19, 18, 20, 21, 7, 8]. Another option rests in utilizing national terrain models (typically produced through LiDAR measurements), which are generally available in many countries.

The snow depth map is obtained from the height difference between the snow-covered and the snow-free surface models. To acquire such a difference, both models have to be accurately georeferenced. All of the above-mentioned research projects, except for [21], utilize indirect georeferencing or visual landmark-based co-registration. IG typically achieves an object accuracy slightly better than that of direct georeferencing (DG) (centimeter-to-decimeter level); however, a serious health risk may arise during the ground survey due to avalanches, especially in mountainous regions. Despite benefits of the DG, the approach is not widely em-

ployed nowadays. Difficulties addressed in the study [21] and other articles utilizing DG in UAS photogrammetry [22, 23, 24] relate to the complexity of the hardware equipment onboard UAS. This fact often causes reliability issues. Furthermore, such systems require calibration and precise time synchronization, higher payload capacity, and last but not least, the overall cost is higher.

As in the case of manned aircraft and satellite-based snow cover mapping, passive microwave (radar) devices can be carried by UASs as well. Such an approach, discussed within [25], is nevertheless rather uncommon.

This article embodies a case study on UAS-based snow depth mapping performed with a multi-sensor system specially designed for direct georeferencing in aerial photogrammetry. The study area, namely, the Mapa republiky snow field, has attracted the interest of scientists because of its particular characteristics; thus, various techniques for estimating snow depth and snow covered area have been tested there to this day. Our approach has the potential to reduce health risks and man-performed field work without significant accuracy limitations. The benefits and drawbacks of the presented method are discussed and compared with the previously employed techniques.

D.2. Materials and Methods

D.2.1. Study Area and the Monitoring History

Our method for estimating snow field parameters was examined at the location called Mapa republiky (Map of the Republic), a snow field having a shape similar to the outlines of former Czechoslovakia; the area is situated in the Krkonose (Giant Mountains, Figure D.1 and D.2a). This snow field, at an altitude of approximately 1,430 m above mean sea level (AMSL), is rather specific as the snow often persists until the summer season, several months longer compared to other locations in the Krkonose or the Czech Republic in general. This is somewhat unusual, considering the fact that the area is located on a south-facing slope exposed to sunlight during most of the day; the reason rests in the amount of snow contained within the field, where the snow depth significantly exceeds the average value in the given location (the maximum snow depth of 15.7 m was established in 2000, Figure D.3). The accumulation is caused by northern and northwestern winds depositing snow in the lee. The phenomenon is further intensified by the terrain depression formed by the snow itself [26, 27].

Depending on the weather conditions during the melting season, together with the precipitation as well as the wind speed and direction in the winter, the snow persists until June to August or, occasionally, does not melt at all (see Figure D.3

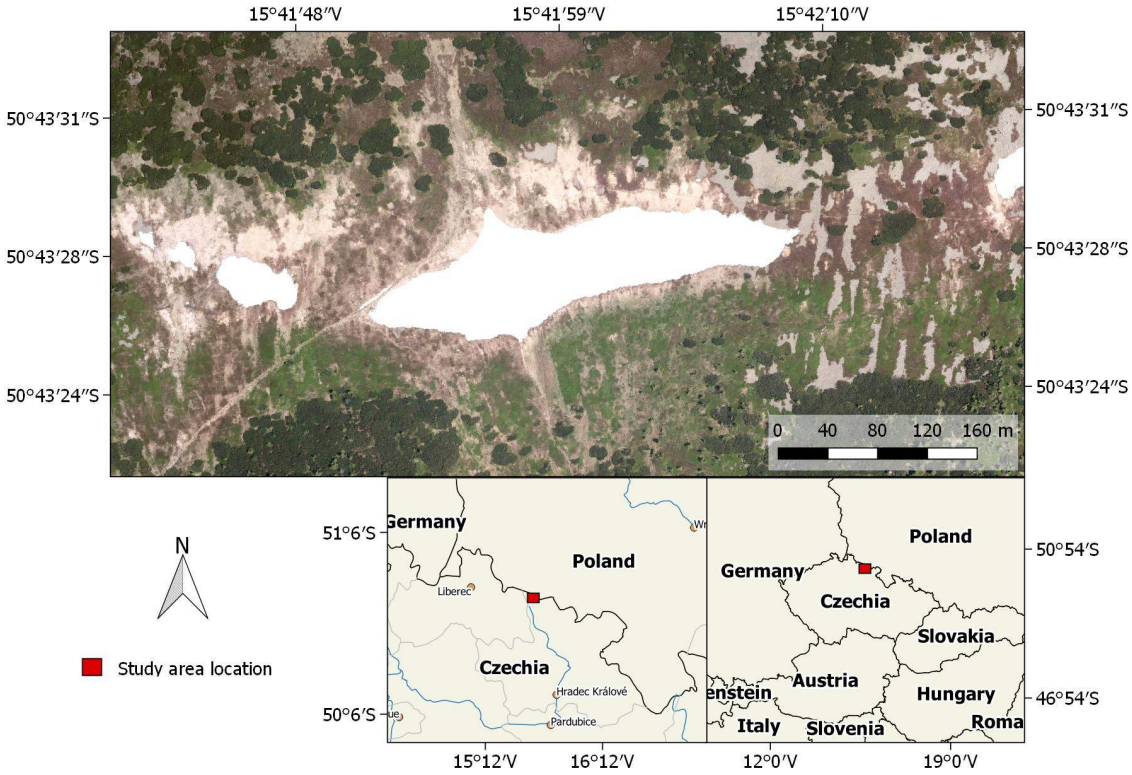

Figure D.1.: The study site location (the orthophoto obtained during the melting season 2012).

(a) (b)

Figure D.2.: The isolated Mapa republiky snow field during the spring season (a), and ground survey-based point determination of the snow field shape (b).

to read the annual statistics). For this reason, the place is of substantial interest to scientists; the examined problems include, for example, the impact of the snow depth on the vegetation pattern [26], the relationship between the geo- and biodiversity in the given area [28], and the water balance of the drainage basin. Such analysis, however, requires relevant input information about the amount of snow.

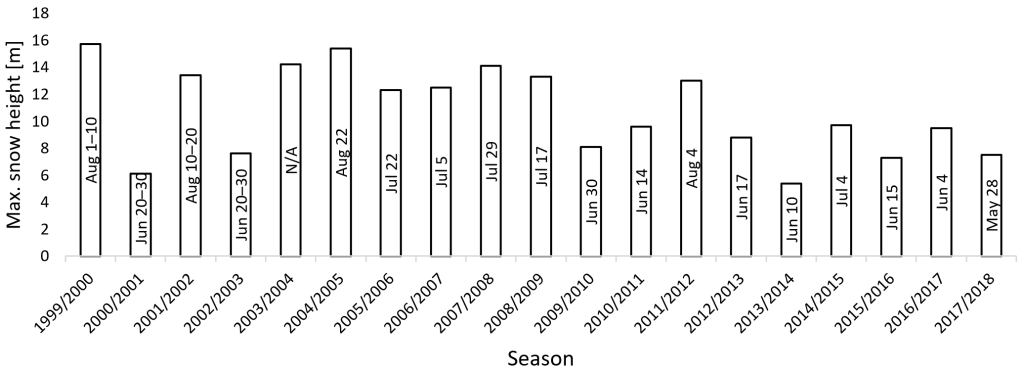

Figure D.3.: The data on the maximum snow height and melting days since 1999 (the year when the GPS-based monitoring was performed for the first time).

The first attempts to estimate the snow depth were conducted more than 100 years ago; throughout the 20th century, the research was nevertheless hampered by a lack of appropriate technical equipment [29, 30]. Wire probes (collapsible avalanche probes) are not applicable if the snowpack is deeper than 3–4 m, and fixed steel poles may fail due to the shear stress of the snow mass [26]. Systematic investigation was, in fact, made possible only after the introduction of the accurate GPS technology. Since 1999, the Krkonose Mountains National Park Administration have been monitoring the location via kinematic carrier phase-enabled GPS receivers. The surface of the snow cover is reconstructed by interpolation of GPS position data collected during walking or slow horizontal skiing. These data collection techniques were further supported by the "stop and go" method (walking with stops to facilitate static collection of point data, Figure D.2b), which ensured accuracy verification; during periods characterized by a serious avalanche risk, a viable alternative consisted in using a rope-driven sledge with a GPS receiver. Employing the same equipment, data for the construction of a snow-free surface model were collected after the melting season. A snow depth map was then computed as the difference between these two models. The described approach enabled us to estimate the depth of thick snow layers for the first time [26, 31], although the spatial resolution was rather low with respect to the amount of time needed for the data collection.

Another turning point came with the use of UASs. Since 2016, a camera-equipped UAS has been utilized to acquire relevant aerial image data to be further employed for the photogrammery-based surface reconstruction. This method significantly reduced the data collection time and, moreover, increased the spatial resolution by two orders of magnitude. Except for the snow depth, computed in the same manner as within the aforementioned method, this approach enabled us to estimate the snow-covered area employing the actual orthophoto. A major drawback of this method is

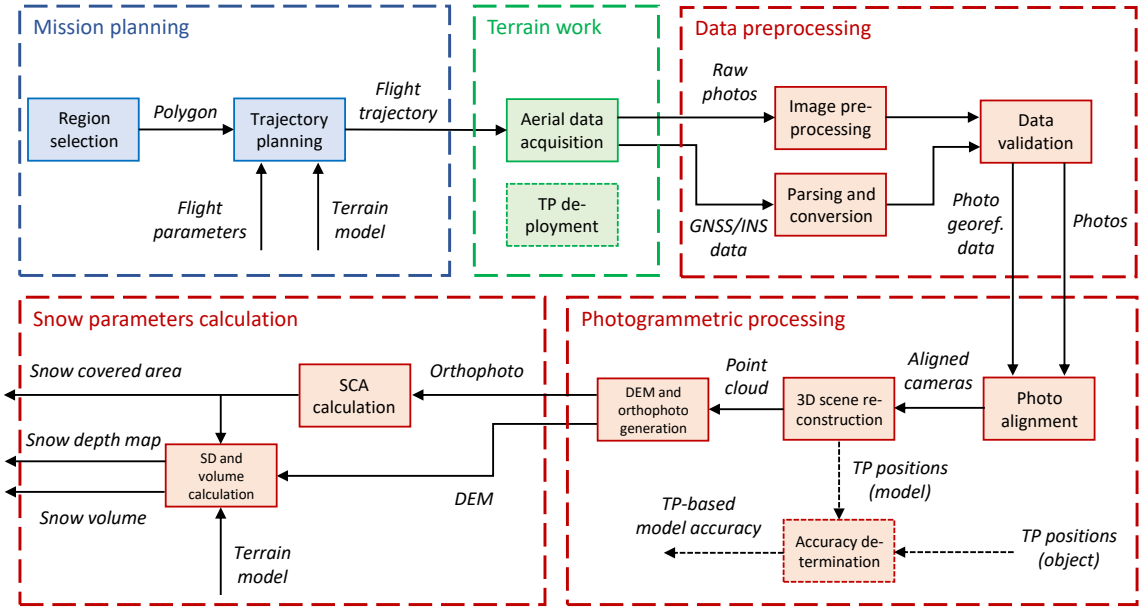

Figure D.4.: The workflow illustrating the entire snow field monitoring procedure. TP – test point; GNSS – global navigation satellite system; INS – inertial navigation system; DEM – digital elevation model; SCA – snow covered area; SD – snow depth.

the necessity of ground targets used for the georeferencing. This task still comprises certain risk due to the avalanche hazard.

D.2.2. Overall Concept

This paper discusses a vision-based snow field monitoring method that utilizes ground control point (GCP)-free UAS photogrammetry (Figure D.4). The approach eliminates a substantial portion of the common field work and is thus usable primarily in inaccessible or dangerous areas. Thanks to its capabilities, the technique offers major potential for automated data processing and, importantly, reduces the data acquisition and processing time. Compared to the other relevant methods, however, complex hardware equipment and more specialized operator skills are needed.

Our technique employs aerial photography-based products for SCA calculations; SD and volume calculations nevertheless require another component, namely, a snow-free terrain model. Since all aerial data are acquired using a UAS operated in an automatic mode, special attention must be paid to mission planning. This is essential especially in regions with rugged terrain. The field work comprises the aerial data acquisition, or the UAS flight itself, and – if required – the test point (TP) deployment. Our UAS is equipped with sensors for direct georeferencing of the imagery, and thus no ground targets (GCPs) are necessary for the processing. In

the proposed experiment, however, we employ several ground targets to enable the previously used indirect georeferencing technique, which will be later compared with our method. By extension, the targets can be utilized for the direct georeferencing quality assessment.

The processing part of the workflow is further divisible into three portions. First of all, the aerial photographs and the data from the global navigation satellite and inertial navigation systems (GNSS and INS, respectively) must be preprocessed and converted into an appropriate format. An important procedure rests in validation, which determines whether the acquired data are consistent and suitable for further processing. The second portion subsumes the photogrammetric processing, comprising tasks well known from UAS photogrammetry, such as the structure from motion (SfM)-based 3D scene reconstruction. In our case study, the quality of this process is assessed thanks to the ground targets, or test points (TPs). The orthophoto and digital elevation model (DEM) as photogrammetric products are then used in the final part of the processing to estimate the snow field parameters. The SCA is computed from the orthophoto, and the SD and volume are estimated primarily from the height differences between the snow-covered and the snow-free terrain models.

Important aspects of the workflow in Figure D.4 are addressed in more detail within the following sections. First of all, the employed UAS and sensors are described in section D.2.3. The ground measurement, a process involving test point deployment (green segment), is then outlined in section D.2.4. Section D.2.5 characterizes the mission planning and aerial data acquisition, strongly related topics highlighted in blue and green, respectively. The remaining (red) portions of the Figure display the actual data processing. The first of these segments, data preprocessing, comprises operations necessary for subsequent processing; such steps are not considered in depth, because their relevance to the presented application is limited. The workflow portions comprising photogrammetric processing and snow parameter calculation are examined within sections D.2.6 and D.2.7, respectively.

D.2.3. UAS and Onboard Sensors

To obtain the aerial data, we used a Mikrokopter Ookto XL UAS, a 95 cm span commercial octocopter capable of flying for approximately 10 minutes with the payload of 2–3 kg. The UAS supports automatic flight based on selected waypoints; the device therefore carries a low-accuracy global positioning system (GPS) receiver. The hoverability and high payload capacity are the central reasons why multi-rotor UASs are often employed in photogrammetry missions similar to that outlined herein [32, 33, 24].

All necessary equipment utilized for the remote sensing is comprised in the custom-

Table D.1.: The parameters of the custom-built multi-sensor system for UASs. The position and attitude accuracy according to the INS manufacturer's specifications (the RTK mode, airborne applications).

Parameter	Value
Position accuracy	hor.: 20 mm, ver.: 40 mm
Attitude accuracy	roll/pitch: 0.1°, heading: 0.4°
Camera sensor resolution	6,000 × 4,000 px
Camera sensor size	36 × 24 mm
Camera principal distance	21 mm
Camera aperture	f/4.5
Operational time	120 mins
Max. distance from base	1,000 m
Dimensions	1.5 × 0.2 × 0.2 m
Weight	2.6 kg

built multi-sensor system mounted on the UAS (Figure D.5b). The device was developed previously at CEITEC laboratories and embodies a part of the ATEROS (Autonomous Telepresence Robotic System) robotic system [34, 35]. The multi-sensor system consists of a Sony Alpha A7 digital camera, a Trimble BD982 GNSS receiver, an SBG Ellipse-E INS, and a single board computer Banana Pi R1. The GNSS receiver measures the position with centimeter-level accuracy when real time kinematic (RTK) correction data are transmitted, and as it is equipped with two antennas for vector measurement, the device also measures the orientation around two axes. The position and orientation data are used as an auxiliary input for the INS, which provides data output at a frequency of up to 200 Hz. All the sensors are precisely synchronized; thus, once an image has been captured, the position and orientation data are saved into the onboard solid-state drive (SSD) data storage (more parameters are contained in Table D.1).

The aforementioned system is relatively uncommon since it is completely independent of the UAS while integrating all equipment necessary for GCP-free aerial photogrammetry. The relevant testing cycles were performed on various unmanned platforms (such as that visible in Figure D.5b) during several missions, with the resulting accuracy assessed in our recent study [36]. Similar setups designed for the DG of aerial imagery but not allowing portability had been published previously [32, 24].

The performance of the applied system may satisfy the requirements of the discussed application. With respect to the utilized snow depth determination method (section D.2.7), the height accuracy of the photogrammetry-based DEM should be

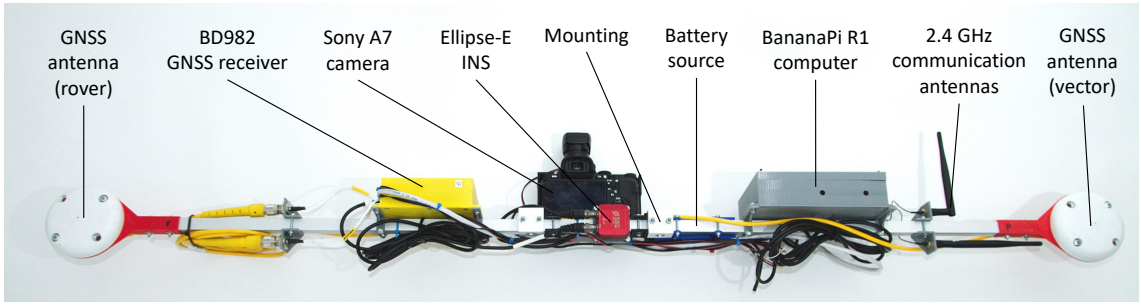

(a)

(b)

Figure D.5.: The custom-built multi-sensor system for direct georeferencing (a), and a UAS fitted with the system during a previous mapping mission (b).

comparable to or better than the snow-free model height accuracy (0.15 m RMSE in our case). Similarly, the horizontal accuracy should reach this level too in order to prevent height errors caused by inaccurate alignment of the elevation models, an effect apparent especially in steep slopes. The applied multi-sensor system meets such requirements: the object error of the model is typically below a decimeter RMS for both the horizontal and the vertical coordinates when flying at 50 m AGL [36]. In addition to the elevation model, our mapping method utilizes the actual orthophoto for the SCA calculation (section D.2.7). With respect to the parameters of the used camera and lens (Table D.1), the ground sample distances are approximately 14 mm and 29 mm for the AGL altitudes of 50 m and 100 m, respectively. These parameters are far beyond the value necessary for an accurate area estimation in a snow field having a size in the order of hundreds of meters.

D.2.4. Ground Measurements

As already mentioned in the previous section, the proposed concept does not require ground targets for the georeferencing and data processing stages; in fact, the UAS flight is the only field work activity in our concept. Despite this, several ground

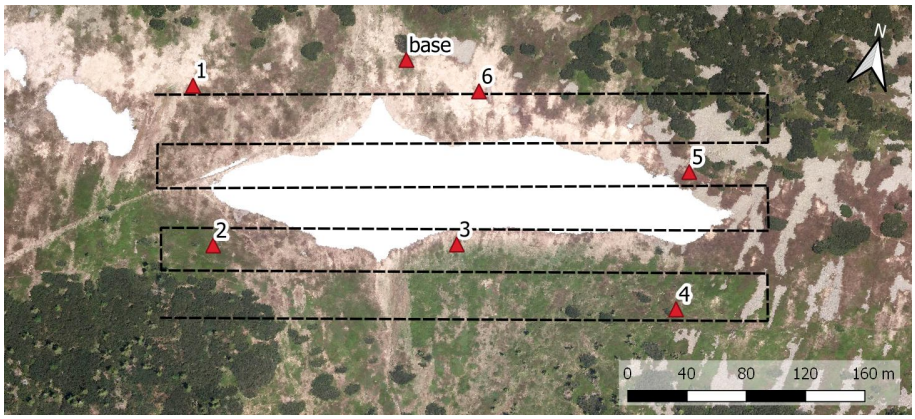

Figure D.6.: The locations of the ground targets and the base station, together with the flight trajectory for the UAS (the orthophoto obtained during the melting season 2012).

targets were employed to ensure backward compatibility with the previously used indirect georeferencing technique. Moreover, the targets enable us to determine the accuracy of the directly georeferenced photogrammetric products.

During late April 2018, the time originally selected for our investigation, the Mapa republiky snow field became completely isolated from the remaining snow cover in the vicinity. This fact allowed the positioning of six ground targets just around the snow field on the peripheral part of the area to be mapped (the distribution is visible in Figure D.6). Such a solution was commonly used in the past, enabling us to compare both georeferencing techniques. The horizontal separation of the peripheral GCPs is 140 m on average, or approximately one ground base. The spatial distribution and number of GCPs play a substantial role in the quality of indirect georeferencing in photogrammetry. This aspect has already been addressed within numerous publications [37, 38]. Our peripheral location of the targets meets the basic GCP distribution requirement; however, a higher density and extra GCPs located in the central part would help us to increase the georeferencing accuracy.

We used 20 cm squared, black and white patterned paper targets having clearly defined centres. All these targets were glued onto a solid support and fixed to the ground by using iron nails. The position of every single target was acquired using a survey-grade Topcon HiPer HR RTK GNSS receiver obtaining correction data from the TopNet (Czech provider of correction data). With the same equipment, the position of the GNSS base station (Figure D.7) was determined. The base station, also indicated within Figure D.6, provides the correction data for the GNSS receiver aboard the UAS, and its accurate position is crucial as regards the quality of the snow field parameters estimation.

Figure D.7.: The base station (located close to the snow field) performing real-time GNSS corrections for the sensors aboard the UAS.

D.2.5. Mission Planning and Aerial Data Acquisition

Mission planning comprises standard tasks known from UAS-based photogrammetry. First of all, a mapping region must be selected; in our experiment, this was a rectangular area around the isolated snow field. Both horizontal coordinates of the region are enlarged by approximately 50% because the exact size and location of the snow field during the melting period is difficult to estimate. Subsequently, we design the trajectory (the waypoints for the automatic flight) within the region, satisfying the following photogrammetric requirements: the desired forward and side image overlaps; ground resolution; and altitude restrictions. The trajectory planning thus also depends on the applied photographic equipment, its intrinsic parameters in particular; these include, for example, the principal distance and sensor size. We use the common parallel strips flight pattern known from both manned and unmanned aerial photogrammetry [39, 40], as shown in Figure D.6. The parameters of the flight trajectory and image data acquisition for the presented case study are summarized in Table D.2.

The mission planning process is, in our case, performed in the field, immediately after assessing the actual situation. For this purpose, a laptop with the MikroKopter-Tool software for automatic waypoint-based mission planning is utilized. Since the location is a steep slope (the height difference between the highest and lowest spots is approximately 100 m), a constant flight altitude above mean sea level (AMSL) would cause high variation in altitude above ground level (AGL) and thus also

Table D.2.: The parameters of the flight trajectory and image acquisition; the values that depend on the flight altitude (AGL) are stated for the average altitude.

Parameter	Value
Distance between strips	30 m
Strip length	400 m
Number of strips	6
Base (distance between consecutive images)	10 m
Flying altitude AGL	90–130 m
Flying speed	5 m s^{-1}
Flying time	10 min.
Time between images	2 s
Photo scale	1:5,200
Forward overlap	92%
Side overlap	84%
Image footprint	190 × 125 m
Ground resolution	3.1 cm px^{-1}
Shutter speed	$1{,}000^{-1}$ s
Aperture	5.6
ISO	Auto (100–400)

ground resolution. For this reason, we adjusted the AMSL altitude of the individual survey lines to minimize variation in ground resolution.

Except for the take-off and landing, the UAS operates in the automatic mode based on the aforementioned settings, uploaded to the device's memory just before the flight. With the employed photogrammetric parameters, the mapping of the area takes approximately 10 minutes. The image and GNSS/INS data, which are hardware-synchronized, are recorded throughout the flight on the SD card and SSD storage, respectively.

D.2.6. Photogrammetric Processing

The method proposed in this paper utilizes photogrammetry to reconstruct the given 3D scene, namely, snow-covered terrain. For this purpose, we utilized Agisoft Photoscan Professional (version 1.4.2), a complex software package to execute all photogrammetric processing stages, from the image and georeferencing-related data to the orthophoto, DEM, and other products. The workflow starts with the align

phase, where the exterior and interior camera orientation [41] is estimated based on the feature points detected in the overlapping images. Further, the locations of the feature points are determined via the structure-from-motion procedure, resulting in a sparse point cloud [42]. Within the following step, a dense point cloud can be generated, utilizing multi-view stereo (MSV) reconstruction. As the operation is performed at the level of pixels, even small details are reconstructed to yield a point cloud containing millions of points.

The camera poses determined in the previous step being relative, Photoscan offers two methods of georeferencing, namely, transformation into geographic coordinates (WGS-84 in our case): one employing the image position data measured by the onboard sensors (section D.2.3), and the other performed via the GCPs positions obtained during a ground measurement (section D.2.4). Both procedures rely on similarity transformation comprising translation, rotation, and scaling [43, 39]. The techniques are also known as direct (DG) and indirect georeferencing (IG), respectively. Although we used a multi-sensor system to carry out the GCP-free photogrammetry, both georeferencing options were tested. For this reason, the georeferencing phase of the workflow was executed twice to evaluate the two methods separately (employing the same image dataset and identical photogrammetric processing settings). In practice, most of today's photogrammetry missions utilize GCPs to reach a centimetre-level spatial accuracy even with consumer-grade equipment onboard a UAS; this scenario is presented in several sources, such as [44, 22, 45]. Direct georeferencing, commonly supported by computer vision (CV) algorithms, typically leads to a slightly lower accuracy; this approach, however, brings certain benefits, as outlined within the above chapters and elsewhere [22, 23, 24].

Based on the georeferenced dense point cloud, a DEM was generated; the model can be considered a digital surface model (DSM). This product is essential for the formation of the orthophoto. The quality of these outputs was determined by utilizing test points, or ground targets with accurately known spatial positions (section D.2.4). We used the targets in two manners, namely, as the TPs in DG and the GCPs in IG. The majority of the references papers employed Photoscan, whose workflow and algorithms are described in more detail within [46].

Photogrammetry-based 3D scene reconstruction fully depends on the features visible in the images, resulting in certain restrictions as regards the presented study. Snow-covered terrain typically lacks a texture because a snow surface normally contains white color that does not vary substantially. Such a property then causes the reconstruction process to fail; however, relevant studies show that snow often contains a texture sufficient for photogrammetric processing [18, 20, 21]. Last but not least, low visibility caused by weather effects, including fog or clouds, will also produce a negative impact on the quality of the results.

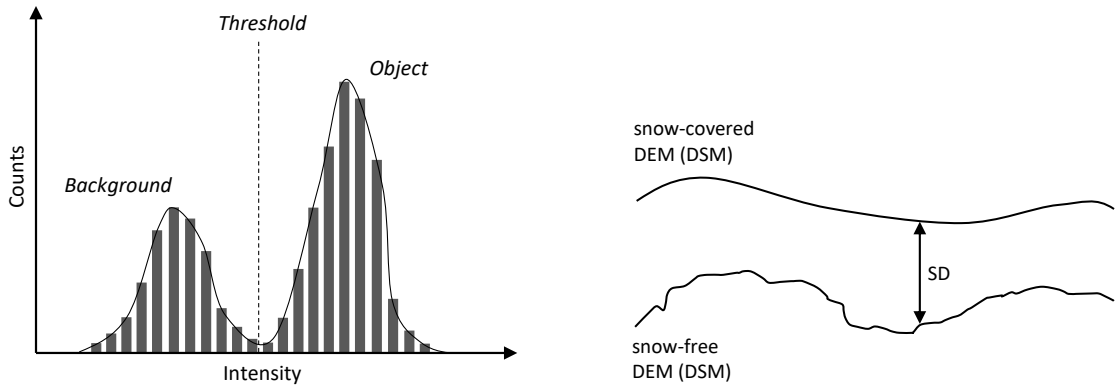

(a) (b)

Figure D.8.: Segmentation by thresholding: a grayscale image histogram and the threshold separating an object and the background (a); the snow depth determination principle (b).

D.2.7. Snow Field Parameter Estimation

For many UAS-based mapping applications, the final output consists in photogrammetry products, such as a georeferenced orthophoto and DEM. However, in our case, these products form the input data for the final processing phase, namely, the calculation of the snow field parameters (see the process flow diagram in Figure D.4). As described in the Introduction, the three main parameters related to snow mapping are snow covered area (SCA); snow depth (SD), or volume; and snow water equivalent (SWA). Our method considers merely the first two of these as the last one typically requires in-situ measurements.

The method utilizes optical-based SCA estimation employing the orthophoto obtained within the previous step. This approach relies on visual separability of the snow cover from the rest of the snow-free terrain, typically covered with vegetation, rocks, water, or artificial objects. The desired effect is achieved through segmentation, an elementary computer vision task that consists in partitioning an image into multiple homogeneous and meaningful regions [47]. A common segmentation technique is thresholding [48], which, in its basic form, separates an object and the background in a grayscale image. The key assumption is that the object class includes levels of gray different from those exhibited by the background class, enabling the user to find the thresholding level (Figure D.8a).

The snow field (representing the object, with a color approaching white) in our study area is clearly separable from the snow-free terrain (or the background, covered with vegetation) via thresholding since the two classes are characterized by different levels in both red-green-blue (RGB) channels and the grayscale interpretation. Within our research, the threshold level was established primarily manually to facili-

tate precise SCA determination; we nevertheless also employed the well-known Otsu method [49] (implemented within the `graythresh` function in Matlab) to test the automatic threshold level determination. Once the snow has been separated from the background, the snow field, Mapa republiky, must be separated from the snow cover in its vicinity. This step was performed using the `bwlabel` function, which labels connected components in the binary image. The largest component then corresponds to the snow field, and its area is determinable thanks to the known pixel size of the orhophoto.

The aforementioned semi-automatic and automatic SCA estimation methods were also compared with the manual technique exploiting an area measurement tool contained in geographic information systems (GISs); this solution allows the operator to measure any area manually. All the approaches are discussed in the final sections of this article.

Snow depth, expressible with a positive real number, describes the height of the snow cover above the terrain at a certain location; a snow depth map is then the 2D SD representation of the given area georeferenced into geographic coordinates. SD, unlike the above-described SCA, cannot be estimated utilizing an orthophoto only. Our method interprets SD as the height difference between a snow-covered and a snow-free DEM, as illustrated in Figure D.8b. The former model was obtained during a melting season via photogrammetry (section D.2.6); the latter, snowless elevation model was acquired from CUZK (the Administration of Land Surveying and Cadastre of the Czech Republic [50]). The Administration provides an airborne laser scanning (ALS)-based digital terrain model (DTM) covering the entire Czech Republic; its height accuracies are 0.15 m and 0.25 m for uncovered and wooded terrain, respectively, and the average density corresponds to 5 points m^{-2} in the very least. This model was resampled to obtain a DTM with the resolution of 0.05 m px^{-1} (the shaded DTM of the study area is illustrated in Figure D.9). Unlike the DSM produced by photogrammetry, the DTM does not involve artificial objects and vegetation. However, this property should not lead to major difficulties, because our study area is mostly covered with grass, and no objects are present. The calculation was performed in QGIS (version 3.0.2) GIS to allow calculations with raster layers and to support various coordinate reference systems. The input raster layers, or DEMs, were obtained using different methods; thus, their pixel resolutions do not coincide. To deal with this issue, the nearest neighbor resampling method was applied.

The drawback of the SD calculation technique is that the height difference between the DEMs does not have to be caused by the snow only. In mountainous regions, a rapid surface change can occur due to, for example, vegetation growth or a rock slide. To minimize the impact of such effects, we consider only areas where the

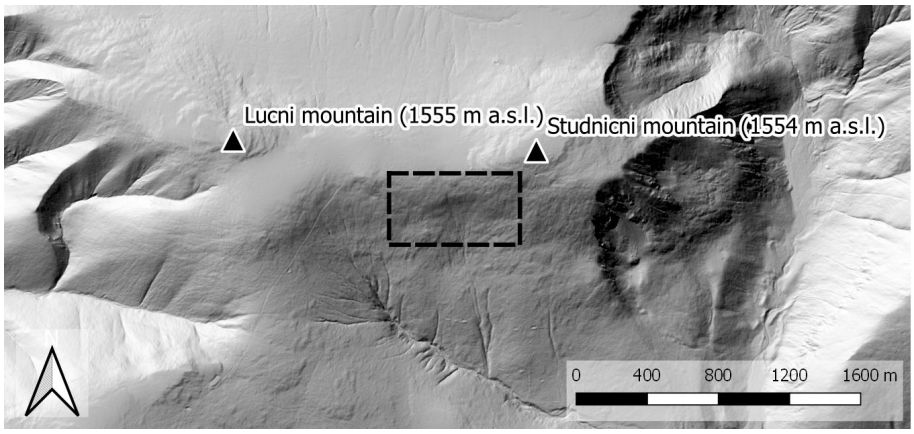

Figure D.9.: The fifth generation, shaded DTM of the Krkonose (obtained from CUZK). The study area is highlighted by the dashed line.

presence of the snow was detected utilizing an orthophoto, as described within the SCA determination earlier in this section. The masked (snow-free) area is thus excluded from the SD calculation.

The snow cover volume is another meaningful indicator. Similarly to the SCA, it informs us about the quantity of snow via a single number. Once the SD map has been obtained, the volume can be computed as the sum of the individual heights multiplied by the map resolution (pixel size). From this point, there remains only a small step to determining the SWE, namely, the amount of water contained in the snow field. Since the snow density oscillates between 50 kg m^{-3} (new snow) and 900 kg m^{-3} (ice, [51]), the parameter must necessarily be obtained. Such a task, however, is not feasible using the sensors onboard our UAS; to obtain relevant data, we would therefore have to rely on in-situ observation.

D.3. Results

D.3.1. Photogrammetry

The aerial data acquisition lasted 14 minutes; during this time, 403 images were collected. In addition to the automatic waypoint-based flight, the operational period included the take-off and landing, namely, manually controlled phases. The data acquired within these latter steps are not relevant; thus, 222 images only were utilized for the processing. This image set was pre-processed using Adobe Photoshop Lightroom (version 6.0) to compensate lens vignetting and to convert the RAW image files into JPG at minimum compression. One of the images is displayed within Figure D.10a.

The GNSS/INS logging was triggered with the camera shutter, and the number

(a) (b)

Figure D.10.: A photo captured from the height of 100 m AGL (a); a zoomed ground target (b).

of records contained in the log file equalled that of images captured. The data were converted into an appropriate format and subsequently analyzed. Figure D.11 shows the measured positions of the cameras in the local system as well as the solution quality indicator estimated by the onboard GNSS. The RTK fixed solution was available for 73% of the time; the RTK float for 5%; the differential GNSS (DGNSS) for 18%; and the autonomous fix for 4%. The RTK fixed solution outages were caused by interruption of the data link that facilitates the transmission corrections. The age of the corrections has a direct impact on the quality of the GNSS solution; the fixed solution was thus lost for several moments, especially in the southeastern part of the flight trajectory, as is evident from Figure D.11. This fact will likely negatively affect the accuracy of the DG and, therefore, also that of the photogrammetric products. The aforementioned figure further comprises the actual locations of the GCPs employed for the IG; one of the targets (as captured in an aerial image) is displayed within Figure D.10b.

The datasets from the onboard sensors, namely, the images and the GNSS/INS derived data were imported into the Photoscan, together with the locations of the ground targets. The photogrammetric processing was performed once with DG and once with IG, using the same settings. These techniques, except for georeferencing itself, require identical processing phases. In the case of DG, the camera locations (and estimated errors) were simply imported from a text file; IG, conversely, involves manual placement of markers on the targets visible in the images. Despite this, the processing times do not differ much, as indicated in Table D.3. However, if we consider also the data collection phase, IG is more time-intensive due to the deployment of ground targets (GCPs).

The parameters of the photogrammetric products are also comparable to a certain extent: Both dense point clouds contain approximately 190 points m^{-2}, the resolutions of the DEMs and the orthophotos are 10.9 cm px^{-1} and 2.7 cm px^{-1},

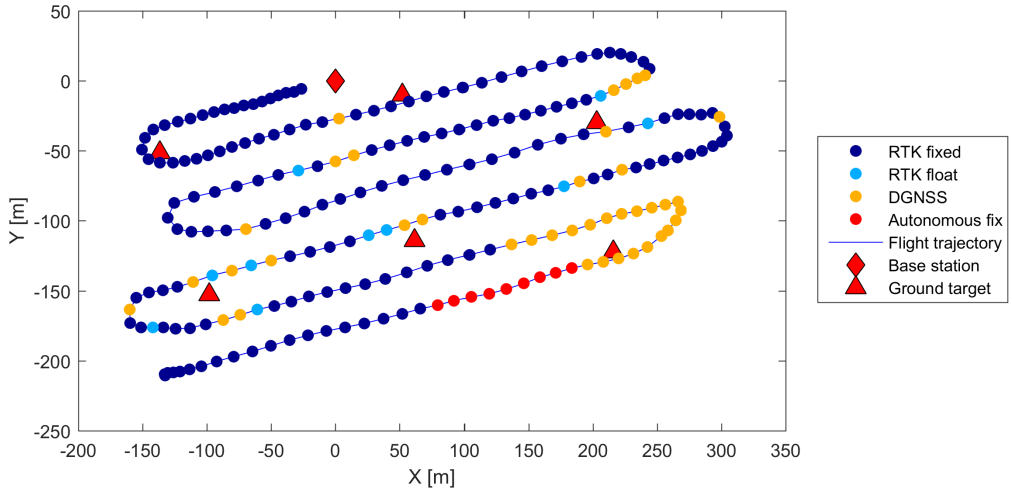

Figure D.11.: The camera locations and the GNSS quality indicator estimated by the onboard GNSS/INS.

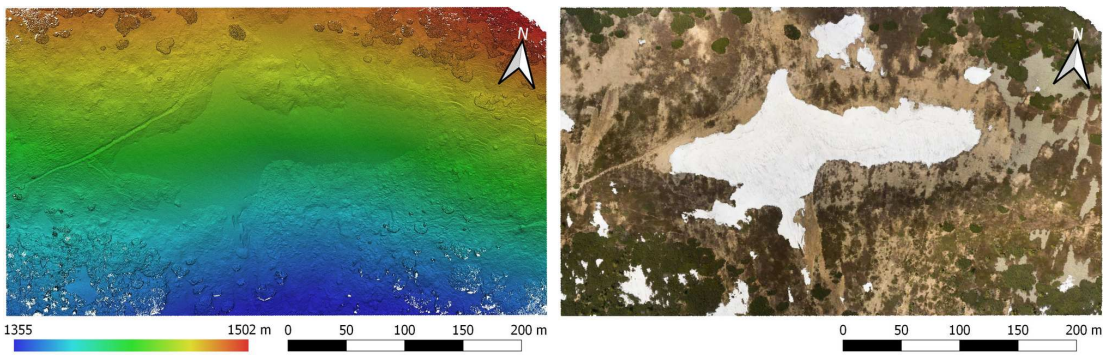

(a) (b)

Figure D.12.: The directly georeferenced, shaded DEM (a) and the relevant orthophoto (b), both representing the output of the photogrammetric processing phase.

respectively (Figure D.12). As expected, the difference shows itself in the georeferencing accuracy. According to the 6 TPs, DG reached the spatial RMS error of 11.4 cm; the RMSE of IG is slightly better, equalling 7.6 cm (Table D.4). It should be noted that although using such a low number of TPs to express accuracy is not sufficiently credible in terms of statistics, we can still benefit from the actual information of whether a problem occurred during the data collection and processing. A detailed analysis of DG accuracy was proposed within our previous study [36]. Further, IG accuracy stated using GCPs (with the targets employed for georeferencing) is also of mainly informative character.

The analysis indicates that, in our study, the georeferencing techniques do not

Table D.3.: The data collection and processing times of the applied techniques; the photogrammetric processing was executed on a personal computer with an Intel Core i7-6700 CPU, 32 GB RAM, and an NVIDIA GeForce GTX 1051 Ti GPU.

Processing phase	Automatic/Manual	DG [h:mm:ss]	IG [h:mm:ss]
Aerial data acquisition	A	0:13:36	0:13:36
Target deployment	M	—	˜0:30:00
Data collection in total	—	0:13:36	˜0:44:00
Photo alignment	A	0:18:33	0:21:00
Marker placement	M	—	0:09:55
Camera calibration	A	0:00:06	0:00:06
Dense point cloud generation	A	1:23:59	1:25:33
DEM generation	A	0:00:36	0:00:26
Orthophoto generation	A	0:09:36	0:08:04
Processing in total	—	1:52:50	2:05:04
Entire process	—	2:06:26	2:49:04

Table D.4.: The accuracy of direct and indirect georeferencing, determined by using 6 ground targets. In the IG procedure, the accuracy was assessed via the GCPs.

	DG [cm]			IG [cm]		
Target	XY	Z	XYZ	XY	Z	XYZ
1	1.3	-1.3	1.8	4.1	-7.7	8.8
2	2.7	2.8	3.9	1.8	6.6	6.9
3	2.2	-0.3	2.2	3.2	3.3	4.6
4	7.5	-6.4	9.9	5.2	-6.6	8.4
5	21.8	10.7	24.3	10.0	1.5	10.1
6	3.5	7.7	8.5	5.6	2.2	5.6
Mean	6.5	2.2	8.4	4.9	-0.1	7.4
RMSE	9.7	6.1	11.4	5.5	5.3	7.6

differ significantly as regards the time intensity and the final accuracy (IG needed 34% more time, Table D.3; DG was slightly less accurate, Table D.4). The main benefit of DG rests in the elimination of human involvement, especially during the data collection procedure, which is potentially hazardous to human health. Moreover, such a scenario enables automation of all major data collection and processing phases.

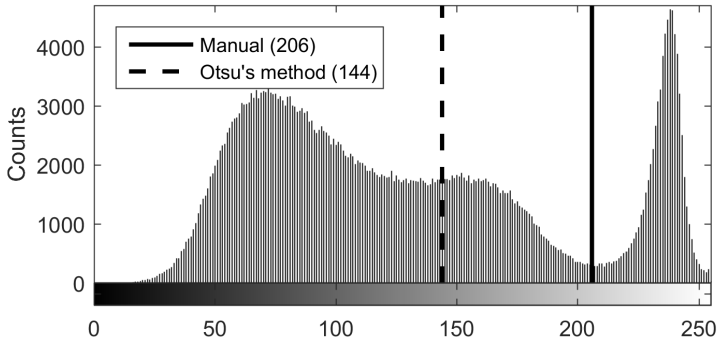

(a)

(b) (c)

Figure D.13.: The histogram (a) of the gray-scaled orthophoto (b), with the snow covered area extracted (the snow field is highlighted in black) (c).

D.3.2. Snow Field Parameters

The calculation of the snow field parameters started with the orthophoto-based SCA estimation, as discussed in section D.2.7. First of all, the orthophoto was converted into an 8-bit grayscale image (Figure D.13b) for segmentation purposes. We determined two threshold levels in the respective histogram: one level, 206, was established manually, while the other, 144, was computed using the Otsu method (Figure D.13a). The Otsu technique was found to produce unsatisfactory results in this application as it does not separate the object from the background precisely; the threshold should lie in the local minimum between the high valued counts (whites) and the darker background. To automate this procedure, a reliable segmentation algorithm would have to be designed; such a step, however, would require an adequate test dataset. For this reason, we applied the manual threshold level. In the segmented image, connected components were found; the component comprising the largest number of pixels corresponded to the snow field (Figure D.13c). Based on the known pixel size, the snow covered area of 15,802 m^2 was estimated. This result was then manually verified utilizing the QGIS area measurement tool, yielding 15,493 m^2, a value 2% lower than the automatically delivered one.

The snow depth map was derived from the elevation models. Since both the

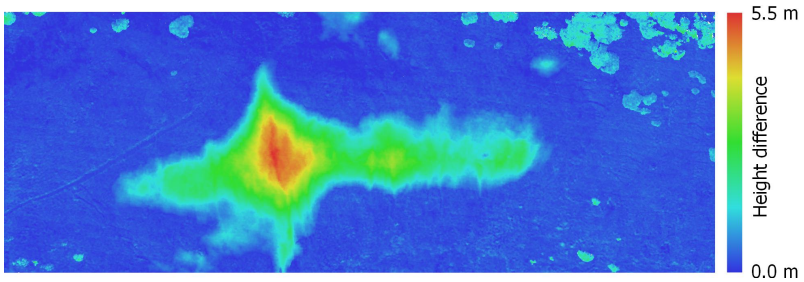

(a)

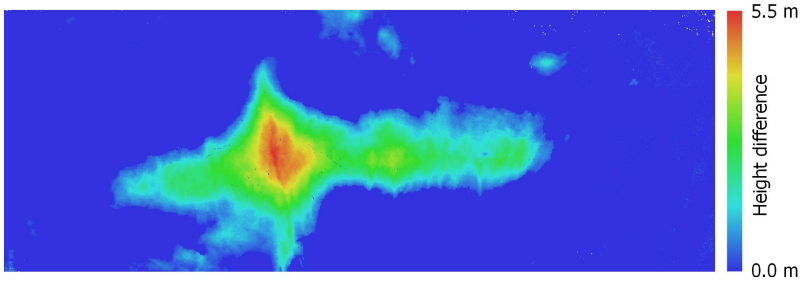

(b)

Figure D.14.: The height difference between the snow-covered, photogrammetry-based DSM and the snow-free, ALS-based DTM (a). This result involves differences caused by not only the snow itself but also other aspects, including, for example, vegetation (upper right corner). After the SCA mask has been applied, the difference map contains the snow depth only (b).

snow-free ALS-based DTM and the snow-covered photogrammetry-based DSM are georeferenced in the same coordinate system, they were used for direct calculation. At the initial stage, we employed the QGIS raster calculator to compute the height difference between the DSM and the DTM. Since the former, unlike the latter, generally includes also vegetation and artificial objects, the difference map does not contain the snow only. This effect is represented in Figure D.14a, where, especially in the upper right corner, the vegetation (scrub mountain pine) causes considerable height differences. To exclude such objects from the SD calculation, we applied the SCA mask computed within the previous step. After that, the difference map contained the snow cover only, as displayed in Figure D.14b. The maximum height of 5.45 m corresponds to the maximum depth of the Mapa republiky snow field, whose volume, computed as the sum of the heights in the individual pixels, equals 26,367 m^3.

As is evident, the study area contains various types of vegetation. Since we used the DTM as the snow-free reference, it cannot be excluded that some of the vegetation is under the snow cover. Such a scenario would negatively affect the accuracy

of the snow depth determination, meaning that the estimated snow depth would be higher than it really is. To deal with this issue, a DSM created via, for example, UAS-based photogrammetry, should be employed as the snow-free reference model.

The high resolution models introduced within our research allow us to analyze cross sections in any direction, leading to better understanding of how the snow is accumulated in relation to the terrain shape. An example of two cross sections through the SD maximum in the east-west and north-south directions is provided in Figure D.15. The east-west direction, for instance, illustrates that the maximum is located exactly in the terrain depression present within the area of interest.

D.4. Discussion

Within this study, we introduced an innovative, state-of-the-art technique for snow field monitoring and tested its performance at Mapa republiky, a location of major scientific interest within the discussed research problem. The method exploits various advanced technologies, such as micro UASs to perform automatic aerial data collection; an embedded RTK GNSS receiver allowing centimeter-level positioning; and photogrammetric software providing powerful tools to create digital orthophotos and elevation models. Our solution thus effectively eliminates most drawbacks inherent in previous approaches to the estimation of snow depth, volume, and covered area.

In the context of the mapping, we can specify several categories to evaluate the quality of each method, and these are as follows: spatial density (resolution) of the collected data; snow depth estimation accuracy; data acquisition time; safety risks; and automation potential. We comprehensively evaluated each of the methods employed previously on Mapa republiky as well as the procedure proposed herein; the results are summarized in Table D.5. As regards the earliest technique, which relied on wire probes, the main drawbacks consisted in the impossibility to penetrate thick snow layers (above 3–4 m); very long measurement time; and low spatial density. The snow depth estimation accuracy is sufficient (less than 10 cm, as established upon comparison with the GNSS-based method [26]) if the probe reaches the ground. Similarly to all methods requiring manual data collection, wire probing is a low safety procedure due to the avalanche risk. The approach shares most of its parameters with the GNSS-based ground procedure, introduced within [26, 31]; significantly, the latter method is nevertheless capable of measuring thick snow layers without accuracy reduction. Since the data collection is realized through continuous walking or skiing, higher space density data can be obtained in less time. Further, a rope-driven sledge can be used instead of the walking and skiing to decrease the safety risk during the avalanche season.

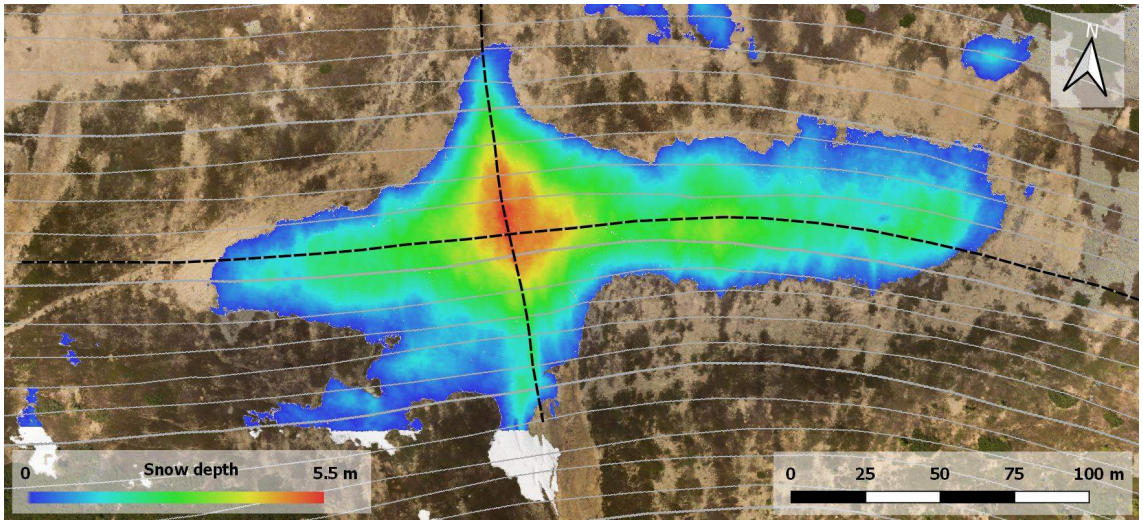

(a)

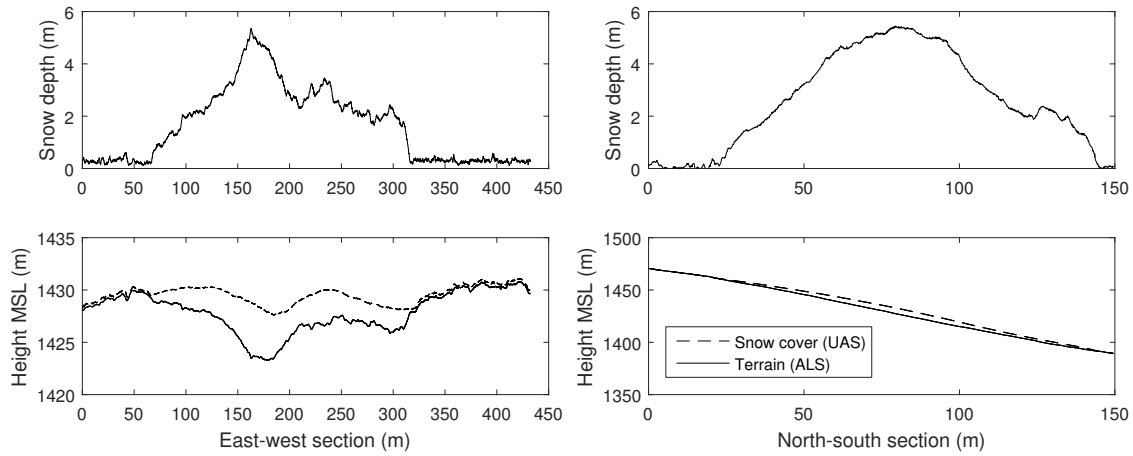

(b) (c)

Figure D.15.: An interpretation of the mapping results (a). The UAS photogrammetry-based orthophoto is supplemented with a layer illustrating the snow depth; both items were created with the multi-sensor system for direct georeferencing. The map includes contour (solid gray) and section (dashed black) lines to facilitate the cross-section analysis. The cross-sections of the snow depth map, the UAS-based surface model, and the ALS-based terrain model, all passing through the snow depth maximum in the east-west direction, are displayed in (b); those that run in the north-south direction are then indicated in (c).

Table D.5.: A comparison of the snow field mapping methods.

Type	Method	Resolution (meter-order)	Accuracy (meter-order)	Time consumption	Safety	Automation potential
Ground	wire probe survey	10^0 – 10^1	10^{-1} – 10^0	hrs	avalanche risk	no
Ground	GNSS survey	10^0 – 10^1	10^{-2}	hrs	avalanche risk	no
Ground + aerial	UAS photo. (IG)	10^{-2}	10^{-2}	mins – hrs	avalanche risk	partial
Aerial	UAS photo. (DG)	10^{-2}	10^{-2} – 10^{-1}	mins	no	high

The UAS-based aerial data acquisition markedly reduced the data collection time without decreasing the accuracy and, simultaneously, ensured superior density (at the centimeter level). In the remaining categories, the quality varies with the applied georeferencing technique. As mentioned in section D.2.6, the indirect georeferencing in UAS-based photogrammetry outperforms the direct technique in terms of the object accuracy. Both approaches, however, allow us to reach a centimeter-level object accuracy [32, 52, 22]. This fact was confirmed during our previous research [36] and within this study as well. We achieved the spatial RMS error of 11.4 cm in the DG, securing sufficient performance for the relevant application, given that the height accuracy of the applied snow-free model was 15 cm RMS. Yet, the snow depth estimation accuracy was not assessed in this study; this topic is discussed, for example, within articles [8, 7]. Indirect georeferencing, compared to DG, does not require very accurate and expensive positioning equipment onboard the UAS; despite this, a survey-grade GNSS receiver is still needed to measure the positions of the GCPs, an operation that consumes substantial extra time (Table D.3 and [7]). In the remaining respects, DG nevertheless brings a major advantage in that the field work comprises only the automatic UAS flight, enabling the operator to control the entire mission from a safe distance. Such a scenario then considerably reduces the health risks and time intensity. Additionally, DG enables us to significantly increase the portion of automatic processing. In terms of the aforementioned aspects, the method that utilizes UAS-based photogrammetry and direct georeferencing can be considered the most appropriate solution for snow mapping at present.

In the context of Mapa republiky, our approach brings undoubtable benefits, the most prominent one being that the snow monitoring can begin already in early spring, namely, at a time when the avalanche risks are usually too high to employ other techniques, terrestrial-based procedures in particular. This advantage enables us to collect complex data over a longer time period, leading to a better insight into the snow melting process and its impact on the local microclimate and hydrological situation. Moreover, the lower time intensity and higher automation potential may facilitate more frequent observations in the future. The method's usability, however, is not limited to the discussed site only: Many other research-relevant, interesting

locations in the Krkonose cannot be easily monitored by UASs today, mainly due to the avalanche risk, inaccessibility, or dense vegetation disallowing GCP deployment.

The only partially unsuccessful portion of the experiment was the correction transmission during the aerial data acquisition, where the datalink outages probably slightly affected the object accuracy. As regards the data processing, the segmentation phase will have to be refined to eliminate operator interventions; we nevertheless believe that the entire data processing cycle can be executed automatically in the future.

It should be noted that the proposed approach exhibits certain limitations. The operation of the UASs, the small ones in particular, depends on the weather conditions: Flying in rain or snowfall is typically prohibited, and the wind speed cannot exceed the pre-defined level. The discussed conditions may embody a markedly limiting factor, especially in mountainous regions and during the winter season, namely, parameters specific to our research. Moreover, poor visibility (due to fog, for example) can affect the quality of the photogrammetric processing or even make this phase impossible.

Further development of the technology will most likely increase the already high effectivity of mapping missions. Thus, our solution relying on a custom-built multi-sensor system and a UAS, with the total weight of the components being approximately 8 kg, may be possibly replaced with a more compact design. RTK GNSS-equipped UASs whose weight ranges below 2 kg have been recently available on the market [53]; using such equipment, the field work could be easily carried out by one person. The quality of this solution, however, is yet to be assessed.

D.5. Conclusions

This article proposed a UAS-based snow-field mapping technique and evaluated its performance at Mapa republiky, a mountainous location of substantial scientific interest. The main benefit of the method rests in utilizing ground control point-free UAS photogrammetry enabled by a custom-built multi-sensor system; this approach allowed us to perform an entire mapping mission from a safe distance, eliminating a major portion of the safety risks associated with avalanches. The parameters observed within the experiment, namely, the georeferencing accuracy (approximately one decimeter RMSE) and spatial resolution of the photogrammetric products (centimeter-level), fully satisfied the requirements of the discussed application. Regrettably, the thick snow cover at the study site did not enable us to evaluate the snow depth mapping results achievable with a direct method, such as wire probing. In terms of the time consumption, our approach proved to be more efficient than the previously employed techniques, facilitating automatic execution

of most processing steps. Despite this, there still remains space for improvements, especially in view of the fact that some processing procedures currently depend on user intervention. Exploiting the outcomes presented herein, those related to safety in particular, the technique generally allows the user to collect data at Mapa republiky very early in spring; such an operation was not feasible previously, meaning that the associated microclimate research at the given location had to face substantial objective limitations. This impediment can now be effectively overcome by using the novel approach.

Bibliography

[1] S. Anttila, S. Metsamaki, J. Pulliainen, and K. Luojus. From EO data to snow covered area (SCA) end products using automated processing system. In *Proceedings. 2005 IEEE International Geoscience and Remote Sensing Symposium, 2005. IGARSS '05.*, pages 1947–1950, July 2005. URL: https://ieeexplore.ieee.org/document/1526392, doi:10.1109/IGARSS.2005.1526392.

[2] Jiancheng Shi, J. Dozier, and H. Rott. Snow mapping in alpine regions with synthetic aperture radar. *IEEE Transactions on Geoscience and Remote Sensing*, 32(1):152–158, January 1994. URL: https://ieeexplore.ieee.org/abstract/document/285197, doi:10.1109/36.285197.

[3] K. Luojus, J. P. Karna, M. Hallikainen, and J. Pulliainen. Development of Techniques to Retrieve Snow Covered Area (SCA) in Boreal Forests from Space-borne Microwave Observations. In *2006 IEEE International Symposium on Geoscience and Remote Sensing*, pages 2180–2182, July 2006. URL: https://ieeexplore.ieee.org/document/4241710, doi:10.1109/IGARSS.2006.563.

[4] Tuomo M. Saloranta. Operational snow mapping with simplified data assimilation using the seNorge snow model. *Journal of Hydrology*, 538:314–325, July 2016. URL: http://www.sciencedirect.com/science/article/pii/S0022169416301755, doi:10.1016/j.jhydrol.2016.03.061.

[5] Ole Einar Tveito, Inge Bjrdal, Arne Oddvar Skjelvg, and Bjrn Aune. A GIS-based agro-ecological decision system based on gridded climatology. *Meteorological Applications*, 12(1):57–68, 2005. URL: https://rmets.onlinelibrary.wiley.com/doi/abs/10.1017/S1350482705001490, doi:10.1017/S1350482705001490.

[6] Nando Foppa, Andreas Stoffel, and Roland Meister. Synergy of in situ and space borne observation for snow depth mapping in the Swiss Alps. *International Journal of Applied Earth Observation and Geoinformation*, 9(3):294–310, August 2007. URL: http://www.sciencedirect.com/science/article/pii/S030324340600047X, doi:10.1016/j.jag.2006.10.001.

[7] Marc S. Adams, Yves Bhler, and Reinhard Fromm. Multitemporal Accuracy and Precision Assessment of Unmanned Aerial System Photogrammetry for Slope-Scale Snow Depth Maps in Alpine Terrain. *Pure and Applied Geophysics*, 175(9):3303–3324, September 2018. URL: https://doi.org/10.1007/s00024-017-1748-y, doi:10.1007/s00024-017-1748-y.

[8] Francesco Avanzi, Alberto Bianchi, Alberto Cina, Carlo De Michele, Paolo Maschio, Diana Pagliari, Daniele Passoni, Livio Pinto, Marco Piras, and Lorenzo Rossi. Centimetric Accuracy in Snow Depth Using Unmanned Aerial System Photogrammetry and a MultiStation. *Remote Sensing*, 10(5):765, May 2018. URL: https://www.mdpi.com/2072-4292/10/5/765, doi:10.3390/rs10050765.

[9] Jeffrey S. Deems, Thomas H. Painter, and David C. Finnegan. Lidar measurement of snow depth: a review. *Journal of Glaciology*, 59(215):467–479, 2013. URL: https://www.cambridge.org/core/journals/journal-of-glaciology/article/lidar-measurement-of-snow-depth-a-review/4419DF5C778946103080CB6187D434C0, doi:10.3189/2013JoG12J154.

[10] Government of Canada. Snow Mapping: Natural resources canada, 2015. [cit. 2018-6-25]. URL: http://www.nrcan.gc.ca/node/9561.

[11] Matias Takala, Kari Luojus, Jouni Pulliainen, Chris Derksen, Juha Lemmetyinen, Juha-Petri Krn, Jarkko Koskinen, and Bojan Bojkov. Estimating northern hemisphere snow water equivalent for climate research through assimilation of space-borne radiometer data and ground-based measurements. *Remote Sensing of Environment*, 115(12):3517–3529, December 2011. URL: http://www.sciencedirect.com/science/article/pii/S0034425711003166, doi:10.1016/j.rse.2011.08.014.

[12] Maziar Arjomandi, Shane Agostino, Matthew Mammone, Matthieu Nelson, and Tong Zhou. *Classification of Unmanned Aerial Vehicles*. Report for Mechanical Engineering class, University of Adelaide, Adelaide, Australia, 2006. URL: http://afrsweb.usda.gov/SP2UserFiles/Place/62351500/Unmanned.pdf.

[13] Jorge Torres-Sanchez, Francisca Lopez-Granados, Irene Borra-Serrano, and Jose Manuel Pena. Assessing UAV-collected image overlap influence on computation time and digital surface model accuracy in olive orchards. *Precision Agriculture*, 19:115–133, February 2017. URL: https://link.springer.com/article/10.1007/s11119-017-9502-0, doi:10.1007/s11119-017-9502-0.

[14] Tom Mikita, Pemysl Janata, and Peter Surov. Forest Stand Inventory Based on Combined Aerial and Terrestrial Close-Range Photogrammetry. *Forests*, 7(8):165, July 2016. URL: http://www.mdpi.com/1999-4907/7/8/165, doi:10.3390/f7080165.

[15] Mike R. James, Stuart Robson, and Mark W. Smith. 3-D uncertainty-based topographic change detection with structure-from-motion photogrammetry: precision maps for ground control and directly georeferenced surveys. *Earth Surface Processes and Landforms*, 42:1769–1788, January 2017. URL: http://onlinelibrary.wiley.com/doi/10.1002/esp.4125/abstract, doi:10.1002/esp.4125.

[16] R. Saleri, V. Cappellini, N. Nony, L. De Luca, M. Pierrot-Deseilligny, E. Bardiere, and M. Campi. UAV photogrammetry for archaeological survey: The Theaters area of Pompeii. In *Digital Heritage International Congress (DigitalHeritage), 2013*, volume 2, pages 497–502, October 2013. doi:10.1109/DigitalHeritage.2013.6744818.

[17] Tomas Lazna, Petr Gabrlik, Tomas Jilek, and Ludek Zalud. Cooperation between an unmanned aerial vehicle and an unmanned ground vehicle in highly accurate localization of gamma radiation hotspots. *International Journal of Advanced Robotic Systems*, 15(1):1–16, January 2018. URL: http://journals.sagepub.com/doi/10.1177/1729881417750787, doi:10.1177/1729881417750787.

[18] Yves Buhler, Marc S. Adams, Andreas Stoffel, and Ruedi Boesch. Photogrammetric reconstruction of homogenous snow surfaces in alpine terrain applying near-infrared UAS imagery. *International Journal of Remote Sensing*, 38(8-10):3135–3158, May 2017. URL: https://www.tandfonline.com/doi/full/10.1080/01431161.2016.1275060, doi:10.1080/01431161.2016.1275060.

[19] Y. Buhler, M. S. Adams, R. Bosch, and A. Stoffel. Mapping snow depth in alpine terrain with unmanned aerial systems (UASs): potential and limitations. *The Cryosphere*, 10(3):1075–1088, May 2016. URL: https://www.the-cryosphere.net/10/1075/2016/, doi:10.5194/tc-10-1075-2016.

[20] Emiliano Cimoli, Marco Marcer, Baptiste Vandecrux, Carl E. Bggild, Guy Williams, and Sebastian B. Simonsen. Application of Low-Cost UASs and Digital Photogrammetry for High-Resolution Snow Depth Mapping in the Arctic. *Remote Sensing*, 9(11):1144, November 2017. URL: http://www.mdpi.com/2072-4292/9/11/1144, doi:10.3390/rs9111144.

[21] Benjamin Vander Jagt, Arko Lucieer, Luke Wallace, Darren Turner, and Michael Durand. Snow Depth Retrieval with UAS Using Photogrammetric Techniques. *Geosciences*, 5(3):264–285, July 2015. URL: http://www.mdpi.com/2076-3263/5/3/264, doi:10.3390/geosciences5030264.

[22] H. Fazeli, F. Samadzadegan, and F. Dadrasjavan. Evaluating the Potential of RTK-UAV for Automatic Point Cloud Generation in 3d Rapid Mapping. In *ISPRS - International Archives of the Photogrammetry, Remote Sensing and Spatial Information Sciences*, volume XLI-B6, pages 221–226. Copernicus GmbH, June 2016. URL: http://www.int-arch-photogramm-remote-sens-spatial-inf-sci.net/XLI-B6/221/2016/, doi:10.5194/isprs-archives-XLI-B6-221-2016.

[23] C. F. Lo, M. L. Tsai, K. W. Chiang, C. H. Chu, G. J. Tsai, C. K. Cheng, N. El-Sheimy, and H. Ayman. The Direct Georeferencing Application and Performance Analysis of Uav Helicopter in Gcp-Free Area. In *The International Archives of Photogrammetry, Remote Sensing and Spatial Information Sciences; Gottingen*, volume XL, pages 151–157, Gottingen, Germany, 2015. Copernicus GmbH. URL: https://search.proquest.com/docview/1756968633/abstract/B238140DB5964263PQ/1, doi:http://dx.doi.org/10.5194/isprsarchives-XL-1-W4-151-2015.

[24] D. Turner, A. Lucieer, and L. Wallace. Direct Georeferencing of Ultrahigh-Resolution UAV Imagery. *IEEE Transactions on Geoscience and Remote Sensing*, 52(5):2738–2745, May 2014. URL: https://ieeexplore.ieee.org/document/6553130, doi:10.1109/TGRS.2013.2265295.

[25] A. Tan, K. Eccleston, I. Platt, I. Woodhead, W. Rack, and J. McCulloch. The design of a UAV mounted snow depth radar: Results of measurements on Antarctic sea ice. In *2017 IEEE Conference on Antenna Measurements Applications (CAMA)*, pages 316–319, December 2017. URL: https://ieeexplore.ieee.org/document/8273437, doi:10.1109/CAMA.2017.8273437.

[26] M. Hejcman, I. J. Dvorak, M. Kocianova, V. Pavlu, P. Nezerkova, O. Vitek, O. Rauch, and J. Jenik. Snow Depth and Vegetation Pattern in a Late-melting Snowbed Analyzed by GPS and GIS in the Giant Mountains, Czech Republic. *Arctic, Antarctic, and Alpine Research*, 38(1):90–98, February 2006. URL: https://www.tandfonline.com/doi/abs/

10.1657/1523-0430%282006%29038%5B0090%3ASDAVPI%5D2.0.CO%3B2, doi:10.1657/1523-0430(2006)038[0090:SDAVPI]2.0.CO;2.

[27] Jiri Dvorak. Odhalene tajemstvi Mapy republiky. *Krkonose – Jizerske hory*, 2005(9):4–8, September 2005. URL: http://krkonose.krnap.cz/apex/f?p=104:4:::NO:RP,4:P4_ID,P4_CP:2005-09-02,7.

[28] Igor Jan Dvorak, Milena Kocianova, Michal Hejcman, Vaclav Treml, and Jan Vanek. Linkage between Geo- and Biodiversity on Example of Snow-patch Map of Republic (Modry dul Valley). In *Geoecological problems of the Giant Mountains : proceedings of the international confeence*, volume 41, Szklarska Poreba, Poland, November 2003. The Krkonose Mountains National Park Administration. ISBN: 80-86418-36-7. URL: http://opera.krnap.cz/apex/f?p=103:8:::NO:8:P8_ROCNIK_ID,P8_CLANEK_ID,P8_CP:41,12,12.

[29] Jan Jenik. Geobotanicka studie lavinoveho pole v Modrem dole v Krkonosich. *Acta Universitatis Carolinae Biologica*, 5(1):49–95, 1958. ISSN: 0567-817X.

[30] Milos Vrba. Snow Accumulation in the Avalanche Region of the Modry Dul Valley in Krkonose Mountains. *Opera Corcontica*, 1(1):55–69, 1964. ISSN: 0139-925X.

[31] Igor Jan Dvorak, Milena Kocianova, and Lucie Pirkova. Example of utilization GPS and GIS technologies by study of cryoplanation terraces on the Lucni Mt. and Studnicni Mt. In *Geoecological problems of the Giant Mountains: proceedings of the international confeence*, volume 41, pages 18–24, Szklarska Poreba, Poland, November 2003. The Krkonose Mountains National Park Administration. ISBN: 80-86418-36-7.

[32] C. Eling, M. Wieland, C. Hess, L. Klingbeil, and H. Kuhlmann. Development and Evaluation of a UAV Based Mapping System for Remote Sensing and Surveying Applications. In *ISPRS - International Archives of the Photogrammetry, Remote Sensing and Spatial Information Sciences*, volume XL-1/W4, pages 233–239, August 2015. URL: http://www.int-arch-photogramm-remote-sens-spatial-inf-sci.net/XL-1-W4/233/2015/, doi:10.5194/isprsarchives-XL-1-W4-233-2015.

[33] M. Rieke, T. Foerster, J. Geipel, and T. Prinz. High-precision Positioning and Real-time Data Processing of UAV-Systems. *ISPRS - International Archives of the Photogrammetry, Remote Sensing and Spatial Information Sciences*, XXXVIII-1/C22:119–124, September 2012. URL: http://www.int-arch-photogramm-remote-sens-spatial-inf-sci.net/XXXVIII-1-C22/119/2011/, doi:10.5194/isprsarchives-XXXVIII-1-C22-119-2011.

[34] Petra Kocmanova and Ludek Zalud. Multispectral Stereoscopic Robotic Head Calibration and Evaluation. In *Modelling and Simulation for Autonomous Systems*, Lecture Notes in Computer Science, pages 173–184. Springer, Cham, April 2015. URL: https://link.springer.com/chapter/10.1007/978-3-319-22383-4_13, doi:10.1007/978-3-319-22383-4_13.

[35] Ludek Zalud, Petra Kocmanova, Frantisek Burian, Tomas Jilek, Petr Kalvoda, and Lukas Kopecny. Calibration and Evaluation of Parameters in A 3d Proximity Rotating Scanner. *Elektronika Ir Elektrotechnika*, 21(1):3–12, 2015. ISSN: 1392-1215. URL: http://eejournal.ktu.lt/index.php/elt/article/view/7299, doi:10.5755/j01.eee.21.1.7299.

[36] Petr Gabrlik, Anders la Cour-Harbo, Petra Kalvodova, Ludek Zalud, and Premysl Janata. Calibration and accuracy assessment in a direct georeferencing system for UAS photogrammetry. *International Journal of Remote Sensing*, 39(15-16):4931–4959, August 2018. URL: https://doi.org/10.1080/01431161.2018.1434331, doi:10.1080/01431161.2018.1434331.

[37] Jos Manuel Galvn Rangel, Gil Rito Gonalves, and Juan Antonio Prez. The impact of number and spatial distribution of GCPs on the positional accuracy of geospatial products derived from low-cost UASs. *International Journal of Remote Sensing*, 39(21):7154–7171, November 2018. URL: https://doi.org/10.1080/01431161.2018.1515508, doi:10.1080/01431161.2018.1515508.

[38] Dami Vericat, James Brasington, Joe Wheaton, and Michaela Cowie. Accuracy assessment of aerial photographs acquired using lighter-than-air blimps: low-cost tools for mapping river corridors. *River Research and Applications*, 25(8):985–1000, October 2009. URL: http://onlinelibrary.wiley.com/doi/10.1002/rra.1198/abstract, doi:10.1002/rra.1198.

[39] Karl Kraus. *Photogrammetry: Geometry from Images and Laser Scans*. Walter de Gruyter, 2007. ISBN: 978-3-11-019007-6.

[40] Tau M. Cabreira, Lisane B. Brisolara, and Paulo R. Ferreira Jr. Survey on Coverage Path Planning with Unmanned Aerial Vehicles. *Drones*, 3(1):4, March 2019. URL: https://www.mdpi.com/2504-446X/3/1/4, doi:10.3390/drones3010004.

[41] Richard Hartley and Andrew Zisserman. *Multiple View Geometry in Computer Vision*, volume 2nd ed. Cambridge University Press, Cambridge, 2003. ISBN: 978-0-521-54051-3. URL: https://www.cambridge.org/core/books/multiple-view-geometry-in-computer-vision/0B6F289C78B2B23F596CAA76D3D43F7A, doi:10.1017/CBO9780511811685.

[42] Richard Szeliski. *Computer Vision: Algorithms and Applications*. Texts in Computer Science. Springer, London, 2011. ISBN: 978-1-84882-934-3. URL: www.springer.com/gp/book/9781848829343.

[43] Michael Cramer. Performance of GPS/Inertial Solutions in Photogrammetry. In *Photogrammetric Week 01*, pages 49–62. Wichmann, Heidelberg, Germany, 2001. ISBN: 3-87907-359-7.

[44] P. Barry and R. Coakley. Field Accuracy Test of RPAS Photogrammetry. *ISPRS - International Archives of the Photogrammetry, Remote Sensing and Spatial Information Sciences*, XL-1/W2:27–31, August 2013. URL: http://www.int-arch-photogramm-remote-sens-spatial-inf-sci.net/XL-1-W2/27/2013/, doi:10.5194/isprsarchives-XL-1-W2-27-2013.

[45] Apostol Panayotov. Photogrammetric Accuracy of Real Time Kinematic Enabled Unmanned Aerial Vehicle Systems, October 2015. [cit. 2016-7-26]. URL: http://uas.usgs.gov/pdf/Reports/USGS_FINAL_REPORT_10212015.pdf.

[46] G. Verhoeven, M. Doneus, Ch. Briese, and F. Vermeulen. Mapping by matching: a computer vision-based approach to fast and accurate georeferencing of archaeological aerial photographs. *Journal of Archaeological Science*, 39(7):2060–2070, July 2012. URL: http://www.sciencedirect.com/science/article/pii/S0305440312000866, doi:10.1016/j.jas.2012.02.022.

[47] Tinku Acharya and Ajoy K. Ray. *Image Processing: Principles and Applications*. John Wiley & Sons, New Jersey, October 2005. ISBN: 978-0-471-74578-5.

[48] Jeng-Horng Chang, Kuo-Chin Fan, and Yang-Lang Chang. Multi-modal gray-level histogram modeling and decomposition. *Image and Vision Computing*, 20(3):203–216, March 2002. URL: http://www.sciencedirect.com/science/article/pii/S0262885601000956, doi:10.1016/S0262-8856(01)00095-6.

[49] N. Otsu. A Threshold Selection Method from Gray-Level Histograms. *IEEE Transactions on Systems, Man, and Cybernetics*, 9(1):62–66, January 1979. ISSN: 0018-9472. URL: https://ieeexplore.ieee.org/document/4310076, doi:10.1109/TSMC.1979.4310076.

[50] CUZK. CUZK - Geoportal, 2010. [cit. 2017-3-15]. URL: http://geoportal.cuzk.cz.

[51] W. S. B. Paterson. *Physics of Glaciers*. Butterworth-Heinemann, Oxford, Great Britain, third edition edition, 1994. ISBN: 978-0-7506-4742-7.

[52] N. Pfeifer, P. Glira, and C. Briese. Direct Georeferencing with on Board Navigation Components of Light Weight Uav Platforms. *ISPRS - International Archives of the Photogrammetry, Remote Sensing and Spatial Information Sciences*, 39B7:487–492, August 2012. URL: http://adsabs.harvard.edu/abs/2012ISPAr39B7..487P, doi:10.5194/isprsarchives-XXXIX-B7-487-2012.

[53] DJI. Phantom 4 RTK, 2019. [cit. 2019-3-1]. URL: https://www.dji.com/cz/phantom-4-rtk.

E. Using an Automated Heterogeneous Robotic System for Radiation Surveys

Outline

E.1. Introduction 160
E.2. Previous Work 166
E.3. Methods 167
E.4. Results 187
E.5. Discussion 199
E.6. Conclusion 205
Bibliography 213

Bibliographic Information

GABRLIK, Petr, Tomas LAZNA, Tomas JILEK, Petr SLADEK a Ludek ZALUD. Using an Automated Heterogeneous Robotic System for Radiation Surveys. Manuscript submitted for publication. Available from: `https://arxiv.org/abs/2006.16066`

Abstract

During missions involving radiation exposure, unmanned robotic platforms may embody a valuable tool, especially thanks to their capability of replacing human operators in certain tasks to eliminate the health risks associated with such an environment. Moreover, rapid development of the technology allows us to increase the automation rate, making the human operator generally less important within the entire process. This article presents a multi-robotic system designed for highly automated radiation mapping and source localization. Our approach includes a three-

phase procedure comprising sequential deployment of two diverse platforms, namely, an unmanned aircraft system (UAS) and an unmanned ground vehicle (UGV), to perform aerial photogrammetry, aerial radiation mapping, and terrestrial radiation mapping. The central idea is to produce a sparse dose rate map of the entire study site via the UAS and, subsequently, to perform detailed UGV-based mapping in limited radiation-contaminated regions. To accomplish these tasks, we designed numerous methods and data processing algorithms to facilitate, for example, digital elevation model (DEM)-based terrain following for the UAS, automatic selection of the regions of interest, obstacle map-based UGV trajectory planning, and source localization. The overall usability of the multi-robotic system was demonstrated by means of a one-day, authentic experiment, namely, a fictitious car accident including the loss of several radiation sources. The ability of the system to localize radiation hotspots and individual sources has been verified.

Author's Contribution

The author was responsible primarily for the tasks related to the aerial system, namely, the mission planning, aerial data acquisition, and relevant processing. Furthermore, he significantly contributed to surveying and analyzing related research, designing the method, and interpreting the results; the author is also credited with writing parts of the manuscript.

Author contribution: 30 %

Acknowledgement

The research was supported by European Regional Development Fund under the project Robotics 4 Industry 4.0 (reg. no. CZ.02.1.01/0.0/0.0/15_003/0000470). Further funding was provided via the National Center of Competence 1 program of the Technology Agency of the Czech Republic, under the project TN01000024/15 "Robotic operations in a hazardous environment and intelligent maintenance".

We thank NUVIA, a.s. for the instrumentation support, and the Air Force and Air Defence Military Technical Institute for the cooperation and provision of the UAS. We also acknowledge the consultation and assistance ensured by the University of Defence in Brno and the Fire Rescue Service of the South Moravian Region.

Version Notice

This is a submitted version of the manuscript; the fulltext is also available at the *arXiv* preprint server: `https://arxiv.org/abs/2006.16066`.

E.1. Introduction

Any radiation mapping, namely, measurement that provides knowledge of the distribution of ionizing radiation in space and time, finds use in various applications related to common activities. In this context, we can mention, for example, geophysical surveys, environmental monitoring of nuclear sites, post-disaster responses, localization of lost radiation sources, and everyday operation of nuclear power plants (NPP). Advantageously, such tasks are often carried out by utilizing unmanned robotic systems, mainly to protect human health. Robots are also capable of reducing the time and increasing the accuracy thanks to semi- or fully autonomous operation. Unmanned systems were employed in resolving the most severe nuclear accidents, including the Chernobyl disaster in 1986 and the Fukuschima Dai-ichi NPP accident in 2011, when personnel safety was of major importance. To improve the efficiency, different assets and techniques may be combined. Thus, for example, one of the oldest and most commonly applied radiation survey methods is helicopter-based airborne spectrometry. The technique is able to quickly cover square kilometres of land, but only at the expense of inadequate accuracy and very high cost. Ground systems, by comparison, may ensure superb accuracy, but their operational ranges are mostly limited to several hundreds of square meters, albeit these are explorable in a reasonably short period. Unmanned aircraft systems (UAS) offer adequate accuracy and survey range; therefore, to recognize the radiological situation in medium-sized areas, a multi-robot system seems to be a promising option.

E.1.1. Robot Deployment

The necessity to employ remotely operated machines in radiation exposure environments appeared with the expansion of nuclear power plants during the second half of the 20th century. Such machines were mostly used to perform inspection, manipulation, and maintenance; however, nuclear accidents shifted the interest towards the development of terrestrial mobile robots intended for disaster response applications [1]. These systems are principally applicable in reconnaissance, data gathering, and object manipulation; due to the complexity of the environment, remote control is generally employed as the most convenient approach. The main challenges and tasks characterizing the robot development stage involve radiation resistance and decontamination, environment traversability, and human-robot interaction [2, 3, 4]. A teleoperated robot was successfully utilized, for example, to inspect the damage after the Fukushima Daiichi Nuclear Power Plant accident in 2011 [5].

The deployment of robots with autonomous functions in post-disaster environ-

ments, especially inside or close to collapsed buildings, remains a major challenge; however, various other applications comprising radiation exposure are available. Ground robots enabling autonomous or semi-autonomous operation can be employed in radioactive waste storage facilities; areas affected by radiation as a result of an accident; uranium mines; and to localize uncontrolled radiation sources. [6] present a six-wheeled unmanned ground vehicle (UGV) specially designed for chemical, biological, radiological, nuclear, and explosive-related (CBRNE) tasks to solve some local navigation problems automatically. Laser scanner-based obstacle detection, together with a local navigation planning algorithm, is employed to find a collision-free path to the desired global positioning system (GPS) coordinate. Autonomous radiation mapping inside pre-defined polygons was discussed by [7]. In this case, precise navigation is enabled thanks to a real-time kinematics (RTK) GPS receiver. The data collected by a four-wheeled robot, equipped with an Na(I) radiation detector, are further utilized for particle swarm optimization-based source localization. The presented solution is, however, suitable for obstacle-free and non-complex areas only. The same UGV platform was deployed in a nuclear storage facility to perform inspections [8]. In such a GPS-denied environment, localization represents the essential task. Within the research, a light detection and ranging (LiDAR)-based simultaneous localization and mapping (SLAM) algorithm facilitates navigation inside an unknown territory, while the data from an RGB-depth (RGB-D) sensor allow the localization of storage cylinders. The discussed problems principally concern localization, navigation, and mapping, and they thus pose fundamental challenges to general terrestrial mobile robotics, including radiation-related tasks.

The rapid growth of UASs applications in the last decade has manifested itself also within the discussed area. Compared to ground robots, there is an evident advantage: the operational environment can be considered obstacle-free and terrain shape-independent while flying outside, at a safe distance from the ground. The fact enables quick radiation data collection over a large area. A UAS as a means to assist in solving nuclear emergency cases was proposed already in 2008, when a 100 kg unmanned helicopter equipped with an 8 kg scintillating detector was employed to estimate dose-rate distribution automatically [9]. A similarly sized unmanned system proved to be beneficial after the Fukushima Daiichi accident, where it provided information about radioactive cesium deposition inside a 5 km radius around the site [10, 11]. During the event, a detailed radiation map was compiled for the first time, considering the legal restrictions placed on manned aircraft operation in the area. Unlike ground robots, UASs operate at relevant distances from the source, typically situated at the ground level, and thus they require a sensitive radiation detection system, which embodies considerable payload. For this reason, micro-unmanned vehicles, a category popular thanks to its flexibility, low price, and safe operation, must

operate as close to the ground as possible to collect radiation data even with less sensitive detectors [12, 13]. Moreover, flying robots are applicable in producing digital elevation models (DEM) thanks to the LiDAR or photogrammetry techniques. The latter method was used by, for example, [14], resulting in a 3D surface model covered with a radiation data layer. [15] present a complex, multi-sensor system for both UASs and UGVs, which integrates various sensors and approaches to present radiation data in 3D and real time. The drawback of low-altitude mapping rests in potential collisions with obstacles, a problem discussed within [16], where the flight height during legacy uranium mines mapping was manually adjusted according to the vegetation height.

In most cases, contrary to terrestrial robots, aerial platforms are enabled by the obstacle-free environment to operate in an automatic manner, utilizing predefined GPS waypoints. However, state-of-the-art technologies have opened up the opportunity to deploy such platforms even indoor, in GPS-denied environments [17], and novel, lightweight radiation sensors may allow the use of even smaller UASs, possibly operated in swarms [18].

The advantages of both ground and aerial robots may be combined within a multi-robotic radiation mapping system. Such an idea was introduced by [19], whose unconventional solution comprises an unmanned helicopter carrying a small UGV. In this case, the UAS is intended to localize potential radiation-contaminated area via an onboard NaI detector and to produce a surface model by exploiting a stereovision system. A UGV, by contrast, is deployed with a winch system, facilitating comprehensive ground inspection and sample collection. The multi-robot system, however, was not subjected to thorough testing; thus, the vehicles' practical capabilities have not been confirmed sufficiently.

A promising approach rests in areal UAS-based mapping to facilitate gathering sparse radiation data within a large area and to produce a relevant map or a 3D model simultaneously, within a short time; these products then allow a UGV to be deployed at certain locations to perform detailed measurements, reconnaissance, and source localization. A similar method was introduced and verified by [20], whose aerial platform yielded a georeferenced orthophoto and a DEM, while also performing measurements with an onboard scintillation detector. A ground robot was then automatically navigated to locations exhibiting a maximal counts per second (CPS) value, and a classified map based on the orthophoto as well as the DEM enabled the choice of an energy-effective path; real-time obstacle avoidance was ensured by a LiDAR. The experiment verified the system's ability to localize an unknown source; however, the simple localization technique detects one maximum only, thus being unsuitable for multi-source or areal contamination scenarios. A promising concept to exploit different robotic platforms is described within the study

[21], where the key idea rests in using an aerial imagery-based DEM to divide the study site into sub-areas according to their suitability for individual robots. Ground radiation measurements are carried out in UGV-passable regions only; a UAS is employed in the rest of the target zone. Moreover, various algorithms exploiting radiation spectra are tested to find the sources, even in the real-time mode. Despite the advantages, the system has not yet been fully prepared to operate in real-world conditions without operator intervention.

E.1.2. Source Localization Methods

One of the common tasks addressed in the literature is the localization of radionuclides, which consists in identifying the parameters of the point sources present in the studied region of interest. The methods usually work with a series of discrete measurements that are assumed to have been taken at known positions; these measurements are performed by either a robotic platform or static sensors. In many cases, the methods are verified only by simulation.

The paper [22] utilizes maximum likelihood estimation (MLE) to find a single source, reducing the problem to two dimensions to acquire a coarse estimate that is improved by using a gradient method. In [23], the artificial potential field approach is adopted to localize one source, too; the attractive force is derived from the source's position estimated via the particle filter (PF) technique, while the repulsive one allows the robot to avoid obstacles. Another example of PF application can be found in [24]; the advantage of the interpretation proposed within the article consists in that it is not necessary to know the number of sources a priori. The algorithm works with a network of detectors measuring at multiple places simultaneously and is thus unsuitable for single-robot scenarios. An array of directional sensitive detectors can be employed for tracking a moving source as well [25]. Fast hotspot localization is characterized by [26], where the proposed algorithm dynamically adopts the UAS trajectory to move towards the hotspot. Two path planners, namely, HexTree and RIG-tree, are compared to demonstrate that the latter converges to the goal more quickly. Localization methods utilizing a UAS to collect data are examined in paper [27]. The authors introduce an algorithm based on recursive Bayesian estimation, showing the disadvantages: The selected approach locates merely one source, requiring knowledge of the nuclide and its activity a priori. Then, a method exploiting the radiation contour is outlined; the related analysis managed via the Hough transform is able to find multiple sources, whose contours may overlap. Surveying the region of interest with more UGVs enabling us to localize multiple sources is covered in [28]; the presented strategy prefers short paths having higher radiation intensity gradients. The parameter estimation utilizes the PF method with disperse resampling (to

prevent particle degeneration). The radiation field model includes previously found sources. The studied area is divided into cells to be visited, with a focus on those that potentially contain a source. A drawback of the method consists in ignoring potential obstacles.

Over the last decade, the localization algorithms have been studied by B. Ristic and his research group, who partially verified the methods by using real data acquired during a field test. The paper [29] compares three approaches to single source localization; the techniques are based on the MLE, the extended Kalman filter (EKF), and the unscented Kalman filter (UKF). The authors also analyzed the theoretical minimum estimation error with a Cramr-Rao bound, indicating that sequential Bayesian estimators (the EKF and the UKF) provide better performance than the MLE. The Bayesian approach is utilizable for a scenario including static detectors and a moving source. The models are fitted via partial Bayes factors, whose values are approximated by the Monte Carlo method denoted as importance sampling with progressive correction. The algorithm is capable of tracking up to four sources; however, their number needs to be known a priori [30]. The radiation field can be modeled as a weighted sum of 2D Gaussians, or a Gaussian mixture [31]. To find the Gaussians' parameters, two estimators, namely, a Gaussian and a Monte Carlo approximation, are employed, with the former yielding better results in both the simulations and the real data application. The algorithm is rather robust, and exact a priori knowledge of the number of sources is not required. In [32], up to three sources are localized, with binary and continuous genetic algorithms constituting alternative implementations of the MLE algorithm and negative-log likelihood being the objective function. The number of sources present in the area can be found by applying the minimum description length (MDL) principle. This method is based on minimizing the function that takes the parameter matrix as the input; this matrix needs to be estimated for every considered number of sources [33]. An information-driven search altering the measurement trajectory during the data acquisition process is outlined in the article [34]. The number of sources is assumed to be unknown; the source are tracked by one or more mobile observers, and their parameters are estimated via a multi-target, track-before-detect particle filter. The particles are initialized with different amounts of sources; at the end of each update step, some of the particles acquire a source while some others lose it. Particle degeneration is prevented via the progressive correction technique. The observer motion control is addressed as a partially observable Markov decision process; a control vector to maximize the estimation of the reward function is selected. The simulations have shown that the information-driven search yields results more accurate than those obtained from the survey along a pre-defined uniform trajectory. The method was also verified by using field data.

E.1.3. Possible Applications

Potential missions for multi-robot systems involve several applications that beneficially combine quick, flexible operation and a large range of aerial assets with the versatility and better radiation measurement conditions ensured by terrestrial robots. A combination of UASs and UGVs provides a synergy of benefits for radiological mapping, bringing both global information from the territory and accurate dosimetry or spectroscopy data from the points of interest. Nuclear safety, radiation and environmental protection, remediation, and decommissioning then embody some of the target fields. Regarding UGVs, a major advantage rests in the possibility of applying semiconductor high-purity germanium (HPGe) detectors with high resolution (radionuclide identification) capabilities; in UASs, conversely, the resolution is still limited by vibrations and the microphonic effect [35], and the onboard heavy sensitive detectors restrain the operation time. In this context, a UGV is significantly more flexible and can carry diverse detection systems, including continuously working dose rate meters with high dynamic range coverages, accurate solid-state spectrometers, neutron detectors and beta contamination meters for occasional static measurements, and alpha contamination indicators. The devices mounted on a UGV may support the monitoring with measurements at a height of 1 m above the ground, which corresponds to the dosimetry standard for radiological mapping. In general terms, robotic systems functionally extend the set of regular nuclear monitoring options, where static station networks embody the most common approach, despite providing the evidence at several discrete points only. The area coverage could be improved by autonomous inspection tasks to enhance the applicability of the existing scenarios.

Comprehensive radiation surveys necessarily involve detailed, laboratory-based analyses of the samples, and the use of UASs/UGVs can improve the applied sampling strategy. Moreover, a ground robot is capable of assisting in remote sample collection if equipped appropriately. Importantly, UASs and UGVs also contribute to the remediation of legacy sites, which embodies a topical issue concerning diverse inactive locations that used to host nuclear technologies. In some cases, small, heavy-duty wireless monitoring stations are distributed across the investigated sites to provide data in a long-term horizon; this task can be also performed by ground-based assets at suitable points indicated via relevant aerial measurement. Finally, the localization of the lost or uncontrolled radiation sources discussed within this article constitutes a use case for robotic systems.

E.1.4. Aims and Objectives

The paper aims to present the options and perspectives of using a multi-robot system to perform highly automated radiation mapping and source localization in an outdoor environment. The illustrative experiment, a car accident involving the loss of several sources, was designed to resemble a real-world scenario as much as possible. Moreover, to increase the authenticity, the entire field work comprised several UAS flights, UGV deployments, and data processing cycles within a single day.

The initial part of the article, namely, the 'Previous work' section, briefly discusses our long-term research activities within this domain. In the next chapter, 'Methods', we provide an overview of the proposed mapping process and experiment setup, followed by a thorough description of the applied equipment and designed algorithms. The acquired data and processing outputs of the radiation mapping and source localization tasks are presented within the 'Results' section, in a chronological order corresponding to reality. Finally, the 'Discussion' chapter compares the achieved results with both our originally planned targets and the outcomes outlined in the referenced literature. As this paper constitutes a part of a comprehensive research concept, we also address tasks to be potentially solved in the future.

E.2. Previous Work

CBRNE robotics and multi-robot systems have for almost two decades embodied the research focus of the Robotics and AI group headed by Prof. Zalud at Brno University of Technology. The Orpheus reconnaissance robot family [36], a central project pursuing the development of four-wheel skid-driving portable CBRNE robots (Figure E.1), is being continuously refined and has been employed in various experiments and missions, such as those devised to determine water contamination [37]. In the context of the topic, we have examined automatic radiation mapping thanks to the robot's built-in RTK global navigation satellite system (GNSS) -based navigation system, establishing that a UGV is capable of substituting for human-performed measurements effectively, more accurately, and without safety risks [38]. However, the approach was not subjected to comprehensive testing, including, for example, obstacle-accommodated environment.

To extend the usability of the terrestrial platforms, we developed a multi-sensor system for UAS photogrammetry to assemble high-resolution orthophotos and surface models [39]. Benefiting from the capability of operating without ground georeferencing targets, the solution is perfectly convenient for radiation-related tasks; the products are applicable in UGV trajectory planning under difficult conditions. Moreover, our simulations suggest that the surface model may find use in aerial ra-

Figure E.1.: The four-wheel Orpheus robot family and other platforms of the heterogeneous reconnaissance mobile robot system ATEROS.

diation mapping, too [40]. In radiation detection system-equipped UASs, flying at a constant altitude above ground level (AGL) collects more consistent data compared to flying at a constant mean sea level (MSL) altitude, thus making source localization more accurate. All the above-mentioned equipment, methods, and experience enabled us to compose a comprehensive multi-platform system for automatic radiation source search. A first attempt in this field was published previously [41]; however, numerous aspects and issues still remain to be addressed to increase the reliability, credibility, robot interoperability, and overall real-world usability, i.e., the main topics dealt with in this research.

E.3. Methods

E.3.1. Experiment Setup

The method for multi-robot radiation mapping and source localization presented in the paper was evaluated by utilizing a fictitious accident at a site in close proximity to the campus of Brno University of Technology, Brno, the Czech Republic, in August 2018 (Figure E.2). The goal was to arrange authentic conditions corresponding to a scenario with several gamma radiation sources lost in a certain area after a car accident. Regarding the parameters known to the tested method, the exact location, number, and activity were undefined; we can nevertheless assume that the sources belong to the class utilized in the civil sector, and the application options thus involve, for example, the calibration of devices for nondestructive testing, flow meters, level measurement systems, nuclear densometers, and density well-logging probes.

The experiment site occupies an area of 20,000 m^2, comprising mainly grassy terrain with various man-made objects such as a road, paths, climbing walls, and several

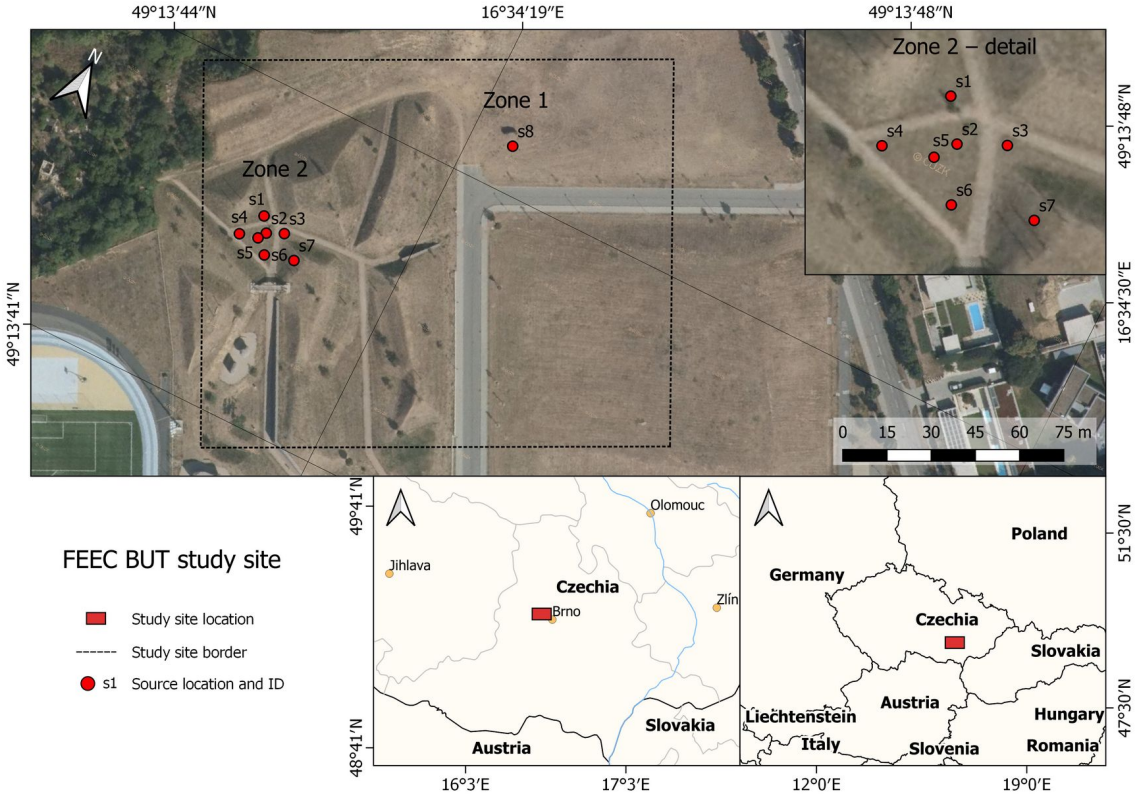

Figure E.2.: The location of the study site, and the spatial distribution of the radiation sources (orthophoto courtesy of the State Administration of Land Surveying and Cadastre [42]. FEEC BUT: Faculty of Electrical Engineering and Communication at Brno University of Technology

vehicles involved in the car accident. While one half of the location is relatively flat ($< 4°$), the other includes hills with slopes up to 30° and other UGV-impassable zones.

Within the experiment site, we planted eight gamma radiation sources, namely, Co-60 and Cs-137 isotopes exhibiting the activity of 2.9–123.8 MBq (Table E.1). As is evident from Figure E.2, the sources are scattered inside two locations: Zone 1, containing a single, high-activity source, and zone 2, which includes seven sources representing the areal contamination. To ensure safety, the relevant area was closed to common access during the experiment.

E.3.2. Method Overview

Robot-based environmental mapping in an outdoor environment generally embodies a challenging task due to the largely variable conditions that may be encountered, especially in terms of the terrain, vegetation diversity, and weather conditions. Moreover, further special requirements may arise as regards the measuring equipment and

Table E.1.: Radiation sources used in the experiment.

Source	Zone	Isotope	Activity [MBq]
s1	2	Co-60	2.85
s2	2	Cs-137	7.53
s3	2	Co-60	2.95
s4	2	Cs-137	7.53
s5	2	Cs-137	79.82
s6	2	Co-60	24.56
s7	2	Co-60	24.76
s8	1	Co-60	123.78

time constraints. In this context, choosing the proper robotic platform is crucial to achieve the desired results.

To perform the radiation mapping and source localization tasks, we designed a method operating two different robots, namely, a hexacopter UAS and a four-wheel, skid-steering UGV. The former platform, described in detail within section E.3.3, enables us to cover a large area within a reasonable time, regardless of the terrain nature; however, the distance from the surface may limit the applicability of some sensors. Advantageously, at the initial stages of the procedure, the vehicle is employed to carry out the aerial photogrammetry and sparse radiation mapping. The latter platform (section E.3.4) is suitable for the reconnaissance and mapping of small areas (hundreds of square meters) only, due to its low operation speed; another limiting factor rests in the reduced terrain negotiability, depending on the slope pattern. Thus, the UGV finds use in precise radiation mapping and source localization, namely, at the final stages.

As is evident from Figure E.3, our approach comprises the following three phases: aerial photogrammetry, aerial radiation mapping, and terrestrial radiation mapping. The first phase aims to create the actual orthophoto and 3D model of the area, meaning products to be utilized later for the trajectory planning and to help operators orientate themselves in the unknown environment. The initial step, namely, defining the area of interest, must be executed by a user considering the current situation; however, the following operations, such as the actual flight, are already fully automatic, with the UAS's trajectory designed according to the photogrammetric requirements. Yet, from the general perspective, the entire operation must still be supervised by a pilot, especially due to safety and legal concerns. The outcomes of the photogrammetric processing (section E.3.5) and the first phase as a whole

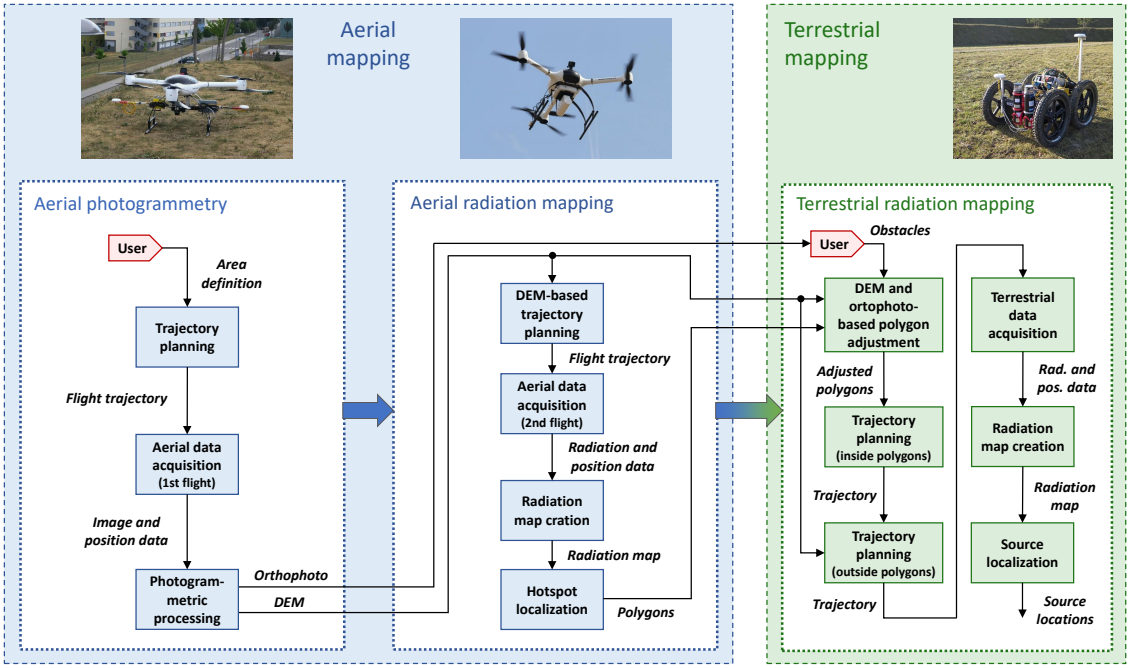

Figure E.3.: The sequence of the operations that form the entire process. The actual mapping comprises the aerial (blue) and terrestrial (green) branches; the user interventions are highlighted in red. DEM: digital elevation model.

embody a georeferenced orthophoto and a DEM.

The second phase is intended to localize potential radiation hotspots by means of aerial radiation mapping of the entire area. In order to obtain credible results, the UAS trajectory design encompasses the DEM acquired within the previous phase to allow us to operate at a constant height above ground level (AGL). This procedure is described thoroughly in section E.3.6. Once the sparse radiation map is available, our algorithm selects the sub-areas that exhibit increased radiation levels (section E.3.7).

The goal of the final phase consists in building detailed radiation maps of the hotspots by using the UGV; this step facilitates the potential localization of individual sources. To perform such a task, we must consider the degree limited terrain negotiability limitation in the relevant platform, and thus the selected regions are adjusted via both the DEM-based obstacle map and the orthophoto, where other possible obstacles and impassable locations are selected by the user. The aforementioned mechanisms are addressed in section E.3.7. The UGV trajectory planning problem can then be divided into two tasks, namely, covering the pre-specified polygons (hotspots) and executing A*-based robot navigation between the polygons (section E.3.8). The collected data are employed to generate a detailed radiation

map and to allow the source localization. This stage, described in section E.3.9, involves utilizing the least-square method to estimate both the precise location of the individual sources and their approximate activity.

E.3.3. Unmanned Aerial System

In our method, the UAS embodies a platform to ensure aerial data acquisition during the initial stage of the mapping process. The system must be capable of carrying various sensors (to perform photogrammetry and ionizing radiation measurement) and flying according to the preprogrammed trajectories. For these tasks, UASs were already employed previously. The discussed approach to aerial photogrammetry is one of the most common applications of UASs in the scientific domain and the commercial sector; the technique finds use in, for example, agriculture, to monitor crop height [43, 44]; forestry, to collect tree inventory data [45]; geodesy, to investigate topographic changes [46]; and archaeology, to deliver spatial site reconstruction [47]. As described in the Introduction, unmanned aircraft have also been deployed for ionizing radiation mapping. At present, there are science-based efforts to utilize the systems in legacy mine mapping, nuclear waste storage inspection, and disaster response scenarios; compared to aerial photogrammetry, however, these domains offer only marginal options to use UASs. The choice of a suitable unmanned platform depends on multiple factors, of which the most substantial ones are the payload capacity and operation range. UASs with rotary wings (helicopters and multicopters) provide excellent payload capacities, with another significant advantage being the ability to operate at low speeds and to hover. Conversely, fixed-wing unmanned aircraft of similar size and weight exhibit better ranges and endurances, but the load capability is typically lower.

The proposed mapping and search method involves low-altitude radiation measurement, which requires high maneuverability and flying at low speeds. For this reason, and also due to the equipment weight, we chose the BRUS rotary-wing UAS (Figure. E.4), a six-rotor aircraft developed and produced by the Military Technical Institute of the Czech Republic [48]. The UAS was designed to perform various tasks, such as those allowing the reconnaissance, monitoring, and rescue missions during natural disasters. The device's in-house control system supports both manual and waypoint-based automatic flight, whereas the automatic mode offers wide configurability. The payload mounting system at the bottom of the fuselage facilitates carrying equipment of up to 4 kg in weight, and the standard endurance is 45 minutes; more parameters are indicated in Table E.2.

At the initial stage of the actual mapping, the UAS is fitted with a custom-built multi-sensor system for aerial photogrammetry, illustrated in Figure E.4a. This

(a) (b)

Figure E.4.: The BRUS UAS configured for the experiment: with a multi-sensor system to perform the photogrammetry (a), and carrying a gamma radiation detection setup (b). UAS: unmanned aircraft system

Table E.2.: The parameters of the BRUS and Orpheus-X3 unmanned platforms. UAS: unmanned aircraft system; UGV: unmanned ground vehicle.

Parameter	UAS	UGV
Dimensions	1.2 × 1.2 × 0.5 m	1.0 × 0.6 × 0.4 m
Weight	4.5 kg	51 kg
Max payload weight	4 kg	30 kg
Standard operational time	45 mins	120 mins
Drive type	multi-rotor	wheel, differential
Operating speed	2 – 5 m/s	0.6 m/s
Max speed	16.7 m/s	4.2 m/s

setup enables us to create georeferenced photogrammetric products, namely, an orthophoto or a DEM, without requiring ground control points (GCPs). The sensors are a consumer-grade Sony Alpha A7 digital camera, a Trimble BD982 dual-antenna GNSS receiver supporting the RTK technology and vector measurement, and an SBG Ellipse-E inertial navigation system (INS). The last-named component performs real-time data fusion to estimate the position and orientation; thanks to precise time synchronization, the exterior orientation parameters of each captured image are collected. To attain high positioning accuracy, a base station transmitting real-time kinematic correction data must be deployed; normally, the station is positioned close to the study site. The system weighs 2.8 kg and is completely independent from the applied UAS platform. The setup was previously described in more detail within article [39] and subsequently found use in, for example, UAS-based aerial snow depth mapping [49]. The existing results indicate that the system

is capable of reaching centimeter-level object accuracy. Even though GCP-free UAS photogrammetry is markedly less common than the approach that relies on ground targets, the concept was already utilized in previous research [50, 51, 52].

The second phase of the mapping cycle comprises ionizing radiation measurement; for this purpose, the UAS is fitted with a NUVIA DRONES-G radiation detection system (Figure E.4b). The setup was specially designed for light airborne radiation monitoring via UASs, and it consists of two modules: a base one and a detection one. The former module contains a processing unit, a data storage device, an RF datalink, a GNSS module, a laser altimeter, a battery source, and other relevant electronic components. The latter module is equipped with a 2×2" NaI(Tl) detector operating in the 50 keV – 3 MeV energy range, allowing us to measure the dose rates in the range of 50 nGy – 100 μGy. The one-second radiation data (spectra recordings) are georeferenced and saved, enabling later analysis. The entire detection system weighs 3 kg and, similarly to the photogrammetry equipment, is independent of the applied airborne platform.

E.3.4. Unmanned Ground Vehicle

An Orpheus-X4 UGV is utilized as the experimentation platform. The robot is a mid-size four-wheeled UGV developed by the Robotics and Artificial Intelligence Group at the Department of Control and Instrumentation, FEEC BUT. The Orpheus-X4 is well-suited for outdoor environments thanks to its tank-like differential drive with four independent actuators; conversely, this type of drive is not convenient for specific types of indoor obstacles, such as stairs. However, we can assume that a radiation accident area resembles a post-disaster site; moreover, the current navigation module is based on the GNSS technology, which requires outdoor operation, and the Orpheus-X4 structure suits the needs of radiation mapping missions. Besides the drive, the robot is equipped with a camera head carried by a 3-degrees of freedom (DOF) manipulator. The head finds use in remote control of the UGV by an operator. The robot contains two computers to run various control algorithms; its parameters are summarized in Table E.2. A more detailed description of Orpheus robots is proposed in articles [53] and [54].

The Orpheus-X4 offers automatic navigation along the planned trajectory, which is represented by a sequence of waypoints. The navigation is designed and implemented at our department, thus allowing fine-tuning for a specific mobile robot and application. The emphasis on parameterizability during the design and implementation stages enables the configuration to be represented by the chassis coefficients and required motion characteristics. The attainable accuracy of the Orpheus-X4 automatic navigation relies on self-localization accuracy. In the case of a good and

stable RTK solution, it is possible to reach 3 cm (1σ) in stable flat surfaces [55]; however, the accuracy is generally much worse in unstable traction terrains.

The self-localization of a mobile robot employs a GNSS, an INS, and wheel odometry. The system relies mainly on the RTK GNSS to solve the 2D position and heading. The dead reckoning solutions from the micro-electro-mechanical systems (MEMS) -based INS and wheel odometry are used to bypass insufficient GNSS solutions. The short-term GNSS position and heading outages in cases of dynamic robot motion are bypassed by the INS. Long-term GNSS outages during low motion stages are bridged by a wheel odometry-based solution that employs INS heading. We use a Trimble BD982 GNSS receiver in a dual antenna setup to obtain the RTK solution of the position and heading. Our configuration exploits dual-frequency tracking of the GPS, GLONASS, and Galileo signals to achieve reasonable position accuracy (better than 10 cm). All data are updated at 50 Hz. The correction data for the RTK processing are typically obtained from our own local GNSS base station, which utilizes the same BD982 module as the rover. Although we need not know the accurate position of the base station antenna, it is beneficial to use such a position to synchronize our work with other systems that do not employ the base station with a mission-specific coordinate system. Alternatively, it is possible to use data from commercial permanent GNSS stations or networks accessible via global system for mobile communications (GSM) network connection.

To perform the robotic mapping of gamma radiation, scintillation detectors seem to make a trade-off for the desired features. The detectors provide a high density and volume, thus being beneficial in maximizing the probability of interaction with gamma rays for good sensitivity. To detect a radiation source from a greater distance, the sensitivity embodies a crucial parameter. Moreover, common inorganic scintillators possess spectrometric abilities; knowledge of the spectra enables us to identify different radionuclides and can facilitate separating useful information from the radiation background. To develop the mapping system, we chose the combination of a $2\times2''$ NaI(Tl) scintillator and a photomultiplier tube, mainly thanks to its accessibility, conventionality, and previous experience. The detection system exhibits an energy resolution of more than 7 % at 662 keV [56]. The detected values are read out by a NUVIA MCB3 multichannel analyzer comprising a high voltage source, a preamplifier, an analog-to-digital converter, a processing unit, and an Ethernet communication interface. The analyzer provides a resolution of up to 4,096 channels and is usually calibrated to the 0.03–3 MeV energy range. If not stated otherwise, the presented algorithms work with the total count (TC) value, i.e., the sum of counts in all channels.

In the applied system, the UGV is equipped with a pair of NaI(Tl) detectors. An advantage of utilizing multiple detectors consists in higher sensitivity of the measure-

Figure E.5.: The Orpheus-X4 UGV equipped with a GNSS receiver and a pair of NaI(Tl) radiation detectors. UGV: unmanned ground vehicle; GNSS: global navigation satellite system.

ment system and better cumulative statistical attributes of the measurements. Even though the detectors influence each other in terms of shading, they still embody two statistically independent sources of information regarding the stochastic nature of radioactive decay. A cumulative spectrum provides information with a statistical significance higher than that of single spectra [57]. The Orpheus-X4 carrying all the presented equipment is shown in Figure E.5.

E.3.5. Aerial Photogrammetry

Aerial photogrammetry embodies the first phase of the mapping method, and its goal is to map an unknown area, yielding an orthophoto and a DEM. These products are of vital importance for the next stages of the technique, trajectory planning to support the UAS- and UGV-based radiation mapping in particular. As our experiment simulates a situation where the relevant area is potentially contaminated and dangerous for humans, the aerial mapping process may not require prior field work. Thus, we employed a custom-built multi-sensor system for aerial photogrammetry to facilitate direct georeferencing (section E.3.3).

The process starts with trajectory planning across the user-defined region. We utilize the common parallel strips flight pattern known from both manned and unmanned aerial photogrammetry [58, 59], as shown in Figure E.6. The trajectory and data acquisition parameters, such as the flying altitude and distance between the strips and images, must satisfy certain photogrammetric rules, including the desired forward and side image overlaps, ground resolution, and altitude restrictions. The trajectory planning also depends on the intrinsic parameters of the applied camera. The relevant values applied in the presented experiment are summarized in

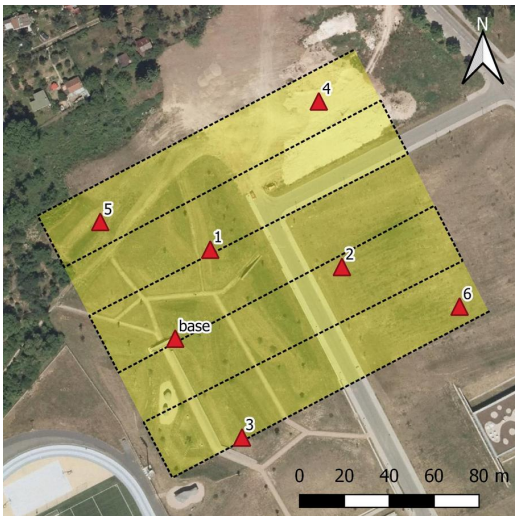

Figure E.6.: The UAS trajectory planned for the photogrammetry flight. The yellow rectangle represents the study site (having an area of 20,000 m^2), and the red triangles indicate the positions of the ground targets. UAS: unmanned aircraft system.

Table E.3. In general terms, the image overlapping rate reaches approximately 90% to achieve high object accuracy, and the ground resolution is selected to range within the centimeter level to capture even the smallest details relative to the dimensions of the UGV which will carry out the terrestrial mapping.

The photogrammetric dataset comprises two types of data: images and georeferencing-related information (positions, orientations, and accuracies). These data are processed with Agisoft Photoscan Professional (version 1.4.2), a comprehensive software package to execute all the photogrammetric processing stages. The workflow starts with the align phase, where the exterior and interior orientations of the camera [60] are estimated based on the feature points detected in the overlapping images. Further, the locations of the feature points are determined via the structure-from-motion procedure, resulting in a sparse point cloud [61]. Within the following step, a dense point cloud can be generated by means of multi-view stereo (MVS) reconstruction. As the operation is performed at the level of pixels, even small details are reconstructed, yielding a point cloud containing millions of points. This product is then employed to generate the orthophoto and DEM.

Photoscan can transform the camera poses and points into a geographic coordinate system in two ways: via data measured by onboard sensors, a method known as direct georeferencing, or with GCPs, namely, the indirect georeferencing approach. In general terms, the latter technique is utilized more frequently, as it allows us to reach high georeferencing accuracy even with inexpensive, consumer-grade onboard sensors; moreover, the results are reliable, and inter-sensor calibration is not required

Table E.3.: The parameters of the flight trajectories and data acquisition for both flights (one enabling the photogrammetry and the other facilitating the radiation mapping). ATOP: above take-off point; AGL: above ground level; ISO: international organization for standardization.

Parameter	1st flight	2nd flight
Number of strips	6	14
Strip length	160 m	140 m
Distance between strips	26 m	10 m
Flying altitude	60 m ATOP	15 m AGL
Flying speed	5 m/s	2 m/s
Sampling period	2 s	1 s
Base	10 m	2 m
Photo scale	1:5,200	—
Forward overlap	92 %	—
Side overlap	84 %	—
Image footprint	190 × 125 m	—
Ground resolution	3.1 cm/px	—
Shutter speed	1/1,000 s	—
Aperture	5.6	—
ISO	Auto (100–400)	—

[62, 63]. The indispensability of well-distributed ground targets, however, makes the method unsuitable for CBRNE tasks. The direct technique, conversely, relies on onboard sensors only, leading to higher requirements on payload capacity and the calibration process; in this context, it should also be stressed that the georeferencing results are typically less accurate, as indicated in relevant studies. [64, 65, 39].

Although we utilized a direct georeferencing system, six ground targets were deployed in the area prior to the experiment (Figure E.6). This step enabled us to determine the accuracy of the photogrammetric products, i.e., the orthophoto and DEM, which will be necessary during the subsequent stages of the radiation mapping method. Moreover, the targets would allow us to perform the georeferencing even under a failure of the onboard GNSS/INS. We used 20 cm-sized, squared, black and white patterned paper targets having clearly defined centers. All the targets were glued onto a solid support and fixed to the ground with iron nails. The position of every single target was acquired by a Trimble BX982 RTK GNSS receiver obtaining the correction data from CZEPOS (Czech provider of correction data).

With the same equipment, we determined the position of the GNSS base station, indicated in Figure E.6; the station provided the correction data for the GNSS receiver aboard the UAS (and the UGV), allowing us to carry out the mission even when the correction data provider was not available.

E.3.6. Aerial Radiation Mapping

Aerial radiation mapping, described within the diagram in Figure E.3, embodies the second phase of the mapping method. The procedure aims to create a sparse ionizing radiation map of the entire study site to localize possible hotspots to be mapped with the UGV. Without any prior knowledge of the hotspots, and lacking a detection system with directional sensitivity, the straightforward flight strategy comprises parallel survey lines, similarly to the previous photogrammetry flight. The main difference rests in the setting of major parameters, including flight altitude, distance between strips, and speed. As the dose rate decreases with the square of the distance, the AGL altitude must be as low as possible to detect even weak sources. In practice, the minimum flight altitude is always limited by the actual precision of the UAS navigation system. Regarding the terrain shape and obstacles, the lowest possible value for the applied UAS equals 15 m AGL. However, the distance d between the source and the detector is, in addition to the vertical component h, formed also by the horizontal distance. The condition $d = h$ applies when the UAS is directly above the source, and the formula (E.1) describes the marginal situation when the source is located exactly between the survey lines being A meters apart (Figure E.7a).

$$d = \sqrt{\left(\frac{A}{2}\right)^2 + h^2} \tag{E.1}$$

The distance A must be chosen with respect to the following factors, attributes, and scenarios: A low value yields high spatial resolution and the possibility of localizing a hotspot in a precise manner, even though it can result in a very long flight trajectory (operation time) and the related necessity to replace the battery frequently. Contrariwise, a high distance between the flight lines is time-saving but can negatively affect the ability to detect low-intensity sources. Considering all the circumstances, the value $A = 10$ m constitutes optimal setting in our experiment, namely, the UAS can cover the relevant area without battery replacement, and the maximum possible distance between the source and the detector (d) is only 5 % greater than the flight height. In this case, the intensity decreases by the acceptable value of 11 % against the $d = h$ condition. The resulting trajectory comprises 14 parallel lines and is approximately 2 kilometers long (Table E.3 and Figure E.7b).

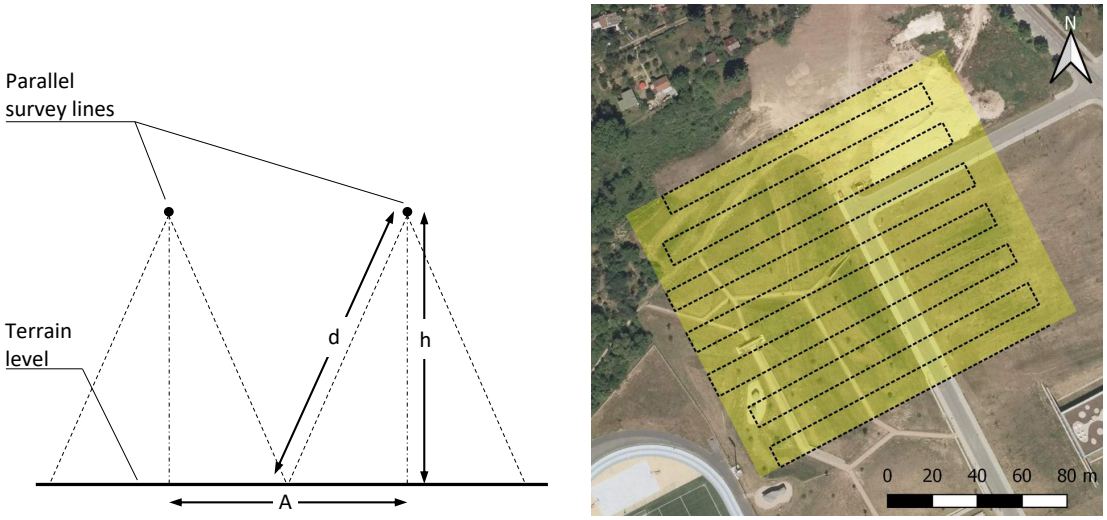

(a) (b)

Figure E.7.: The basic parameters of the UAS trajectory for the radiation mapping procedure (a). The UAS trajectory planned for the radiation measurement flight (the yellow rectangle represents the study site) (b).

In UAS-based radiation mapping, the common approach involves operating at a constant MSL altitude [20, 16], an option applicable at locations that lack significant height differences. As indicated within one of our previous papers [40], major variations in the flight height above ground level produce non-homogeneous and unreliable data; thus, a means to secure a constant AGL height is essential in hilly sites. The proposed method utilizes a photogrammetry-based DEM, the output of the initial UAS flight (section E.3.5), to adjust the radiation mapping trajectory (Algorithm 1). The vertical components of the trajectory are computed as the sum of the DEM heights at the given waypoints and the desired AGL flight height h. To follow the terrain precisely, the trajectory is split into smaller segments having a size s, whose value is chosen with respect to the character of the terrain. Such a trajectory, however, may contain multiple height changes; this variability, then, is not energy-efficient and can increase the operation time. To avoid the behavior, we apply a low-pass filter to obtain a smooth trajectory and to prevent sudden UAS altitude variations. The principle is illustrated in Figure E.8. A drawback to the approach rests in the extensive amount of waypoints to be stored in the UAS memory. Within the presented experiment, we use $s = 10$ m, the appropriate distance for the discussed study site, leading to approximately 200 waypoints.

The last parameter associated with the aerial data acquisition is flight speed. As the UAS is intended to fly close to the terrain and to change altitude markedly, we apply the rather low horizontal speed of 2 m/s. Considering the detection system

Algorithm 1 The DEM-based trajectory adjustment.

Input: The horizontal trajectory T, digital elevation model D, AGL height h, and segment size s.

Output: The terrain-adjusted spatial trajectory T_t.

1: **Trajectory segmentation:** Splitting the lines defined by the points T into smaller segments having a maximum size s to obtain dense trajectory points T_s.

2: **Find the corresponding DEM points:** For every point defined in T_s find the nearest horizontal point of D.

3: **Compose the 3D trajectory:** Use the height values of the obtained DEM points as the height coordinates for the trajectory T_s.

4: **Compute a new altitude:** Increase the altitude of every point in T_s by the height h.

5: **Filter the trajectory:** Apply the low-pass filter to the T_s point sequence to obtain the filtered trajectory T_t.

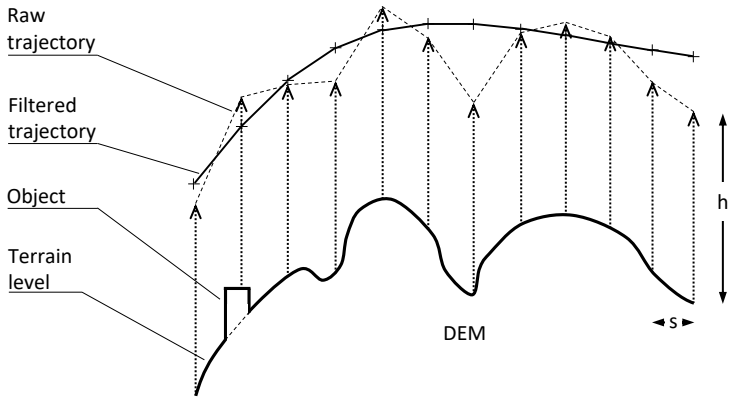

Figure E.8.: The principle of the terrain-based trajectory adjustment. DEM: digital elevation model.

sampling period of 1 s, we obtain the sampling distance of 2 m .

E.3.7. Automatic Selection of the Terrestrial Mapping Areas

Aerial radiation mapping yields a set of scattered data points, each comprising the coordinates and spectrum acquired by the detection system during a measurement period. The data points are not very suitable for visualization and further processing of the map, namely, finding hotspots to be applied in the terrestrial survey. Thus, calculating the radiation intensity (dose rate) at points in a regular grid is required; this step can be carried out through the Delaunay triangulation [66]. The density of the data points in the axis parallel to the flight direction is approximately five times higher than that in the perpendicular axis, due to the chosen flight speed, sampling

period, and distance between the strips. Regrettably, such point distribution is not convenient for the interpolation, and each four subsequent spectra are thus summed and assigned to a single position in order to achieve an even distance of points in both axes. The statistics of the cumulative spectra are significantly better, although information on areal distribution of the dose rate is partially lost; this is, however, not a cardinal issue in the given case, as more detailed terrestrial measurement follows.

Once the interpolated radiation map is available, the operator can manually mark the hotspots, or regions of interest (ROIs); this step is nevertheless best performed automatically. A possible approach is to employ a two-dimensional peak detector; such an option is unsuitable for the general case, as the data do not always represent a clear sharp peak, e.g., if

- the peak comprises contributions by multiple radiation sources;
- the magnitude of the peak is comparable to the radiation background, as the data are very noisy due to statistical laws;
- the magnitude of the peak exceeds the capacity of the detector, and the dead time is over 50 %, causing the data to exhibit a rapid decrease.

The first two cases can be certainly expected during aerial radiation mapping; thus, we adopt a different method. The basic idea is as follows: By eliminating the radiation background, a connected set will be left for each significant peak. The problem is in identifying the background, as it not only depends on the geographical location but, generally, can be increased by strong artificial sources. The unnecessary data may be assumed to lie within the three-sigma band around their mean value. To find such an *a*daptive threshold, the statistical parameters of the background must be estimated. An analytical solution to the described problem is not feasible, because we cannot anticipate the number of radiation sources or their activity relative to natural radionuclides and cosmic rays. Instead, an empirical threshold T_{bg} is derived from the statistical parameters of the complete dataset as a sum of the dataset's mean value and a half of its standard deviation:

$$T_{bg} = \mu + \frac{\sigma}{2} \tag{E.2}$$

From points having an intensity lower than T_{bg}, the threshold of the hotspots is derived:

$$T_{hotspots} = \mu_{bg} + 3 \cdot \sigma_{bg} \tag{E.3}$$

The adaptive thresholding method was verified with both simulated [40] and previously measured terrestrial data. An example relating to a single source in which the

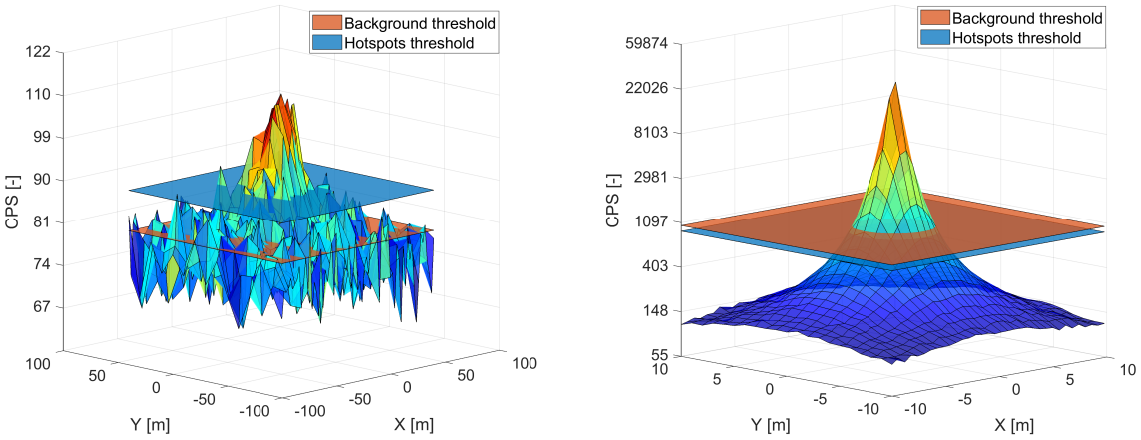

Figure E.9.: An example of adaptive thresholding related to UAS-based (a) and UGV-based (b) measurement. CPS: counts per second; UAS: unmanned aircraft system; UGV: unmanned ground vehicle.

emission at the distance of 1 meter reaches ten times higher than in the background is shown in Figure E.9 for both aerial and terrestrial survey.

Once the thresholding is applied to the interpolated points arranged in a regular grid, the remaining connected sets are enclosed by contours using the marching squares algorithm [67]. Apparently, only contours having a certain minimal length should be accepted in order to eliminate random noise-induced peaks; we suggest that a valid contour should encircle at least four aerial samples. Finally, the regions are smoothed and optionally enlarged via the Minkowski addition [68] with a circle-shaped structuring element. The hotspots are eroded at first to suppress the noise; subsequently, they may be dilated again to adjust their sizes. The resulting ROIs are passed, as connected sets of points in a regular grid, on to the next stage for further processing; such a grid is then denoted as the *R*OI map.

E.3.8. Terrestrial Radiation Mapping

The first task for a UGV is to move from a safe zone to the first detected contaminated area. A system user selects in the map suitable places where the robot can be potentially unloaded. This task requires the knowledge of obstacles in the area of interest. The required obstacle map is computed from the previously created DEM.

Further utilization (path planning in particular) of the obstacle map does not require a resolution as high as DEMs typically have. Satisfactory path planning accuracy can be achieved even with a reduced pixel size. Our approach towards creating the obstacle map also involves reducing the pixel count; this operation,

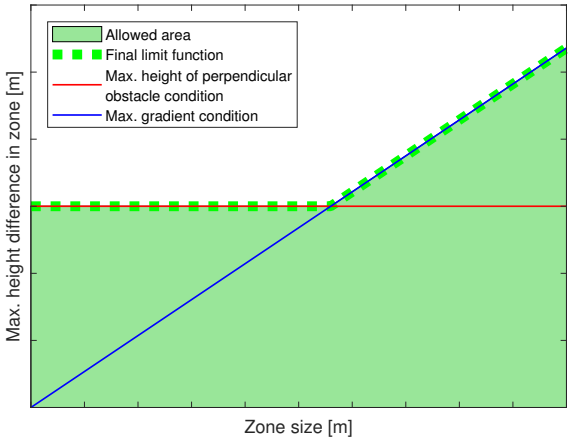

Figure E.10.: The obstacle function.

however, is not implemented as separate downscaling. The input parameters for the obstacle map creation process are as follows:

- the maximum operation angle of the mobile robot,
- the maximum height of a negotiable obstacle perpendicular to the terrain,
- the pixel size of the obstacle map.

From these parameters, we can define the obstacle function (Figure E.10) of the employed UGV. The function is used for detecting the impassable area in the group of DEM pixels that forms one pixel of the obstacle map. Each square sub-groups of the DEM pixels for every obstacle map pixel is checked by passing the obstacle function. In the case that a sub-group of DEM pixels is found that does not meet the obstacle function, the corresponding pixel of the obstacle map is marked as the obstacle. The process produces a binary map whose pixel size equals the integer multiple of the DEM pixel size. The principle of the operation is demonstrated for a sample DEM (Figure E.11), including terrain gradients that are below (10 deg) or above (20 deg) the robot's limit (15 deg). The sample DEM also includes perpendicular obstacles with a height of 10 or 20 cm; the robot's limit for this type of obstacles is 15 cm.

To find the optimal scenario of moving a UGV to the contaminated areas, the system operator must manually select the places where the robot can be potentially unloaded. From these starting points, we plan three types of trajectories: towards the detected contaminated areas; between these zones; and back from the last area to the unloading place. To move between the contaminated areas, the starting point for the path planning is the waypoint at the end of the trajectory inside the current area, while the final point is marked by one of the endpoints of the trajectory inside

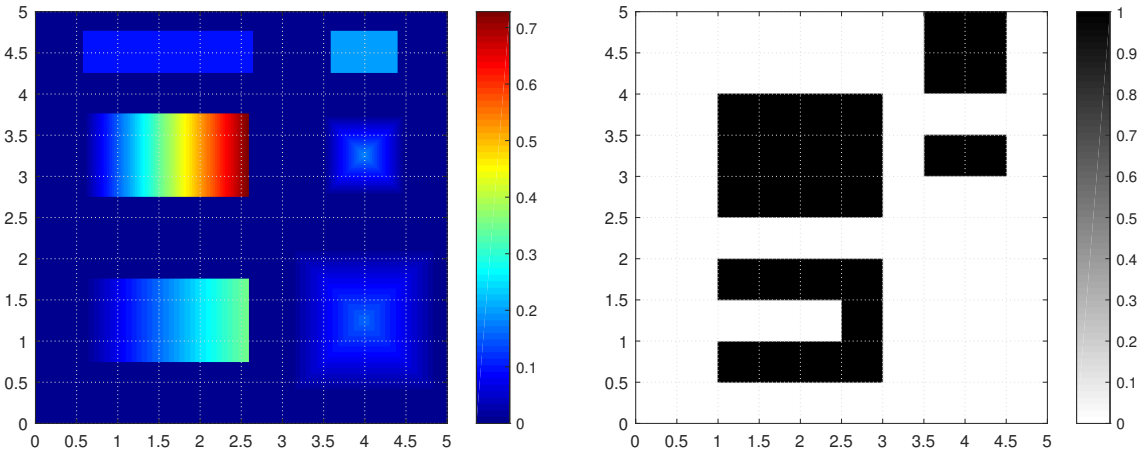

Figure E.11.: A sample DEM (a) with a color scale representing the height in meters; and the resulting obstacle map (b) with a gray scale to indicate the obstacle probability. DEM: digital elevation model.

the next area. These path planning tasks can be generally solved by any A* based algorithm [69]; the shortest sequence of paths from the set of all possible solutions is used.

To plan a trajectory inside the regions of interest, we have to describe each such region with a set of polygons, one 'envelope' representing the outer limits of the area; optionally, the description can be expanded to include multiple 'holes' that characterize obstacles not traversable by the UGV. At this point, both the coarse characterization of the terrestrial-mapped hotspots (Section E.3.7) and the obstacle map are available and need to be fused. This is also the moment when the operator should intervene to validate if all of the actual obstacles are contained in the map; alternatively, the operator inserts the missing objects manually. Note that this step can utilize the earlier acquired orthophoto to identify restrictions.

First, the obstacle map is resampled to exhibit the same resolution, or cell size, as the ROI map. Both maps are composed of binary value cells, which can be either empty or occupied. In the ROI map, the empty cells represent the areas where the terrestrial mapping is to be performed. The maps are fused through a relatively simple intersection: If corresponding cells in the maps are empty, then the cell is empty; conversely, it is occupied when the occupancy condition has been met in at least one of the maps. An example of the fusion producing a $f$used map is shown in Figure E.12.

Generally, a single region of interest may be divided by obstacles into multiple subregions; thus, the fused map is subjected to connected-component labeling [70] to distinguish individual areas enclosed by the envelopes. Subsequently, each area

Figure E.12.: An example of how a fused map is generated; the white color represents the free space.

greater than the rationally chosen threshold (the criterion being applied to exclude miniature portions of the region) is searched for contours in order to identify its envelope and holes. For practical reasons, namely, to reduce the computational requirements for the trajectory planning, the contours are reduced to polygons with a limited number of edges. The reduction is carried out incrementally, by successive removal of the least important vertices; the importance i depends on the lengths of adjacent edges and the angle between them. We have

$$i = \left| \arccos \left(\frac{\boldsymbol{x_1} \cdot \boldsymbol{x_2}}{\|\boldsymbol{x_1}\| \cdot \|\boldsymbol{x_2}\|} \right) \right| \cdot \|\boldsymbol{x_1}\| \cdot \|\boldsymbol{x_2}\| \tag{E.4}$$

where $\boldsymbol{x_1}$ and $\boldsymbol{x_2}$ are the vectors of adjacent vertices.

Then, each mapped region is divided into a set of disjoint obstacle-free subregions by using the Boustrophedon decomposition [71], a procedure suitable for problems where obstacles are defined by polygons. The principle of this algorithm is to acquire subregions, or cells, that can be completely covered by a uniform 'zig-zag' trajectory; each cell has two edges parallel to the *s*weep line, which, in turn, is parallel to the survey direction. The result of the decomposition depends on the selected sweep line orientation (relative to the ROI); in general terms, it is desirable to minimize the number of cells. Finally, the region is described by a graph whose nodes represent the subregions and edges define their adjacency.

To determine the order in which the subregions are explored, the depth-first search algorithm is applied; this method guarantees that all nodes (cells) are visited and prefers transitions between adjacent ones. Trajectory planning inside the cells is rather straightforward, as the survey lines are parallel to the sweep line, their mutual distance remains constant, and the orientation varies in order to achieve the 'zig-zag' shape of the trajectory. In some cases, when moving from one cell to another, a direct connecting path may collide with an obstacle. Since the non-traversable zones are already described by the polygons, the visibility graph algorithm [72] is utilized to find the shortest non-colliding path; to preserve a clearance from the obstacles, the corresponding polygons are dilated. The situation is illustrated in Figure E.13.

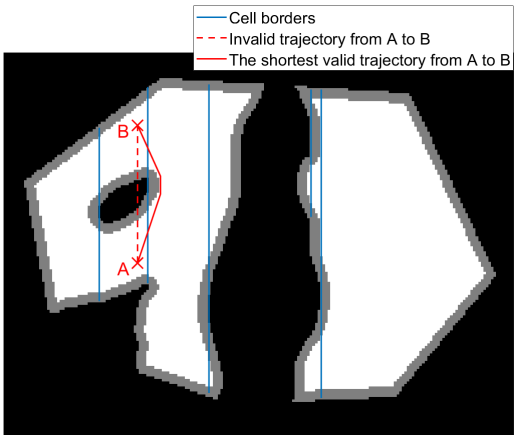

Figure E.13.: An example of the Boustrophedon decomposition and interconnection of subsequent cells; the black color represents the obstacles, while their dilation is in grey.

Eventually, the whole region of interest is covered with evenly distributed parallel portions of the survey trajectory, along with connecting paths between consecutive subregions, and the obstacles are avoided.

E.3.9. Radiation Data Processing and Source Localization

Handling the terrestrial data is largely similar to the aerial radiation data processing presented in Section E.3.7. The localization of the sources can be characterized by three steps:

1. Estimating the number of sources, R.
2. Estimating the initial coarse parameters of R sources.
3. Increasing the accuracy of the parameters in accordance with the measured data.

The first step utilizes the adaptive thresholding algorithm. Although multiple sources in a single region form a sole hotspot within the primary map, they may yield more peaks inside the detailed secondary map built from the UGV data, which are acquired in a finer grid and from a closer distance than the aerial dataset. To perform the estimation, the following steps are applied:

1.a Compute the peak threshold.

1.b Interpolate the data into a regular grid.

1.c Eliminate the radiation background.

1.d Find valid contours in the map; their count equals the number of sources.

Regarding the source parameters, three items are sought for each source; these items include the emission intensity and coordinates in two axes. Let us have a source i with the vector $\boldsymbol{\theta}_i = (\alpha_i, x_i, y_i)$; all of the sources are then characterized by the parameter matrix $\boldsymbol{\theta} = (\boldsymbol{\theta}_1, \boldsymbol{\theta}_2, \ldots, \boldsymbol{\theta}_R)^\intercal$. To initiate the matrix, we suggest choosing a central point within each contour to define the coordinates and taking the greatest corresponding total count value to estimate the intensity. By filling in the matrix, the second localization step is completed.

Finally, the accuracy of the parameters is iteratively improved via the Gauss-Newton (G-N) method [73], which finds use in solving non-linear least squares problems. Given a matrix of M measurements, $\boldsymbol{z} = (\boldsymbol{z}_1, \boldsymbol{z}_2, \ldots, \boldsymbol{z}_M)^\intercal$, where $\boldsymbol{z}_i = (c_i, x_i, y_i)$ to denote the total count obtained and the coordinates where the measurement has been taken, the G-N algorithm minimizes the sum of residuals (the differences between the expected and the measured values); the residual m is expressed as:

$$r_m = c_m - \sum_{r=1}^{R} \frac{\alpha_r}{(x_m - x_r)^2 + (y_m - y_r)^2 + h^2}, \tag{E.5}$$

where h is the height of the detectors above the terrain. The parameter matrix is updated in each step according to the equation

$$\boldsymbol{\theta}_{k+1} = \boldsymbol{\theta}_k - (\boldsymbol{J}^\intercal \boldsymbol{J})^{-1} \boldsymbol{J}^\intercal \boldsymbol{r}(\boldsymbol{\theta}_k), \tag{E.6}$$

where $\boldsymbol{J}$ is the $M \times 3R$ Jacobi matrix of the partial derivatives of the residuals. The iterations continue until the sum of the squared residuals stops decreasing significantly.

E.4. Results

E.4.1. Aerial Photogrammetry

The data collected during the first UAS flight were processed immediately after landing, as the photogrammetry products are essential for the subsequent mapping phases. From the total amount of 211 images, we utilized only 124 items; those captured during the take-off and landing procedures were excluded because they are not relevant to the actual processing. As expected from the designed trajectory, the automatic waypoint-based flight lasted approximately 10 minutes and was 1 kilometer long. One of the images, together with the maximum zoom available, is shown in Figure E.14.

Figure E.14.: A sample image captured at 60 m AGL during the initial flight. The detail shows the car accident simulated in zone 2. AGL: above ground level.

The photographs were directly georeferenced by using the onboard multi-sensor system, making the exterior orientation parameters accessible immediately after the flight, regardless of the GCPs' availability. In addition to the position and orientation, the system offers various indicators facilitating analyses of its operation quality. Figure E.15 summarizes the estimation of the GNSS-aided INS 1σ spatial error at image taking. Based on the presented data, the average and maximum errors equalled 0.74 m and 5.3 m, respectively. The reason for the conspicuous accuracy decrease consisted in the GNSS' RTK fix solution outages caused by insufficient quality of the signal necessary for the carrier-phase tracking. At one moment, the INS excluded the inaccurate GNSS-produced aiding data from the computation, and the position error increased sharply to up to five meters.

The dataset was processed in Agisoft Photoscan at a low quality in order to reduce the processing time. We used images downscaled by a factor of four to perform the alignment stage, and 16-fold downscaled images were employed in the dense point cloud generation to yield 7.6 million points ($\sim$200 points/m^2). The digital elevation model constructed from the point cloud delivered the resolution of 7.4 cm/pix; the subsequent product, namely, the orthophoto, exhibited 1.9 cm/pix (Figure E.16a and E.16b). The entire photogrammetry processing lasted approximately 45 minutes.

To determine the georeferencing quality, namely, to assess the method, we utilized six GCPs (Figure E.6). Despite the issues with the GNSS/INS, we obtained the georeferencing root mean square error (RMSE) values of 0.55, 0.34, and 1.13 m for the latitude, longitude, and altitude, respectively; the errors in the individual

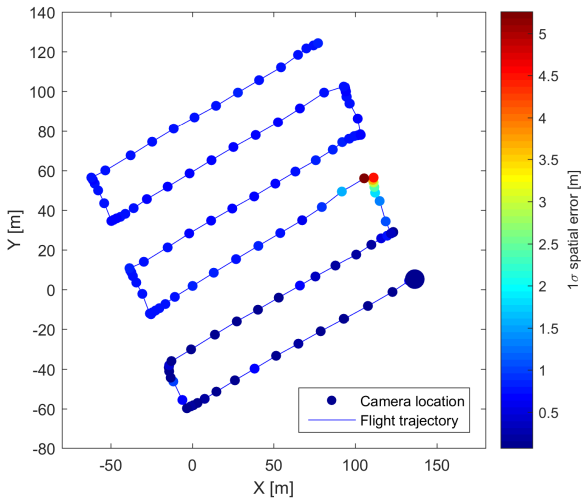

Figure E.15.: The flight trajectory and the INS spatial error estimation at the camera locations, with the starting point highlighted. The zero coordinates correspond to the position of the base station. INS: inertial navigation system.

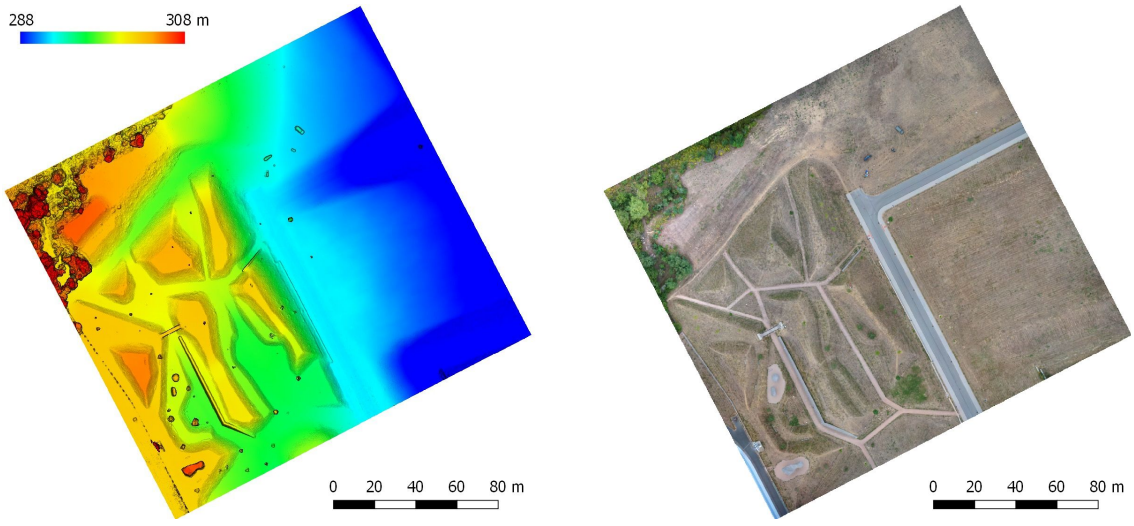

(a) (b)

Figure E.16.: The UAS photogrammetry-based DEM (indicating the spectral color-scaled elevation and black-marked slopes) (a) and orthophoto (b). DEM: digital elevation model

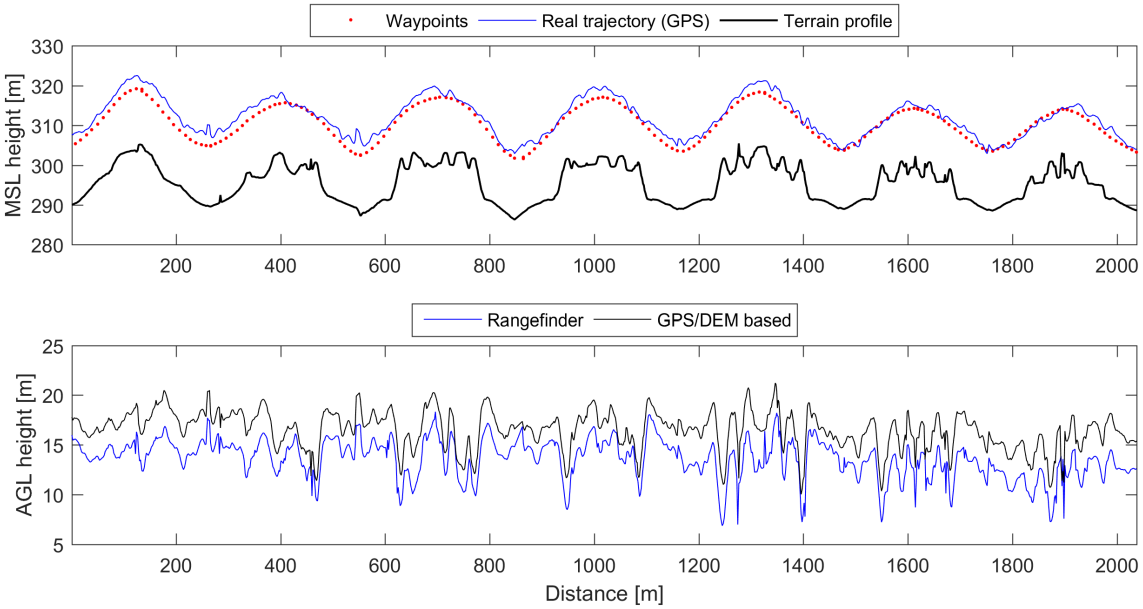

Figure E.17.: The vertical profile of the UAS trajectory during the radiation-mapping phase, completed with the trajectory waypoints and underlying terrain (upper graph). The AGL flight height recorded by the rangefinger, represented together with the related GPS/DEM-based estimation (bottom graph). MSL: mean sea level; AGL: above ground level; DEM: digital elevation model; GPS: global positioning system.

targets were computed in Photoscan as the distances between the measured and the estimated positions. The resulting accuracy is below expectations and does not correspond to the capabilities of the system; however, the level remains acceptable for the subsequent mapping phases.

E.4.2. Aerial Radiation Mapping

Using the algorithm described in section E.3.6, and utilizing the DEM obtained within the previous step, we automatically adjusted the vertical components of the trajectory for the aerial radiation mapping. At the inital stage, the trajectory (Figure E.7b) was split into 10 m segments, resulting in 209 waypoints; subsequently, the MSL height for every waypoint was computed (the red points in Figure E.17).

Compared to the photogrammetry flight, the second UAS mission lasted longer (approximately 20 minutes) due to the trajectory length and lower operating speed. Thanks to the GPS receiver and laser rangefinder, both integrated in the onboard radiation detection system, we can analyze the 'terrain-following' algorithm performance. The upper part of Figure E.17 displays the vertical coordinate of the actual GPS trajectory and the underlying terrain; the bottom graph shows the height above

ground level. The presented data refer to the UAS flown at a relatively constant distance from the surface; at some moments, however, deviation from the desired value of 15 m is obvious. In this context, the rangefinder reports the height of 13.7 m RMSE, while the GPS-DEM derived value (GPS height minus surface height) is slightly higher, reaching 16.6 m RMSE. It should be noted that none of the sources is accurate enough for detailed assessment: The distance value measured by the rangefinder is biased due to the UAS tilting, and both the GPS and the DEM errors lie within the order of meters. Despite these facts, the presented data clearly indicate that the terrain following method has met the expectations, allowing us to collect radiation data at a sufficiently constant distance from the ground, regardless of the surface shape.

Given the one-second sampling period of the radiation detection system, the dataset comprises 1,100 measurements (excluding the data gathered during the take-off and landing procedures), with the minimum and maximum values of 0.042 and 0.207 $\mu Gy \cdot h^{-1}$, respectively. Note that the mean radiation background intensity approximately equalled 0.07 $\mu Gy \cdot h^{-1}$. Considering the horizontal coordinates of the individual measurements (Figure E.18a), we can clearly identify two separated hotspots, namely, areas with increased radiation intensity. As already discussed within section E.3.7, the scattered data had to be downsampled prior to the actual processing in order to achieve comparable data density in both axes, parallel and perpendicular to the flight direction. The processed and interpolated data presented in Figure E.18b clearly define the situation at the location and, above all, facilitate automatic selection of the ROI (section E.4.3). The radiation data were interpolated to a 0.1 m regular grid.

The collected data contains, in addition to the dose rate values, also raw data allowing spectral analysis and radionuclide identification; this step, however, is not necessary for the subsequent stage (hotspot localization) and was thus not performed during the experiment. The spectral analysis potential is outlined in section E.5.

E.4.3. Areas Selected for the Terrestrial Mapping

The interpolated radiation map has been subjected to the automatic ROI selection algorithm. First, the background threshold was computed, equaling 0.090 $\mu Gy \cdot h^{-1}$; such a result is in good accordance with the actual background intensity, which reached up to about 0.095 $\mu Gy \cdot h^{-1}$. Subsequently, the script was able to determine the hotspot separation threshold, attaining 0.103 $\mu Gy \cdot h^{-1}$. A 3D visualization of the thresholding process is shown in Figure E.19a. Note the small 'spikes' around the two major radiation intensity peaks, induced by the measurement noise. In order to eliminate these spikes and to smoothen the region's borders slightly, the

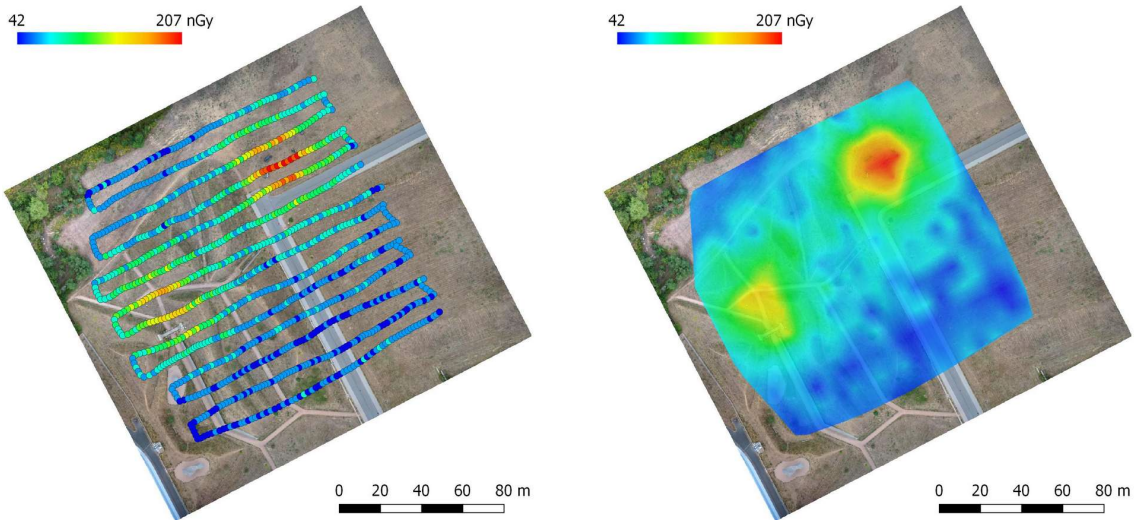

(a) (b)

Figure E.18.: The dose rates obtained during the UAS-based radiation mapping procedure (a); the acquired data were downsampled and interpolated for the subsequent processing (b). UAS: unmanned aircraft system.

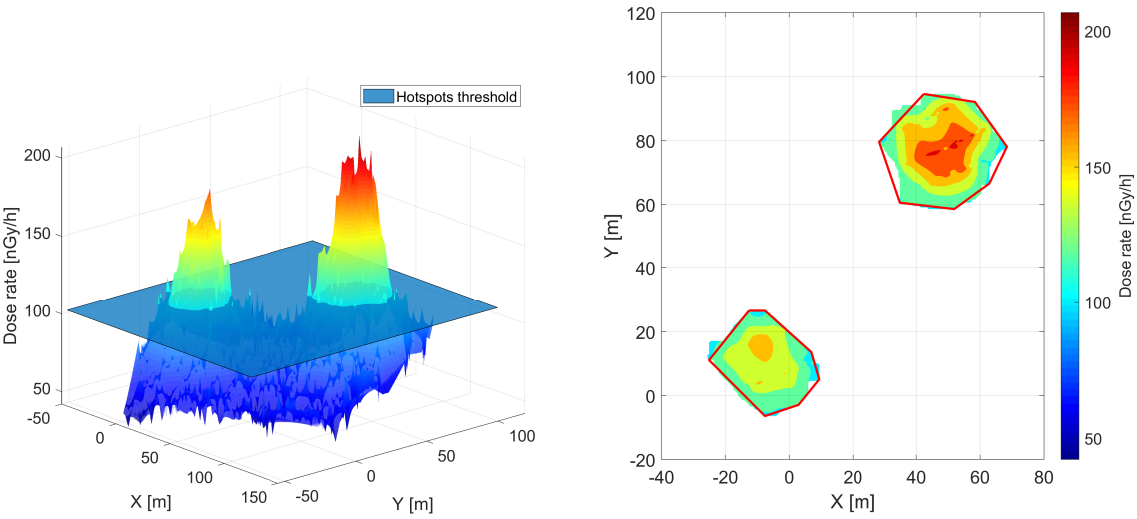

(a) (b)

Figure E.19.: The adaptive thresholding applied to the aerial radiation data (a), and polygonal approximation of the hotspots (b).

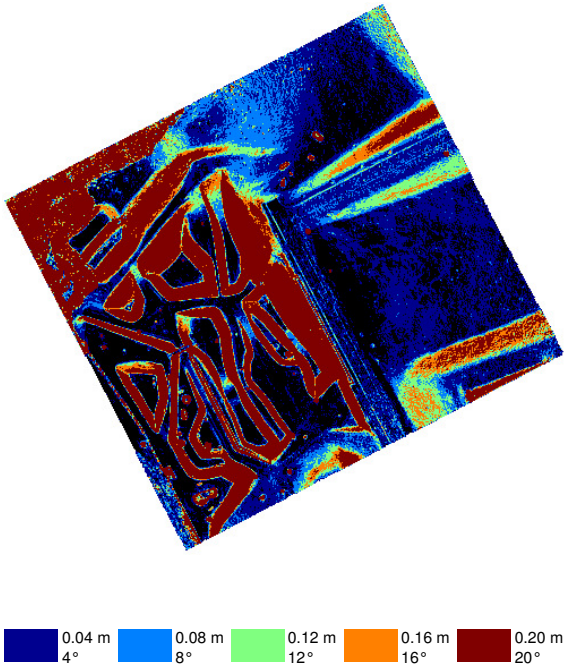

Figure E.20.: The obstacle maps computed for the different UGV limits. UGV: unmanned ground vehicle

imprint of the hotspots was morphologically eroded by a structuring element of a size corresponding to 3 meters. Finally, both of the remaining regions were roughly approximated by polygons with 7 vertices (Figure E.19b).

E.4.4. Terrestrial Radiation Mapping

The obstacle map for the path planning is computed from all pixels of the source DEM. Generally, the size of a DEM pixel (74 mm) is too small to be applied in the obstacle map suited for outdoor path planning tasks; in this context, we can point out that larger pixels reduce the time required for the subsequent processing operations. At such stages, the pixel size approaches the actual width of the employed UGV. To carry out the planned mission, we selected the value of 0.518 m, namely, the integer multiple of the DEM pixel size. The resulting obstacle maps (Figure E.20) computed for five different terrain limits show the terrain negotiability differences. When in the automatic navigation mode, our UGV can safely pass a terrain characterized by a gradient of 16 degrees or surmount obstacles having 0.16 m; if operated manually, however, the vehicle is capable of managing 20 degrees and 0.2 m. The results described below are based on the obstacle map computed for the 0.16 m and 16 deg limits (the orange layer in Figure E.20).

Subsequently, the obstacle map is fused with the hotspot polygons. Prior to the processing by the automatic script, several additional obstacles, in particular a curb

and plants that formed a new boundary limiting the southern side of the upper-right ROI (corresponding to zone 1), had to be defined manually. Moreover, two minor obstacles, namely, a small barrel and the remains of a tree, were added inside the lower-left ROI (zone 2). In Figure E.21, these adjustments are marked in gray. The rough hotspot borders, modified in accordance with the obstacle map, form the 'envelopes' of the regions to be mapped and are visualized as the green polygons; the blue polygons inside the green ones then represent the 'holes' to be avoided. Note that the algorithm yielded two distinct subregions within the lower-left ROI; one of these areas, however, is inaccessible to the UGV (as can be proved via the path-planning algorithm) and will not be further examined within the article.

Both envelopes and their corresponding holes are passed to the algorithm responsible for the decomposition. Zone 1, whose area corresponded to approximately 750 m^2, was divided into 13 cells, as shown in Figure E.22a. The sweep line orientation was eventually chosen manually because the implementation had not been robust enough to handle an arbitrary case. In the trajectory planning, the first phase consists in selecting the initial point to start the survey; in our case, this step was performed manually. The cells were automatically ordered as follows: $3 \rightarrow 1 \rightarrow 2 \rightarrow 4 \rightarrow 10 \rightarrow 9 \rightarrow 8 \rightarrow 6 \rightarrow 5 \rightarrow 7 \rightarrow 11 \rightarrow 13 \rightarrow 12$. The resulting trajectory is plotted in Figure E.22b, and it consists of two elements: a) 'zig-zag' shaped paths covering the whole area (except for the holes), and b) links connecting portions of the inspection routes to ensure that the holes are avoided safely. The theoretical length of the complete trajectory equals 448 m; note that this value applies only to holonomic robots without kinematic constraints.

The same procedure was utilized also in zone 2, where the Boustrophedon algorithm split the area of 250 m^2 into 10 distinct partitions (Figure E.23a). The trajectory planning was initiated in the last cell (10) to yield the following survey sequence: $10 \rightarrow 8 \rightarrow 6 \rightarrow 7 \rightarrow 9 \rightarrow 5 \rightarrow 4 \rightarrow 3 \rightarrow 1 \rightarrow 2$. In zone 2, the complete trajectory has the length of 192 m and is shown in Figure E.23b.

The last path planning task interconnects the regions of interest and the zone most convenient for unloading the UGV. The operator selects suitable points to start the mission; we chose two spots (the green and pink circles in Figure E.24) on the road at the edge of the mapped area, where the contamination level is within the safe limits. The start and end points of the planned trajectory inside the ROI are fixed and cannot be altered during this phase. Using the A* algorithm implemented in the project presented in [74], three paths were planned: from the unloading zone to a ROI, from this ROI to the next ROI, and from this last ROI back to the unloading zone. The sums of the path lengths are evaluated to select the lowest value. To reduce the UGV collision probability, all of the obstacles are expanded with an enclosing pixel (the red areas in Figure E.24). The resulting shortest sequence of

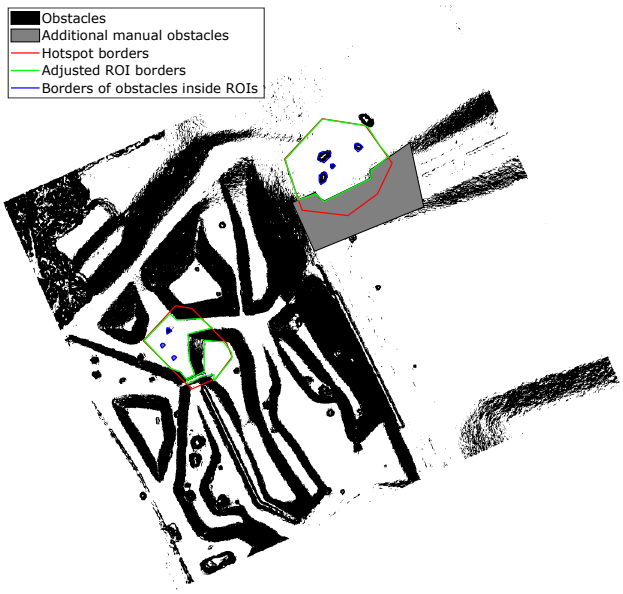

Figure E.21.: The adjustment of the regions of interest via the obstacle map.

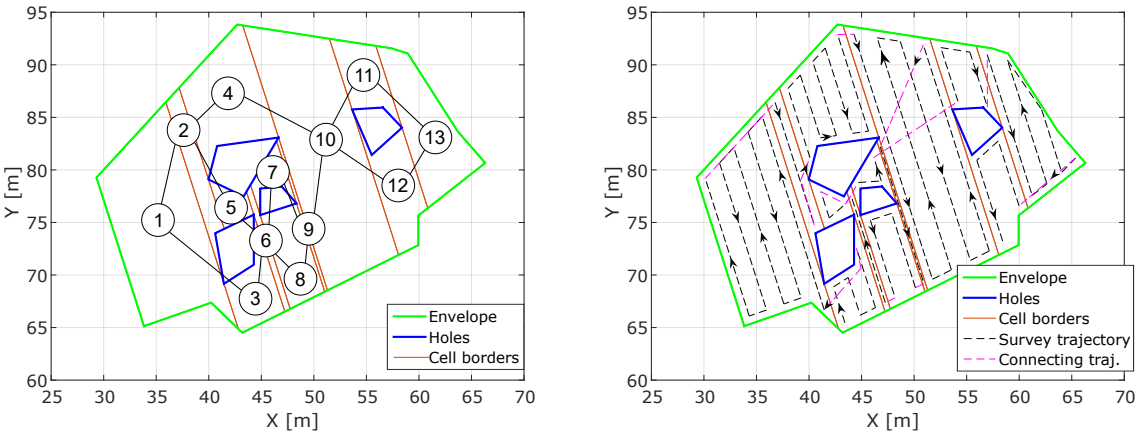

(a) (b)

Figure E.22.: The result of the Boustrophedon cell decomposition for the first ROI, complemented with a cell adjacency graph (a); the planned trajectory within the first ROI (b). ROI: region of interest

the three paths is shown in a modified obstacle map (Figure E.24). The paths are 200 m long in total, and the UGV completed them in 6 minutes and 20 seconds (the speed varied from 0.4 to 0.6 m/s).

E.4.5. Radiation Data Processing and Source Localization

After completing the path planning phases, we employed the UGV to acquire the radiation data in both zones. The robot's minimal turning radius was set to 0.6 m;

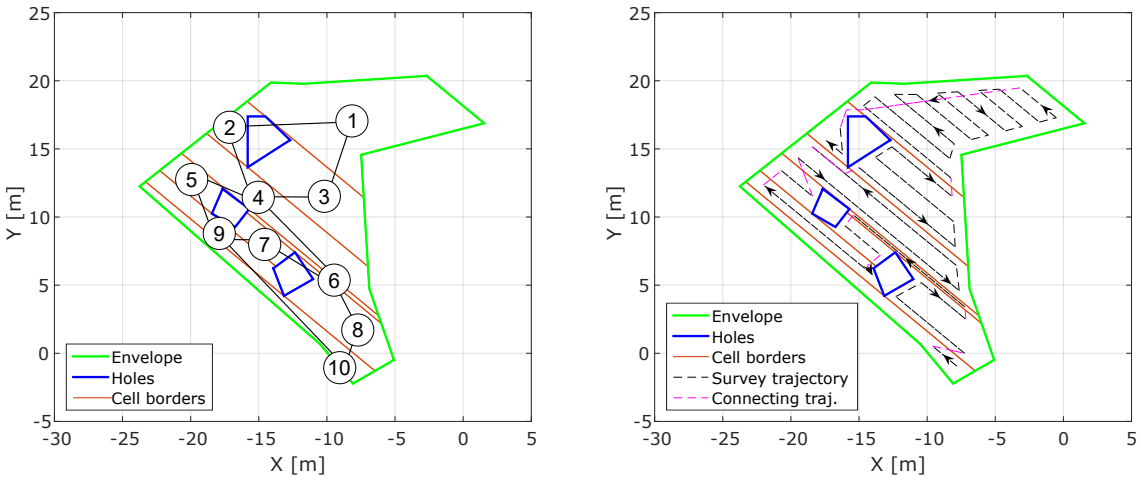

(a) (b)

Figure E.23.: The result of the Boustrophedon cell decomposition for the second ROI, complemented with a cell adjacency graph (a); the planned trajectory within the second ROI (b). ROI: region of interest

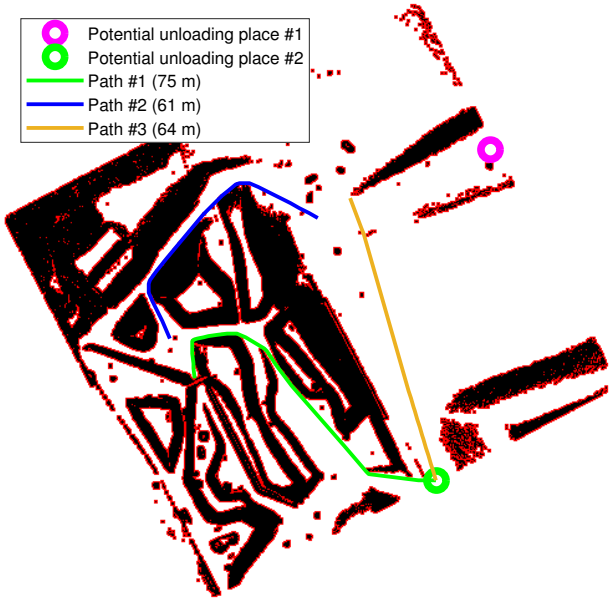

Figure E.24.: The A* planned trajectories between the unloading zone and the regions of interest.

thus, the shape of the actual trajectory differed from that of the pre-generated one. With the maximal forward speed equaling 0.6 m/s (0.4 m/s while turning), the measurement took 15 minutes and 10 seconds in zone 1, while the time relevant to zone 2 was 7 minutes and 35 seconds.

The individual radiation data points comprise geographical coordinates and the total count of one-second measurement cycles delivered by the two detectors. The actual result is embodied in radiation spectra; at this stage, however, the spectra are relatively unimportant, and we therefore sum them into the TC. The measurement outcomes for zone 1 are presented in Figure E.25a; the relevant path was 495 m long. Subsequently, the data were interpolated and the background removed (the background and hotspot threshold exhibited the values of 1645 CPS and 2124 CPS, respectively). As the zone included merely a single source, the thresholding left a sole peak, and the parameter matrix was initialized smoothly. The initial and the improved estimates, the latter one based on the Gauss-Newton method, are indicated in Figure E.25b. The localization error equaled 0.123 m (Table E.4).

The situation was more problematic in zone 2, where we placed 7 sources in total. The individual data points captured are shown in Figure E.26a; the length of the actual trajectory corresponded to 221 m. Three sources, namely, radionuclides s1, s4, and s7, were located outside the surveyed area. In terms of further description, s7 was positioned on a steep slope and thus remained inaccessible to the UGV; s1 and s4 then lay in a free space and were omitted by the planning algorithm because the primary ROI borders had not been broad enough (these radionuclides ranked among the weakest ones and thus did not leave a noticeable signature on the aerial data). The threshold levels for the background and the hotspots equaled 2707 CPS and 4684 CPS, respectively; note that the values are greater than those relating to zone 1, as the major portion of the data points lay in the vicinity of the sources. The adaptive thresholding yielded three distinct peaks, correspondingly to sources s3, s5, and s6; the last peak (s2, weak caesium 137) was overshadowed by the strong Cs-137 in its close proximity. Consequently, only 3 out of the 7 sources were localized successfully, as is obvious from the detailed results in Table E.4. The average localization error in both of the zones (considering only sources whose parameters were found) equals approximately 0.10 cm RMS.

To quantify the benefits of employing the UGV in more detailed measurement, the localization algorithm was also applied to the aerial data. The thresholding result remained the same as in the ROI selection (Figure E.19), yielding two source estimates. Clearly, the localization error in zone 2 cannot be computed, because the 7 sources present there appear as a single one in the aerial radiation map. However, we can compare the results obtained within zone 1, where the UAS localization error equals 2.82 m after application of the Gauss-Newton algorithm (Table E.4).

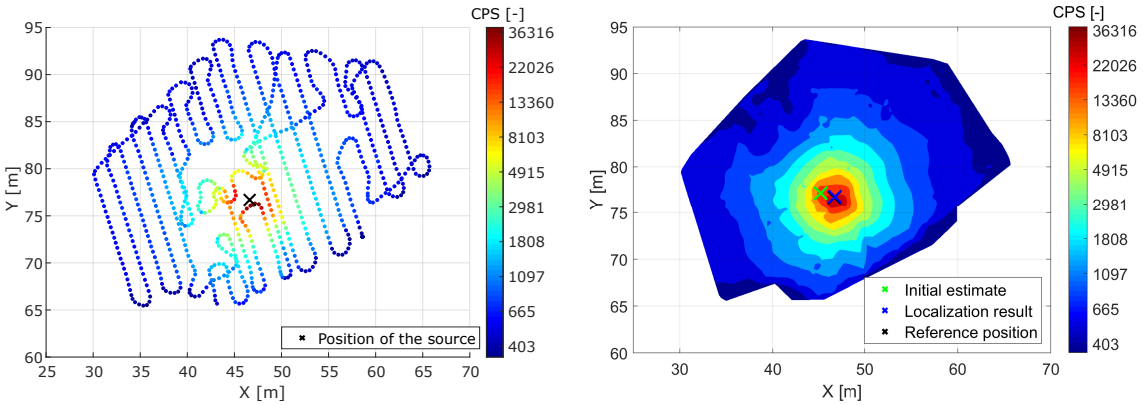

(a) (b)

Figure E.25.: The individual data points measured along the planned trajectory; the points capture the total count in the first ROI (a). The interpolated radiation map highlighting the result of the source localization procedure (b). CPS: counts per second; ROI: region of interest.

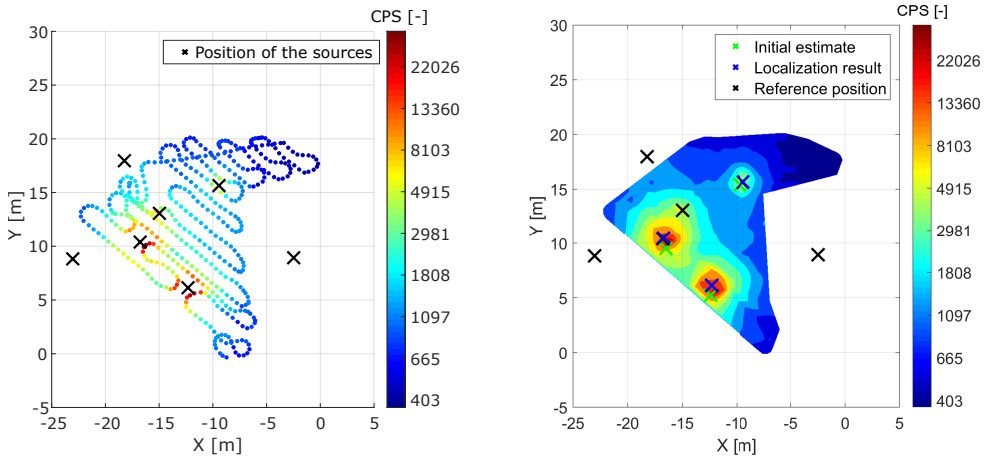

(a) (b)

Figure E.26.: The individual data points measured along the planned trajectory; the points capture the total count in the second ROI (a). The interpolated radiation map highlighting the result of the source localization procedure (b). CPS: counts per second; ROI: region of interest.

Table E.4.: The source localization results: N-q stands for non-quantifiable, as the UAS localization error for zone 2 cannot be expressed in the usual manner. UGV: unmanned ground vehicle; UAS: unmanned aircraft system; ROI: region of interest.

Source	Zone	Error UGV [m]	Error UAS [m]	Isotope	Activity [MBq]	Comment
s1	2	–		Co-60	2.85	Outside the ROI
s2	2	–		Cs-137	7.53	–
s3	2	0.067		Co-60	2.95	–
s4	2	–	N-q	Cs-137	7.53	Outside the ROI
s5	2	0.138		Cs-137	79.82	–
s6	2	0.018		Co-60	24.56	–
s7	2	–		Co-60	24.76	Inaccessible to the UGV
s8	1	0.123	2.82	Co-60	123.78	–

E.5. Discussion

Within the presented experiment, we introduced and successfully tested a multi-robot radiation mapping method consisting of numerous steps (the essential mapping outputs are summarized in Figure E.27). The entire operation lasted 24 hours; this continuous time interval comprised not only the necessary tasks, namely, the data gathering and processing, but also the site preparation and cleanup, safety-related steps, and activities not directly associated with the experiment. The time intensity of the operations relevant to the mapping and processing are summarized within the Gantt chart in Figure E.28. The individual items include the time spent on the automatic tasks (data processing, robot operation), operator interventions, and robot preparation and manipulation. The most time-intensive stages are the UGV operation and the photogrammetric processing. Theoretically, an ideal mission takes less than 4 hours; in reality, however, we had to face numerous minor issues that eventually prolonged the whole process, mainly as the mission marked the first time the systems were deployed together.

The UAS photogrammetry survey involved the use of our custom-built multi-sensor system and was carried out repeatedly; during the procedures, we thoroughly evaluated the achievable accuracy. Despite this, the attained values did not meet our expectations: As described in section E.4.1, the RMS object error determined by using the six test points lay within the order of decimeters in the horizontal

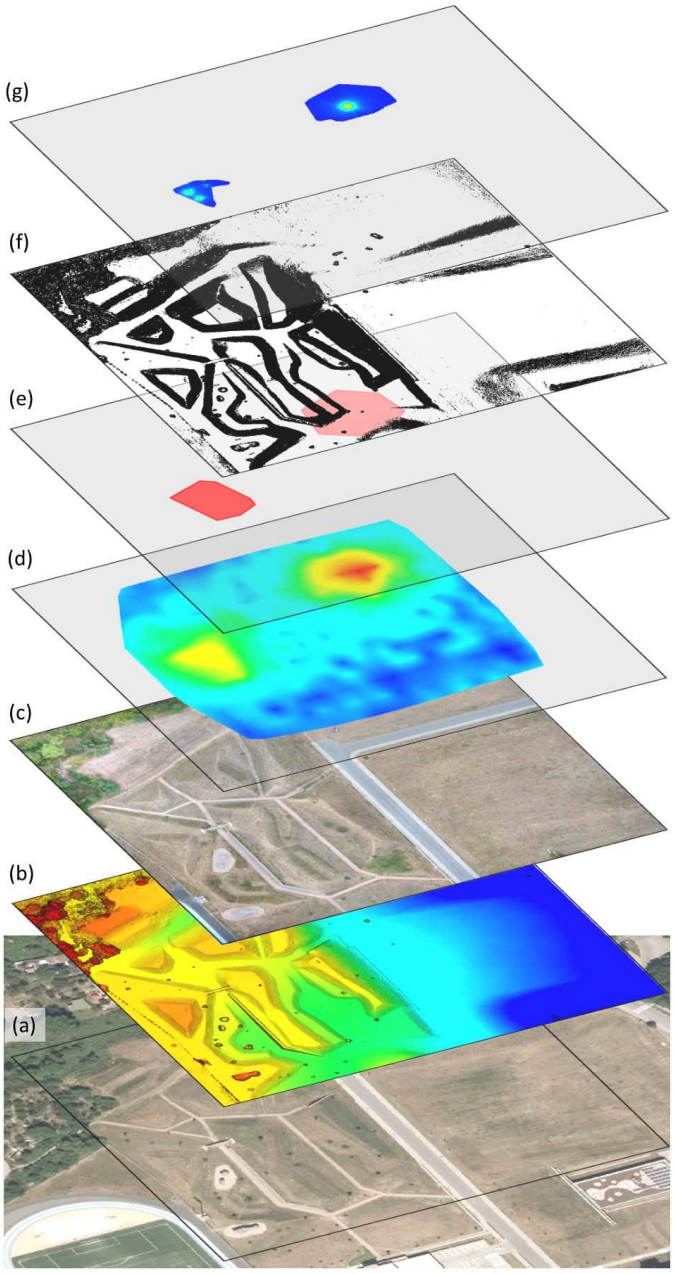

Figure E.27.: The most significant map layers assembled during the mapping and processing. The layers are arranged according to their times of origin, from the bottom upwards: the primary orthophoto (a); the UAS-based, shaded DEM (b); the UAS-made orthophoto (c); the UAS-delivered radiation map (d); the detected regions of interest (e); the DEM-based UGV traversability map (f); and the UGV-made radiation map (g). UAS: unmanned aircraft system; DEM: digital elevation model; UGV: unmanned ground vehicle.

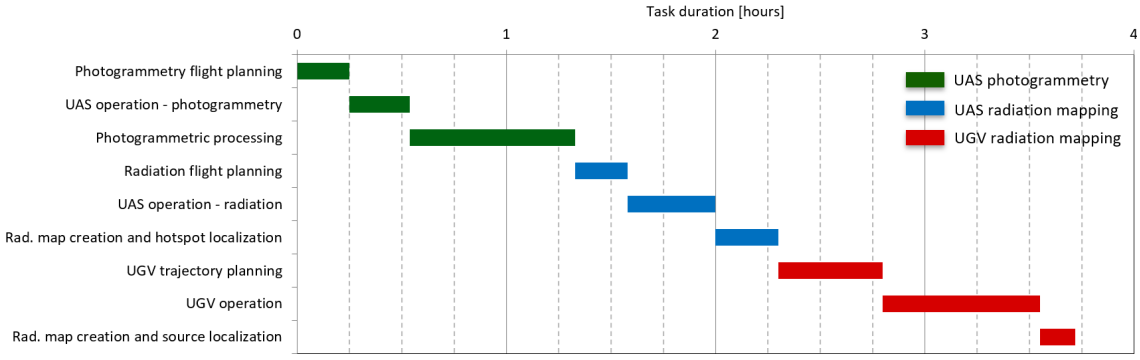

Figure E.28.: The approximate times of the individual tasks during the experiment. UAS: unmanned aircraft system; UGV: unmanned ground vehicle.

coordinates and rose slightly above a meter in the vertical one. According to our investigation and data analysis, all systems performed properly (including the RTK correction transmission); however, the signals on the GNSS receiver's antennas were rather weak, caused insufficient conditions for the carrier phase tracking during the entire flight. This problem resulted in RTK-fixed solution outages and made the INS exclude the GNSS data from the position and orientation estimates for a moment; the issue affected the beginning of the third survey line (Figure E.15). Since the multi-sensor system was combined with the BRUS UAS for the first time, the problem may have been generated by interferences from the UAS's electronic systems. Fortunately, the lower georeferencing quality did not manifest itself in the subsequent phases, and we still consider direct georeferencing crucial with respect to radiation-related missions.

Aerial radiation mapping proved to be a very effective tool for hotspot localization. The innovative approach involving flying at a constant AGL height regardless of the surface character allowed us to collect homogeneous data. Outside this scenario, the distance separating the ground and the detector would vary between 15 and 30 meters in a flight 15 meters above the highest location (at a fixed MSL altitude); such a diversity would certainly mean inconsistent data, and lower-positioned hotspots would be localized inaccurately or not at all. However, the DEM-based trajectory adjustment algorithm needs to be improved in several respects, of which the two most prominent ones are as follows: First, the method does not deliver the desired distance from the surface at high gradient locations, as it modifies the vertical coordinates of the waypoints only (as shown in Figure E.17); second, the algorithm should consider the UAS dynamics because some UAS control units fully ensure the horizontal speed while providing merely limited vertical speed, thus causing inaccurate waypoint following in steep parts. Based on the UAS-collected data, two regions of interests were automatically defined; this action reduced the original area

to less than 10 %, with only 1,500 m^2 left for the terrestrial mapping.

Using only a DEM to select regions inaccessible to UGVs within the mapped area cannot yield 100% reliable outputs. Deformable objects (such as blades of grass and light bushes) satisfy the definition of an obstacle in terms of the height and gradient, despite being effectively bypassable by a UGV; moreover, such objects cannot be separated from non-deformable obstacles, because in a DEM they are represented by the same data. Although the decision-making can utilize an orthophoto (automatically or manually), this approach produces only probable bypassability, which does not constitute a reliable option. Other issues arise from the actual capabilities of a DEM, one of the main limitations being that some free spaces, such as those under bridges, are not covered by the model. If no safe path for a UGV is found, we can follow that with the highest passability rate, albeit exclusively in the operator-assisted mode.

For many reasons, autonomous UGVs designed to participate in diverse missions require real-time obstacle avoidance. In view of this parameter, the DEM-based method is markedly limited in that the model captures only the situation existing at the time the source data were acquired, and thus the technique's applicability remains solely within the representation of fixed obstacles. including hills and mountains. Another set of incorrectly evaluated obstacles comprises objects undetected due to inaccuracies stemming from either the low resolution (e.g., in thin items such as columns and fences) provided by a DEM or poor object texture (e.g., the light being outside the usable sensor range). Such collisions can be prevented by a real-time obstacle avoidance system installed on board the UGV. In the context of our mission, it is important to emphasize that objects inside the mapped area are very likely to occur or change unexpectedly, and this type of system would significantly increase the efficiency of the entire reconnaissance process.

Considering the requirement for short overall mission time, an adequate DEM resolution has to be selected. For this purpose, we tested higher resolutions (up to 16x) to determine that while they did not improve the resulting obstacle map, the processing time and noise level increased significantly. Based on the attempts to fine-tune the whole task, we may conclude that computing a DEM with resolutions above 5 cm/pix does not bring any substantial benefits. Regarding the UAS path planning for the second flight, which also embodies the second task employing a DEM, it is possible to point out the lower sensitivity to DEM accuracy, an aspect that enables us to achieve satisfactory results even at values below 5 cm/pixel.

Although all of the algorithms worked only with either the dose rate or the raw total count during the entire source localization procedure, the use of spectrometric detectors in the experiment enabled further processing of the acquired data. Figure E.29 shows the sample spectrum integrated over the period of 10 s along the

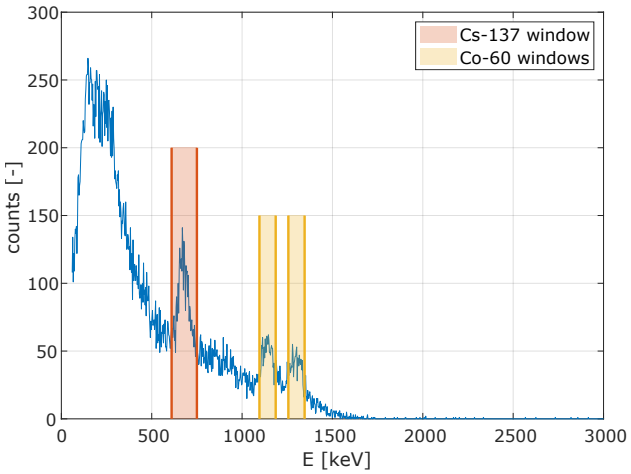

Figure E.29.: A radiation spectrum measured by the UGV's on-board detector; the graph indicates the energy windows of the applied radionuclides. UGV: unmanned ground vehicle

trajectory between the distinct radionuclides. The graph visualizes three photopeaks, which essentially embody the 'fingerprints' of the incident photons, namely, the photons' energy that is unique for each radioactive element. The net counts in the energy windows are proportional to the contribution of the relevant isotopes towards the overall measured intensity; note that the width of a window depends on the energy resolution of the detector, usually expressed by full width at half maximum (FWHM). To compute the net value, it is necessary to subtract the average background level and also the counts yielded through the impact of the higher-energy photons (in our experiment, the cobalt 60 affects the caesium 137 window via Compton scattering). The photons' influence can be quantified via the stripping coefficient, acquired from those measurements where the cobalt is present while the caesium is not; such a scenario was performed in area 1. As an example of the spectral isotope separation, maps relating to the two radionuclides are presented in Figure E.30; the images clearly show that Cs-137 sources were located in only one of the hotspots. Note that this result was not intended to be part of the experiment and was supplied additionally.

The experiment indicated that both aerial and terrestrial radiation mapping procedures involve specific drawbacks, as follows: The information density of the data acquired by the UAS suffices for localizing a single isolated source (s8), providing a result that could be accurate enough in practice; however, given the coarse aerial radiation map, it is virtually impossible to distinguish between a strong source, multiple radionuclides, and non-point areal contamination, as demonstrated in zone 2. By contrast, the UGV-based measurements characterized the actual radiological situation in a better manner, yet still not precisely enough; the reason lay in that

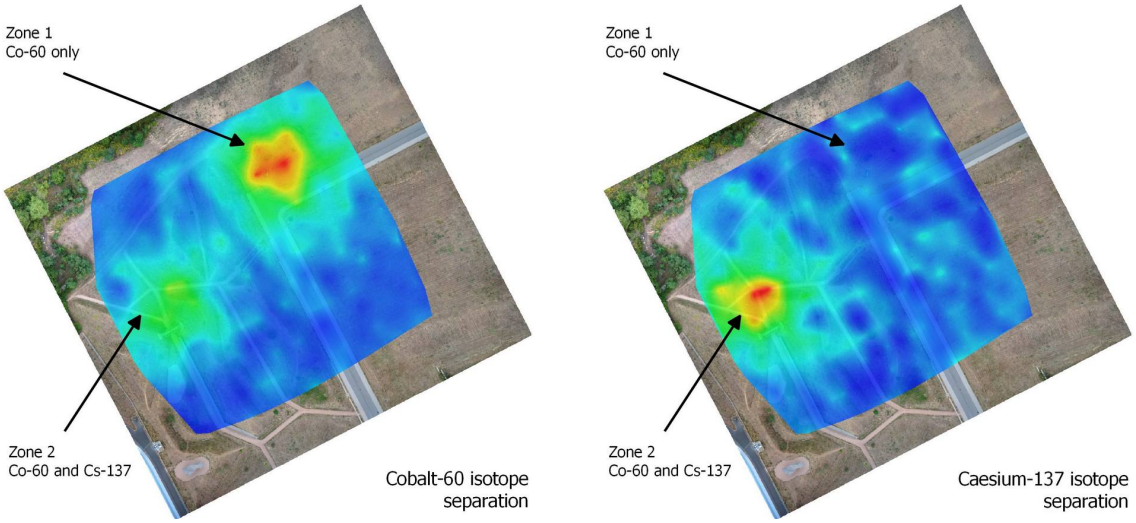

(a) (b)

Figure E.30.: The maps with separated radiation intensities for the cobalt 60 (a) and the caesium 137 (b).

the hypothetical 'center of radiation' (an analogy to a center of mass) in zone 2 was shifted towards the east by the relatively strong source s7, causing the weak radionuclides to be left outside the region of interest. In the future, this problem could be easily eliminated by enlarging the ROI prior to executing the UGV path planning phase. Obviously, a terrestrial robot is incapable of localizing sources positioned in a space classified as an obstacle (s7), and this deficiency, in general terms, requires further application of a UAS to explore such portions of the ROI that remain inaccessible to other robots. Using a UAS in this scenario nevertheless also invokes the question of safety, as the aerial vehicle needs to be brought closer to the terrain. Regarding the ground inspection, another disadvantage consisted in that the procedure failed to separate the overshadowed weak source (s2); however, performing a measurement detailed enough to localize this source would probably be more time-intensive than repeating the entire survey after other sources had been removed from the area. Yet, despite the difficulties, the UGV has proved to be a significant component of the system because it provides a more accurate overview of the radiological situation within the hotspots.

Contrary to our previously published research, we did not attempt to employ information driven localization, i.e., real-time UGV trajectory adaptation according to continuously acquired data. Instead, the goal was to compile a radiation map as precise as possible to cover also sources that are generally difficult to detect. With some prior information, such as that only one radionuclide is sought, we could utilize the partial directional sensitivity provided by the two-detector system to head

towards the radiation source immediately after its presence has been indicated. To achieve this purpose, it would be necessary to assure obstacle avoidance, fusing the source direction estimation with the obstacle map via exploiting the potential field algorithm if feasible.

If we compare the results achieved within our research with those presented in articles focused on the same or similar topics, namely, [20] and [21], several key differences stand out. The former paper offers semantic classification of the surface type, providing useful information for navigating a terrestrial robot. Importantly, the applied UGV is equipped with an obstacle avoidance system that can be especially helpful in environments with dynamically occurring obstacles. By contrast, however, the authors do not utilize any sophisticated aerial data processing method to recognize multiple points of interest (POI) on the ground. The latter article introduces algorithms that exploit the measured spectra in selecting the POIs to perform information-driven localization of a single source; advantageously, the authors also compare multiple methods applicable for the given purpose. Considering the outcomes of these two research projects, we can stress that the novelty and benefit of our concept consist in other aspects, defined as follows: the terrain- following capability and directly georeferenced photogrammetry delivered by the UAS; automatic selection of the ROIs; and higher-accuracy, isotope-independent localization of multiple sources, performed with a UGV whose navigation and trajectory planning are fully autonomous (except for the necessity to validate the obstacle map by an operator). Finally, it is worth mentioning in the given context that the whole experiment was completed in a single day.

E.6. Conclusion

Using relevant experiments, this paper verified a concept of exploiting aerial and terrestrial robotic platforms to localize uncontrolled radiation sources in a previously unknown outdoor area. After completing the three phases of the designed survey process, we found four of the eight radionuclides (or three of the four significant ones); the achieved accuracy was below 0.2 m, a value sufficient to support subsequent steps such as the removal of the sources from the area. The experiment was implemented in 24 hours, including the elimination of various technical issues. Theoretically, the area of 20,000 m^2 can be explored in only 4 hours, assuming conditions similar to those presented herein. To complete the entire task smoothly, however, the system would require further modifications. In this context, there remain major constraints as related to the weather, environment, radiological situation, and other relevant aspects: The systems must operate in adequate flight conditions, and satisfactory GNSS reception as well as the accessibility of a significant part of the area

to the UGV need to be ensured. Moreover, the radiation intensities have to be well detectable yet not hazardous for the electronics. At this point, it is also vital to emphasize that the cooperation between aerial and terrestrial robots should be promoted because the same results cannot be achieved with one of the variants only; a UAS, for example, is incapable of ensuring either conclusive localization accuracy or differentiation between sources concentrated within an area of hundreds of square meters. By contrast, a UGV, if operated without the aerial data, has to explore the inspected area globally, and the lack of an obstacle map causes serious navigation problems, especially where the applied vehicle is not equipped with an evasion module. Our future research will be directed towards employing information-driven localization and fitting the UGV with an obstacle avoidance system.

Bibliography

[1] Ioannis Tsitsimpelis, C. James Taylor, Barry Lennox, and Malcolm J. Joyce. A review of ground-based robotic systems for the characterization of nuclear environments. *Progress in Nuclear Energy*, 111:109–124, March 2019. URL: http://www.sciencedirect.com/science/article/pii/S0149197018302750, doi:10.1016/j.pnucene.2018.10.023.

[2] Kui Qian, Aiguo Song, Jiatong Bao, and Huatao Zhang. Small Teleoperated Robot for Nuclear Radiation and Chemical Leak Detection. *International Journal of Advanced Robotic Systems*, 9(3):70, 2012. ISSN: 1729-8814. URL: https://journals.sagepub.com/doi/10.5772/50720, doi:10.5772/50720.

[3] Roberto Guzman, Roman Navarro, Juan Ferre, and Miguel Moreno. RESCUER: Development of a Modular Chemical, Biological, Radiological, and Nuclear Robot for Intervention, Sampling, and Situation Awareness. *Journal of Field Robotics*, 33(7):931–945, 2016. ISSN: 1556-4967. URL: https://onlinelibrary.wiley.com/doi/abs/10.1002/rob.21588, doi:10.1002/rob.21588.

[4] Christian Ducros, Grard Hauser, Najib Mahjoubi, Philippe Girones, Laurence Boisset, Antoine Sorin, Eric Jonquet, Jean Michel Falciola, and Albert Benhamou. RICA: A Tracked Robot for Sampling and Radiological Characterization in the Nuclear Field. *Journal of Field Robotics*, 34(3):583–599, 2017. ISSN: 1556-4967. URL: https://onlinelibrary.wiley.com/doi/abs/10.1002/rob.21650, doi:10.1002/rob.21650.

[5] Keiji Nagatani, Seiga Kiribayashi, Yoshito Okada, Kazuki Otake, Kazuya Yoshida, Satoshi Tadokoro, Takeshi Nishimura, Tomoaki Yoshida, Eiji Koyanagi, Mineo Fukushima, and Shinji Kawatsuma. Emergency response to the nuclear accident at the Fukushima Daiichi Nuclear Power Plants using mobile rescue robots. *Journal of Field Robotics*, 30(1):44–63, 2013. ISSN: 1556-4967. URL: https://onlinelibrary.wiley.com/doi/abs/10.1002/rob.21439, doi:10.1002/rob.21439.

[6] Frank E. Schneider and Dennis Wildermuth. An autonomous unmanned vehicle for CBRNE reconnaissance. In *2011 12th International Carpathian Control Conference (ICCC)*, pages 347–352, May 2011. URL: https://ieeexplore.ieee.org/document/5945877, doi:10.1109/CarpathianCC.2011.5945877.

[7] M. E. Hosmar, S. B. Nokleby, and E. Waller. Experimental Testing of an Autonomous Radiation Mapping Robot. In *2017 CCToMM M3 Symposium*, 2017. [cit. 2020-3-27]. URL: http://www.cctomm.ca/2017/110.pdf.

[8] Maozhen Wang, Xianchao Long, Peng Chang, and Takln Padlr. Autonomous Robot Navigation with Rich Information Mapping in Nuclear Storage Environments. In *2018 IEEE International Symposium on Safety, Security, and Rescue Robotics (SSRR)*, pages 1–6, August 2018. ISSN: 2475-8426. URL: https://ieeexplore.ieee.org/document/8468634, doi:10.1109/SSRR.2018.8468634.

[9] Shin-ichi Okuyama, Tatsuo Torii, Akihiko Suzuki, Masanori Shibuya, and Nobuyuki Miyazaki. A Remote Radiation Monitoring System Using an Autonomous Unmanned Helicopter for Nuclear Emergencies. *Journal of Nuclear Science and Technology*, 45(sup5):414–416, June 2008. ISSN: 0022-3131. URL: https://www.tandfonline.com/doi/abs/10.1080/00223131.2008.10875877, doi:10.1080/00223131.2008.10875877.

[10] Yukihisa Sanada and Tatsuo Torii. Aerial radiation monitoring around the Fukushima Dai-ichi nuclear power plant using an unmanned helicopter. *Journal of Environmental Radioactivity*, 139:294–299, January 2015. URL: http://www.sciencedirect.com/science/article/pii/S0265931X14001994, doi:10.1016/j.jenvrad.2014.06.027.

[11] Yukihisa Sanada, Tadashi Orita, and Tatsuo Torii. Temporal variation of dose rate distribution around the Fukushima Daiichi nuclear power station using unmanned helicopter. *Applied Radiation and Isotopes*, 118:308–316, December 2016. URL: http://www.sciencedirect.com/science/article/pii/S0969804316306868, doi:10.1016/j.apradiso.2016.09.008.

[12] P. G. Martin, S. Kwong, N. T. Smith, Y. Yamashiki, O. D. Payton, F. S. Russell-Pavier, J. S. Fardoulis, D. A. Richards, and T. B. Scott. 3D unmanned aerial vehicle radiation mapping for assessing contaminant distribution and mobility. *International Journal of Applied Earth Observation and Geoinformation*, 52:12–19, October 2016. URL: http://www.sciencedirect.com/science/article/pii/S0303243416300733, doi:10.1016/j.jag.2016.05.007.

[13] J. W. MacFarlane, O. D. Payton, A. C. Keatley, G. P. T. Scott, H. Pullin, R. A. Crane, M. Smilion, I. Popescu, V. Curlea, and T. B. Scott. Lightweight aerial vehicles for monitoring, assessment and mapping of radiation anomalies. *Journal of Environmental Radioactivity*, 136:127–130, October 2014. URL: http://www.sciencedirect.com/science/article/pii/S0265931X14001489, doi:10.1016/j.jenvrad.2014.05.008.

[14] D. T. Connor, P. G. Martin, N. T. Smith, L. Payne, C. Hutson, O. D. Payton, Y. Yamashiki, and T. B. Scott. Application of airborne photogrammetry for the visualisation and assessment of contamination migration arising from a Fukushima waste storage facility. *Environmental Pollution*, 234:610–619, March 2018. URL: http://www.sciencedirect.com/science/article/pii/S0269749117323357, doi:10.1016/j.envpol.2017.10.098.

[15] Kai Vetter, Ross Barnowski, Joshua W. Cates, Andrew Haefner, Tenzing H. Y. Joshi, Ryan Pavlovsky, and Brian J. Quiter. Advances in Nuclear Radiation Sensing: Enabling 3-D Gamma-Ray Vision. *Sensors*, 19(11):2541, January 2019. URL: https://www.mdpi.com/1424-8220/19/11/2541, doi:10.3390/s19112541.

[16] P. G. Martin, O. D. Payton, J. S. Fardoulis, D. A. Richards, and T. B. Scott. The use of unmanned aerial systems for the mapping of legacy uranium mines. *Journal of Environmental Radioactivity*, 143:135–140, May 2015. URL: http://www.sciencedirect.com/science/article/pii/S0265931X15000314, doi:10.1016/j.jenvrad.2015.02.004.

[17] Frank Mascarich, Taylor Wilson, Christos Papachristos, and Kostas Alexis. Radiation Source Localization in GPS-Denied Environments Using Aerial Robots. In *2018 IEEE International Conference on Robotics and Automation (ICRA)*, pages 6537–6544, 2018. ISSN: 2577-087X. URL: https://ieeexplore.ieee.org/document/8460760, doi:10.1109/ICRA.2018.8460760.

[18] Tomas Baca, Martin Jilek, Petr Manek, Petr Stibinger, Vladimir Linhart, Jan Jakubek, and Martin Saska. Timepix Radiation Detector for Autonomous Radiation Localization and Mapping by Micro Unmanned Vehicles. In *2019 IEEE/RSJ International Conference on Intelligent Robots and Systems (IROS)*, pages 1129–1136, November 2019. ISSN: 2153-0866. URL: https://ieeexplore.ieee.org/document/8968514, doi:10.1109/IROS40897.2019.8968514.

[19] Kevin Kochersberger, Kenneth Kroeger, Bryan Krawiec, Eric Brewer, and Thomas Weber. Post-disaster Remote Sensing and Sampling via an Autonomous Helicopter. *Journal of Field Robotics*, 31(4):510–521, 2014. ISSN: 1556-4967. URL: https://onlinelibrary.wiley.com/doi/abs/10.1002/rob.21502, doi:10.1002/rob.21502.

[20] Gordon Christie, Adam Shoemaker, Kevin Kochersberger, Pratap Tokekar, Lance McLean, and Alexander Leonessa. Radiation search operations using scene understanding with autonomous UAV and UGV. *Journal of Field Robotics*, 34(8):1450–1468, November 2017. ISSN: 1556-4959. URL: https://onlinelibrary-wiley-com.ezproxy.lib.vutbr.cz/doi/full/10.1002/rob.21723, doi:10.1002/rob.21723.

[21] John Peterson, Weilin Li, Brian CesarTondreau, John Bird, Kevin Kochersberger, Wojciech Czaja, and Morgan McLean. Experiments in unmanned aerial vehicle/unmanned ground vehicle radiation search. *Journal of Field Robotics*, 36(4):818–845, 2019. ISSN: 1556-4967. URL: https://onlinelibrary.wiley.com/doi/abs/10.1002/rob.21867, doi:10.1002/rob.21867.

[22] E. w Bai, K. Yosief, S. Dasgupta, and R. Mudumbai. The maximum likelihood estimate for radiation source localization: Initializing an iterative search. In *53rd IEEE Conference on Decision and Control*, pages 277–282, December 2014. URL: https://ieeexplore.ieee.org/document/7039394, doi:10.1109/CDC.2014.7039394.

[23] H. I. Lin and H. J. Tzeng. Searching a radiological source by a mobile robot. In *2015 International Conference on Fuzzy Theory and Its Applications (iFUZZY)*, pages 1–5, November 2015. doi:10.1109/iFUZZY.2015.7391884.

[24] J. C. Chin, D. K. Y. Yau, and N. S. V. Rao. Efficient and Robust Localization of Multiple Radiation Sources in Complex Environments. In *2011 31st International Conference on Distributed Computing Systems*, pages 780–789, June 2011. URL: https://ieeexplore.ieee.org/document/5961730, doi:10.1109/ICDCS.2011.94.

[25] C. Liu, P. L. Drouin, G. St-Jean, M. Dziel, and D. Waller. Wireless Radiation Sensor Network with directional radiation detectors. In *2014 IEEE Nuclear Science Symposium and Medical Imaging Conference (NSS/MIC)*, pages 1–6, November 2014. URL: https://ieeexplore.ieee.org/document/7431111, doi:10.1109/NSSMIC.2014.7431111.

[26] A. A. R. Newaz, S. Jeong, and N. Y. Chong. Fast radioactive hotspot localization using a UAV. In *2016 IEEE International Conference on Simulation, Modeling, and Programming for Autonomous Robots (SIMPAR)*, pages 9–15, December 2016. URL: https://ieeexplore.ieee.org/document/7862348, doi:10.1109/SIMPAR.2016.7862348.

[27] Jerry Towler, Bryan Krawiec, and Kevin Kochersberger. Radiation Mapping in Post-Disaster Environments Using an Autonomous Helicopter. *Remote Sensing*, 4(7):1995–2015, July 2012. URL: http://www.mdpi.com/2072-4292/4/7/1995, doi:10.3390/rs4071995.

[28] N. Pinkam, S. Jeong, and N. Y. Chong. Exploration of a group of mobile robots for multiple radiation sources estimation. In *2016 IEEE International Symposium on Robotics and Intelligent Sensors (IRIS)*, pages 199–206, December 2016. URL: https://ieeexplore.ieee.org/document/8066091, doi:10.1109/IRIS.2016.8066091.

[29] A. Gunatilaka, B. Ristic, and R. Gailis. On Localisation of a Radiological Point Source. In *2007 Information, Decision and Control*, pages 236–241, 2007. URL: https://ieeexplore.ieee.org/document/4252508, doi:10.1109/IDC.2007.374556.

[30] M. R. Morelande and B. Ristic. Radiological Source Detection and Localisation Using Bayesian Techniques. *IEEE Transactions on Signal Processing*, 57(11):4220–4231, November 2009. ISSN: 1053-587X. URL: https://ieeexplore.ieee.org/document/5153354, doi:10.1109/TSP.2009.2026618.

[31] M. R. Morelande and A. Skvortsov. Radiation field estimation using a Gaussian mixture. In *2009 12th International Conference on Information Fusion*, pages 2247–2254, July 2009. ISBN: 978-0-9824-4380-4. URL: https://ieeexplore.ieee.org/document/5203720.

[32] C. Mendis, A. Gunatilaka, B. Ristic, S. Karunasekera, and A. Skvortsov. Experimental verification of evolutionary estimation algorithms for radioactive source localisation. In *2009 International Conference on Intelligent Sensors, Sensor Networks and Information Processing (ISSNIP)*, pages 151–156, December 2009. URL: https://ieeexplore.ieee.org/document/5416811, doi:10.1109/ISSNIP.2009.5416811.

[33] A. Gunatilaka, B. Ristic, and M. Morelande. Experimental verification of algorithms for detection and estimation of radioactive sources. In *2010 13th International Conference on Information Fusion*, pages 1–8, July 2010. URL: https://ieeexplore.ieee.org/document/5711880, doi:10.1109/ICIF.2010.5711880.

[34] Branko Ristic, Mark Morelande, and Ajith Gunatilaka. Information driven search for point sources of gamma radiation. *Signal Processing*, 90(4):1225–1239, April 2010. URL: http://www.sciencedirect.com/science/article/pii/S0165168409004277, doi:10.1016/j.sigpro.2009.10.006.

[35] Sergio Zimmermann. Active microphonic noise cancellation in radiation detectors. *Nuclear Instruments and Methods in Physics Research Section A: Accelerators, Spectrometers, Detectors and Associated Equipment*, 729:404–409, November 2013. URL: http://www.sciencedirect.com/science/article/pii/S0168900213008930, doi:10.1016/j.nima.2013.06.060.

[36] F. Burian, L. Zalud, P. Kocmanova, T. Jilek, and L. Kopecny. Multi-robot system for disaster area exploration. volume 184, pages 263–274, June 2014. URL: http://library.witpress.com/viewpaper.asp?pcode=FRIAR14-022-1, doi:10.2495/FRIAR140221.

[37] Lukas Nejdl, Jiri Kudr, Branislav Ruttkay-Nedecky, Zbynek Heger, Lukas Zima, Ludek Zalud, Sona Krizkova, Vojtech Adam, Marketa Vaculovicova, and Rene Kizek. Remote-Controlled Robotic Platform for Electrochemical Determination of Water Contaminated by Heavy Metal Ions. *International Journal of Electrochemical Science*, 10(4):3635–3643, April 2015. ISSN: 1452-3981. URL: http://www.electrochemsci.org/papers/vol10/100403635.pdf.

[38] T. Jilek. Radiation intensity mapping in outdoor environments using a mobile robot with RTK GNSS. In *International Conference on Military Technologies (ICMT) 2015*, pages 1–7. IEEE, May 2015. doi:10.1109/MILTECHS.2015.7153755.

[39] Petr Gabrlik, Anders la Cour-Harbo, Petra Kalvodova, Ludek Zalud, and Premysl Janata. Calibration and accuracy assessment in a direct georeferencing system for UAS photogrammetry. *International Journal of Remote Sensing*, 39(15-16):4931–4959, August 2018. URL: https://doi.org/10.1080/01431161.2018.1434331, doi:10.1080/01431161.2018.1434331.

[40] Petr Gabrlik and Tomas Lazna. Simulation of a Gamma Radiation Mapping Using Unmanned Aerial System. In *IFAC-PapersOnLine*, volume 51, pages 256–262, Amsterdam, May 2018. Elsevier. URL: http://www.sciencedirect.com/science/article/pii/S2405896318309091, doi:10.1016/j.ifacol.2018.07.163.

[41] Tomas Lazna, Petr Gabrlik, Tomas Jilek, and Ludek Zalud. Cooperation between an unmanned aerial vehicle and an unmanned ground vehicle in highly accurate localization of gamma radiation hotspots. *International Journal of Advanced Robotic Systems*, 15(1):1–16, January 2018. URL: https://doi.org/10.1177/1729881417750787, doi:10.1177/1729881417750787.

[42] CUZK. CUZK - Geoportal, 2010. [cit. 2017-3-15. URL: http://geoportal.cuzk.cz.

[43] Jorge Torres-Snchez, Francisca Lpez-Granados, Irene Borra-Serrano, and Jos Manuel Pea. Assessing UAV-collected image overlap influence on computation time and digital surface model accuracy in olive orchards. *Precision Agriculture*, pages 1–19, February 2017. URL: https://link.springer.com/article/10.1007/s11119-017-9502-0, doi:10.1007/s11119-017-9502-0.

[44] D. Belton, P. Helmholz, J. Long, and A. Zerihun. Crop Height Monitoring Using a Consumer-Grade Camera and UAV Technology. *PFG Journal of Photogrammetry, Remote Sensing and Geoinformation Science*, 87(5):249–262, December 2019. URL: https://doi.org/10.1007/s41064-019-00087-8, doi:10.1007/s41064-019-00087-8.

[45] Tom Mikita, Pemysl Janata, and Peter Surov. Forest Stand Inventory Based on Combined Aerial and Terrestrial Close-Range Photogrammetry. *Forests*, 7(8):165, July 2016. URL: http://www.mdpi.com/1999-4907/7/8/165, doi:10.3390/f7080165.

[46] Mike R. James, Stuart Robson, and Mark W. Smith. 3-D uncertainty-based topographic change detection with structure-from-motion photogrammetry: precision maps for ground control and directly georeferenced surveys. *Earth Surface Processes and Landforms*, 42:1769–1788, January 2017. ISSN: 1096-9837. URL: http://onlinelibrary.wiley.com/doi/10.1002/esp.4125/abstract, doi:10.1002/esp.4125.

[47] Jitte Waagen. New technology and archaeological practice. Improving the primary archaeological recording process in excavation by means of UAS photogrammetry. *Journal of Archaeological Science*, 101:11–20, 2019. URL: http://www.sciencedirect.com/science/article/pii/S0305440318306423, doi:https://doi.org/10.1016/j.jas.2018.10.011.

[48] Military Technical Institute. BRUS Unmanned Aerial Vehicle, 2018. [cit. 2018-10-24]. URL: http://www.vtusp.cz/en/a/brus-unmanned-aerial-vehicle.

[49] Petr Gabrlik, Premysl Janata, Ludek Zalud, and Josef Harcarik. Towards Automatic UAS-Based Snow-Field Monitoring for Microclimate Research. *Sensors*, 19(8):1945, January 2019. URL: https://www.mdpi.com/1424-8220/19/8/1945, doi:10.3390/s19081945.

[50] C. Eling, M. Wieland, C. Hess, L. Klingbeil, and H. Kuhlmann. Development and Evaluation of a UAV Based Mapping System for Remote Sensing and Surveying Applications. In *ISPRS - International Archives of the Photogrammetry, Remote Sensing and Spatial Information Sciences*, volume XL-1/W4, pages 233–239, August 2015. URL: http://www.int-arch-photogramm-remote-sens-spatial-inf-sci.net/XL-1-W4/233/2015/, doi:10.5194/isprsarchives-XL-1-W4-233-2015.

[51] D. P. Bliakharskii, I. V. Florinsky, and T. N. Skrypitsyna. Modelling glacier topography in Antarctica using unmanned aerial survey: assessment of opportunities. *International Journal of Remote Sensing*, 40(7):2517–2541, April 2019. ISSN: 0143-1161. URL: https://www.tandfonline.com/doi/full/10.1080/01431161.2019.1584926, doi:10.1080/01431161.2019.1584926.

[52] Seyyed Meghdad Hasheminasab, Tian Zhou, and Ayman Habib. GNSS/INS-Assisted Structure from Motion Strategies for UAV-Based Imagery over Mechanized Agricultural Fields. *Remote Sensing*, 12(3):351, January 2020. URL: https://www.mdpi.com/2072-4292/12/3/351, doi:10.3390/rs12030351.

[53] Petra Kocmanova and Ludek Zalud. Effective Calibration and Evaluation of Multi-Camera Robotic Head. *International Journal of Advanced Computer Science and Applications*, 6:143–152, October 2015. URL: https://thesai.org/Publications/ViewPaper?Volume=6&Issue=10&Code=ijacsa&SerialNo=20, doi:10.14569/IJACSA.2015.061020.

[54] Ludek Zalud, Lukas Kopecny, and Frantisek Burian. Orpheus Reconnissance Robots. In *2008 IEEE International Workshop on Safety, Security and Rescue Robotics*, pages 31–34, October 2008. ISSN: 2374-3247. doi:10.1109/SSRR.2008.4745873.

[55] T. Jilek. *Advanced Navigation in Heterogeneous Multi-robot Systems in Outdoor Environment.* PhD thesis, Brno University of Technology, Technicka 10, Brno, Czech Republic, 12 2015. URL: https://dspace.vutbr.cz/handle/11012/51783.

[56] Syed Naeem Ahmed. *Physics and Engineering of Radiation Detection.* Academic Press, Amsterdam, April 2007. ISBN: 978-0-12-045581-2.

[57] Glenn F. Knoll. *Radiation Detection and Measurement.* John Wiley & Sons, Hoboken, New Jersey, 3rd edition edition, August 2010. ISBN: 978-0-470-13148-0.

[58] Karl Kraus. *Photogrammetry: Geometry from Images and Laser Scans.* Walter de Gruyter, 2007. ISBN: 978-3-11-019007-6.

[59] Tau M. Cabreira, Lisane B. Brisolara, and Paulo R. Ferreira Jr. Survey on Coverage Path Planning with Unmanned Aerial Vehicles. *Drones*, 3(1):4, March 2019. URL: https://www.mdpi.com/2504-446X/3/1/4, doi:10.3390/drones3010004.

[60] Richard Hartley and Andrew Zisserman. *Multiple View Geometry in Computer Vision*, volume 2nd ed. Cambridge University Press, Cambridge, 2003. ISBN: 978-0-521-54051-3. URL: https://www.cambridge.org/core/books/multiple-view-geometry-in-computer-vision/0B6F289C78B2B23F596CAA76D3D43F7A, doi:10.1017/CBO9780511811685.

[61] Richard Szeliski. *Computer Vision: Algorithms and Applications*. Texts in Computer Science. Springer, London, 2011. ISBN: 978-1-84882-934-3. URL: www.springer.com/gp/book/9781848829343.

[62] G. Verhoeven, M. Doneus, Ch. Briese, and F. Vermeulen. Mapping by matching: a computer vision-based approach to fast and accurate georeferencing of archaeological aerial photographs. *Journal of Archaeological Science*, 39(7):2060–2070, July 2012. URL: http://www.sciencedirect.com/science/article/pii/S0305440312000866, doi:10.1016/j.jas.2012.02.022.

[63] Valeria-Ersilia Oniga, Ana-Ioana Breaban, Norbert Pfeifer, and Constantin Chirila. Determining the Suitable Number of Ground Control Points for UAS Images Georeferencing by Varying Number and Spatial Distribution. *Remote Sensing*, 12(5):876, January 2020. URL: https://www.mdpi.com/2072-4292/12/5/876, doi:10.3390/rs12050876.

[64] Mozhdeh Shahbazi, Gunho Sohn, Jrme Thau, and Patrick Menard. Development and Evaluation of a UAV-Photogrammetry System for Precise 3d Environmental Modeling. *Sensors*, 15(11):27493–27524, November 2015. URL: https://www.mdpi.com/1424-8220/15/11/27493, doi:10.3390/s151127493.

[65] H. Fazeli, F. Samadzadegan, and F. Dadrasjavan. Evaluating the Potential of RTK-UAV for Automatic Point Cloud Generation in 3d Rapid Mapping. In *ISPRS - International Archives of the Photogrammetry, Remote Sensing and Spatial Information Sciences*, volume XLI-B6, pages 221–226. Copernicus GmbH, June 2016. URL: http://www.int-arch-photogramm-remote-sens-spatial-inf-sci.net/XLI-B6/221/2016/, doi:10.5194/isprs-archives-XLI-B6-221-2016.

[66] Isaac Amidror. Scattered data interpolation methods for electronic imaging systems: a survey. *Journal of Electronic Imaging*, 11(2):157–176, 2002. URL: http://molly.magic.rit.edu/~mac/test/paper_pdf.pdf.

[67] C. Maple. Geometric design and space planning using the marching squares and marching cube algorithms. In *2003 International Conference on Geometric Modeling and Graphics, 2003. Proceedings*, pages 90–95, July 2003. ISBN: 0-7695-1985-7. doi:10.1109/GMAG.2003.1219671.

[68] Jyh-Ming Lien. Covering Minkowski sum boundary using points with applications. *Computer Aided Geometric Design*, 25(8):652–666, November 2008. URL: http://www.sciencedirect.com/science/article/pii/S0167839608000423, doi:10.1016/j.cagd.2008.06.006.

[69] P. E. Hart, N. J. Nilsson, and B. Raphael. A formal basis for the heuristic determination of minimum cost paths. *IEEE Transactions on Systems Science and Cybernetics*, 4(2):100–107, 1968. URL: https://ieeexplore.ieee.org/document/4082128, doi:10.1109/TSSC.1968.300136.

[70] Lifeng He, Yuyan Chao, Kenji Suzuki, and Kesheng Wu. Fast connected-component labeling. *Pattern Recognition*, 42(9):1977–1987, September 2009. URL: http://www.sciencedirect.com/science/article/pii/S0031320308004573, doi:10.1016/j.patcog.2008.10.013.

[71] Howie Choset. Coverage of Known Spaces: The Boustrophedon Cellular Decomposition. *Autonomous Robots*, 9(3):247–253, December 2000. URL: https://link.springer.com/article/10.1023/A:1008958800904, doi:10.1023/A:1008958800904.

[72] Han-Pang Huang and Shu-Yun Chung. Dynamic visibility graph for path planning. In *2004 IEEE/RSJ International Conference on Intelligent Robots and Systems (IROS)*, volume 3, pages 2813–2818 vol.3, September 2004. ISSN: null. doi:10.1109/IROS.2004.1389835.

[73] Peter Deuflhard. Least Squares Problems: Gauss-Newton Methods. In *Newton Methods for Nonlinear Problems*, Springer Series in Computational Mathematics, pages 173–231. Springer, Berlin, Heidelberg, 2011. URL: https://link.springer.com/chapter/10.1007/978-3-642-23899-4_4, doi:10.1007/978-3-642-23899-4_4.

[74] Einar S. Ueland, Roger Skjetne, and Andreas R. Dahl. Marine Autonomous Exploration Using a Lidar and SLAM. volume 6 of *International Conference on Offshore Mechanics and Arctic Engineering*, 6 2017. URL: https://asmedigitalcollection.asme.org/OMAE/proceedings-abstract/OMAE2017/57724/V006T05A029/281072, doi:10.1115/OMAE2017-61880.

Part III.

Appendices

A. List of Author's Publications

Journal Articles With Impact Factor

GABRLIK, Petr, Premysl JANATA, Ludek ZALUD and Josef HARCARIK, Josef. Towards Automatic UAS-Based Snow-Field Monitoring for Microclimate Research. *Sensors* [online]. 2019, **19**(8), 1–23 [cit. 2020-08-25]. DOI: 10.3390/s19081945. ISSN 1424-8220. Available from: `https://www.mdpi.com/1424-8220/19/8/1945`

GABRLIK, Petr, Anders la COUR-HARBO, Petra KALVODOVA, Ludek ZALUD and Premysl JANATA. Calibration and accuracy assessment in a direct georeferencing system for UAS photogrammetry. *International Journal of Remote Sensing* [online]. 2018, **39**(15–16), 4931–4959 [cit. 2020-08-25]. DOI: 10.1080/01431161.2018.1434331. ISSN 0143-1161. Available from: `https://www.tandfonline.com/doi/full/10.1080/01431161.2018.1434331`

LAZNA, Tomas, Petr GABRLIK, Tomas JILEK and Ludek ZALUD. Cooperation between an unmanned aerial vehicle and an unmanned ground vehicle in highly accurate localization of gamma radiation hotspots. *International Journal of Advanced Robotic Systems* [online]. 2018, **15**(1), 1–16 [cit. 2020-08-25]. DOI: 10.1177/1729881417750787. ISSN 1729-8814. Available from: `http://journals.sagepub.com/doi/10.1177/1729881417750787`

Scopus/WoS Indexed Articles

LAZNA, Tomas, Petr GABRLIK, Tomas JILEK and Frantisek BURIAN. Simulating UAS-Based Radiation Mapping on a Building Surface. In: *Modelling and Simulation for Autonomous Systems* [online]. Cham: Springer, 2020, pp. 130–147 [cit. 2020-08-25]. Lecture Notes in Computer Science, 11995. DOI: 10.1007/978-3-030-43890-6_11. ISBN 978-3-030-43889-0. Available from: `http://link.springer.com/10.1007/978-3-030-43890-6_11`

GABRLIK, Petr. Boresight Calibration of a Multi-Sensor System for UAS Photogrammetry. In: *2018 ELEKTRO* [online]. Piscataway (NJ): IEEE, 2018, pp. 1–6 [cit. 2020-08-25]. DOI: 10.1109/ELEKTRO.2018.8398362. ISBN 978-1-5386-4759-2. Available from: `https://ieeexplore.ieee.org/document/8398362/`

GABRLIK, Petr and Tomas LAZNA. Simulation of Gamma Radiation Mapping Using an Unmanned Aerial System. In: *IFAC-PapersOnLine* [online]. Amsterdam: Elsevier, 2018, pp. 256–262 [cit. 2020-08-25]. DOI: 10.1016/j.ifacol.2018.07.163. ISSN 2405-8963. Available from: https://linkinghub.elsevier.com/retrieve/pii/S2405896318309091

LAZNA, Tomas, Tomas JILEK, Petr GABRLIK and Ludek ZALUD. Multi-robotic Area Exploration for Environmental Protection. In: *Industrial Applications of Holonic and Multi-Agent Systems* [online]. Cham: Springer, 2017, pp. 240–254 [cit. 2020-08-25]. Lecture Notes in Computer Science, 10444. DOI: 10.1007/978-3-319-64635-0_18. ISBN 978-3-319-64635-0. ISSN 1611-3349. Available from: http://link.springer.com/10.1007/978-3-319-64635-0_18

GABRLIK, Petr, Ales JELINEK and Premysl JANATA. Precise Multi-Sensor Georeferencing System for Micro UAVs. In: *IFAC-PapersOnLine* [online]. Cham: Elsevier, 2016, pp. 170–175 [cit. 2020-08-25]. DOI: 10.1016/j.ifacol.2016.12.029. ISSN 2405-8963. Available from: https://linkinghub.elsevier.com/retrieve/pii/S2405896316326659

GABRLIK, Petr. The Use of Direct Georeferencing in Aerial Photogrammetry with Micro UAV. In: *IFAC-PapersOnLine* [online]. Cham: Elsevier, 2015, pp. 380–385 [cit. 2020-08-25]. DOI: 10.1016/j.ifacol.2015.07.064. ISSN 2405-8963. Available from: https://linkinghub.elsevier.com/retrieve/pii/S2405896315008393

KRIZ, Vlastimil and Petr GABRLIK. UranusLink - Communication Protocol for UAV with Small Overhead and Encryption Ability. In: *IFAC-PapersOnLine* [online]. Cham: Elsevier, 2015, pp. 474–479 [cit. 2020-08-25]. DOI: 10.1016/j.ifacol.2015.07.080. ISSN 2405-8963. Available from: https://linkinghub.elsevier.com/retrieve/pii/S2405896315008551

GABRLIK, Petr, Vlastimil KRIZ, Jan VOMOCIL and Ludek ZALUD. The Design and Implementation of Quadrotor UAV. In: *Emergent Trends in Robotics and Intelligent Systems* [online]. Cham: Springer, 2015, pp. 47–56 [cit. 2020-08-25]. Advances in Intelligent Systems and Computing, 316. DOI: 10.1007/978-3-319-10783-7_5. ISBN 978-3-319-10782-0. Available from: http://link.springer.com/10.1007/978-3-319-10783-7_5

GABRLIK, Petr, Jan VOMOCIL and Ludek ZALUD. The Design and Implementation of 4 DOF Control of the Quadrotor. In: *IFAC Proceedings Volumes* [online]. Cham: Elsevier, 2013, pp. 68–73 [cit. 2020-08-25]. DOI: 10.3182/20130925-3-CZ-3023.00047. ISSN 1474-6670. Available from: https://linkinghub.elsevier.com/retrieve/pii/S1474667015373006

Other Publications

GABRLIK, Petr, Tomas LAZNA, Tomas JILEK, Petr SLADEK and Ludek ZALUD. Using an Automated Heterogeneous Robotic System for Radiation Surveys. *arXiv* [online]. Cornell University, 2020, 1–32 [cit. 2020-08-25]. Available from: http://arxiv.org/abs/2006.16066

GABRLIK, Petr. Transformation of UAV Attitude and Position for Use in Direct Georeferencing. In: *Proceedings of the 22nd Conference STUDENT EEICT 2016* [online]. Brno: Brno University of Technology, 2016, pp. 451–455 [cit. 2020-08-25]. ISBN 978-80-214-5350-0. Available from: http://hdl.handle.net/11012/83974

GABRLIK, Petr, Vlastimil KRIZ and Ludek ZALUD. Reconnaissance micro UAV system. In: *Acta Polytechnica CTU Proceedings* [online]. Prague: Czech Technical University in Prague, 2015, pp. 15–21 [cit. 2020-08-25]. DOI: 10.14311/APP.2015.1.0015. ISSN 2336-5382. Available from: https://ojs.cvut.cz/ojs/index.php/APP/article/view/3395

GABRLIK, Petr. The Techniques of Terrain Mapping and Modeling Using UAVs. In: *Proceedings of the 20th Conference STUDENT EEICT 2014* [online]. Brno: Brno University of Technology, 2014, pp. 1–5 [cit. 2020-08-25]. Available from: https://www.fekt.vut.cz/conf/EEICT/archiv/sborniky/EEICT_2014_sbornik/03doktorskeprojekty/03kybernetikaaautomatizace/03-xgabrl00@stud.feec.vutbr.cz.pdf

GABRLIK, Petr. Qadrocopter - Stabilisation and Control. In: *Proceedings of the 17th Conference STUDENT EEICT 2011* [online]. Brno: Brno University of Technology, 2011, pp. 1–3 [cit. 2020-08-26]. Available from: https://www.fekt.vut.cz/conf/EEICT/archiv/sborniky/EEICT_2011_sbornik/02-Magisterske%20projekty/03-Kybernetika%20a%20automatizace/03-xgabrl00.pdf